# IMPACTS OF BIOGENIC AND ANTHROPOGENIC EMISSIONS ON OZONE AND SECONDARY ORGANIC AEROSOL

A Dissertation

by

PENG WANG

Submitted to the Office of Graduate and Professional Studies of
Texas A&M University
in partial fulfillment of the requirements for the degree of

DOCTOR OF PHILOSOPHY

| | |
|---|---|
| Chair of Committee, | Qi Ying |
| Committee Members, | Bill Batchelor |
| | Sarah Brooks |
| | Renyi Zhang |
| Head of Department, | Robin Autenrieth |

May 2018

Major Subject: Civil Engineering

# ABSTRACT

Atmospheric fine particles and ozone ($O_3$) are correlated with adverse health effects, visibility reduction, and climate change. In recent decades, China has suffered from the record-breaking severe haze event and elevated ozone problems. Recent field measurements show that organic carbon (OC) was one of the major components during haze events, and it has been suggested that secondary organic aerosol (SOA) could account for a significant fraction of the total observed OC. Quantitative knowledge of the contributions of different emissions sources to SOA and ozone concentrations is significant to better understand their formation mechanisms and is useful to develop the effective emission control strategies. A Community Multiscale Air Quality (CMAQ) model with source-oriented lumped SAPRC-11 (S11L) photochemical mechanism is applied to determine the contributions of anthropogenic and biogenic sources to SOA and ozone concentrations in China.

In China, predicted SOA concentrations are generally higher in summer (10-15 $\mu g \cdot m^{-3}$) due to large contributions of biogenic emissions within China (country average $\sim$60%) and in winter due to industrial and residential sectors (country average $\sim$78% total) based on the Multi-resolution Emission Inventory for China (MEIC) emission inventory. However, the transportation sector ($\sim$30-40% vs. $\sim$5% by MEIC) is predicted to be much more important while the residential ($\sim$21-24% vs. $\sim$42%) sector is predicted to be less important based on The Regional Emission inventory in ASia v2.1(REAS2) emissions. These discrepancies in source contributions to SOA needs to be further investigated as the country seeks optimal emission control strategies to fight severe air pollution.

The ozone attribution scheme based on the three-regime definition was incorporated into the CMAQ model to quantify NOx and VOC contributions to ozone concentrations in China in August 2013. Most of the areas considered by the two-regime approach as

NOx or VOC-limited are classified as transitional under the new three-regime scheme, and the scattered VOC-limited regimes are located in urban areas. This three-regime approach represents an improvement from the traditional two-regime approach with only NOx or VOC-limited regimes. This three-regime method then is applied in the ozone source apportionment as well, and it is reported that the industries, transportation, power and biogenic sources are four major emission contributors to ozone with different spatial distributions.

# DEDICATION

I would like to thank my committee chair, Dr. Qi Ying, and my committee members, Dr. Batchelor, Dr. Brooks, and Dr. Zhang for their guidance and support throughout the course of this research.

Thanks also go to my friends and colleagues and the department faculty and staff for making my time at Texas A&M University a great experience.

Finally, thanks to my mother and father for their encouragement and to my husband Dr. Han Cai for his patience and love. Han also helps me edit the format of the current dissertation.

CONTRIBUTORS AND FUNDING SOURCES

## Contributors

This work was supervised by a dissertation committee consisting of Professor Qi Ying (advisor) and Bill Batchelor from Department of Civil Engineering, Professor Sarah Brooks and Renyi Zhang from the Department of Atmospheric Sciences. All work for the dissertation was completed by the student, in collaboration with Qi Ying of the Department of Civil Engineering.

## Funding Sources

Graduate study was supported by Texas A&M Engineering Experiment Station (TEES) and Department of Civil Engineering of Texas A&M University. The computer simulations described in this thesis were conducted with the advanced computing resources provided by Texas A&M High Performance Research Computing.

TABLE OF CONTENTS

Page

LIST OF FIGURES

FIGURE Page

LIST OF TABLES

# 1. INTRODUCTION

Due to the fast economic development and rapid industrialization and urbanization in the past several decades, China suffers severe air pollution in many regions [1]. Secondary organic aerosol (SOA) contributes to a significant portion of the total observed organic aerosol [2, 3, 4]. However, modeling analyses of SOA formation in China have not been widely reported until recent years and most of the studies are for economically developed regions such as the Pearl River Delta (PRD) [5, 6, 7] and the mega city clusters in the east China [8] for relatively short durations. In most of the studies, SOA concentrations are significantly underestimated, partly due to missing significant SOA formation pathways. For example, recent experimental studies demonstrated that reactions on particle surfaces or with particle water under acidic conditions of certain compounds such as dicarbonyls (e.g. glyoxal, or GLY) and epoxydiols from isoprene lead to rapid formation of low volatile oligomers, organo-sulfate and organo-nitrates [9]. The GLY reactive surface uptake pathway to form SOA has been investigated in the PRD region and is shown to lead to significantly higher SOA predictions that better match with observations. Isoprene, which is mainly emitted from biogenic sources, can also be a significant contributor to SOA. Its oxidation products, epoxydiols (IEPOX) (under low NOx condition) and methacrylic acid epoxide (MAE) (under high NOx condition) [10], have been found to contribute to the formation of low-volatile organic products in aerosol water under strong acidic conditions [11, 12]. The isoprene pathway has been included in some recent modeling studies by applying a surface-controlled reactive uptake approach [13, 14] or a more mechanistic approach based on detailed aqueous reactions [12]. In these studies, it was found that the IEPOX could take up to about 34% of total isoprene SOA (iSOA) in summer [14]. $O_3$

However, most of the theses studies have focused on the North America region. Whether

these processes are important to SOA formation in China, especially regions with significant anthropogenic emissions, remains unclear. Modeling studies on source contributions to SOA or regional transport of SOA in China have also been reported theses years. Previous study [15] developed a vehicular emission inventory of Shanghai for the year of 2012 and estimated based on SOA yield that 40-60% OA production in Shanghai was due to vehicle emissions. This estimation was based on emissions only without chemical transport modeling. He et al [16] applied the CAMx model with updated SOA yields based on smog chamber studies [17] to study regional contributions to SOA in Beijing in the summer time. It stated that about 40.4% SOA was from the local emissions and the rest of the SOA was formed emissions outside Beijing. However, there is no complete picture of the contributions of different VOCs from different sources to SOA concentrations in China.

Due to the deteriorate air quality, ozone concentrations in many urban areas are high [18] and are showing increasing trends [19, 20, 21] that are projected to continue in future [22] in China. High levels of tropospheric ozone can adversely affect human [23, 24, 25] and ecosystems health [26, 27] and reduce crop yields [28, 29]. Thus, as ozone pollution gradually becomes a serious concern of the central and local governments and the public, a comprehensive evaluation and quantification of the sources that contributes to ozone is essential in formulating cost-effective emission control policies that co-benefit both PM and ozone reductions.

Tropospheric ozone is generated from nonlinear photochemical reactions involving VOCs and nitrogen oxides (NOx). Quantitative attribution of ozone formed to precursor NOx and VOCs from various emission sources is needed to help designing economically effective control measures. The effectiveness of NOx and VOC emission controls depends not only on the absolute concentration of the precursors but also their relative abundances. Based on the ozone isopleth, $O_3$ formation sensitivity to precursor emissions is typically classified as NOx-limited or VOC-limited. In the NOx-limited regime, NOx emission

control is considered more effective in reducing $O_3$. If ozone formation is in the VOC-limited regime, reducing NOx emissions are not effective and may inadvertently lead to increase of ozone. This two-regime classification scheme has become the foundation of the ozone source apportionment techniques implemented in current state-of-the-science chemical transport models (CTMs) such as the Ozone Source Apportionment Technique (OSAT) in CAMx [30] and Integrated Source Apportionment Method (ISAM) in CMAQ [31], which attribute in-situ ozone formation to either VOC or NOx sources based on the value of some ozone formation regime indicators, such as the production rate ratios of hydrogen peroxides to nitric acid ($pH_2O_2/pHNO_3$). A review of the regime indicators and the threshold values used in current source apportionment models can be found in Kwok et al. [31] and the references therein.

This designation of NOx- and VOC-limited regimes based on a single threshold value might be intrinsically inappropriate because ozone formation can be sensitive to both NOx and VOC controls and thus needs to be attributed to both NOx and VOC sources. The existence of this ŕransitionŕegime or ḿixed-controlŕegime of ozone formation can be theoretically proved based on analysis of ozone production efficiency or formation kinetics [32]. It is obvious in traditional ozone isopleth [33, 34] and sensitivity analyses designed to derive the threshold indicator values [35, 36]. In the transition regime, either NOx or VOC reduction leads to lower $O_3$ concentrations, thus it is also called a mixed-control regime. However, even though this transition regime of ozone formation is known to exist, no method has been developed to quantitatively split ozone formed in the transition regime to NOx and VOC sources in regional ozone source apportionment models.

Existing ozone formation and source apportionment studies in China mostly focused on three densely populated metropolitan areas, the Beijing-Tianjin-Hebei (BTH) region, the Yangtze River Delta (YRD) and the Pearl River Delta (PRD). Source contributions to ozone was studied using regular CTMs with a brute-force (BF) method that excludes emis-

sions from one source sector at a time and compare the resulted ozone concentrations with a base case simulation [37, 38]. However, due to non-linear dependence of ozone on precursor concentrations, the BF approach for ozone is usually considered less accurate due to its underlying linear assumption. Wang et al. [39] and Ying et al. [40] applied the Ozone Source Apportionment Technology (OSAT) in the Comprehensive Air Quality Model with Extensions (CAMx) to study local and regional contributions to ozone in Beijing (summer 2000) and the PRD region (summer and fall 2006), respectively. The OSAT attributes in-situ ozone formation to either NOx or VOC sources based on the value of an indicator that determines ozone formation sensitivity regime as NOx-limited or VOC-limited without tracking NOx and VOC related ozone attributed to different sectors or source regions using non-reactive tracers. A technique similar to OSAT has been incorporated into the coupled Weather Research and Forecasting/Chemistry (WRF/Chem) model by Zhang et al. [41] to attribute ozone to local and regional sources in the YRD region in May 2013. In Beijing, mobile and industrial sources are two leading sources of ozone followed by point and biogenic sources, as reported by Wang et al. [39]. In the PRD region, OSAT reported that motor vehicles and area source were the most important sources, and contributions from point and biogenic sources were also important [41].

Accurately estimating the influence of isoprene on regional and global air quality and climate requires accurate estimation of the emissions of isoprene from vegetated surfaces. For either regional or global scale air quality modeling studies, isoprene emissions are estimated via various biogenic emission modeling systems, such as the Global Biosphere Emissions and Interactions System (GloBEIS) [42], Biogenic Emissions Inventory System version 3 (BEIS3) [43] or Model of Emissions of Gases and Aerosols from Nature (MEGAN) [44, 45]. All the isoprene emission models are based on emission factors (EFs) of isoprene under standard temperature and photosynthetically active radiation (PAR) conditions. However, the EF data adopted by different models can be different, and slightly

differing algorithms are used to account for leaf temperatures, radiation levels, and soil moisture, among other factors, on the isoprene emission rates; together with influences of the selected biomass distribution, this can lead to very different estimates of isoprene emissions. It is unclear currently whether different EF fields will give significantly different emission estimations and which EF fields provides the best estimation on a regional scale.

The overall objective of this project is to investigate the impacts of anthropogenic and biogenic emissions on ozone and secondary organic aerosols in China, and to evaluate and improve the estimation of biogenic emissions using the MEGAN model. Chapter 2 is to investigate the contributions of different emission source sectors to SOA. Contributions of five major VOC sources (industry, wildfire, power, residential, and biogenic) to SOA in China will be determined. Chapter 3 is develop an improved ozone attribution technique that allows ozone formed in the transition regime to be attributed to NOx and VOC sources accordingly based on previously defined regime indicators. Chapter 4 is to investigate the contributions of different emission sources to ground-level ozone in China using a novel approach of determining NOx-limited or VOC-limited ozone formation regime based on the dominant form of the peroxy radicals (RO2). Chapter 5 is aimed at evaluating and improving the MEGAN biogenic emission estimation by studying different emission factor (EF) fields on predicted isoprene concentrations using all available surface isoprene measurements as well as satellite observations to determine if alternative EF fields could give more satisfactory estimations of isoprene emissions.

# 2. SOURCE APPORTIONMENT OF SECONDARY ORGANIC AEROSOL IN CHINA USING A REGIONAL CHEMICAL TRANSPORT MODEL AND TWO EMISSION INVENTORIES*

## 2.1 Introduction

Atmospheric fine particles are correlated with adverse health effects, visibility reduction, and climate change 1-5. In January 2013, China experienced a record-breaking severe haze event that covered over 1.4 million square kilometers and affected the health of more than 800 million people in North China Plain (NCP) and central eastern China 6-9. The daily concentrations of PM2.5 (airborne particles with aerodynamic diameters less than 2.5 Âţm) in some cities in NCP such as Beijing and Shijiazhuang were reported as more than 500 $\mu g \cdot m^{-3}$. Recent field measurements show that organic carbon (OC) was one of the major components during haze events with contributions ranging from 35% to 80% 10-16. It has been suggested that secondary organic aerosol (SOA) could account for a significant fraction of the total observed OC [17, 18, 19] but the magnitude and source contributions to SOA in China have not been extensively studied.

Several experimental studies have been reported to determine the magnitude of SOA in China recently. The amount of SOA in total organic aerosol can be estimated by routine measurements of elemental carbon (EC) and OC, using ratios of the mass concentrations of OC to EC collected at a single location over an extended period [20, 21]. While significant levels of SOA were estimated [22], the OC/EC ratio method was considered to have significant uncertainties due to its underlying assumptions. In addition, source-specific SOA organic tracers have been applied to determine the amount of SOA from aromatic

*Reprinted with permission from "Source apportionment of secondary organic aerosol in China using a regional source-oriented chemical transport model and two emission inventories" by Wang, P., Ying, Q., Zhang, H., Hu, J., Lin, Y., & Mao, H., 2017. Environmental Pollution [46], Copyright 2017 by Elsevier

and biogenic precursors in organic aerosols [23, 24, 25]. However, a comparison study showed that SOA concentrations estimated using the tracer method were much lower than those estimated by radiocarbon dating [26]. Detailed analysis of the aerosol chemical composition using aerosol mass spectrometer (AMS) and the positive matrix factorization technique illustrated that oxygenated organic aerosols, which is considered as surrogates of SOA, could account for more than 50% of organic aerosols [27]. SOA determination based on field measurements is usually expensive and can only provide SOA estimation at the monitoring sites. Modeling analyses are typically needed to illustrate the spatial distribution and regional source apportionment of SOA.

Modeling studies of SOA formation in China reported in the literature range from relatively simple box models [28] to full-blown three-dimensional (3D) chemical transport models (CTMs) [29, 30, 31]. Hu et al. [31] simulated ground level SOA concentrations using a precursor-tracking method in a regional 3D CTM. The model includes extended isoprene gas phase reactions that lead to the production of epoxydiols of isoprene (IEPOX) and methacrylic acid epoxide (MAE), and an SOA mechanism with updated SOA yields and reactive surface uptake of dicarbonyls and IEPOX and MAE. Lin et al. [32] applied a CAMx model with SOA yields based on smog chamber studies 33 to investigate local and distant sources of SOA in Beijing during summertime. It was found that approximately 40% of SOA was from the local sources and the rest of the SOA was formed from distant sources. However, source contributions to SOA were not determined in these studies. The amount of SOA predicted in a CTM model also depends on the spatial and temporal distribution of precursor emissions. Analyses of several popular inventories showed that estimations of emissions of $\mathrm{NO_x}$, volatile organic compounds (VOCs) and $\mathrm{NH_3}$ from China were highly uncertain, leading to different predictions of $\mathrm{PM_{2.5}}$ and its chemical components [34] and no single inventory showed definitively better performance than other inventories [35]. Thus, the uncertainty in predicted SOA concentrations and source contributions due

to different emission inventories need to be further evaluated. The overall objective of this study is to investigate the contributions of different emission sectors to SOA in China. Contributions of major anthropogenic (industries, power generation, residential sources, extraction and solvent utilization) and natural (biogenic and wildfire) VOC sources to SOA in China are determined using two different emission inventories. This is the first mechanistic SOA source apportionment study using a 3D source-oriented CTM for the entire China. It also represents, to the best of the author's knowledge, the first study that investigates the sensitivity of source apportionment of SOA to different anthropogenic emission inventories in China.

## 2.2 Method

### 2.2.1 Model Setup

The CTM used in this study is based on the Community Multiscale Air Quality (CMAQ) model v5.0.1 [36, 37, 38]. An updated SAPRC-11 lumped gas phase photochemical mechanism (S11L) [47] and a revised SOA module with reactive surface uptake of dicarbonyls and isoprene epoxides are used to improve SOA predictions [40] and the refereces therein. Further updates of the SOA module regarding the mass yields of SOA to account for wall loss of organic vapor during chamber experiments were described in detail by Hu et al. (2017). The S11L gas phase mechanism and the SOA module are further updated in this study to track emissions of precursors from different sources categories separately so that the formation of SOA from different sources can be directly determined. The general approach for SOA source tracking in source-oriented regional models has been previously described by Ying et al. [40] and Zhang et al. [41], and is summarized in section 2.2.2.

The model domain covers China and its neighboring countries in east and southeast Asia, with a horizontal resolution of 36 km. Details of the domain setup have been described by Hu et al. [42]. Meteorological inputs for the CMAQ model were generated

using the Weather Research and Forecasting (WRF) model v3.6.1 with the boundary and initial conditions from the National Centers for Environmental Prediction (NCEP) Final (FNL) Operational Model Global Tropospheric Analyses dataset. In general, the WRF model has acceptable performance on meteorological parameters. The detailed validation of meteorology can also be found in Hu et al. [42].

The anthropogenic emissions are based on two widely-used regional inventories: the Regional Emission inventory in ASia v2.1 (REAS2) [43] and the Multi-resolution Emission Inventory for China (MEIC) [44]. The MEIC is developed based on year 2012 and the REAS2 is developed based on year 2008. More details of the two inventories and their processing to generate model ready emission input files are described in section 2.3. Biogenic emissions were generated using the Model of Emissions of Gases and Aerosols from Nature (MEGAN) v2.1 [45] with year-specific (2013) leaf area index (LAI) data from the 8-day Moderate Resolution Imaging Spectroradiometer (MODIS) LAI product (MOD15A2) based on the SAPRC 99 mechanism [48, 49, 49]. The detail of the MEGAN model can be found in Qiao, et al. [50]. The Fire Inventory from National Center for Atmospheric Research (NCAR FINN) was used for open biomass burning emissions [51]. Emissions of sea salt aerosols and windblown mineral dust particles were generated inline during CMAQ simulations.

### 2.2.2 Source Apportionment Of SOA

The S11L photochemical mechanism and the SOA module in the CMAQ model are modified to develop a source-oriented treatment of the SOA formation process. In the modified S11L mechanism, precursor VOCs and their oxidation products from an explicit source are differentiated from those from other sources using additional tagged species and reactions. A brief explanation of this method is described in the following. For example, the reaction of the lumped species ALK5 (long chain alkanes) with OH (have kOH greater

than $1 \times 10^4$ ppm$^{-1}$ min$^{-1}$) in the original S11L mechanism can be expanded into two similar reactions:

$$\mathrm{ALK_5^{x+}OH} \longrightarrow ... + \mathrm{ALK_5RXN^x} \tag{2.1}$$

$$\mathrm{ALK^{x+}OH} \longrightarrow ... + \mathrm{ALK_5RXN} \tag{2.2}$$

The superscript X on ALK5 in reaction R1 can be used to represent ALK5 from an explicit source X (for example, biogenic) while the non-tagged ALK5 represents the lumped emissions of ALK5 from all other sources as well as from the initial and boundary conditions. ALK5RXN is a counter species used to track the amount of ALK5 reacted during a model time step and is used by the aerosol module to calculate the amount of semi-volatile products produced. Thus, in addition to the changes in the gas phase reactions, the aerosol module is also expanded to include additional source-tagged species SV_ALK5$^x$ and AALK5J$^x$, which represent the total amount of semi-volatile oxidation products and fine mode SOA from ALK5$^x$, respectively. Tracking the precursor ALK5, the counter species ALK5RXN, the semi-volatile product SV_ALK5 and the SOA component AALK5J from source X separately from other sources makes it possible to determine the amount of SOA formed by ALK5 from that source. The same approach is applied for other SOA precursors.

While this approach can be further expanded to simultaneously track more than one explicit source at a time, the number of species and reactions need to be tracked in the gas phase mechanism increases rapidly. To reduce the complexity in the gas phase reactions, only one explicit source was tracked in a single simulation in this study. This implies that to determine the source contributions for 8 explicit sources, 8 simulations are needed as an example.

### 2.2.3 Anthropogenic Emission Inventories And Speciation Of VOC Emissions

Two anthropogenic emission inventories are applied in this study. The MEIC emission inventory has a resolution of $0.25^\circ \times 0.25^\circ$ and only covers mainland China. The REAS2 has the same spatial resolution and covers China and all its neighboring countries. The MEIC divides the total anthropogenic emissions in China into four general sectors: industries, transportation, power generation, and residential sources. The REAS2 divides the total emissions into 12 general emission sectors. These sectors were further grouped into six categories (industries, transportation, power plants, residential sources, extraction and solvent, see Table 2- 1) in this study to better compare with the source apportionment results from MEIC. Emissions from solvent utilization, and extraction and processing of fossil fuel (extraction hereafter) were not grouped with other sectors so that their respective contributions can be determined. The sector-separated emissions are prepared for emissions originated from China only. Emissions from other countries are lumped into a single category (i.e. other countries) in the study.

Emissions of VOCs in the emission inventories are usually represented as total amount of non-methane hydrocarbons (NMHC) or VOCs, and need to be broken down into model species for the S11L mechanism. The MEIC provides speciated VOCs for the SAPRC-99 (S99, an older version of the SAPRC mechanism) photochemical mechanism natively. Since the primary VOC species used in S11L are almost identical to those used in S99, these species are directly used as inputs for the S11L mechanism. The major difference is benzene, which is an explicit species in S11L but is lumped with other aromatics as ARO1 in S99. The REAS2 provides total NMHC emissions for each sector as well as speciated VOCs based on their functional groups (Table A- 1). However, the partially speciated VOCs do not match the S11L model species. To generate model ready species for S11L from the REAS2 inventory, two different approaches are used. In the first approach, repre-

Table 2.1: Profiles from the SPECIATE4.2 profile data base used to speciate REAS2 VOCs emissions from different sectors

| Profile # | Original REAS2 Sectors | Grouped REAS2 Sectors* |
|---|---|---|
| 5561<br>5651 | Domestic<br>Waste | Residential |
| 1185 | Industry | Industries |
| 1178<br>1178 | Power Plants Point<br>Power Plants Non-Point | Power Generation |
| 4674, 4556 and 4557<br>3161<br>3161 | Road Transportation<br>International Navigation<br>Other Transportation | Transportation |
| 1016,1003,1013,197 and 3144 | Solvent and Paint Use | Solvent Utilization |
| 1010 | Extraction | Extraction Process |

*Emissions are speciated first for the original REAS2 sectors before being grouped. Emissions from power plants in Japan (point and non-point) are separated from other power plant emissions but are processed using the same speciation profile.

sentative speciation profiles for each REAS2 emission sector are chosen from SPECIATE 4.3, a profile database maintained by the United States Environmental Protection Agency (see Table 2- 1 for these speciation profiles and the index number to locate them in SPECIATE). The profiles from the SPECIATE database with detailed VOC species (mostly individual compounds) are processed using a speciation profile processor (SpecDB, available from http://www.cert.ucr.edu/ carter/emitdb/) provided by Dr. William Carter to generate speciation profiles suitable for a specific chemical mechanism by mapping the detailed VOCs into model species. The mechanism specific speciation profiles from SpecDB are used to split the total NMHC emissions to S11L model species. The emissions generated using this approach are referred to as REAS2-a in this study.

Since the raw REAS2 also provides speciated VOC emissions, an alternative approach is designed in this study to map the REAS2 speciated VOCs into S11L model species so that the emission rates of these pre-speciated VOCs are retained as much as possible.

For REAS2 VOC species that have their exact counterparts in the S11L mechanism (e.g. ethene) or belong entirely to a lumped S11L species (e.g. toluene belongs to ARO1 in S11L), this is a straightforward one-to-one mapping. However, some lumped VOC groups in REAS2 contain multiple species that belong to several S11L model species. For example, the "other alkanes" (see Table A- 1) in REAS2 is a lumped VOC group for all C6+ alkanes and thus non-unity mapping factors are needed to split the emission rates into various ALK species in S11L. The source specific mapping factors for each REAS2 lumped VOC are generated by using modified detailed speciation profiles (from the SPECIATE database for that source) with only the species belonging to the target REAS2 lumped VOC. For example, a modified profile for road transport is prepared that only contains "other alkanes", i.e., it includes all alkane species except the REAS2 explicit alkanes (ethane, propane, butanes and pentanes). The modified profile is then processed by SpecDB to determine the mapping factors to split "other alkanes" into S11L species for the road transport sector. This process is repeated for the combination of all REAS2 sectors and six lumped REAS2 VOC species to generate the source-specific mapping factors as shown in Table A- 1. Emissions of S11L VOCs using this approach are referred to REAS2-b emissions in this study.

A total of three sets of CMAQ simulations are conducted, using MEIC, REAS2-a and REAS2-b as emission inputs. As MEIC does not have emissions from other countries, REAS2-a emissions are used for emissions from other countries in all three simulations.

## 2.3 Results

### 2.3.1 Annual SOA Source Apportionment Based On MEIC

Figure 2- 1 shows the average seasonal SOA source apportionment results in China. In spring, predicted SOA concentrations peak in Southeast Asian (Figure 2- 2) , which is associated with open burning emissions [52]. In addition, higher temperature and stronger

solar radiation in that region enhance the emission of biogenic VOCs and photochemical production of SOA. Part of the SOA formed in that region and precursor emitted can be transported to China. This leads to the high fractional contribution to SOA in China due to emissions from other countries (46.3%). In China, Yunnan and part of Guangxi provinces have the highest spring-time SOA concentration of more than 12 $\mu g \cdot m^{-3}$ (Figure A-2). In addition, relatively high SOA concentrations are also predicted in other southern provinces and in the Sichuan Basin (SCB), with seasonal average concentrations reaching 10 $\mu g \cdot m^{-3}$. Predicted SOA concentrations are low in the north and northeast provinces. On average, contributions of local emission to SOA are mostly due to biogenic ( 20.6%) and industrial ( 19.5%) emissions. Regional distributions of source contributions to SOA are shown in Figure A- 1. The regional transport of SOA due to emissions from other countries can be seen clearly. In the previous study by Hu et al. [31], combined contributions of isoprene, monoterpene and sequiterpene to SOA in China was estimated to be approximately 60% in spring, which includes biogenic emissions from both China and other countries (mainly southeast Asia). The amount of SOA due to regional transport was not quantified in that study. The results of the current study indicate that approximately 2/3 of the biogenic SOA in China were due to biogenic emissions in other countries during spring time. In summer, as shown in Figure S3, the higher SOA regions move northward due to changes in the wind direction [31]. The SOA concentrations are commonly more than 6 $\mu g \cdot m^{-3}$ and can be as high as 10-15 $\mu g \cdot m^{-3}$ in central and eastern China. As shown in Figure 2- 1(b), biogenic emissions become the most important contributor to SOA in summer. Throughout China, the biogenic emissions contribute to approximately 60% SOA. In most areas, biogenic emissions are the most important contributors with relative contributions reaching as high as 80%, even in areas without significant emissions of isoprene. Under the influences of the southerly wind in the summertime, the precursors from high biogenic emission regions in south China are transported to central China and

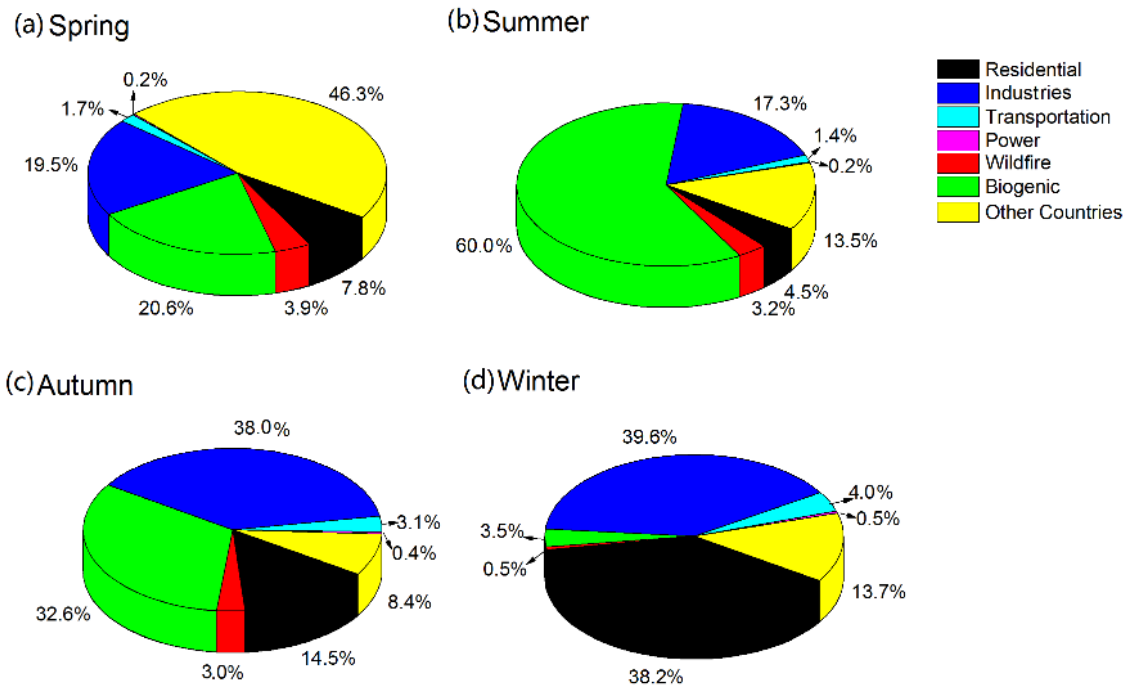


Figure 2.1: Predicted fractional source contributions to SOA in (a) spring (March, April and May), (b) summer (June, July and August), (c) fall (September, October and November), and (d) winter (December, January and February) 2013, based on the MEIC emission inventory.

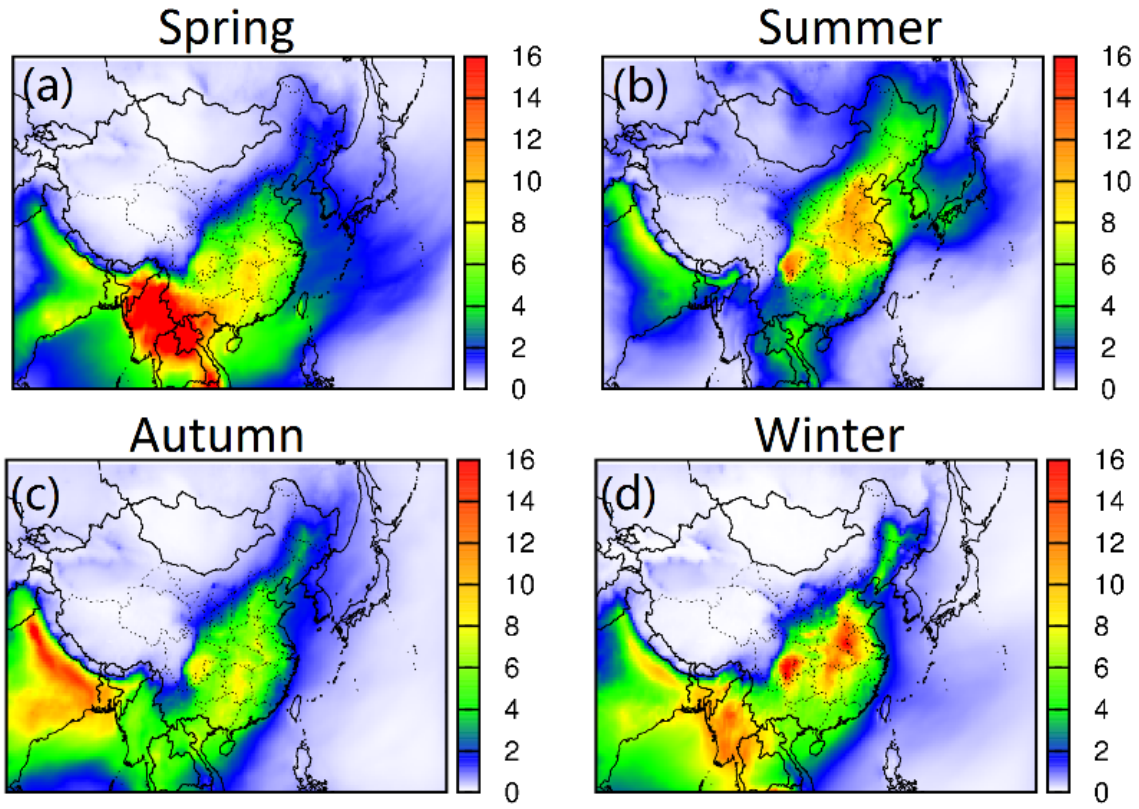


Figure 2.2: Predicted seasonal average SOA concentrations in (a) spring (March, April and May), (b) summer (June, July and August), (c) fall (September, October and November), and (d) winter (December, January and February) 2013, based on the MEIC emission inventory. Units are $\mu g \cdot m^{-3}$.

the NCP areas. Increases in the solar radiation and temperature in summer also enhance the biogenic emissions, which leads to the high country-average contribution to SOA from biogenic emissions. Industries are the second largest contributor to SOA, accounting for 17.3% of total SOA in China annually. Higher influence of industrial SOA is mostly located in coastal areas, with maximum contribution of approximately 50%.

The highest SOA concentration in autumn is reduced to approximately 8-10 $\mu g \cdot m^{-3}$ and higher SOA concentration regions move southward (Figure A- 3). The spatial distribution of SOA in autumn is similar to that in spring, except that SOA concentrations along the south border of China are reduced. With the reduction of biogenic emissions, industrial sources become the most important contributor (38.0%) followed by biogenic (32.6%) and residential (14.5%) sources. As the temperature decreases, relative contribution of residential sources increases, especially in the north and northeast China.

In winter the highest seasonal SOA concentrations reach more than 14 $\mu g \cdot m^{-3}$ in the SCB and the central part of China (see Figure A- 4). The industrial and residential sectors are the two largest SOA contributors, with country-average contributions of 39.6% and 38.2%, respectively. As a result, the most important precursor changes from isoprene to aromatic compounds. The spatial distribution of the industrial and residential sources contributions is different. As shown in Figure S5, the fraction of industrial SOA is higher in east and south China (up to 60%) while the residential is higher in the north (up to 80%) due to residential heating.

Figure 2- 3 shows the predicted regional distribution of annual average SOA concentrations and source apportionment results. On the annual average basis, SCB has the highest SOA concentration of approximately 12 $\mu g \cdot m^{-3}$ and concentration in central China is approximately 8-10 $\mu g \cdot m^{-3}$. Industries, residential, and biogenic sources are three major emission sectors that contribute to SOA formation. The regions with high fractional contribution of the industrial sector are mainly located in east coast and the fractional con-

tributions due to residential sector is higher in north, northeast, and central China. The high fractional contribution of biogenic sector is located in central and south China. Besides, cross-country transport plays a significant role in SOA formation in the southern boulder provinces such as Yunnan. Transportation and power generation sectors are not predicted to be significant SOA contributors based on MEIC, and the sum of the contributions from the two sectors and from the wildfires are less than 10% in most parts of China.

### 2.3.2 Effect Of Different Emission Inventories On SOA Source Apportionment

Figure 2- 4 shows the regional differences in the predicted total SOA concentrations between MEIC and two different sets of emissions of REAS2 in January and August 2013. In most parts of China, the MEIC inventory leads to higher SOA concentrations in January than those using the REAS2 inventories, and the largest difference occurs in SCB. Both simulations with REAS2 predict significantly lower SOA concentrations in SCB. In January, the difference can reach up to 12 $\mu g \cdot m^{-3}$ for REAS2-a and 10 $\mu g \cdot m^{-3}$ for REAS2-b. In August, the difference in SOA concentrations are not as significant, with 2 $\mu g \cdot m^{-3}$ for REAS2-a and 1.5 $\mu g \cdot m^{-3}$ for REAS2-b. In August, biogenic emissions are the dominant contributors to SOA as all three sets of simulations used the same biogenic emission from the MEGAN model. As a result, the SOA concentration differences among these three sets of simulations in August is not as significant as those in January.

By examining the precursor species' contributions to SOA, it can be seen that the difference in the predicted SOA is mainly caused by the differences in SOA formed by the aromatic compounds and SOA from glyoxal and methylglyoxal, especially in January, as shown in Figure A- 5 and Figure A- 6 for spatial distributions and Figure A- 9 and Figure A- 10 for China average. The difference of SOA formed by the aromatic compounds between MEIC and REAS2 inventories can reach up to 2 $\mu g \cdot m^{-3}$ in SCB in January. The difference of SOA from glyoxal and methylglyoxal among these three sets of simulations

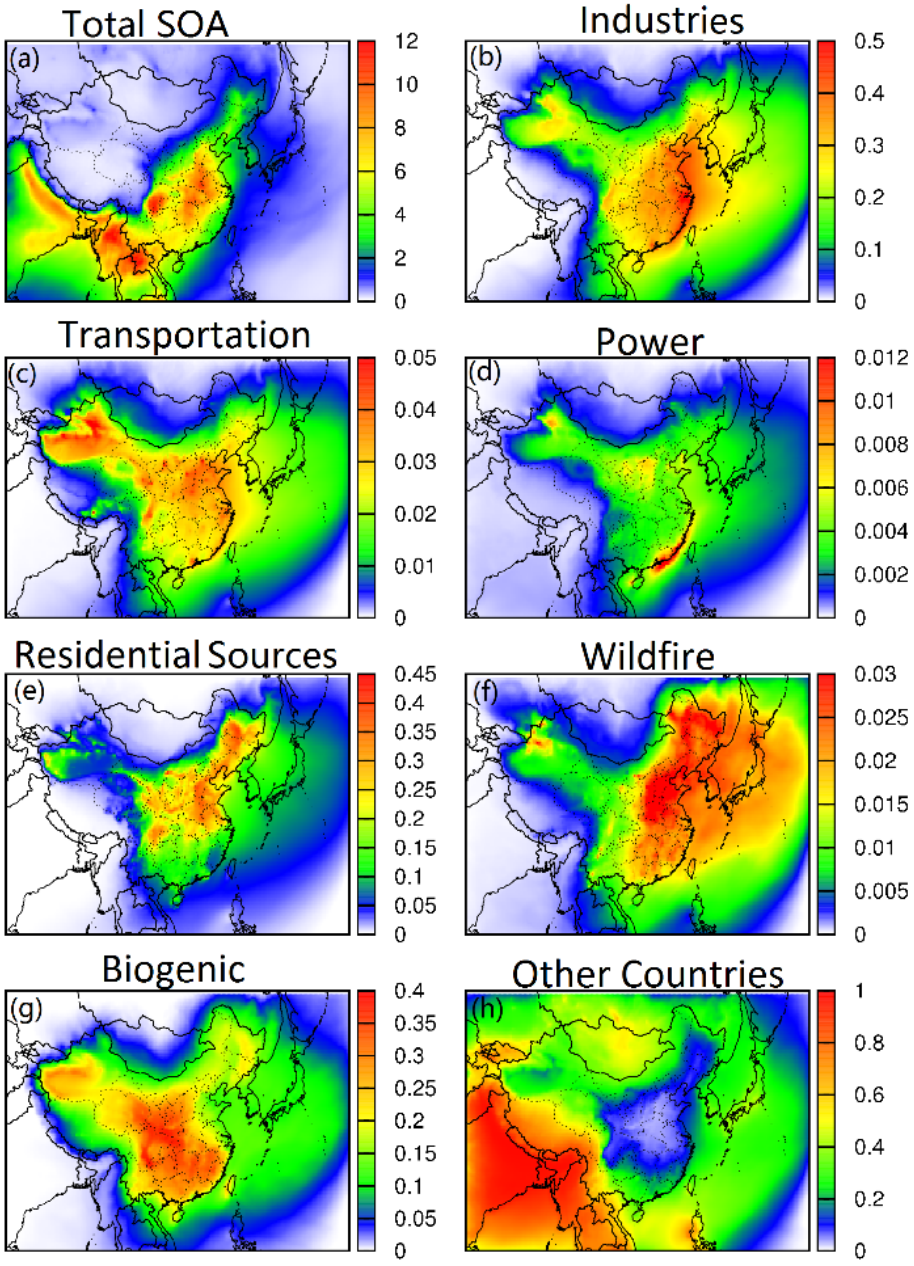


Figure 2.3: Predicted annual average SOA concentration (in $\mu g \cdot m^{-3}$, panel (a)) and fractional source contributions due (b) industries, (c) transportation, (d) power, (e) residential sources, (f) wildfire, (g) biogenic and (h) other countries.

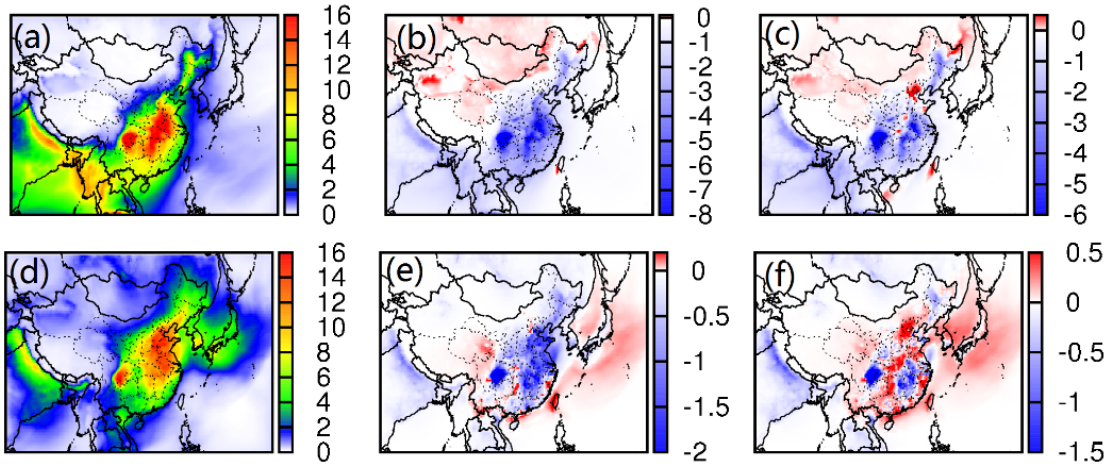


Figure 2.4: Predicted spatial distribution of SOA for January and August 2013 using MEIC emission inventory (a, d), and change of SOA concentrations due to REAS2-a (b, e) and REAS2-b (c, f) emission inventories. Units are $\mu g \cdot m^{-3}$.

are as high as 6 $\mu g \cdot m^{-3}$ for REAS2-a and 4 $\mu g \cdot m^{-3}$ for REAS2-b in SCB. Based on Table 2- 2 and Table 2- 3, REAS2-a has the lowest emission rates of aromatic compounds, glyoxal and methylglyoxal. The relatively small differences in SOA due to precursors mainly emitted from biogenic sources are illustrated in Figure A- 7. The differences between SOA from long chain alkanes are also quite small, as shown in Figure A- 8.

Figure 2- 5 summarizes the relative source concentrations to SOA based on the two emission inventories in January and August. Regional distributions of source contributions to SOA based on REAS2-a and REAS2-b are shown in Figure A- 11-Figure A- 14. In January, the biggest difference lies in the transportation sector. For MEIC, the transportation sector only accounts for approximately 4% of SOA while the relative contributions increase to 34.8% for REAS2-a and 38.0% for REAS2-b, which are almost an order of magnitude higher. For both REAS2 simulations, the transportation sector is the most significant source of aromatic compounds, which lead to the higher SOA contributions. The higher contribution of the transportation sector is located in large areas of China for both

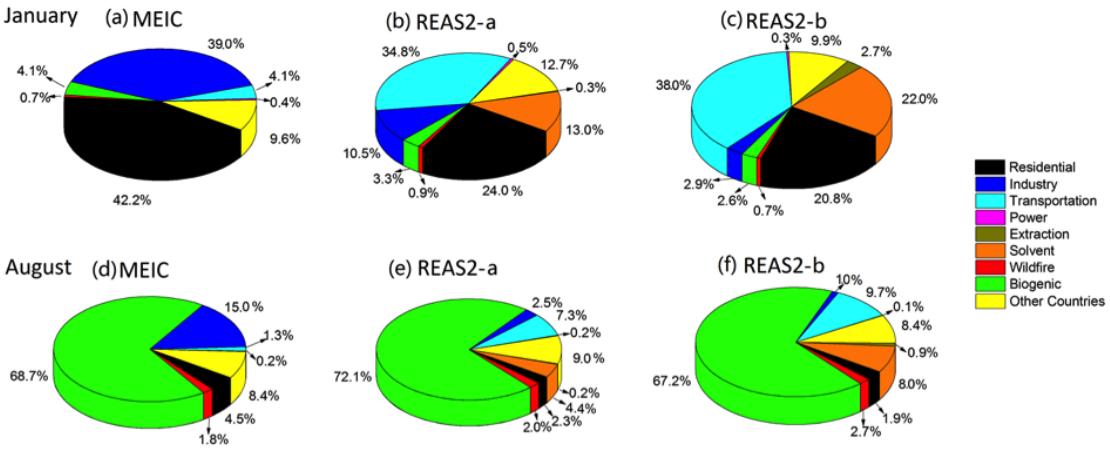


Figure 2.5: Predicted fractional SOA source contributions using (a) MEIC, (b) REAS2-a, (c) REAS2-b for January and August (d, e, f) 2013

REAS2-a and REAS2-b cases. In the central, east and south part of NCP, the contribution of transportation sector to total SOA can be higher than 40

For MEIC, the major sources of SOA in January are residential sources (42.2%) and industries (39.9%). For the REAS2-a and REAS2-b inventories, the major sources following the transportation (34.8% and 38.0% for REAS2-a and -b, respectively) sector are residential (24.0% and 20.8%) and solvent (13.0% and 22.0%). Contributions of the residential and industrial sectors (10.5% and 2.9%) are significantly lower based on the REAS2 emissions while the fractional contributions of the biogenic sector to SOA are almost the same. The REAS2-a and REAS2-b have similar SOA source apportionment results except that the REAS2-b has more SOA from the solvent sector and less from the industrial sector. The discrepancy in the industrial contributions between REAS2 and MEIC would be reduced if the solvent and extraction source sectors were grouped into the industrial sector when processing the REAS2 emissions. In August, biogenic emissions contribute to more than 65% SOA in China in all emission inventories. The transportation sector is still predicted to play a more important role in the REAS2-a (7.3%) and REAS2-b (9.7%) cases

than that of MEIC (1.3%).

Figure 2- 6 and Figure 2- 7 illustrate the time series of SOA in January and August of 2013 at four cities, i.e., Beijing in NCP, Shanghai in YRD, Guangzhou in PRD and Chengdu in SCB for three sets of simulations based on two emission inventories. The predicted SOA at Chengdu using the REAS2 inventories are significantly lower than those using the MEIC inventory, especially in January. Chengdu has experienced the highest SOA concentrations among the four cities both in winter and summer based on MEIC, with the highest hourly concentrations of 35 $\mu g \cdot m^{-3}$ and 50 $\mu g \cdot m^{-3}$ in January and August, respectively. Peak hourly SOA concentrations in other cities in January are approximately 20-25 $\mu g \cdot m^{-3}$, regardless of the emission inventories used. In contrast, the SOA peak concentrations in Beijing and Shanghai can reach approximately 40 $\mu g \cdot m^{-3}$ during summertime. In August, biogenic emissions are the most significant contributor in all cities, regardless of the anthropogenic emission inventories used. In January, the most important emission sectors for MEIC case are industrial and residential sources. However, transportation, residential, and solvent are important for REAS2-a and REAS2-b cases.

## 2.4 Discussion

The MEIC and REAS2 inventories lead to significantly different quantification of SOA source contributions. However in summer, the biogenic sector becomes the most important contributors and in winter the anthropogenic sources contributions become more significant in all these inventory, which consistent from previous researches 52, 53 . The transportation sector is much more important in the REAS2 cases. This is because the precursor VOCs emission rates of that sector is about 6-7 times higher in the REAS2 inventories than those of the MEIC inventory. The possible causes of the differences in the transportation emissions are explored below. The MEIC inventory was calculated based on the emission factors and activity data of 2012 while the REAS2 was prepared for a base

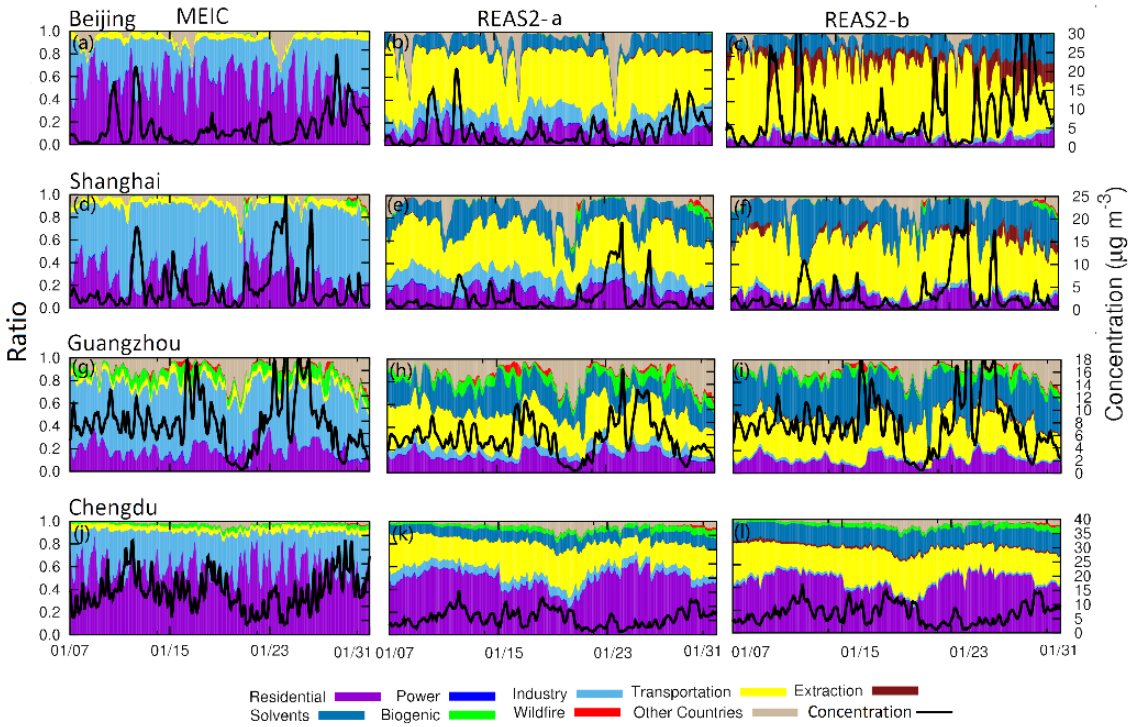


Figure 2.6: Predicted time series of SOA concentrations (secondary y axis, units are $\mu g \cdot m^{-3}$), and fractional contributions to SOA from three sets of simulations (MEIC, REAS2-a and REAS2-b) at four cities (Beijing, Shanghai, Guangzhou and Chengdu) in January 2013.

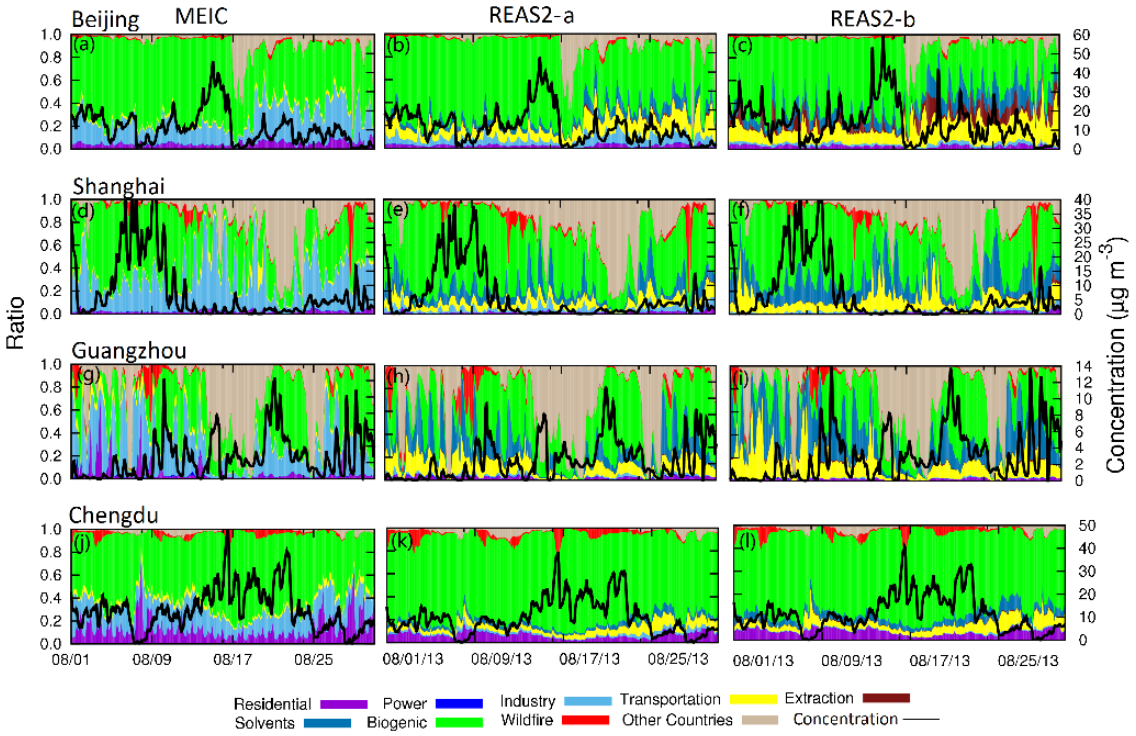


Figure 2.7: Predicted time series of SOA concentrations (secondary y axis, units are $\mu g \cdot m^{-3}$), and fractional contributions to SOA from three sets of simulations (MEIC, REAS2-a and REAS2-b) at four cities (Beijing, Shanghai, Guangzhou and Chengdu) in August 2013.

year of 2008. Between year 2008 and 2012, the total number of vehicles in China was almost doubled 54, 55. However, emission standards for vehicles have also been tightened. During this time, the emission standard for light duty vehicles (LDV) changed from GB III (i.e. Chinese National Standard III) to GB IV and heavy duty vehicles (HDV) standard changed from GB III to GB V. Table 2- 4 shows the details of emission factors for different standards. For LDV, hydrocarbon emission factors decreased by 33% and 60% for diesel and gasoline vehicles, respectively. For HDV, hydrocarbon emission factors decreased by 59% for both diesel and gasoline vehicles. As there are significant changes are in hydrocarbon emission factors for both LDV and HDV, the reduction could lead to a decrease of SOA from the transportation sector during the period if other factors remained the same. Implementation of higher fuel quality standard from GB II to GB III for both diesel and gasoline could further reduce the emissions.

Overall, the reduced vehicle emission factors lead to the reduction of emissions from vehicles even though the number of vehicles increased. Zhang et al. 56 showed that in Beijing, the total emission of hydrocarbon decreased approximately 50% from 2008 to 2011. However, this amount of reduction still cannot explain the approximately an order of magnitude difference in the precursor emissions and SOA formed from the transportation sector between these three sets of simulations. Huang et al. [53] developed a vehicular emission inventory of Shanghai for the year of 2012. Based on the reported SOA yields, they estimated that the contribution of vehicle emissions to SOA was approximately 40-60%. This appears to be more consistent with REAS2 estimations and much higher than the estimations based on MEIC.

The differences in vehicle emissions among the REAS2 and MEIC emission inventories should be investigated in the future studies. In addition to the difference in the transportation sectors, emissions from industrial and residential sectors and resulted SOA also showed significant differences. Differences in the residential and industrial emis-

sion estimations are likely caused by a combined effect of different emission factors and activity estimations. This will lead to significant differences in determining the over contributions of a source sector to particulate air pollution and thus very different emission control strategies. The emission modeler should make the data used in their emission estimation more publicly available so that the large differences in emission estimations can be reconciled eventually.

## 2.5 Conclusions

In China, predicted SOA concentrations are generally higher in summer (10-15 $\mu$g $\cdot$ $m^{-3}$) due to large contributions of biogenic emissions within China (country average 60%) and in winter due to industrial and residential sectors (country average 78% total) based on the MEIC emission inventory. However, the transportation sector is predicted to be much more important while the residential sector is predicted to be less important based on REAS2 emissions. The SOA source apportionment differences among these three sets of simulations based on two emission inventories are consistent with the emission differences. Changes in vehicle numbers and emission and fuel standards between 2008 and 2012 alone cannot explain the large differences in the emissions from the transportation sector. In addition, the amount of VOC residential emissions during winter time is much lower in REAS2 than in MEIC. These differences need to be investigated in future studies in order to set up efficient SOA and particulate pollution control policies.

Table 2.2: Profiles from the SPECIATE4.2 profile data base used to speciate REAS2 VOCs emissions from different sectors

| MEIC | industries | Transpor -tation | Power | Residential Sources | Anthro -pogenic Total | Biogenic | Wildfire |
|---|---|---|---|---|---|---|---|
| ARO1[(1)] | 3841.5 | 173.4 | 16.8 | 922.6 | 4954.3 | 10.6 | 194.3 |
| ARO2[(1)] | 1979.4 | 248.3 | 44.5 | 782.5 | 3054.7 | 7.4 | 8.7 |
| ALK5[(1)] | 2682.2 | 320.9 | 1.6 | 1265.1 | 4269.8 | 6.7 | 3.9 |
| GLY[(1)] | 0.3 | 6.6 | 0.0 | 1170.4 | 1177.2 | 0.0 | 0.0 |
| MGLY[(1)] | 0.2 | 4.1 | 0.0 | 441.0 | 445.2 | 0.0 | 48.8 |
| ISOP[(1)] | 7.6 | 1.8 | 0.0 | 41.2 | 50.5 | 1136.2 | 14.4 |
| TERP[(1)] | 15.8 | 4.5 | 0.0 | 128.6 | 148.9 | 522.0 | 3.8 |
| SESQ[(1)] | 0.0 | 0.0 | 0.0 | 0.0 | 0.0 | 13.1 | 0.0 |
| REAS2-a[(2)] | Industries | Transpor -tation | Power | Residential Sources | Extraction | Solvent | Anthro -pogenic Total |
| ARO1 | 489.9 | 1428.4 | 12.4 | 1065.5 | 0.8 | 1222.3 | 4219.3 |
| ARO2 | 415.9 | 1504.5 | 33.5 | 716.3 | 0.8 | 239.7 | 2910.9 |
| ALK5 | 0.0 | 1263.7 | 0.0 | 28.9 | 198.0 | 3038.1 | 4528.7 |
| GLY | 0.0 | 25.9 | 0.0 | 0.0 | 0.0 | 0.0 | 25.9 |
| MGLY | 0.0 | 10.2 | 0.0 | 0.0 | 0.0 | 0.0 | 10.2 |
| ISOP | 0.0 | 0.9 | 0.0 | 182.5 | 0.0 | 0.0 | 183.4 |
| TERP | 0.0 | 5.5 | 0.0 | 48.0 | 0.0 | 4.7 | 58.2 |
| SESQ | 0.0 | 0.0 | 0.0 | 0.0 | 0.0 | 0.0 | 0.0 |
| REAS2-b[(3)] | Industries | Transpor -tation | Power | Residential Sources | Extraction | Solvent | Anthro -pogenic Total |
| ARO1 | 328.6 | 1466.4 | 12.5 | 1708.7 | 234.9 | 3064.0 | 6815.2 |
| ARO2 | 45.3 | 1379.2 | 25.1 | 471.6 | 63.4 | 595.0 | 2579.6 |
| ALK5 | 0.0 | 1111.3 | 0.0 | 23.6 | 225.5 | 3346.4 | 4706.8 |
| GLY | 0.0 | 660.0 | 0.0 | 0.0 | 0.0 | 0.0 | 660.0 |
| MGLY | 0.0 | 160.2 | 0.0 | 0.0 | 0.0 | 0.0 | 160.2 |
| ISOP | 0.0 | 0.9 | 0.0 | 45.2 | 0.0 | 0.0 | 46.1 |
| TERP | 0.0 | 1.6 | 0.0 | 38.6 | 0.0 | 18.4 | 58.5 |
| SESQ | 0.0 | 0.0 | 0.0 | 0.0 | 0.0 | 0.0 | 0.0 |

(1) ARO1: Aromatics with kOH < $2 \times 10^4$ $ppm^{-1}$ $min^{-1}$. ARO2: Aromatics with kOH > 2x104 ppm-1 min-1. ALK5: Alkanes and other non-aromatic compounds that react only with OH, and have kOH greater than $11 \times 10^4$ $ppm^{-1}$ $min^{-1}$. GLY: Glyoxal. MGLY: Methyl-glyoxal. ISOP: Isoprene. TERP: Terpenes. SESQ: Sesquiterpenes.
(2) REAS2-a: Based on total NMHC emission reported in REAS2 and the VOC speciation profiles in Table S2. REAS2-b: Based on speciated VOCs reported in REAS2 and remapped to S11L species using the splitting factors in Table S1.

Table 2.3: Daily average emission rate of SOA precursor VOCs in August 2013. Units are $10^3$ moles day$^{-1}$

| MEIC | industries | Transpor -tation | Power | Residential Sources | Anthro -pogenic Total | Biogenic | Wildfire |
|---|---|---|---|---|---|---|---|
| ARO1 | 4202.9 | 166.0 | 19.8 | 288.3 | 4677.0 | 241.7 | 326.9 |
| ARO2 | 2149.4 | 233.9 | 52.5 | 245.7 | 2681.5 | 88.7 | 18.6 |
| ALK5 | 2935.5 | 302.3 | 1.8 | 492.1 | 3731.7 | 112.8 | 8.3 |
| GLY | 0.3 | 6.4 | 0.0 | 299.6 | 306.3 | 0.0 | 0.0 |
| MGLY | 0.2 | 4.0 | 0.0 | 115.4 | 119.5 | 0.0 | 91.6 |
| ISOP | 8.3 | 1.7 | 0.0 | 10.5 | 20.5 | 51133.1 | 153.8 |
| TERP | 17.6 | 4.3 | 0.0 | 56.0 | 77.8 | 6801.7 | 1.3 |
| SESQ | 0.0 | 0.0 | 0.0 | 0.0 | 0.0 | 390.3 | 0.0 |
| REAS2-a | Industries | Transpor -tation | Power | Residential Sources | Extraction | Solvent | Anthro -pogenic Total |
| ARO1 | 487.1 | 1215.2 | 13.5 | 455.8 | 0.8 | 1210.2 | 3382.5 |
| ARO2 | 413.6 | 1280.1 | 36.3 | 306.5 | 0.8 | 237.3 | 2274.6 |
| ALK5 | 0.0 | 1076.6 | 0.0 | 12.4 | 196.0 | 3007.8 | 4292.9 |
| GLY | 0.0 | 22.0 | 0.0 | 0.0 | 0.0 | 0.0 | 22.0 |
| MGLY | 0.0 | 8.7 | 0.0 | 0.0 | 0.0 | 0.0 | 8.7 |
| ISOP | 0.0 | 0.8 | 0.0 | 78.1 | 0.0 | 0.0 | 78.9 |
| TERP | 0.0 | 4.9 | 0.0 | 20.6 | 0.0 | 4.7 | 30.1 |
| SESQ | 0.0 | 0.0 | 0.0 | 0.0 | 0.0 | 0.0 | 0.0 |
| REAS2-b | Industries | Transpor -tation | Power | Residential Sources | Extraction | Solvent | Anthro -pogenic Total |
| ARO1 | 327.8 | 1257.7 | 13.6 | 767.4 | 232.6 | 3033.5 | 5632.6 |
| ARO2 | 45.8 | 1176.0 | 27.0 | 205.3 | 62.8 | 589.1 | 2106.0 |
| ALK5 | 0.0 | 940.9 | 0.0 | 18.6 | 223.3 | 3313.1 | 4495.8 |
| GLY | 0.0 | 530.9 | 0.0 | 0.0 | 0.0 | 0.0 | 530.9 |
| MGLY | 0.0 | 128.9 | 0.0 | 0.0 | 0.0 | 0.0 | 128.9 |
| ISOP | 0.0 | 0.8 | 0.0 | 18.9 | 0.0 | 0.0 | 19.8 |
| TERP | 0.0 | 1.6 | 0.0 | 24.6 | 0.0 | 18.2 | 44.3 |
| SESQ | 0.0 | 0.0 | 0.0 | 0.0 | 0.0 | 0.0 | 0.0 |

(1) ARO1: Aromatics with kOH < $2 \times 10^4$ ppm$^{-1}$ min$^{-1}$. ARO2: Aromatics with kOH > 2x104 ppm-1 min-1. ALK5: Alkanes and other non-aromatic compounds that react only with OH, and have kOH greater than $11 \times 10^4$ ppm$^{-1}$ min$^{-1}$. GLY: Glyoxal. MGLY: Methyl-glyoxal. ISOP: Isoprene. TERP: Terpenes. SESQ: Sesquiterpenes.
(2) REAS2-a: Based on total NMHC emission reported in REAS2 and the VOC speciation profiles in Table S2. REAS2-b: Based on speciated VOCs reported in REAS2 and remapped to S11L species using the splitting factors in Table S1.

Table 2.4: Emission factors of LDV and HDV for different Chinese emission standards (GB)[(1)]. Units are g $km^{-1}$.

LDV(2)

| Pollutants | CO | | Hydrocarbon | | $NO_x$ | | $PM_{2.5}$ | |
|---|---|---|---|---|---|---|---|---|
| Fuel Type | D(3) | G(3) | D | G | D | G | D | G |
| GB III | 0.140 | 1.180 | 0.024 | 0.191 | 0.841 | 0.100 | 0.032 | 0.007 |
| GB IV | 0.130 | 0.680 | 0.016 | 0.075 | 0.679 | 0.032 | 0.031 | 0.003 |

HDV(2)

| Pollutants | CO | | Hydrocarbon | | $NO_x$ | | $PM_{2.5}$ | |
|---|---|---|---|---|---|---|---|---|
| Fuel Type | D | G | D | G | D | G | D | G |
| GB III | 2.790 | 10.710 | 0.255 | 1.354 | 7.934 | 1.713 | 0.243 | 0.044 |
| GB V | 2.200 | 4.500 | 0.129 | 0.555 | 4.721 | 0.680 | 0.027 | 0.044 |

(1): Data from http://www.zhb.gov.cn/gkml/hbb/bgg/201501/W020150107594587831090.pdf (in Chinese).
(2): LDV: vehicle seats are less than 9 and length is less than 6000mm. HDV: vehicle total weight is equal or larger than 12000kg.
(3): D: diesel fuel type. G: gasoline fuel type.

# 3. ATTRIBUTION OF TROPOSPHERIC OZONE TO $NO_x$ AND VOC EMISSIONS: CONSIDERING OZONE FORMATION IN THE TRANSITION REGIME

## 3.1 Introduction

Tropospheric ozone ($O_3$) is generated from nonlinear photochemical reactions involving volatile organic compounds (VOCs) and nitrogen oxides ($NO_x$). High levels of tropospheric $O_3$ can adversely affect human [54, 55, 56]and ecosystems health [57, 58] and reduce crop yields [59, 60]. Initially reported in Los Angeles [61], ozone pollution has been observed in major urban areas round the globe [62]. Even in relatively clean rural areas, elevated ozone concentrations have been reported due to interactions of locally emitted biogenic emissions with anthropogenic emissions transported over long distances [63]. Quantitative attribution of ozone formed to precursor $NO_x$ and volatile organic compounds (VOCs) from various emission sources is needed to help designing economically effective control measures. The effectiveness of $NO_x$ and VOC emission controls depends not only on the absolute concentration of the precursors but also their relative abundances. Ozone isopleth diagrams can be constructed from a series of sensitivity calculations that systematically alter the $NO_x$ and VOC emissions to help assessing the response of ozone to changes in $NO_x$ and VOC emissions [64]. Based on the ozone isopleth, $O_3$ formation sensitivity to precursor emissions is typically classified as $NO_x$-limited or VOC-limited. In the $NO_x$-limited regime, $NO_x$ emission control is considered more effective in reducing $O_3$. If ozone formation is in the VOC-limited regime, reducing $NO_x$ emissions are not effective and may inadvertently lead to increase of ozone.

This two-regime classification scheme has become the foundation of the ozone source apportionment techniques implemented in current state-of-the-science chemical transport models (CTMs) such as the Ozone Source Apportionment Technique (OSAT) in CAMx

[65] and Integrated Source Apportionment Method (ISAM) in CMAQ [66], which attribute in-situ ozone formation to either VOC or $NO_x$ sources based on the value of some ozone formation regime indicators, such as the production rate ratios of hydrogen peroxides to nitric acid (pH2O2/p$HNO_3$). The local value of the regime indicator is compared with a predetermined threshold value to determine the ozone formation regime. Several regime indicator definitions have been used in the literature. A review of the regime indicators and the threshold values used in current source apportionment models can be found in Kwok et al. [66] and the references therein. The threshold values were developed based on mechanisms that are no longer in wide use. The formation rate or concentrations of the required species (such as $HNO_3$ and H2O2) derived from these ancient mechanisms could be very different from the ones derived from the modern Carbon Bond (CB) or SAPRC family of mechanisms, and thus need to be reevaluated. This designation of $NO_x$- and VOC-limited regimes based on a single threshold value might be intrinsically inappropriate because ozone formation can be sensitive to both $NO_x$ and VOC controls and thus needs to be attributed to both $NO_x$ and VOC sources. The existence of this 'transition' regime or 'mixed-control' regime of ozone formation can be theoretically proved based on analysis of ozone production efficiency or formation kinetics [67]. It is obvious in traditional ozone isopleth [68, 69] and sensitivity analyses designed to derive the threshold indicator values [70, 71]. In the transition regime, either $NO_x$ or VOC reduction leads to lower $O_3$ concentrations, thus it is also called a mixed-control regime. However, even though this transition regime of ozone formation is known to exist, no method has been developed to quantitatively split ozone formed in the transition regime to $NO_x$ and VOC sources in regional ozone source apportionment models.

The objective of this study is to develop an improved ozone attribution technique that allows ozone formed in the transition regime to be attributed to $NO_x$ and VOC sources accordingly based on previously defined regime indicators. The threshold values of five com-

mon regime indicators [72], including (pH2O2+pROOH)/pHN$O_3$ (R1), pH2O2/ pHN$O_3$ (R2), $O_3$/NOy (R3), HCHO/NOy (R4), and H2O2/NOy (R5), are developed for the newly proposed transition regime using data generated from a modern SARPC photochemical mechanism, and the existing threshold values for the two-regime scheme are reevaluated using data generated from this study. This improved attribution technique is then applied to study contributions of $NO_x$ and VOCs to ozone formation in China during a typical summer month. The $NO_x$-VOC attribution results are compared with those based on the traditional two-regime scheme. To the best knowledge of the authors, this is the first time $O_3$ formation in the transition regime is quantified in a regional photochemical transport model. The methods and data developed in this study may lead to improved $O_3$ control strategies in the future when it is coupled with a source apportionment technique that differentiates the contributions of different $NO_x$ and VOC emissions sources to ozone formation.

## 3.2 Method

### 3.2.1 Baseline And Sensitivity Simulations

A base case simulation for regional ozone concentrations in China in August 2013 was conducted using the Community Multiscale Air Quality (CMAQ) model (version 5.0.1) configured with a modified SARPC-11L (S11L) photochemical mechanism39 and the 6th version of the aerosol module. The original S11L was modified to include a more detailed oxidation scheme of isoprene to improve SOA predictions [40]. Emissions from anthropogenic sources in China and other countries in the model domain were based on the Multi-resolution Emission Inventory for China (MEIC) (http://www.meicmodel.org)[44] and the Regional Emissions of Asia v2 (REAS2) [45], respectively. Biogenic emissions were generated using the Model of Emissions of Gases and Aerosols from Nature (MEGAN) v2.178. The horizontal resolution of the model is 36ÃŮ36 m2. More details of the model

setup have been documented elsewhere31. Hourly averaged concentrations of all the gas phase species in the first layer were saved for each day for further ozone formation sensitivity analysis as described below.

To determine how ozone formation responses to changes in $\mathrm{NO_x}$ or VOCs emissions, a baseline simulation and two of sensitivity calculations were subsequently conducted using an offline box model equipped wit h the same S11L gas phase mechanism. The Kinetic PreProcessor (KPP) version 2.179 was used to implement the chemical mechanism for the box model and the chemical reaction kinetics in the box model was solved using the Rosenbrock solver with double precision arithmetic. The box model calculates the changes in the concentration of the gas phase species due to chemical reactions and does not include emission and removal processes. The baseline simulation with the box model was conducted using the saved concentration of all gas phase species in each grid cell as initial conditions to calculate the evolution of the gas phase species for ten minutes. The relative increase of ozone in this simulation is calculated by equation E3-1:

$$\delta_{3,b} = \frac{O_{3,b} - O_{3,i}}{O_{3,b}} \tag{3.1}$$

where $O_{3,i}$ is the initial ozone concentration and $O_{3,b}$ is the ozone concentration at the end of the 10-minute simulation. Only the grid cells with $\delta O_{3,b}$ >1% are used in the subsequent sensitivity simulations. Two additional 10-minute simulations were conducted to determine the ozone formation sensitivity due to $\mathrm{NO_x}$ and VOC changes, respectively. In the $\mathrm{NO_x}$-sensitivity simulation, initial concentrations of all species are identical to the baseline simulation but the concentrations of NO and NO2 were increased by 20%. Similarly, in the VOC-sensitivity simulation, initial concentrations of all primary emitted VOC species were increased by 20%. The relative change of ozone concentration for a given

$NO_x$ or VOCs sensitivity run $\delta O_{3,b}$ to the baseline ozone is defined in equation E3-2:

$$\delta_{3,s} = \frac{O_{3,s} - O_{3,b}}{O_{3,b}} \tag{3.2}$$

where $O_{3,s}$ is the concentration of ozone after the 10-minute sensitivity simulation. The sensitivity simulations were then repeated for relative increases of $NO_x$ and VOCs by 10% and 40% to verify the robustness of the regime threshold values derived from the sensitivity runs.

### 3.2.2 Threshold Values And $NO_x$-VOC Attribution Function For The Transition Regime

In this study, the entire range of $O_3$ formation sensitivity to reductions in precursor emissions are divided into three regimes: VOC-limited, transition, and $NO_x$-limited, based on the value of a regime indicator R. Table 3- 1 summarizes the threshold values for the five indicators reported in the literature. These are the cut-off values that divide ozone formation into $NO_x$ or VOC-limited regimes. However, a transition regime was not clearly defined in these previous studies. Thus, in the following, methods used to determine the start and end of the transition regime are described in detail and an equation to split ozone formation in the transition regime to $NO_x$ and VOC emissions is developed.

For each grid cell, the value of the regime indicator R is determined in the base case CMAQ simulation. The $\delta O_3$ values are plotted with respect to R in two plots, for the $NO_x$ and VOC sensitivity simulations, respectively. Based on the results from previous sensitivity studies, $\delta O_3$ increases from negative values to positive values as R increases in the $NO_x$ sensitivity simulations but decreases with R in the VOC sensitivity simulations. The threshold R value for the start of the transition regime (Rts) can be determined from the $NO_x$ sensitivity simulation alone as where $\delta O_3$(Rts)=0. As it is expected that the data points do not fall strictly on a single line and could have considerable scatterings, $\delta O_3$

Table 3.1: Lower (Rts) and upper (Rte) limits for the transition regime and the fitted equation (FNOx) to attribute the $O_3$ formed in the transition regime to $NO_x$

| Indica -tors[a] | Rt[b,c] | Rts | R1x[f] | Rtef | $FNO_x$[g] A | $FNO_x$[g] B | $FNO_x$[g] C |
|---|---|---|---|---|---|---|---|
| R1 | 0.5 | 0.047±0.006[h] | 0.142±0.024 | 5.142±0.411 | 3.718 | 1.049 | 0.136 |
| R2 | 0.2[d] | 0.033±0.006 | 0.096±0.014 | 3.248±0.197 | 5.322 | 1.049 | 0.093 |
| R3 | 7 | 5.059±0.223 | 6.879±0.285 | 30.730±2.018 | -22.268 | 0.982 | 0.940 |
| R4 | 0.28 | 0.303±0.011 | 0.401±0.020 | 1.260±0.041 | -7.541 | 89.338 | 0.978 |
| R5 | 0.20[e] | 0.139±0.011 | 0.231±0.016 | 1.285±0.066 | -1.473 | 43.043 | 0.931 |

a.R1=($pH_2O_2$ + pROOH)/$pHNO_3$; R2=$pH_2O_2$/$pHNO_3$; R3=$O_3$/$NO_y$; R4=HCHO/$NO_y$; R5=$H_2O_2$/$NO_y$; R1 and R2 are based on local production rates of the species while R3 to R5 are based on concentrations of the species.
b. Threshold values reported in the literature to divide ozone formation into VOC- and NOx-limited regimes. They are referred to as the threshold values for the 'two-regime' approach in the text.
c. Based on Zhang et al.80 and the references therein.
d. According to Zhang et al. 80, Tonnesen and Dennis 81, 82 reported transition values of pH2O2/pHNO3 of <0.06, 0.06âĂŞ0.2, and >0.2, corresponding to VOC-limited, ridgeline, and NOx-limited conditions, respectively.
e. Sillman (1995) 71
f. The R1x and Rte are the points where FNOx=0.5 and 0.91, respectively.
g. For R1 and R2, FNOx=A*R; for Rts<R<R1x, FNOx=R/(B*R+C) for R>R1x. For R3-R5, FNOx=A/(1+B*R2)+C for all R>Rts. The parameters are determined using results from the simulations with 20% changes of NOx and VOCs.
h. Reported Rts, Rte and R1x values and standard deviations are based on three sets of sensitivity simulations with 10%, 20% and 40% changes of NOx and VOCs.

values can be grouped into discrete R value bins (Ri$\pm\delta$R, i is the bin index and $\delta$R is the bin width). A medium $\delta O_3$-R curve can be constructed using the data pairs $\delta O_{3,i}^{medium}$, $R_i$) where $\delta O_{3,i}^{medium}$ is the medium $\delta O_3$ in the ith R value bin. Linear interpolation can be applied to data points near $\delta O_3$=0 to find Rts. When R<Rts, reducing VOC leads to a reduction in $O_3$ while reducing $NO_x$ leads to an undesired increase of $O_3$, thus ozone formation is in the VOC-limited regime. The range of the Rts value can be estimated using the 75th and 25th $\delta O_3$-R curves. Liang et al.83 proposed a similar concept and named the regime with R<Rts as the "$NO_x$-detrimental regime" and R>Rts as the "$NO_x$-

benefit regime". Estimations of the range of Rts for several concentration-based indicators are also provided. In Sillman and He73, the "$NO_x$-detrimental regime" is called the "$NO_x$-titration" regime.

As R increases beyond Rts, $\delta O_3$ due to $NO_x$ emission increase ($\delta O_3^{NO_x}$) gradually increases while $\delta o_3^{VOC}$ decreases. Since $\delta o_3^{VOC}$ is usually positive83, the threshold R value to indicate the end of the transition regime (Rte) can be operationally defined as $\delta O_3^{NO_x}(R_{te}) = \delta o_3^{VOC}(R_te)$ from the two sensitivity simulations. As data points show considerable scattering, the medium $\delta O_3$-R curves are applied to determine Rte. When R>Rte, ozone responses positively with $NO_x$ emission changes but is not very sensitive to the same amount of relative changes in VOC emissions.

To attribute ozone formation in the transition regime ($R \in [R_{ts}, R_{te}]$) to VOC and $NO_x$ emissions, an attribution factor for $NO_x$ as a function of R is defined in equation E3-3:

$$F_{NO_x}(R) = \frac{\delta O_3^{NO_x}(R)}{\delta O_3^{VOC}(R) + \delta O_3^{NO_x}(R)} \tag{3.3}$$

For ozone produced in the transition regime, $F_{NO_x}$ defines the fraction of the produced ozone to attribute to $NO_x$, and the rest is attributed to VOCs. Based on this definition, Rte corresponds to R when $F_{NO_x}$=0.909. Using the medium $\delta O_3$-R data points, an analytical form of $F_{NO_x}$ can be determined. The attribution function is only applied for the transition regime. Ozone formation is attributed entirely to VOCs (i.e., $F_{NO_x}$ is set to 0) when R<Rts, or to $NO_x$ (i.e., $F_{NO_x}$ is set to 1) when R>Rte. This treatment creates a small discontinuity at Rte, but it does not expect to introduce much error in the attribution results. This approach yields a general smooth change in the $NO_x$-VOC attributions in the entire ranges of R. In comparison, the two-regime approach leads to a significant discontinuity in the attribution results at R close to the transition threshold. A similar equation is adopted by Xie, et al. 84, who used $\delta O_3^{NO_x}/\delta O_3^{VOC}$ calculated from sensitivity simulations with 35%

reductions of $NO_x$ and VOCs and a threshold of 1 to differentiate $NO_x$-limited and VOC-limited regimes. However, their approach is still confined to the two-regime framework and didn't consider the transition regime.

Note the term "transition regime" or "mixed regime" has been used in other studies with various definitions. Care should be taken when comparing the "transition regime" from this study and from other studies. For example, Liang et al.83 defined the "transition" range as the lower and upper limit of the indicator value when the same amount of $NO_x$ reduction and VOC reduction leads to equal reductions in ozone. This is similar to the range of R1x with $F_{NO_x}$(R1x)=0.5. Sillman and He73 defined the "mixed" sensitivity grid cells as those have $\delta O_3^{NO_x}$ and $\delta O_3^{VOC}$ within 5 ppb of each other ($\Delta$ denotes absolute ozone difference between the base case and the sensitivity cases), and both $\delta O_3^{NO_x}$ and $\delta O_3^{VOC}$ are greater than 5 ppb. This definition is also similar to R1x but has imposed more strict requirements.

### 3.2.3 Attributing Ozone Formation To $NO_x$ And VOCs In CMAQ

Two non-reactive ozone species ($O_3^{NO_x}$ and $O_3^{VOC}$) were added to the CMAQ model used in the base case simulation to separately track the amount of ozone attributable to $NO_x$ and VOCs, respectively. In addition, two more tracers are added to differentiate ozone formed in the transition regime attributable to $NO_x$ ($O_3\_NO_x\_TRS$) and VOCs ($O_3$_VOC_TRS). The amount of ozone formed in the VOC and $NO_x$-limited regimes ($O_3$_VOC_limited and $O_3\_NO_x\_limited$) can be calculated from these four tracers during post-processing, as shown in equations E3-4 and E3-5 :

$$O_3\_VOC\_limited = O_3\_VOC - O_3\_VOC\_TRS \tag{3.4}$$

$$O_3\_NO_x\_limited = O_3\_NO_x - O_3\_VOC\_TRS \tag{3.5}$$

These non-reactive tracers are not actively involved in gas-phase chemistry, but they go through model simulations of transport and removal processes the same way as the regular ozone species. The method to update the non-reactive tracers is based on Kwok et al. [66] and is summarized below. At each gas chemistry time step, the concentrations of the ozone tracers are updated using the ozone production ($\mathrm{pO_3}$) and removal rate ($\mathrm{dO_3}$) from the Integrated Reaction Rate (IRR) module within CMAQ. Rate parameters needed to calculate the regime indicator R are also obtained from the IRR module. Once the ozone formation regime is determined based on R and the corresponding threshold values, intermediate concentrations of the ozone tracers (with superscript int in the following equations) are calculated from the concentrations in the previous time step t-$\Delta$t, considering only the ozone production, as shown in equations E3-6 and E3-7 :

$$O_3\_NO_x^{int} = O_3\_NO_x^{t-\Delta t} + pO_3 F_{NO_x} \tag{3.6}$$

$$O_3\_VOC^{int} = O_3\_VOC^{t-\Delta t} + pO_3(1 - F_{NO_x}) \tag{3.7}$$

Ozone removal are subtracted from the intermediate concentrations to get the final concentrations of the tracers for the current time step t, according to equations E3-8 - E3-11 :

$$O_3\_NO_x^{t} = O_3\_NO_x^{int} - dO_3 f_{NO_x} \tag{3.8}$$

$$O_3\_VOC^{t} = O_3\_VOC^{int} - dO_3 f_{VOC} \tag{3.9}$$

$$f_{NO_x} = \frac{O_3\_NO_x^{int}}{O_3\_NO_x^{int} + O_3\_VOC^{int}} \tag{3.10}$$

$$f_{VOC} = \frac{O_3\_VOC^{int}}{O_3\_NO_x^{int} + O_3\_VOC^{int}} \tag{3.11}$$

## 3.3 Results And Discussions

### 3.3.1 Determination Of $NO_x$-limited, VOC-limited And Transition Regimes

#### *3.3.1.1 Determination Of Rts*

Figure 3- 1 shows $\delta O_3$ as a function of indicator R1 in sensitivity simulations with 20% increase of $\mathrm{NO_x}$ (1a) and primary VOCs (1b). The figure includes hourly data during the entire August episode for hour 8, 12 and 14. Most of the points are located within R values of 0.01 and 10 in both sensitivity simulations. Transitional R from negative to positive $\delta \mathrm{O_3}$ in the $\mathrm{NO_x}$ sensitivity simulation occurs between 0.01 and 0.1. The R value for the start of the transition regime (Rts) based on the medium $\delta \mathrm{O_3}$-R curve is 0.045 (see inset in Figure 3- 1a). Sensitivity simulations with 10% and 40% increase of $\mathrm{NO_x}$ lead to similar Rts values of 0.042 and 0.054, respectively (Figure B- 2). The average Rts for R1 is 0.047$\pm$0.006, based on these three different levels of sensitivity simulations. This sensitivity analysis was repeated for four other indicators (R2-R5 in Table 3- 1) as shown in Figure B- 1 and Figure B- 2 and the resulted Rts values are summarized in Table 3- 1. The spread of Rts within a single sensitivity simulation was also investigated. For indicator R1 and 20% $\mathrm{NO_x}$ increase, using the 25- and 75- percentile $\delta \mathrm{O_3}$-R curves gives an estimation of Rts of 0.025 and 0.05, respectively. R2 has a similar spread of Rts. The Rts spread range for R3-R5 are 3.98-6.31, 0.22-0.4, and 0.07- 0.25, respectively, using the same estimation method. The upper limit of these spread estimations is close to the R1x values 6.879, 0.401 and 0.231 for R3-R5. In comparison, the upper limit spread estimation for R1 is 0.05, much smaller than its R1x of 0.142. Thus, it is recommended in this study that R1 and R2 are more appropriate as regime indicators than the other three forms investigated in this study.

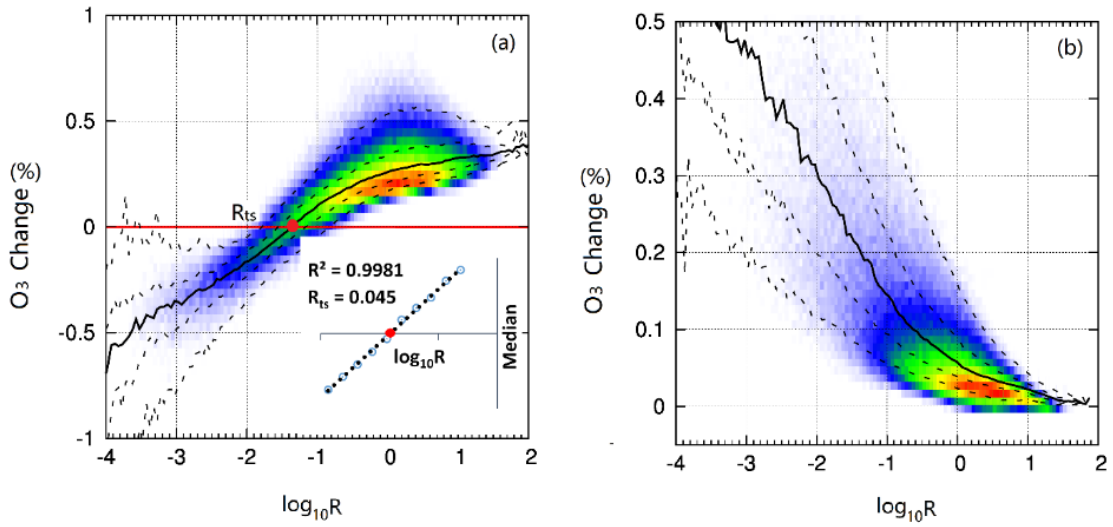


Figure 3.1: Relative change of $O_3$ with respect to indicator R1 (log scale) due to 20% increase of (a) $NO_x$ and (b) primary VOCs based on hourly predicted concentrations at 10 am, noon and 2 pm in August 2013. All grid cells at the surface level with net $O_3$ formation (defined as >1% ozone increase in a 10-minute simulation using the concentrations from the base case) are included. The solid black line is the median value of $O_3$ change, and the dashed lines show the 95, 75, 25, and 5 percentile values from top to bottom. The color shows the relative frequency of occurrence of the data. Inset panel in (a) shows the linear interpolation used to find the Rts value using adjacent data points near zero. The primary VOCs include: ACET, ALK1, ALK2, ALK3, ALK4, ALK5, ARO1, ARO2, BACL, BALD, CCHO, CCOOH, CRES, HCHO, ETHE, GLY, HCOOH, ISOP, IPRD, MACR, MEK, MEOH, MGLY, MVK, MEOH, MGLY, MVK, OLE1, OLE2, PHEN, PROD2, RCHO, RCOOH, TERP, $RNO_3$, and SESQ.

#### *3.3.1.2 Determination Of Rte And $F_{NO_x}$*

Figure 3- 2 (a) shows the determination of Rte using $F_{NO_x}$ calculated from the $\delta O_3^{NO_x}$ and $\delta O_3^{VOC}$ values taken from the medium $\delta \mathrm{O_3}$-R curves in 20% $\mathrm{NO_x}$ and VOC increase simulations. Based on the $F_{NO_x}$ data, Rte for indicator R1 is 4.846 from linear interpolation of two data points adjacent of $F_{NO_x}$=10. The same calculation was repeated for $F_{NO_x}$ based on 10% and 40% increase of $\mathrm{NO_x}$ and VOCs. The resulted Rte values are not significantly different, with an average and standard deviation of 5.142±0.411. The average and standard deviation of Rte values for all five indicators, and parameters for the fitted $F_{NO_x}$ equations (based on the 20% $\mathrm{NO_x}$ and VOC increase simulations) are listed in Figure 3- 1. For R1 and R2, linear (Rts<R<R1x) and inverse (R>R1x) functions are used to better fit the data. A simple Lorentzian function is used to fit all the data points in the entire range of R>Rts for indicators R3-R5 (Figure B- 4). The spread of Rte within a single sensitivity simulation was also quantified by plotting $F_{NO_x}$ as a function of R in a density plot as shown in Figure 2(b). For R1, Rte based on the 75th and 25th percentile curves are in the range of 3-7. The spread ranges of Rte are 1.8-4, 16.5-40, 1-1.7, and 0.85-2.15 for R2-R5 respectively (Figure B- 5).

To investigate if the Rts and Rte values are mechanisms dependent, the same procedures were performed for indicator R2 (pH2O2/pH$\mathrm{NO_3}$) using SAPRC-07 (version SAPRC07tb in CMAQ). The Rts, R1x and Rte values are 0.041±0.006, 0.127±0.013 and 6.520±0.205, respectively. In comparison, the threshold values based on SAPRC-11 are 0.033±0.006, 0.096±0.014, 3.248±0.197 for Rts, R1x and Rts, respectively. Both Rts and Rte based on SAPRC-07 are greater than those based on SAPRC-11. SAPRC-07 shows slightly higher $\mathrm{NO_x}$ and VOC sensitivity in general but the main difference is likely because SAPRC-07 predicts higher indicator values (Figure B- 6). While a more detailed analysis of the cause of this difference is beyond the scope of this study, the results shows

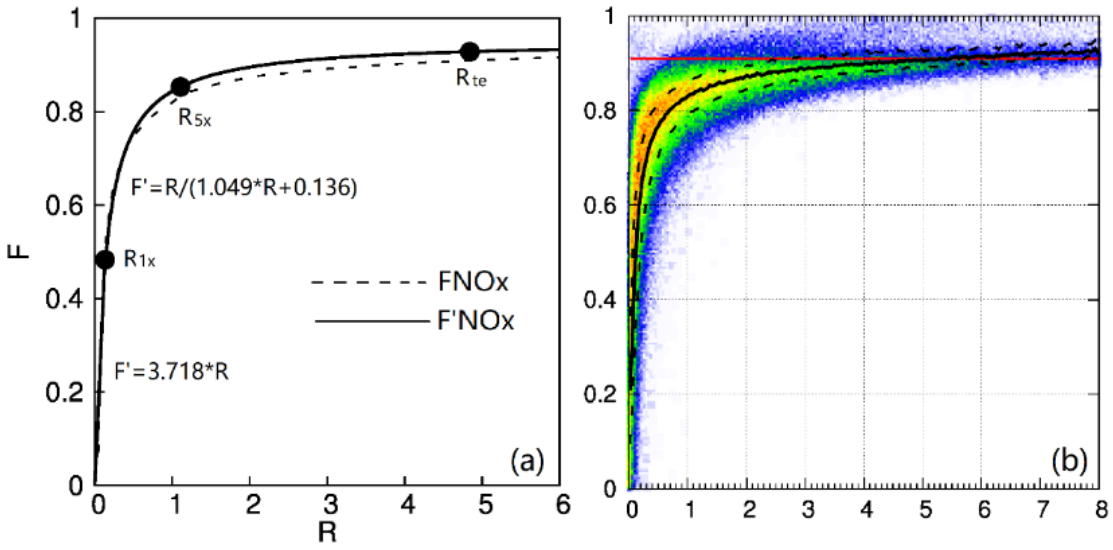


Figure 3.2: (a) Fraction of $O_3$ formation in the transition regime attributed to $NO_x$ ($F_{NO_x}$) based on the 20% sensitivity calculations (dashed line) and fitted equations (solid line). (b) Spread of $F_{NO_x}$ based on the 20% sensitivity calculations. The solid red line is $F_{NO_x}$= 0.91. The dashed lines are based on 25th and 75th percentile $F_{NO_x}$ at each R bin. The color shows the relative frequency. In both panels, predicted $F_{NO_x}$ based on hourly sensitivity concentrations at 10 am, noon and 2 pm in August 2013 at the surface level grid cells with net $O_3$ formation >1% in the baseline simulation are used.

that the threshold values are indeed mechanism dependent. Different sets of threshold values should be developed for different chemical mechanisms 3.3.1.3 Compare with the two-regime threshold values

The widely used threshold value in traditional two-regime scheme for R1 is 0.5, which is located within the transition regime of R1. At this R value, ozone formation is in obvious mix-control regime and is slightly more sensitive to $\mathrm{NO_x}$ changes ($F_{NO_x}$=0.66). For grid cells with R values between 0.045 and 0.5, the traditional method leads to overestimation of the contributions of VOCs but under-estimate the contributions $\mathrm{NO_x}$ because these data points will be classified as entirely VOC-limited. For points with R>0.5, the traditional analysis would classify them as entirely $\mathrm{NO_x}$-limited and thus might over-estimate the contributions of $\mathrm{NO_x}$ but under-estimate the contributions of VOCs to $\mathrm{O_3}$ formation. For indicator R2, the traditional threshold value is either 0.2 or 0.35, both are within the transition regime (R=0.033-3.125) defined in this study, with a corresponding $F_{NO_x}$ of 0.66 and 0.76, respectively. The traditional two-regime threshold values for R3 and R5 (7 and 0.2) are both within the transition regime close to $F_{NO_x}$=0.5 (i.e. R1x). The two-regime threshold value for R4 is 0.28, which is closer to Rts (0.303) with $F_{NO_x}$=0.036. Thus, for most of the indicators except HCHO/NOy, the accepted threshold values used by Kwok et al.[66] are near the equal $\mathrm{NO_x}$-VOC-$\mathrm{O_3}$ sensitivity point.

### 3.3.2 Attributing Regional Ozone To VOC And $\mathrm{NO}_x$ Emissions

The overall model performance of ozone and other gas and particulate species in the regional simulation have been evaluated in previous studies [42, 73, 74]. In general, the model can reasonably reproduce observed hourly ozone concentrations in most cities. In this section, the ozone attribution results from the modified CMAQ model using indicator R1 and the regime threshold values determined in the above section are examined in detail to determine the spatial and temporal variations of the summertime ozone formation

regimes in China and the relative importance of $NO_x$ and VOC emissions.

#### *3.3.2.1 Ozone Attribution Based On The Two-regime Approach*

To compare the ozone attribution results with the new regimes definitions and threshold values, ozone attribution to $NO_x$ and VOCs are first performed using the traditional two-regime approach with a threshold value of R1=0.5. The monthly average CMAQ predicted 8-hr ozone concentrations and ozone attributed to $NO_x$ and VOC emissions are shown in Figure 3- 3. In August 2013, the higher 8-hr ozone occurs in the Beijing-Tianjin-Hebei (BTH) area located in north China, the Yangtze-River Delta region (YRD) in east China, and the Sichuan Basin (SCB) region in southeast China, with the highest value of approximately 80 ppb. These areas are generally more economically developed and have higher emissions of $NO_x$ and VOCs. Figure 3- 3(b) shows that based on the traditional threshold value for indicator R1 (see Figure B- 8a), several highly developed metropolitan areas, mostly in the BTH, YRD, Pearl River Delta (PRD) and small portions of the urban areas in SCB belong to the VOC-limited regime. These results are consistent with the conclusions from previous ozone formation studies [75, 76]. In other regions, mostly in less populated provinces in west China such as Xinjiang, Tibet and Gansu, ozone formation is insignificant and most of the ozone is due to the background ozone entered the domain as boundary conditions. More than 60% of ozone formation is attributed to $NO_x$ emission and with the highest contribution of over 40 ppb in NCP and SCB. Unlike $NO_x$, VOCs contributions are only significant near the highly developed urban areas, where approximately 40 ppb of ozone is attributed to VOCs.

#### *3.3.2.2 Ozone Attribution With Transition Regime*

In contrast, Figure 3- 4 shows the spatial coverage of predicted $NO_x$-limited, VOC-limited and transition regimes of ozone formation based on indicator R1, as well as calculated $NO_x$ contribution splitting factor $F_{NO_x}$ using the threshold values and equations

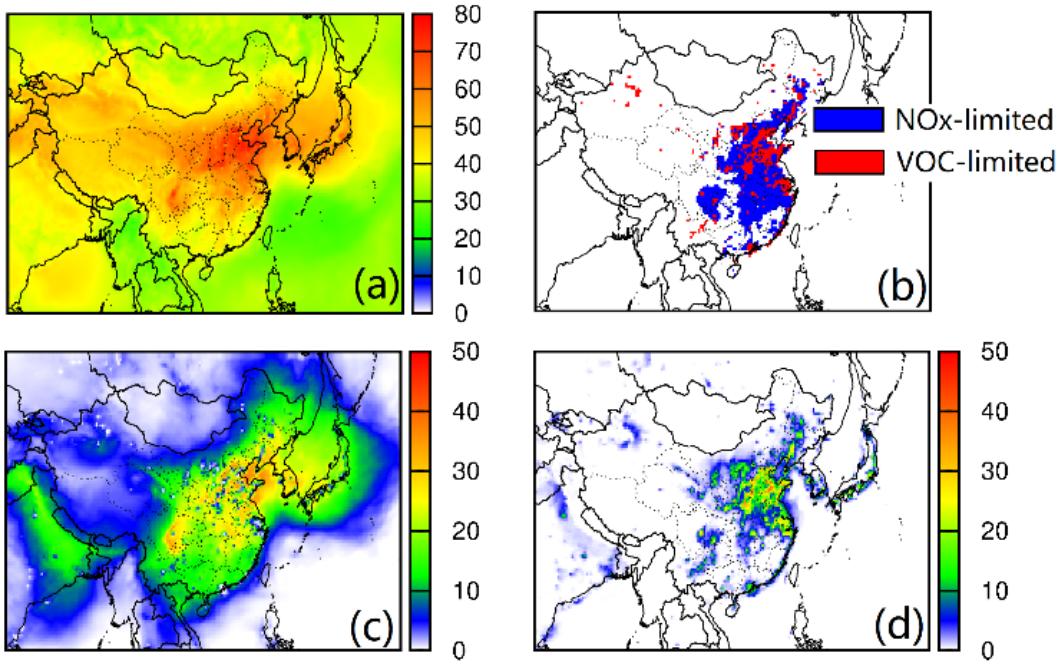


Figure 3.3: Predicted monthly average (a) 8-hr $O_3$, (b) $O_3$ sensitivity regime designations, (c) $O_3$ attributed to $NO_x$ ($O_3\_NO_x$), and (d) $O_3$ attributed to VOCs ($O_3\_VOC$) in August 2013. The results are based on indictor R1 with the traditional two-regime designation and a threshold value of R=0.5. Units are ppb for panels (a), (c) and (d). The average regime designation is based on R averaged during the 8-hr period. Grid cells with small ozone formation (greater than zero but less than 20 ppb in 8-hr averaging window) are excluded when generating panel (b).

defined in Table 1. The transition regime covers a wide area, including many of the areas previously considered as $\mathrm{NO_x}$-limited by the traditional threshold. The $F_{NO_x}$ values in these areas are usually larger than 0.6, which means that ozone formed in these areas is more attributed to $\mathrm{NO_x}$ than to VOC emissions. Most of the VOC-limited areas in the two-regime approach are also classified as transitional in this three-regime approach. The $F_{NO_x}$ values in these areas are approximately 0.2-0.4, thus ozone formed in these areas is more attributed to VOC than to $\mathrm{NO_x}$. The $\mathrm{NO_x}$-limited regime is mainly located in south China, mostly in the rural mountainous areas with high VOC emissions from biogenic sources and less influence from anthropogenic emissions. In addition to a few scattered grid cells in urban centers, areas classified as entirely VOC-limited are mostly in the YRD and PRD regions. The relatively broad distribution of the mixed-control areas, which are predicted to have ozone sensitivity to both $\mathrm{NO_x}$ and VOC changes, and the limited spatial distribution of VOC-limited areas mainly at YRD and PRD regions are in excellent agreement with sensitivity simulations reported by Liu et al. [76].

Regime designations using indicators R2-R5 as well as the corresponding $F_{NO_x}$ values are illustrated in Figure B- 8. The regional distribution of actual R values for these indicators are shown in Figure B- 8(b)-(e). Generally, different ozone sensitivity indicators lead to different ozone sensitivity regime results. The results for R2 are similar to those for R1, with a relatively large $\mathrm{NO_x}$-limited regime in the mountainous areas in south China. Indicators R3-R5 predict more transition-regime areas and the $F_{NO_x}$ values in north China are lower than those predicted using R1 and R2. For all these indicators, the VOC-limited regions are located at highly-developed urban areas. On a monthly-average basis, as much as 42.7 ppb of 8-hr $\mathrm{O_3}$ is formed in the transition regime, among which as much as 29.5 ppb of ozone is attributed to $\mathrm{NO_x}$ ($O_3\_NO_x\_TRS$) and 13.2 ppb is attributed to VOCs ($O_3\_VOC\_TRS$) (Figure 3- 5a and b). When $\mathrm{O_3}$ formed in the $\mathrm{NO_x}$-limited regime ($O_3\_NO_x\_limited$) and VOC-limited regime ($O_3\_VOC\_limited$) are also considered,

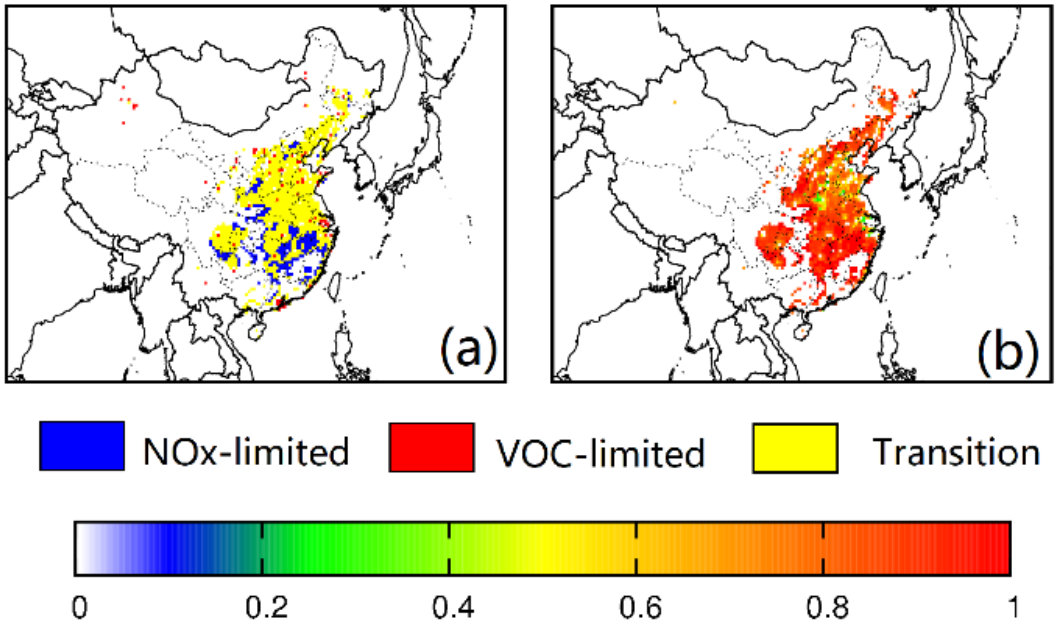


Figure 3.4: Predicted monthly average (a) $O_3$ sensitivity regimes based on indicator R1 and its corresponding threshold values Rts and Rte, and (b) $F_{NO_x}$ for the transition regime in August 2013. Grid cells with small ozone formation (greater than zero but less than 20 ppb in 8-hr averaging window) are excluded when generating panel (b).

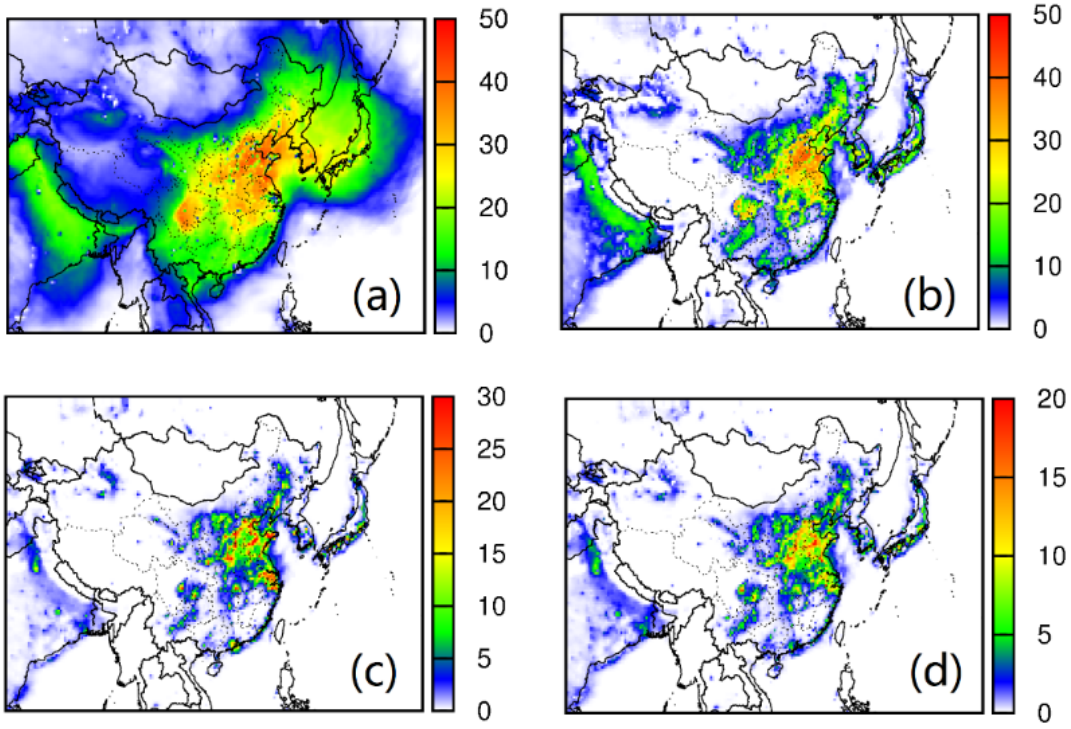


Figure 3.5: Predicted August average 8-hr ozone concentrations attributed to (a) $\mathrm{NO_x}$ ($O_3$_$NO_x$) and (c) VOC ($O_3$_$VOC$), as well as the ozone formed in the transition regime attributed to (b) $\mathrm{NO_x}$ ($O_3$_$NO_x$_$TRS$) and (d) VOC ($O_3$_$NO_x$_$TRS$). Units are ppb.

1.2-55.7% of the 8-hr ozone formed are still attributed to $\mathrm{NO_x}$, with the highest $O_3$_$NO_x$ concentration of approximately 76 ppb in NCP and SCB (Figure 3- 5c). Approximately 0.9-48.6% of the ozone are attributed to VOCs. The contributions of $\mathrm{O_3}$ attributed to VOC emissions ($O_3$_$VOC$) in urban areas in NCP and YRD can be as high as 30 ppb, and areas with non-negligible $O_3$_$VOC$ has a broader spatial distribution than those determined using the classical two-regime classification scheme due to contributions to $O_3$_$VOC$ from ozone formed in the transition regime.

This new three-regime approach leads to significant differences in the attribution of

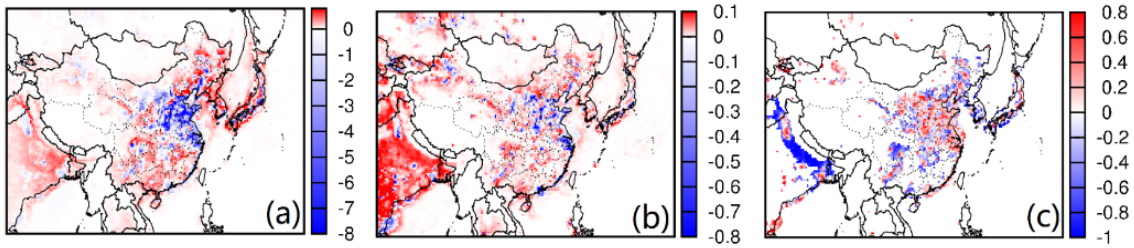


Figure 3.6: (a) Absolute and (b) relative differences in monthly average 8-hr $O_3\_NO_x$, and (c) relative difference in monthly average $O_3\_VOC$ for August 2013 based on R1 using the two-regime ($R1_t$) and three-regime (R1) approaches. The absolute difference in panel (a) is calculated by $R1_t R1$ (units are ppb) and the relative difference is $(R1_t - R1)/R1$.

8-hr ozone to $NO_x$ and VOCs as shown in Figure 3- 6. The classical two-regime approach predicts lower $O_3\_NO_x$ but higher contributions of $O_3\_VOC$ (up to 10 ppb, Figure 3-6a) in urban areas which are classified as VOC-limited regime but reclassified as transition regime in the three-regime approach. In other areas, the two-regime approach predicts slightly higher contributions of $NO_x$ but lower contributions of VOCs to ozone (up to 2 ppb). The relative differences between the two-regime and three-regime approaches in ozone attributed to $NO_x$, using the three-regime results as a reference, ranges from -80% to 10%. The relative difference in ozone attributed to VOCs are more significant, ranging from -100% to 100%.

#### *3.3.2.3 Comparison Of Ozone Attribution Time Series*

Figure 3- 7 shows the time series of ozone attributed to VOC and $NO_x$ in different sensitivity regimes based on indicator R1 and the three-regime approach for four large cities, Beijing (in NCP), Shanghai (in YRD), Guangzhou (in PRD) and Chengdu (in SCB). The model has generally captured the diurnal variations of the observations even though it under-predicts peak ozone concentration on a few high ozone days. Among the four cities, Beijing and Chengdu have more days with peak ozone concentration reaching or exceeding 100 ppb, and ozone formation in the relatively isolated Sichuan Basin is more

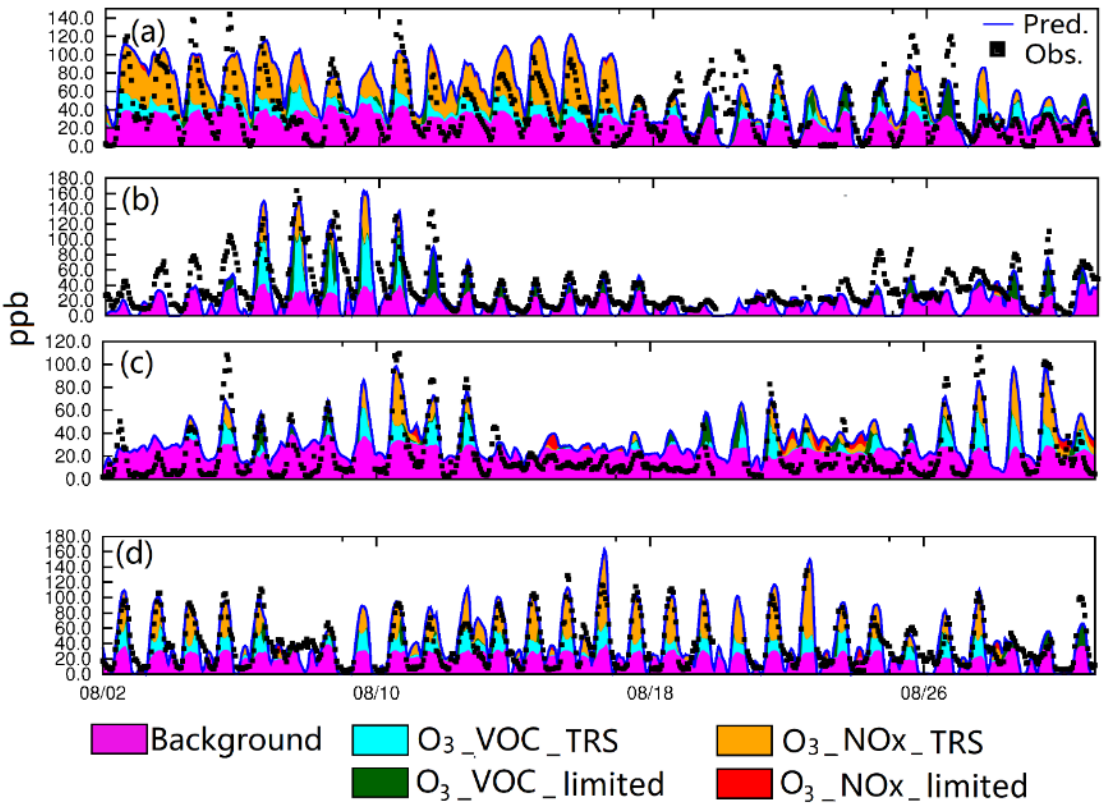


Figure 3.7: Time series of $O_3$ attributed to VOC and $NO_x$ based on the three-regime approach and indicator R1 for (a) Beijing, (b) Shanghai, (c) Guangzhou and (d) Chengdu in August 2013. Units are ppb. Background ozone is estimated by subtracting the concentrations of the four ozone attribution tracers from the total ozone.

persistent during the month. Shanghai has experienced the high hourly ozone of over 140 ppb on a few days in early August. Guangzhou has the lowest ozone concentration among the four cities. Several typical cyclones affecting east and southeast China are responsible for the lower ozone concentrations in Shanghai and Guangzhou during the second half of the month.

In Beijing, background ozone is approximately 40 ppb and in the first half of the month

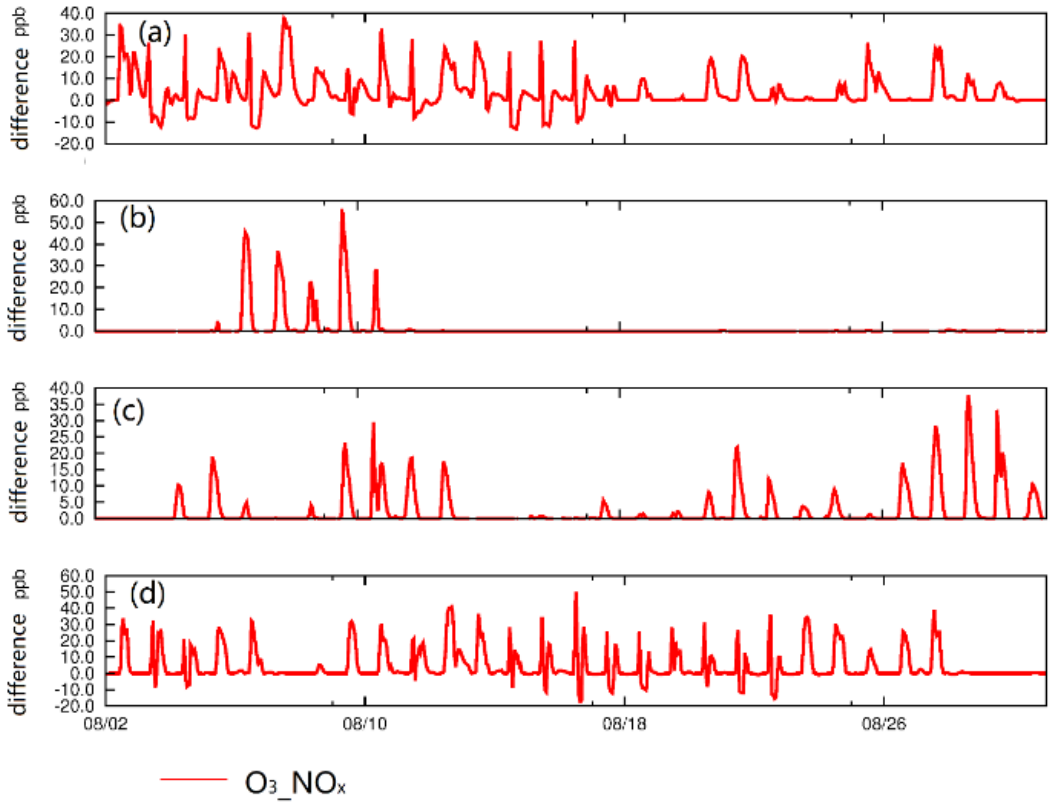


Figure 3.8: Time series of differences of $O_3$ attributed to $NO_x$ based on the three-regime and two-regime approaches (three-regime - two-regime) with indicator R1 for (a) Beijing, (b) Shanghai, (c) Guangzhou and (d) Chengdu in August 2013. Units are ppb.

most of the ozone formed (i.e. non-background ozone) is attributed to $O_3\_NO_x\_TRS$ (as much as 60 ppb) and only a smaller fraction (approximately 10-15 ppb) attributed to $O_3\_VOC\_TRS$. This is consistent with the regime classification in Figure 4a and the $F_{NO_x}$ values shown in Figure 3- 4b. The time series of the difference in total $O_3\_NO_x$ and $O_3\_VOC$ between the new three-regime and the traditional two-regime approaches are shown in Figure 3- 8(a). The difference in $O_3\_NO_x$ can be as large as 40 ppb (thus -40 ppb for $O_3\_VOC$), with the three-regime approach predicting higher $O_3\_NO_x$ concentrations but lower $O_3\_VOC$ contributions.

There appears to be a relatively sharp spatial gradient of R in this area, which leads to significant differences in the attribution results in surrounding areas as shown in Figure B-9. Of the eight grid cells surrounding the grid cell where urban Beijing is located, ozone formation in the grid cells to the west are more $NO_x$-controlled but the grid cells to the east and northeast show more contributions from $O_3\_VOC\_TRS$. The $NO_x$-controlled ozone formation in rural areas in the west and northwest of Beijing is consistent with an earlier field that ozone concentration in a rural area north of Beijing is highly correlated with NOy, which suggests that $NO_x$ plays an important role in ozone formation in Beijing. This difference in ozone formation regime in areas surrounding Beijing is further supported by examining the time series of the molar ratio of VOCs to $NO_x$, as shown in Figure B- 10. High VOC/$NO_x$ ratios up to 50 occurred in the grid cells in the west and northwest but the VOC/$NO_x$ ratios are generally below 5 for the east and northeast grid cells. The large VOC/$NO_x$ ratio for grid cells in the west and northwest is likely due to the influence of air mass coming from northwest during the first half of the month as illustrated by the back-trajectories shown in Figure B- 11. The air from that direction is relatively clean, low in $NO_x$ but high in VOC from biogenic emissions. Wind direction changed to south in the second half of the month starting from August 17, 2013 and the air parcels are generally from south/southwest. Air mass from more polluted regions in the south is typically high in $NO_x$ emissions thus has a lower VOC/$NO_x$ ratio. This shift in the wind direction leads to a higher fraction of ozone attributed to ${}_3\_VOC\_TRS$ in the second half of the month.

Ozone formation attributions in Shanghai are very different from those in Beijing. Most of the ozone above the 20-ppb background concentration on high ozone days is attributed to $O_3\_VOC\_TRS$ (70-80 ppb) or $O_3\_VOC\_limited$. Also, there appears to be a higher fraction of $O_3\_VOC\_TRS$ during the morning traffic hours, likely related with large emissions of $NO_x$ from the transportation sector that shift the ozone formation regime towards VOC-limited. Figure B- 12 further confirms that the fraction of $O_3\_VOC$

(as well as $O_3$_$VOC$_$TRS$) at 8 am is higher than that at noon and 4 pm. $O_3$_$VOC$ in many areas in NCP and PRD reaches 30-40% and highest fraction of $O_3$_$VOC$_$TRS$ reaches 15-20% in areas between NCP and YRD. The contributions of $O_3$_$VOC$ and $O_3$_$VOC$_$TRS$ decrease at noon in most places although contributions at urban areas remains high. Their relative contributions only increase slightly in the afternoon. In Chengdu and Guangzhou, ozone formation is mostly from the transition regime and both $O_3$_$VOC$_$TRS$ and $O_3$_$NO_x$_$TRS$ account for significant fractions of non-background ozone. For the four cities, Shanghai has the largest difference in total hourly $O_3$_$NO_x$ and $O_3$_$VOC$ between these two approaches ( 58 ppb). The largest differences in the attribution of hourly ozone in Guangzhou and Chengdu are 39 ppb and 50 ppb, respectively. The three-regime approach generally has higher $O_3$_$NO_x$ but lower $O_3$_$VOC$ than the two-regime approach for all four cities. 3.4 Conclusions The Rts and Rte values for regime indicators (pH2O2+pROOH)/pHNO$_3$ and pH2O2/pHNO$_3$ are (0.047$\pm$0.006, 5.142$\pm$0.411) and (0.033$\pm$0.006, 3.248$\pm$0.197), respectively. Most of the areas considered by the two-regime approach as $NO_x$ or VOC-limited are classified as transitional under the new three-regime scheme. For all these indicators, the VOC-limited regimes are located at urban areas, particularly in the YRD and PRD regions. The two ozone classification schemes lead to relatively large differences in the assessment of the importance of $NO_x$ and VOCs to ozone formation in large areas in the NCP, the YRD and the PRD. The three-regime approach predicts higher $NO_x$ contributions to 8-hr ozone in these areas by up to 8 ppb. The relative differences between the two and three-regime approach are as high as 80%. In other areas, the two attribution schemes give close assessment of the $NO_x$ and VOC contributions to 8-hr ozone, with differences less than 1 ppb.

# 4. SOURCE APPORTIONMENT OF SUMMERTIME OZONE IN CHINA USING A SOURCE-ORIENTED CHEMICAL TRANSPORT MODEL

## 4.1 Introduction

High concentrations of tropospheric ozone ($O_3$) can cause significant health problems on human, such as irritation of the respiratory system and aggravation of asthma [77, 78, 79, 80]. Exposure to high concentrations of ozone is also known to have adverse effects on crops and ecosystems [81, 82]. While fine particulate matter has been the pollutant of focus in recent years and is the key factor that raises public awareness of severe air pollution problems in China, ozone concentrations in many urban areas are high [83] and are showing increasing trends [84, 85, 86] that are projected to continue in future [87]. Thus, as ozone pollution gradually becomes a serious concern of the central and local governments and the public, a comprehensive evaluation and quantification of the sources that contributes to ozone is essential in formulating cost-effective emission control policies that co-benefit both PM and ozone reductions. Existing ozone formation and source apportionment studies in China mostly focused on three densely populated metropolitan areas, the Beijing-Tianjin-Hebei (BTH) region, the Yangtze River Delta (YRD) and the Pearl River Delta (PRD). As the ozone formation reactions in the troposphere involve a variety of volatile organic compounds (VOCs) and nitrogen oxides ($NO_x$, NO + $NO_2$) and are highly nonlinear, most of the studies used emission-based chemical transport models (CTMs) to investigate the complex source-receptor relationships between ozone precursors from different sources and source regions and ozone in target areas. Source contributions to ozone was studied using regular CTMs with a brute-force (BF) method that excludes emissions from one source sector at a time and compare the resulted ozone concentrations with a base case simulation [88, 89]. However, due to non-linear dependence of ozone on pre-

cursor concentrations, the BF approach for ozone is usually considered less accurate due to its underlying linear assumption. Qu et al. [90] attempted to improve the BF method by introducing additional simulations that remove more than one source at a time in order to estimate non-linear interactions. However, 32 regional CTM simulations are needed to fully determine contributions from 5 sectors, making it inefficient to apply the technique in long-term simulations.

Wang et al. [91] and Li et al. [92] applied the Ozone Source Apportionment Technology (OSAT) in the Comprehensive Air Quality Model with Extensions (CAMx) to study local and regional contributions to ozone in Beijing (summer 2000) and the PRD region (summer and fall 2006), respectively. The OSAT attributes in-situ ozone formation to either NOx or VOC sources based on the value of an indicator that determines ozone formation sensitivity regime as NOx-limited or VOC-limited. Non-reactive tracers are used to track NOx and VOC related ozone attributed to different sectors or source regions. A technique similar to OSAT has been incorporated into the coupled Weather Research and Forecasting/Chemistry (WRF/Chem) model by Gao et al. [93] to attribute ozone to local and regional sources in the YRD region in May 2013. In Beijing, mobile and industrial sources are two leading sources of ozone followed by point and biogenic sources, as reported by Wang et al. [91]. In the PRD region, OSAT reported that motor vehicles and area source were the most important sources, and contributions from point and biogenic sources were also important [92]. In all these studies, it was found that a significant fraction of ozone can be attributed to regional transport. This is not surprising because of the relatively small target areas used in these studies and the relatively long atmospheric life time of ozone and its precursors. A comprehensive source apportionment study that reports source contributions to ozone in the entire China is needed to provide a complete understanding of the importance of difference sources. In OSAT and similar source apportionment techniques that classify in-situ ozone formation into either

NOx-limited or VOC-limited regimes, misallocation of ozone to NOx and VOC sources can occur if in-situ ozone formation is in a transitional regime where both NOx and VOC changes can lead to perturbation of ozone formation in the same direction [66]. Wang et al. [**?**] improved the traditional two-regime approach with a three-regime approach. Ozone formation sensitivity is classified into VOC-limited, transition and NOx-limited regimes. In the transition regime, ozone formation is proportionally attributed to NOx and VOC sources depending on the relative sensitivity of ozone to NOx and VOC changes. Using this improved approach, Wang et al. [**?**] defined threshold indicator values for the transition regimes and illustrated that during summertime a significant fraction of ozone formation occurs in the transitional regime. Approximately 20-30% of non-background ozone formed in the high ozone regions such as the BTH previously attributed to VOCs should be attributed to NOx instead. However, detailed source apportionment simulations were not conducted thus it is unclear how this change in NOx and VOC attributions can affect source apportionment results. The objective of this study is to determine the contributions of major anthropogenic (industries, power plants, residential and transportation) and biogenic sources to summertime ozone in the whole China using the improve ozone attribution scheme in a regional chemical transport model. Source contributions to ozone from these sectors are quantified for each province. Difference in source apportionment of ozone using the traditional two-regime approach and the improved three-regime approach is evaluated. In addition, difference in source contributions to ozone during high and low ozone periods are compared to improve the understanding of the cause of high ozone days.

## 4.2 Methods

### 4.2.1 Attributing In-situ Ozone To NOx And/Or VOCs Based On A Three-regime Classification

An improve attribution of in-situ ozone to NOx and VOCs based on an improved NOx-VOC-O3 sensitivity regime classification scheme [**?**] was implemented into a modified CMAQ model and is the foundation of the source apportionment technique used in this study. In summary, the new NOx-VOC-O3 sensitivity scheme classifies in-situ ozone formation at each grid cell into one of the three regimes, VOC-limited, transition and NOx-limited, based on the value of a regime indicator. While the regime transition values for several different regime indicators were reported in Wang et al. [**?**], in the current study, the regime indicator R defined in equation E4-1 is used:

$$R = \frac{P_{\mathrm{H_2O_2}} + P_{\mathrm{ROOH}}}{P_{\mathrm{HNO_3}}} \tag{4.1}$$

where $P_{\mathrm{H_2O_2}}$ is the formation rate of hydrogen peroxide; $P_{\mathrm{ROOH}}$ is the formation rate of organic peroxide, and $P_{\mathrm{HNO_3}}$ is the formation rate of nitric acid in each chemistry time step. The threshold value for the start (Rts, i.e. switching from VOC-limited to transition regime) and end (Rte, i.e. switching from transition to NOx-limited regime) of the transition regime for this indicator is 0.047 and 5.142. Similar to the traditional two-regime classification used in previous ozone source apportionment models 108, and the references therein, when the in-situ formation of ozone is considered in the NOx-limited (R>Rte) or VOC-limited (R<Rts) regime, the newly formed ozone is attributed entirely to NOx and VOC sources. However, when the ozone formation is classified as in the transition regime (Rts$\leq$R$\leq$Rte), in-situ ozone is attributed to both NOx and VOC sources. The fraction of ozone formed in the transition regime attributed to NOx (FNOx) can be expressed in equations E4-2 and E4-3, both are functions of the indicator R:

$$F_{NO_x} = 3.718R, R_{ts} < R < R_{1x} \tag{4.2}$$

$$F_{NO_x} = R/(1.049R + 0.136), R_{1x} < R < R_{te} \tag{4.3}$$

where R1x = 0.142 is the indicator value when approximately half of the ozone in the transition regime is attributed to NOx.

### 4.2.2 Source Apportionment Of Ozone

Once the amount of in-situ ozone attributed to NOx (henceforth $O_3\_NO_x$) and VOCs (henceforth $O_3\_VOC$) are determined, they need to be apportioned to different NOx and VOC sources accordingly. In this study, concentrations of $O_3\_NO_x$ and $O_3\_VOC$ from different sources are tracked using non-reactive ozone tracers. The concentrations of these tracers are not updated during the regular gas phase chemistry time step but are updated afterwards based on the ozone production and removal rate as well as the concentrations of the NOx and VOCs from different sources, which are actively tracked in the gas phase chemistry using additional model species. The source-oriented framework to actively track NOx or VOCs from different sources has been previously developed and applied in many studies. The method to simultaneously track NOx and VOC sources is summarized in the next section. In the following, the approach to apportion in-situ ozone formation to different NOx and VOC sources, which is mostly based on the method used by Kwok et al. 108, are described. The concentrations of ozone attributed to NOx ($O_3\_NO_x$,i) and VOC ($O_3\_VOC_i$) from the ith source are updated. The first step in the calculation is to calculate the intermediate concentrations of $O_3\_NO_x$,i and $O_3\_VOC_i$ by considering the production of ozone ($P_{O_3}$, ppb/time step), as shown in equations E4-4 and E4-5:

$$O_3\_NO_{x,i}^{int} = O_3\_NO_{x,i}^{t-\Delta t} + P_{O_3} F_{NO_x} S_{NO_x,i}, i = 1, 2, ...N_s \tag{4.4}$$

$$O_3\_VOC_{i}^{int} = O_3\_VOC_{i}^{t-\Delta t} + P_{O_3}(1 - F_{NO_x}) S_{VOC,i}, i = 1, 2, ...N_s \tag{4.5}$$

where i is the source index; the superscript int indicates intermediate concentrations, and superscript t-âĹĘt denotes concentrations from the previous time step; FNOx is the attribution function defined in equations (2) and (3); SNOx,i and SVOC,i are source apportionment functions to apportion incremental $O_3\_NO_x$ and $O_3\_VOC$ to the ith source of NOx and VOCs, respectively. These two equations are applied to the entire range of the ozone sensitivity regime. FNOx is zero when R<Rts, and FNOx = 1 when R>Rte. In this study, SNOx and SVOC are calculated from equations E4-6 and E4-7, as shown below:

$$S_{NO_{x,i}} = \frac{P_{O\cdot|NO_{2,i}}}{\sum_{i=1}^{N_s} P_{O\cdot|NO_{2,i}}} \tag{4.6}$$

$$S_{VOC_i} = \frac{P_{NO_2|HO_{2,i}} + \sum_{j=1}^{N_R} P_{NO_2}|RO_{2,j,i}}{\sum_{i=1}^{N_s}(P_{NO_2|HO_{2,i}} + \sum_{j=1}^{N_R} P_{NO_2}|RO_{2,j,i}))} \tag{4.7}$$

where $P_{O\cdot|NO_{2,i}}$ is the formation of $O^{3P}$ radical from photolysis of NO2 from the ith source; $P_{NO_2|HO_{2,i}}$ and $P_{NO_2}|RO_{2,j,i}$ are the formation of NO2 due to NO reacting with HO2 and organic peroxy radicals (RO2) generated from degradation of organic compounds from the ith source, respectively, and j is peroxy radical index. NR is the total number of RO2 radicals in the photochemical mechanism. Using $\mathrm{NO_2}$ photolysis rate to differentiate local and background $\mathrm{O_3}$ has been first used by Zhang and Ying [94]. Using NO to NO2 conversion by organic peroxy radicals has been suggested and applied by Ying et al. [95] to study contributions of different VOC sources to ozone formation in southeast Texas. In the traditional source apportionment method, SNOx and SVOC are calculated using total NOx and maximum incremental reactivity (MIR) weighted VOC concentrations, as shown

in equations E4-6' and E4-7':

$$S_{NO_{x,i}} = \frac{C_{NO,i} + C_{NO_2,i}}{\sum_{i=1}^{N_s} C_{NO,i} + C_{NO_2,i}} \tag{4.8}$$

$$S_{VOC_i} = \frac{\sum_{j=1}^{N_c} C_{VOC,j,i} MIR_j}{\sum_{i=1}^{N_s} \sum_{j=1}^{N_c} C_{VOC,j,i} MIR_j} \tag{4.9}$$

where Nc is the number of VOCs included in the calculation, $C_{VOC,j,i}$ is the concentration of the jth VOC from the ith source, and MIRj is the maximum incremental reactivity of the $j^{th}$ VOC. $C_{NO,i}$ and $C_{NO_{2,i}}$ are concentrations of NO and NO2 from the ith source, respectively. The MIR values for the VOC species included in equation (7') are listed in Table S1. The difference in the expected source apportionment results due to different source attribution functions is discussed in Section 3.5.2.

The intermediate concentrations are then used to update the concentrations of $O_3\_NO_{x,i}$ and $O_3\_VOC_i$ by including the ozone removal terms, as shown in equations E4-8 and E4-9:

$$O_3\_NO_{x,i}^t = O_3\_NO_{x,i}^i nt - D_{O_3} \frac{O_3\_NO_{x,i}^{int}}{\sum_{i=1}^{N_s}(O_3\_NO_{x,i}^{int} + O_3\_NO_{x,i}^{int} + O_3\_VOC_i^{int})}, i = 1, 2...N_s \tag{4.10}$$

$$O_3\_VOC_i^t = O_3\_VOC_i^i nt - D_{O_3} \frac{O_3\_VOC_i^{int}}{\sum_{i=1}^{N_s}(O_3\_NO_{x,i}^{int} + O_3\_NO_{x,i}^{int} + O_3\_VOC_i^{int})}, i = 1, 2...N_s \tag{4.11}$$

where $D_{O_3}$ is the in-situ ozone removal rate. To quantify contributions of difference sources to ozone formed in the transition regime, another set of ozone tracers $O_3\_TRS\_NO_{x,i}$ and $O_3\_TRS\_VOC_i$ are included in the analysis. Equations to update their concentrations are similar to equations (4)-(9) and are not repeated here.

### 4.2.3 Source Apportionment Of NOx And VOCs

The source-resolved formation rates needed for equations E4-6 and E4-7 and the concentrations of NOx and VOCs needed for equations E4-6' and E4-7' are calculated at each chemistry time step using an expanded source-oriented photochemical mechanism that tracks the emissions of NOx and VOCs from different sources and their reaction products using reactive source-tagged species. Reactions of these source-tagged species are generated based on the reactions of their corresponding non-tagged species. The source-oriented approach using reactive tagged species has been applied previously to the NOx related reactions for source apportionment of nitrate aerosol [41] and to VOC related reactions for source apportionment of SOA [46]. In this study, a modified lumped SAPRC-11 mechanism [47, 40] was expanded to simultaneously track NOx, primary VOCs and their reaction products from two separate sources. The entire expanded reaction system includes 1356 reactions and 350 species. A few reactions to explain the concept are provided below. Reaction sets R4-1, R4-2 and R4-3 show examples of the reactions of NOx species, organic peroxy and hydroperoxyl radicals, and double tagged species with both NOx and VOC precursors, respectively:

$$\begin{aligned} \mathrm{OH} + \mathrm{NO_2^{x_1}} &= \mathrm{HNO_3^{x_1}} \\ \mathrm{OH} + \mathrm{NO_2^{x_2}} &= \mathrm{HNO_3^{x_2}} \end{aligned} \tag{4.12}$$

$$\begin{aligned} \mathrm{MEO_2^{x_1}} + \mathrm{NO^{x_1}} &= \mathrm{NO_2^{x_1}} + \mathrm{HCHO^{x_1}} + \mathrm{HO_2^{x_1}} \\ \mathrm{MEO_2^{x_1}} + \mathrm{NO^{x_2}} &= \mathrm{NO_2^{x_2}} + \mathrm{HCHO^{x_1}} + \mathrm{HO_2^{x_1}} \\ \mathrm{MEO_2^{x_2}} + \mathrm{NO^{x_1}} &= \mathrm{NO_2^{x_1}} + \mathrm{HCHO^{x_2}} + \mathrm{HO_2^{x_2}} \\ \mathrm{MEO_2^{x_2}} + \mathrm{NO^{x_2}} &= \mathrm{NO_2^{x_2}} + \mathrm{HCHO^{x_2}} + \mathrm{HO_2^{x_2}} \end{aligned} \tag{4.13}$$

$$
\begin{aligned}
\mathrm{MECO_3^{X1}} + \mathrm{NO_2^{X1}} &= \mathrm{PAN^{X1\_1}} \\
\mathrm{MECO_3^{X1}} + \mathrm{NO_2^{X2}} &= \mathrm{PAN^{X1\_2}} \\
\mathrm{MECO_3^{X2}} + \mathrm{NO_2^{X1}} &= \mathrm{PAN^{X2\_1}} \\
\mathrm{MECO_3^{X2}} + \mathrm{NO_2^{X2}} &= \mathrm{PAN^{X2\_2}}
\end{aligned}
\tag{4.14}
$$

MEO2 and MECO3 represent methoxy and peroxyacetyl radicals in SARPC-11, and PAN is peroxyacetyl nitrate. In reaction set (RS2), the HO2 species produced from the RO2+NO reaction has the same source tag as its RO2 precursor. PAN is a double-tagged species so that the correct sources of MECO3 and NO2 can be determined during its thermal decomposition reaction. While this source-oriented approach can be applied to develop mechanisms with more than two groups of tagged species, the number of reactions increases rapidly due to reactions with multiple tag-species such as RS2 and RS3. Thus, as an illustration of concept, it is limited to two sources in this study. For source apportionment calculations for N sources, N model simulations need to be carried out. In each simulation, emissions from one explicit source will be tracked using X1 species, and emissions from all other sources, including initial and boundary conditions, will be treated as X2 species.

### 4.3 Model Application

The method described in Section 2 was implemented in CMAQ model (version 5.0.1) [36, 37, 38] to determine source contributions to ozone in China in August 2013. The model domain has a horizontal resolution of $36 \times 36km^2$ and covers China and surrounding areas (Figure S1). Meteorological inputs for the CMAQ model were generated using the Weather Research and Forecasting (WRF) model version 3.6.1, driven by initial and boundary conditions based on the FNL reanalysis data from the National Centers for Environmental Prediction (NCEP). Anthropogenic emissions in China were based on the Mul-

tiresolution Emission Inventory for China (MEIC) version 1.0, which groups emissions into four sectors, industries, residential, power plants and transportation. Open burning emissions were generated using an in-house program using inputs from the FINN inventory from the National Center for Atmospheric Research (NCAR) [51]. Emissions from biogenic sources were generated using MEGAN v2.1. The Regional Emission inventory in ASia v2.1 (REAS2) [43] was used to generate emissions for other countries in the model domain. The CMAQ vertical domain is divided into 12 layers with increasing layer thickness. The surface layer is  35 m and the total height of the model is approximately 10 km. The initial and boundary conditions for the simulation were based on the CMAQ default profiles which represent clean continental conditions. More details of the meteorological and emission processing for this episode can be found in Hu et al. [42]. The capability of this WRF/CMAQ setup in reproducing observed pollutant concentrations, including O3, PM2.5, VOCs, and PM2.5 primary and secondary components has been extensively evaluated in previous studies [21, 31, 42, 73, 96]. In this study, source contributions to regional ozone were determined for industries, residential, power plants, transportation, open burning and biogenic sources. In addition, contributions due to anthropogenic emissions from other countries and upwind NOx and VOCs enter the domain as boundary conditions were also explicitly determined. The ozone directly entering the domain via initial and boundary conditions was considered as background ozone. The background ozone concentration at each grid was estimated by the difference between the overall ozone concentration and the sum of the ozone attributed to the above source categories. Two sets of source apportionment calculations were performed. One with the three-regime approach described in Section 3.2 and other using the traditional two-regime approach with a threshold value of 0.5 [97] to determine whether ozone formation in the NOx-limited or VOC-limited regime. Both sets of simulations use the ozone-sensitivity regime indicator as defined in equation E4-1, and the source apportionment function equations E4-6 and E4-7.

## 4.4 Results

### 4.4.1 Regional Source Apportionment Of Ozone

Figure 4- 1 and Figure C- 2 show the regional concentrations and fractional contributions of August monthly average 8-hr ozone attributed to different sources of NOx and VOCs. Industries, transportation, power and biogenic sources are four major emission sectors that contribute to $O_3\_NO_x$ with different spatial distributions. The high $O_3\_NO_x$ areas of the industrial sector (generally 8-15 ppb or approximately 20-25% of total ozone, with a maximum concentration of 20 ppb) are mainly located in north and northeast China (Liaoning, Hebei, and Shandong provinces; locations of the provinces in China can be found in Figure C- 1), the YRD and part of SCB. The ozone concentrations attributed to this sector in other areas is generally between 4-8 ppb with relative contributions between 5-15%. The $O_3\_NO_x$ attributed to the transportation sector reaches a maximum value of 15 ppb, with a spatial distribution similar to that of the industrial sector although the relatively high concentration regions cover a broader area from the BTH down south to the east of the YRD in central China. In most of the areas, the relative contribution is approximately 5-1% with higher fractions of 10-15% in many urban areas. For power sector, the high $O_3\_NO_x$ regions are located in Shanxi, Shaanxi, Ningxia and part of Shandong and Jiangsu provinces, with 10-15% relative contributions to total ozone. In other areas, its relative contribution is approximately 5-10%. In mountainous regions in west, central and south China, especially the areas with low NOx emissions from anthropogenic sources, ozone formation is in the NOx-limited regime. NO emitted from microbial activities in the soil can contribute to a significant fraction (as high as 30-40%) of total NO2 (see Figure C- 3). Ozone attributed to biogenic NOx in these areas reaches as high as 10-15% of total ozone and a maximum concentration of 12 ppb. In most regions, however, ozone attributed to biogenic NOx is approximately 2-3 ppb. The $O_3\_NO_x$ formed in the transition

regime ($O_3$_$NO_x$_$TRS$) accounts for a significant fraction of the total $O_3$_$NO_x$ (column 2 in Figure 4- 1), mostly in the high ozone concentration areas in north, central and east China.

Ozone attributed to VOCs does not have an as broad regional distribution as that attributed to NOx. This is because most of the VOC-limited grid cells are located at urban cores in big cities as well as some large city clusters in the YRD and PRD regions [**?**]. The transition areas with more ozone formation attributed to VOC sources are mostly located in the urban areas near the VOC-limited grid cells. Biogenic and industrial sectors are the most important emission sectors that contribute to $O_3$_$VOC$. The high concentration areas of the biogenic sector are located in Shandong, Jiangsu, Henan and Anhui provinces with the highest fraction to total ozone of $20\%$. It is interesting to note that this does not agree with the spatial distribution of the emissions of biogenic VOCs (BVOCs). The areas with high BVOC emissions are located in the mountainous areas in south and southeast China, such as Zhejiang, Fujian, Guangdong and Guizhou [31] but ozone formation in these intense BVOC emission areas is NOx-limited [**?**]. The industrial sector has high relative contributions to $O_3$_$VOC$ in areas along the east coast from Tianjin to Shanghai. In addition, high relative contributions to total ozone up to $20\%$ are also predicted for urban areas in the PRD and SCB regions. Overall, more than $85\%$ of the $O_3$_$VOC$ in China is from the biogenic and industrial sectors. Based on the current version of the MEIC emission inventory, contributions from traffic emissions to $O_3$_$VOC$ are small, on the order of a few percent in most urban areas. VOC emission rates from transportation sources are rather uncertain 113, thus this conclusion requires more scrutiny in future studies.

The source contributions to $O_3$_$NO_x$ and $O_3$_$VOC$ for each province can be found in Table C- 2 and Table C- 3, respectively. A total of 12 provinces have monthly 8-hr $O_3$_$NO_x$ of more than 20 ppb, and Beijing is leading the list with 26 ppb. The contributions of three anthropogenic sources (industries, power plants and transportation) account

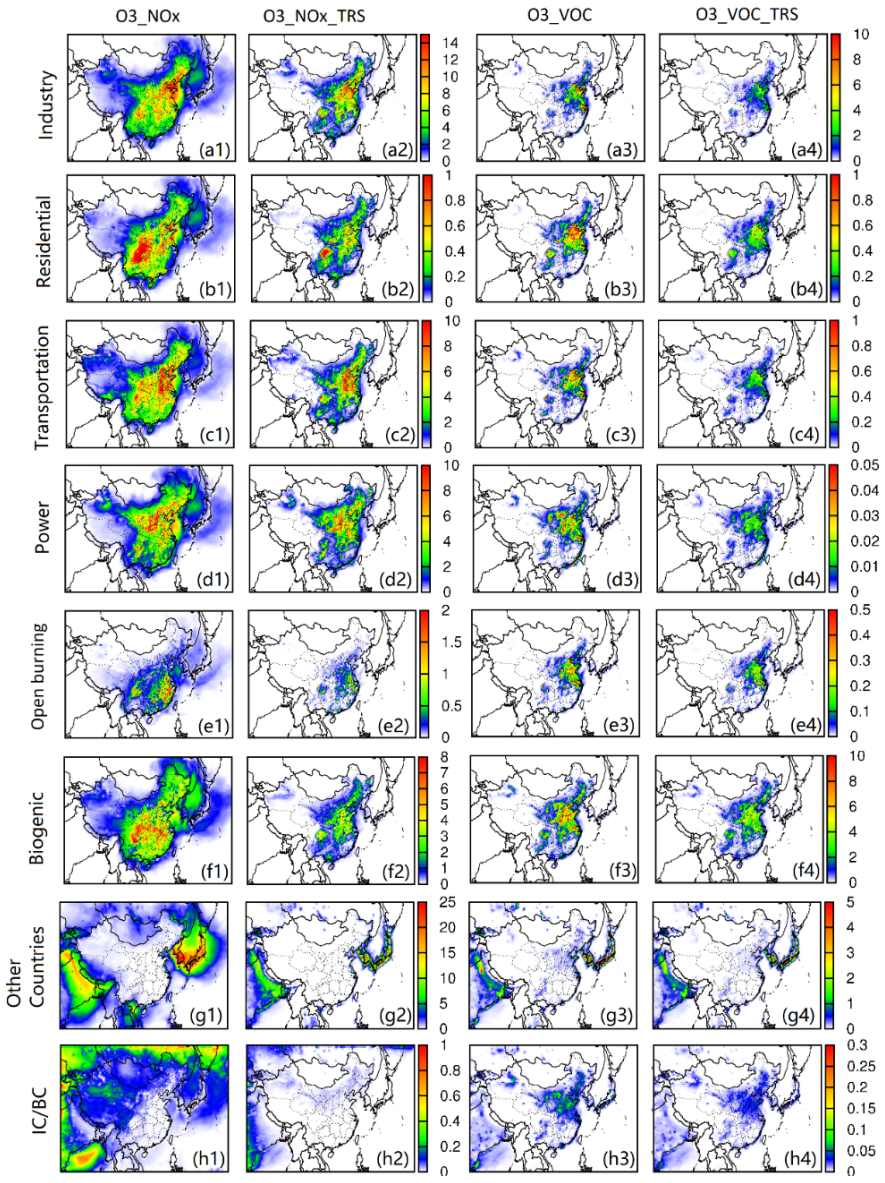


Figure 4.1: Average source contributions to 8-hr ozone attributed to NOx ($O_3$_$NO_x$, column 1), VOCs ($O_3$_$VOC$, column 3), and to 8-hr ozone formed in the transition regime attributed to NOx ($O_3$_$NO_x$_$TRS$, column 2) and VOCs ($O_3$_$VOC$_$TRS$, column 4). Emissions from different sectors in other counties are combined and considered as a single class. The IC/BC contributions are ozone formed attributed to NOx and VOCs entered the domain through initial and boundary conditions. Ozone directly enters the domain though initial and boundary conditions are referred to as "background" ozone and is not included in the IC/BC class.

for 73% (Anhui) to 88% (Tianjin) of $O_3$_$NO_x$. For $O_3$_$VOC$, Tianjin is leading the list with 14 ppb. Other provinces with 10 ppb or more $O_3$_$VOC$ are Shandong (13 ppb), Shanghai (12 ppb), Shanxi (11 ppb) and Jiangsu (10 ppb). Beijing follows the top group with $O_3$_$VOC$ of 9 ppb. Industrial sector contributions to $O_3$_$VOC$ is highest in the two municipalities of Shanghai (52%) and Tianjin (42%). Contributions of transportation sources to $O_3$_$VOC$ range from 3.3% to 5.3% among these provinces, and contributions of residential sources are also similar. Biogenic contributions among these provinces are 40-50%.

The overall regional source contributions ($O_3$_$NO_x$ + $O_3$_$VOC$) to monthly average 8-hr ozone are shown in Figure 4- 2, with fractional contribution shown in Figure C- 4. A more quantitative summery Due to its high contributions to both $O_3$_$NO_x$ and $O_3$_$VOC$, the industrial sector has the highest concentrations and contributions to ozone in large areas, particularly in the south part of the Hebei province, the traditional industrial regions in northeast China and SCB, and urban and industrial regions long the east coast. In these areas, the relative contribution can be as high as 30%. In other regions, it contributes to approximately 10% of total ozone. For transportation and power plant sectors, their contributions to $O_3$_$VOC$ are small, so their overall regional contributions are similar to those in Figure 4- 1. Biogenic emissions also contribute to both $O_3$_$VOC$ and $O_3$_$NO_x$ but their spatial distributions are different. The overall contributions of biogenic sources to ozone are 8-12 ppb, or 12-15%, in areas in central and east China, and in SCB. In other areas, its contributions are approximately 5-10%. Contributions of residential source to ozone is small in the summer, with a maximum contribution of 4.5% in SCB. Figure 4-2(g) and (i) show that NOx and VOC emissions from other countries in the domain and from initial and boundary conditions have negligible contributions to ozone in China during this episode. The background ozone is highest ( 50 ppb) in high elevation areas in Tibet, Xinjiang and part of the Inner Mongolia. It accounts for almost 100% of the total

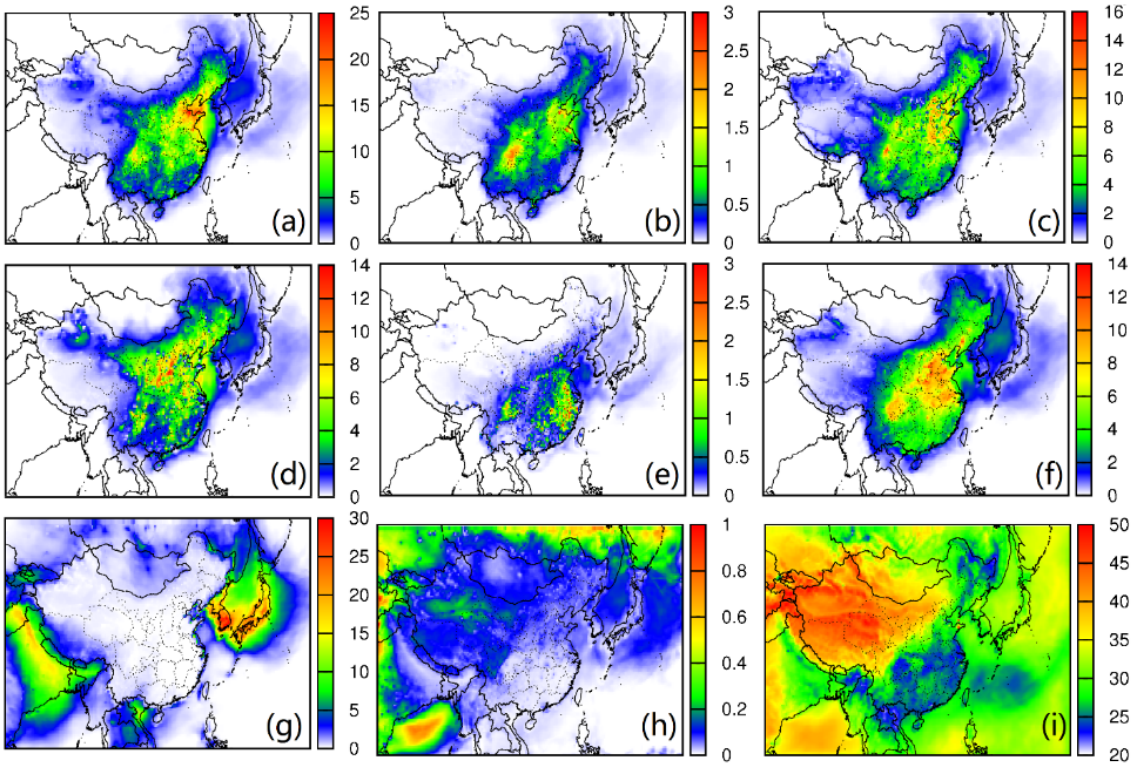


Figure 4.2: Monthly average contributions to 8-hr ozone attributed to NOx and VOCs ($O_3\_NO_x$ + $O_3\_VOC$) emitted from (a) industries, (b) residential, (c) transportation, (d) power, (e) open burning, (f) biogenic, (g) other countries and (h) initial and boundary conditions. Estimated concentrations of background ozone are shown in panel (i). Units are ppb.

ozone concentrations in these areas. In east and southeast China, a background concentration of 25 ppb is predicted. The relative contribution of background ozone is less than 40% in high ozone areas in south Hebei, Shandong and Jiangsu provinces and the SCB. In other densely populated areas, background ozone accounts for approximately 50-60% of total 8-hr ozone.

Table 4- 1 summarizes the monthly average 8-hr total and non-background ozone, and source contributions to non-background ozone for each province. Nine provinces have a non-background ozone fraction of more than 50%. Shandong (57%, total ozone 66 ppb),

Jiangsu (55%, 58 ppb) and Anhui (53%, 55 ppb) in east China are the top three provinces. Provinces in north China, including Shanxi (52%, 65 ppb), Tianjin (52%, 69 ppb) and Beijing (51%, 69 ppb) are also among the nine provinces. Hebei province in north China also has high overall 8-hr ozone and non-background fraction (47.5%, 65 ppb). The provinces in north China generally have higher overall ozone than provinces in east China as they have higher background ozone as well as high ozone formation from emissions. On average, the BTH region has an area-averaged 8-hr ozone of 66 ppb in August 2013 and about half of it is non-background (32 ppb). Contributions of industries, transportation, power and biogenic sources to non-background ozone are 33%, 20%, 19% and 24%, respectively. Provinces in west China and two island provinces are not experiencing ozone problem, with less than 10 ppb non-background ozone in general.

Figure 4- 3 shows the diurnal and day-to-day variation and source apportionment of hourly $O_3\_NO_x$, $O_3\_VOC$ and total non-background ozone ($O_3\_VOC$+$O_3\_NO_x$) in four megacities: Beijing, Shanghai, Guangzhou and Chengdu in August 2013. Overall, the model predictions reproduced observed diurnal and day-to-day variations although several ozone peaks were under-predicted. This good agreement between observations and predictions provides confidence in the predicted source apportionment results. Hourly concentrations of $O_3\_NO_x$ can reach high concentrations in all four cities, with peak $O_3\_NO_x$ approaching 80 ppb in Beijing, Shanghai and Chengdu on several days. Peak $O_3\_NO_x$ in Guangzhou is usually low although on a few days it can reach 40-50 ppb. Industries and transportation are the two major contributors in all four cities. Power plant contributions are significant in three of the four cities except Chengdu, where transportation sector contributions are on par with the industrial sector. Concentrations of $O_3\_VOC$ are lower than $O_3\_NO_x$ in general. Peak hourly concentrations reach 20 ppb with contributions mostly due to industrial and biogenic sources. In Shanghai, contributions to $O_3\_VOC$ due to industrial sources can be much higher on high ozone days, reaching 40

Table 4.1: Monthly average 8-hr ozone and source contributions to non-background 8-h ozone for each province in China, August 2013.

| Province | Avg. ppb | NB ppb | Relative contributions to non-background (NB) ozone (%) | | | | | | | |
|---|---|---|---|---|---|---|---|---|---|---|
| | | | Ind. | Res. | Transp. | Power | OB | Biog. | Other | IC/BC |
| Beijing (BJ) | 69.2 | 35.6 | 34.4 | 2.9 | 25.4 | 13.6 | 0.6 | 22.6 | 0.4 | 0.1 |
| Tianjin (TJ) | 69.3 | 36.0 | 42.0 | 3.1 | 19.3 | 11.1 | 1.2 | 22.3 | 0.8 | 0.2 |
| Hebei (HE) | 65.0 | 30.9 | 31.9 | 2.8 | 19.5 | 19.7 | 0.9 | 24.5 | 0.6 | 0.2 |
| Shanxi (SX) | 64.7 | 33.7 | 33.2 | 1.8 | 14.1 | 26.7 | 0.9 | 22.8 | 0.5 | 0.2 |
| Inner Mongolia (NM) | 46.1 | 10.0 | 22.7 | 2.1 | 15.1 | 32.5 | 0.4 | 21.9 | 4.4 | 1.0 |
| Liaoning (LN) | 59.4 | 29.9 | 37.1 | 1.9 | 19.2 | 18.1 | 0.7 | 19.4 | 3.4 | 0.2 |
| Jilin (JL) | 51.6 | 22.8 | 34.0 | 1.9 | 17.9 | 20.9 | 0.6 | 18.7 | 5.8 | 0.3 |
| Heilongjiang (HL) | 40.3 | 13.9 | 25.6 | 2.2 | 21.5 | 19.7 | 0.4 | 23.3 | 6.6 | 0.7 |
| Shanghai (SH) | 49.8 | 23.1 | 46.5 | 1.4 | 11.5 | 10.9 | 4.0 | 21.1 | 4.6 | 0.2 |
| Jiangsu (JS) | 58.2 | 31.9 | 34.8 | 2.3 | 19.0 | 14.8 | 3.5 | 24.6 | 0.9 | 0.1 |
| Zhejiang (ZJ) | 45.1 | 20.0 | 34.0 | 0.9 | 23.1 | 12.1 | 6.2 | 22.1 | 1.5 | 0.1 |
| Anhui (AH) | 54.8 | 29.1 | 26.4 | 2.7 | 23.2 | 17.2 | 3.2 | 27.0 | 0.3 | 0.1 |
| Fujian (FJ) | 39.3 | 13.9 | 29.8 | 1.1 | 21.4 | 18.1 | 5.8 | 22.7 | 0.9 | 0.1 |
| Jiangxi (JX) | 45.4 | 19.7 | 26.4 | 1.9 | 24.9 | 17.7 | 3.7 | 24.8 | 0.6 | 0.1 |
| Shandong (SD) | 66.3 | 37.7 | 39.6 | 3.0 | 19.1 | 13.3 | 1.5 | 22.6 | 0.8 | 0.2 |
| Henan (HA) | 58.1 | 29.8 | 32.1 | 2.6 | 21.3 | 15.2 | 1.2 | 27.1 | 0.5 | 0.1 |
| Hubei (HB) | 49.4 | 23.5 | 33.5 | 3.0 | 20.0 | 14.0 | 2.0 | 26.9 | 0.6 | 0.1 |
| Hunan (HN) | 43.9 | 17.9 | 31.4 | 2.6 | 22.6 | 15.3 | 2.7 | 24.5 | 0.9 | 0.1 |
| Guangdong (GD) | 39.4 | 13.9 | 28.1 | 3.1 | 21.3 | 19.4 | 1.8 | 22.8 | 3.3 | 0.1 |
| Guangxi (GX) | 38.5 | 13.4 | 29.4 | 2.8 | 22.6 | 11.3 | 1.9 | 26.8 | 5.1 | 0.1 |
| Hainan (HI) | 32.6 | 6.7 | 23.4 | 3.8 | 21.3 | 12.0 | 0.9 | 18.3 | 20.2 | 0.2 |
| Chongqing (CQ) | 48.1 | 22.1 | 30.6 | 3.9 | 23.0 | 13.6 | 1.6 | 26.0 | 1.3 | 0.1 |
| Sichuan (SC) | 49.4 | 17.7 | 30.2 | 5.0 | 23.0 | 11.1 | 2.3 | 25.9 | 2.1 | 0.5 |
| Guizhou (GZ) | 41.0 | 15.5 | 28.9 | 4.2 | 19.4 | 18.9 | 1.1 | 23.8 | 3.5 | 0.2 |
| Yunnan (YN) | 37.4 | 10.8 | 30.7 | 3.8 | 26.4 | 11.4 | 1.5 | 19.6 | 6.2 | 0.3 |
| Xizang (XZ) | 44.7 | 5.0 | 9.4 | 0.8 | 18.6 | 3.5 | 0.8 | 10.5 | 54.6 | 1.9 |
| Shaanxi (SN) | 55.8 | 24.3 | 27.5 | 3.4 | 22.5 | 20.2 | 1.0 | 24.4 | 0.8 | 0.2 |
| Gansu (GS) | 52.9 | 12.5 | 28.6 | 2.7 | 25.0 | 20.8 | 0.7 | 19.7 | 1.7 | 0.9 |
| Qinghai (QH) | 48.7 | 5.1 | 28.9 | 2.1 | 23.9 | 12.5 | 0.9 | 22.4 | 7.1 | 2.2 |
| Ningxia (NX) | 59.0 | 19.1 | 25.5 | 2.7 | 25.6 | 22.9 | 0.8 | 21.5 | 0.7 | 0.5 |
| Xinjiang (XJ) | 47.1 | 3.7 | 26.4 | 0.8 | 20.9 | 19.2 | 0.3 | 15.9 | 13.1 | 3.4 |
| Taiwan (TW) | 29.1 | 2.7 | 14.8 | 0.7 | 10.2 | 12.8 | 3.8 | 24.8 | 32.6 | 0.4 |

ppb in several days, which leads to overall $O_3\_VOC$ concentrations of approximately 60 ppb. The biogenic sector is a more significant contributor in Beijing and Chengdu with the highest values  15 ppb and  20 ppb, respectively. On several days, contributions of open

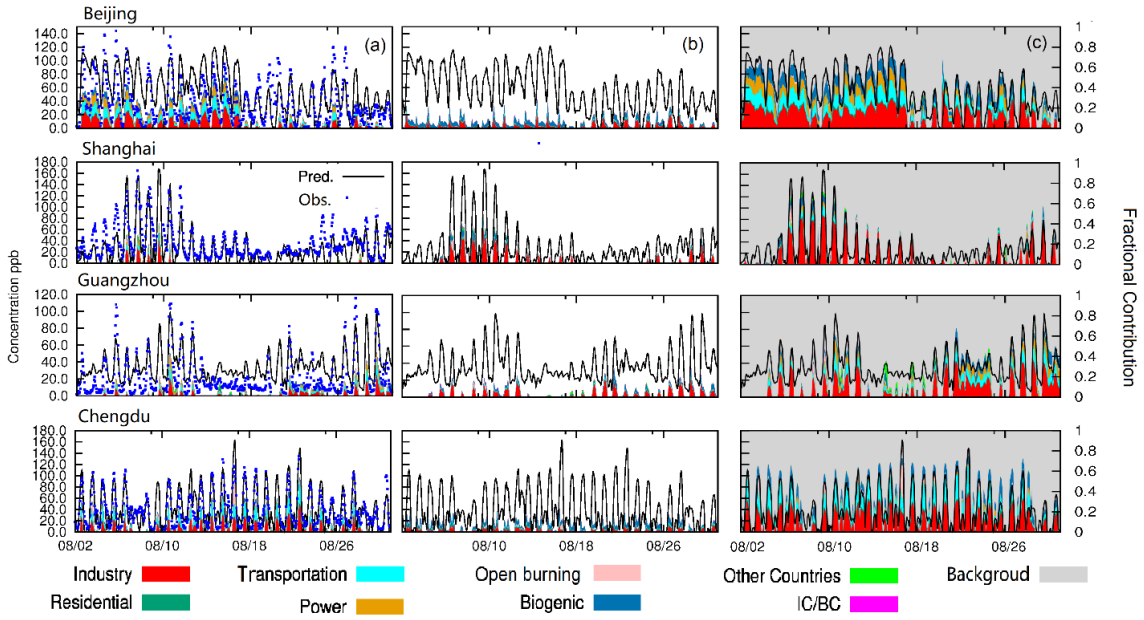


Figure 4.3: MDiurnal variations of hourly averaged ozone and the contributions of each sector to (column a) $O_3$_$VOC$, (column b) $O_3$_$NO_x$ and (column c) fractional contributions of combined $O_3$_$VOC$+ $O_3$_$NO_x$ to total ozone concentrations in Beijing, Shanghai, Guangzhou and Chengdu, China in August 2013. Ozone concentrations in column (a) and (b) are in units of ppb.

burning to $O_3$_$VOC$ are also predicted, with a highest hourly concentration of approximately 20 ppb in Shanghai on August 6. When both $O_3$_$NO_x$ and $O_3$_$VOC$ are included, non-background ozone can be responsible for as much as 60-70% of total ozone on high ozone days in Beijing, Guangzhou and Chengdu. In Shanghai, this fraction can be as high as 80%.

### 4.4.2 Difference In Source Contributions On Low And High Ozone Days

Understanding the cause of high ozone concentrations is essential in developing effective ozone control strategies. The source contributions to ozone on high ozone (8-h O3 > 80 ppb) and low ozone (40 ppb < 8-h O3 $\leq$ 80 ppb) days are investigated. From Figure 4-4(a), areas experienced at least one high ozone day are mainly located at the BTH region

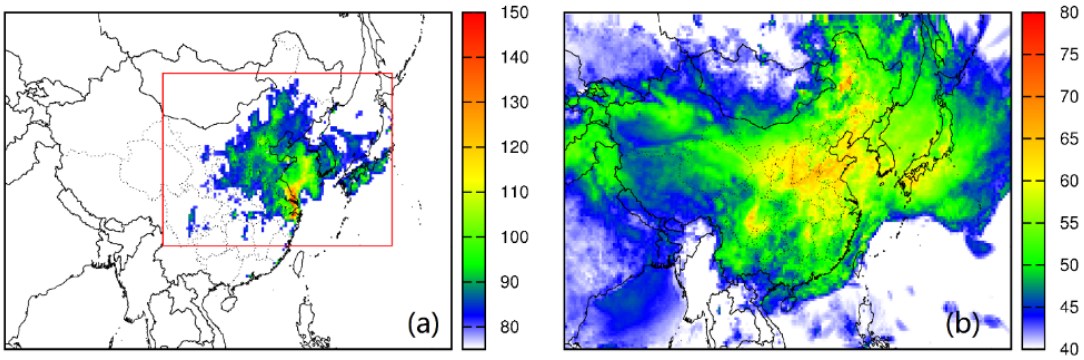


Figure 4.4: MAverage 8-hr ozone concentrations on (a) high ozone days (8-hr ozone > 80 ppb) and (b) low ozone days (8-hr ozone within 40 and 80 ppb) during August 2013. The red box marks the region with high ozone concentrations where detailed source contributions are shown in Figure 5.

and Liaoning, Shanxi, Henan and Jiangsu provinces and Shanghai municipality. In Shanghai and south of Jiangsu province the average 8-h ozone on high ozone days is over 140 ppb, which is approximately 1.75 times that of the Class II daily maximum 8-hr average ozone standard of 160 $\mu g \cdot m^{-3}$ (or approximately 75 ppb under 273K and 1 atm) required by the Ministry of Environmental Protection (MEP) of China [98]. For days with 8-hr ozone less than 80 ppb, higher average concentrations occur in north and central China with an average concentration of approximately 60-65 ppb (Figure 4- 4b).

Average relative source contributions to non-background 8-hr ozone on low and high ozone days are compared in Figure 4- 5. While ozone concentrations attributed to all major source sectors increase during high ozone days (Figure C- 5), relative source contributions to non-background ozone due to biogenic sources on low ozone days in August are generally higher than on high ozone days. The decrease in biogenic contributions leads to increase in contributions due to anthropogenic sources, most noticeably in the industrial and power plant sectors. Since the emissions of anthropogenic sources in the same month

in this study only have weekday-weekend differences but biogenic emissions are calculated based on meteorological conditions and do have day-to-day variations built in, this decrease in biogenic relative contributions is likely due to decrease in biogenic emissions due to higher temperature on high ozone days. If changes in anthropogenic emissions due to meteorological conditions have also been considered properly (e.g. increase of power plant emissions on high temperature days due to higher energy demand), the relative contributions of biogenic emissions would have been even lower.

## 4.5 Discussions

### 4.5.1 Compare With The Two-regime Source Apportionment Results

The source apportionment results reported in previous sections are based on the three-regime approach. The source apportionment results are compared with those from the traditional two-regime approach as shown in Figure 4- 6 for industries, transportation, power plants and biogenic sectors for monthly average 8-hr ozone concentrations. The two-regime approach leads to lower estimation of the contributions of $O_3\_NO_x$ and higher contributions of $O_3\_VOC$ by as much as 8-10 ppb in urban areas where the two-regime approach classifies them as VOC-limited, but the three-regime approach classifies them as transitional. Since the industrial sector accounts for a larger fraction of NOx than the power plant and transportation sectors, it has the biggest difference by up to 4 ppb in $O_3\_NO_x$. The transportation and power plant sectors show a difference of 1-2 ppb $O_3\_NO_x$ each. For $O_3\_VOC$, the three-regime approach predicts lower contributions than the two-regime approach. The biggest differences are in the industrial and biogenic sectors, by as much as 2 and 4 ppb, respectively. When the overall source apportionment results (i.e., $O_3\_NO_x$ + $O_3\_VOC$) are considered for culpability assessments for each sector, the difference between the two-regime and three-regime approaches may not be as significant. This is because the higher prediction in $O_3\_NO_x$ and lower prediction in

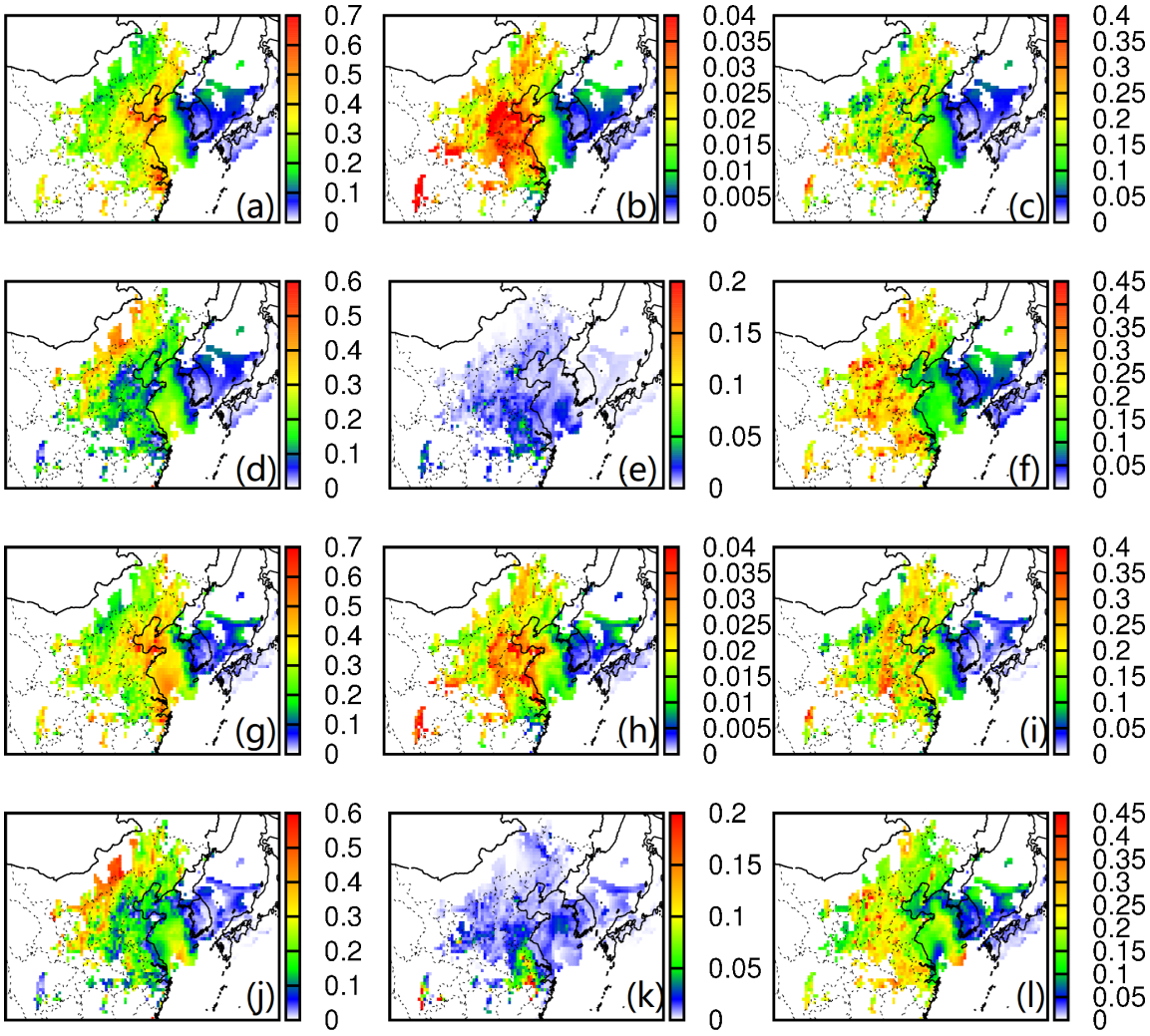


Figure 4.5: Average relative source contributions of (a) industries, (b) residential, (c) transportation, (d) power, (e) open burning and (f) biogenic emissions to non-background 8-hr ozone on low ozone days (8-hr ozone within 40 and 80 ppb), and (g) industries, (h) residential, (i) transportation, (j) power, (k) open burning and (l) biogenic emissions to 8-hr ozone on high ozone days (8-hr ozone > 80 ppb) in August 2013. Only the regions with high ozone days are shown in the panels.

$O_3$_$VOC$ can compensate each other out.

Figure 4- 7 shows a comparison of source apportionment results using the two-regime and three-regime approaches for the four cities discussed in Figure 4- 3. In cities where both $O_3$_$VOC$ and $O_3$_$NO_x$ are important contributors to total ozone (Beijing and Chengdu), the two approaches lead to relatively large differences in the total $O_3$_$VOC$ and $O_3$_$NO_x$ estimations. For example, the two-regime approach estimates that VOC is slightly more important (18.4 ppb vs. 14.6 ppb) while the three-regime approach estimates that NOx is more important (19.6 ppb vs 13.4 ppb). This difference in $O_3$_$VOC$ and $O_3$_$NO_x$ is more obvious in Chengdu. In those two cities, the relative source contributions to $O_3$_$VOC$ and $O_3$_$NO_x$ between the two approaches are very similar but the overall source apportionment shows bigger differences. In general, the overall source contributions determined by the two-regime approach are lower than the three-regime approach for anthropogenic sources but are higher for the biogenic sector. In Shanghai, $O_3$_$VOC$ contributions are much higher than $O_3$_$NO_x$. The two approaches give similar source apportionment results for $O_3$_$VOC$ and total non-background ozone. Although the difference in $O_3$_$NO_x$ is quite significant, the total concentration of $O_3$_$NO_x$ is small and thus does not lead to significant differences in the source apportionment results for non-background ozone. In Guangzhou, the two-regime approach estimates that $O_3$_$VOC$ dominates the total non-background ozone (11.6 ppb vs. 1.6 ppb), but the three-regime approach suggests that although $O_3$_$VOC$ is still more important, the contributions of NOx to ozone cannot be ignored (5.0 ppb vs. 8.2 ppb). Thus, although the two approaches lead to similar overall source contribution assessments, they are still significantly different in their assessment of the relative importance of NOx vs. VOC sources in ozone formation, which may lead to different assessments of the priorities of the sources in emission control.

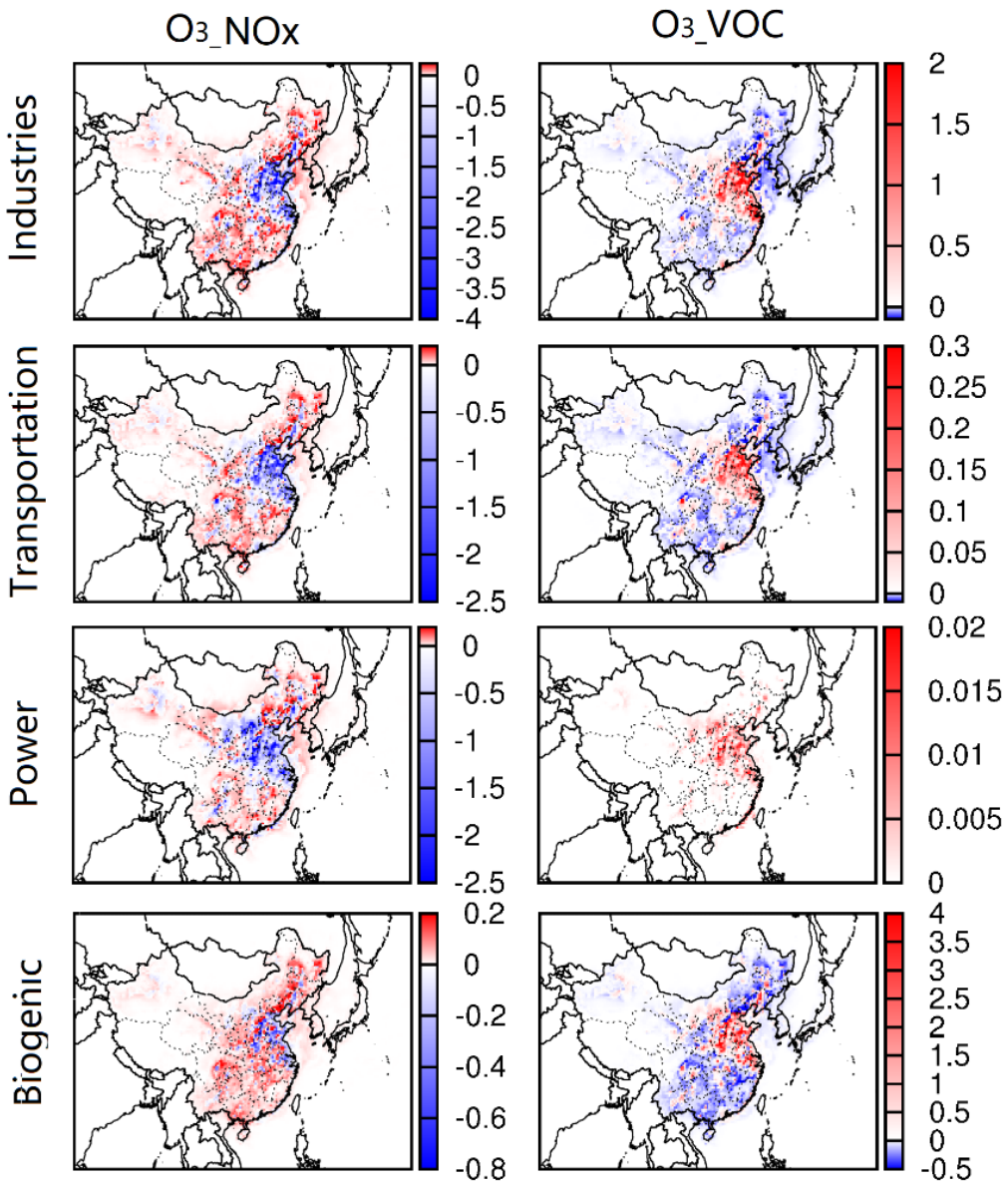


Figure 4.6: Difference in predicted monthly averaged 8-hr ozone when the ozone formation regime is determined using the two-regime approach with a regime threshold value of 0.5. The differences are calculated by subtracting the three-regime approach results from the corresponding two-regime approach results. Units are ppb.

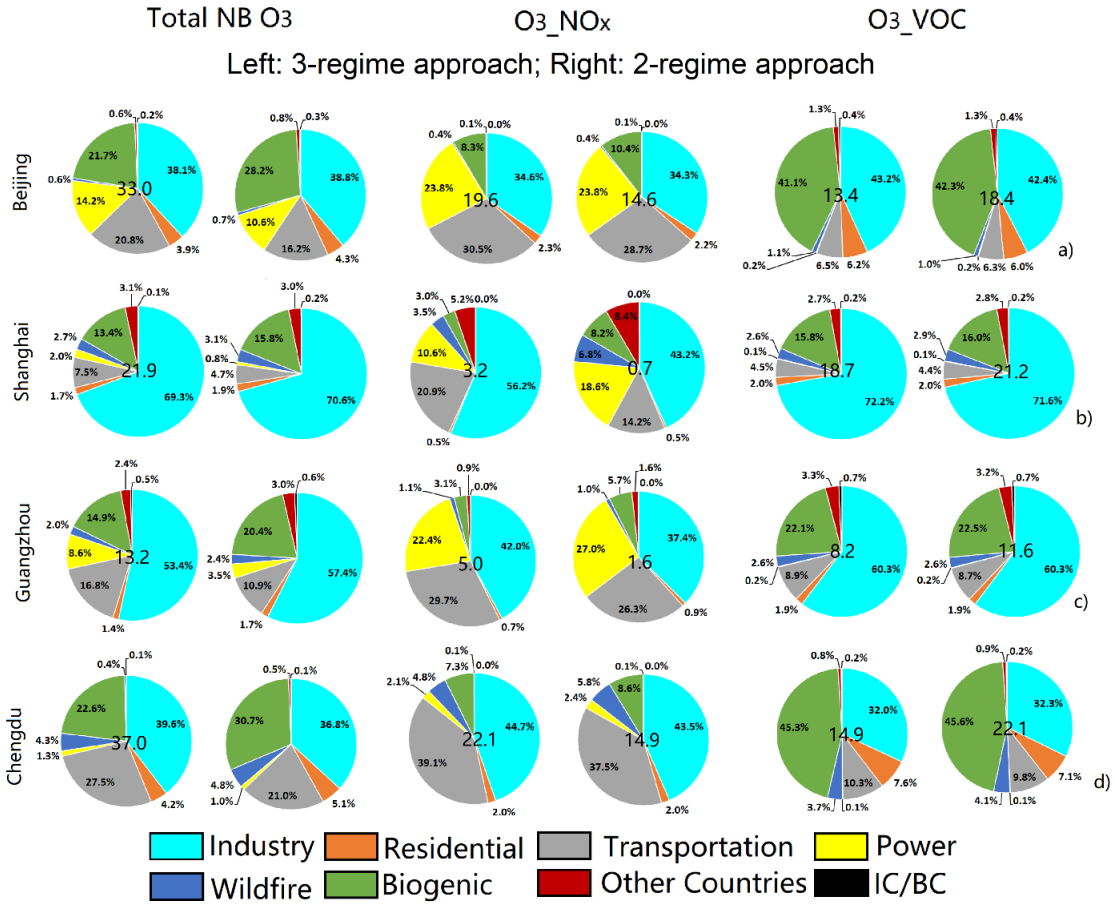


Figure 4.7: Monthly averaged source contributions to $O_3\_NO_x$, $O_3\_VOC$ and total non-background ozone in Beijing, Shanghai, Guangzhou and Chengdu estimated by the three-regime and two-regime approaches. Numbers at the center of the pie charts are average concentrations in ppb.

### 4.5.2 Source Attribution Functions For NOx And VOCs

Another uncertainty in ozone source apportionment comes from the source apportionment functions. Figure 4- 8 shows the VOC source apportionment factors (E4-7 and E4-7') for industry and biogenic sectors based on monthly average concentrations and conversion rates during the hours for 8-hr ozone calculations. For the industry sector, the attribution factor based on MIR weighted concentrations (E4-7') are usually higher than that based on the NO to NO2 conversion rates (E4-7), with a difference of 5-10%. The trend is opposite for the biogenic sector. The MIR-based approach leads to a smaller fraction of 5-10%. Difference for other source sectors is generally small (Figure C- 6). The difference in NOx apportionment factors, arising from equations E4-6 and E4-6' is generally small and is not expected to cause major difference in source apportionment estimations for $O_3\_NO_x$ (Figure C- 7 and Figure C- 8). In conclusion, using the source apportionment functions in traditional ozone source apportionment techniques are not expected to cause significant differences in source apportionment estimations for most sources except in areas where $O_3\_VOC$ is high, and are significantly influenced by industrial or biogenic VOC emissions.

## 4.6 Conclusions

Industries, transportation, power and biogenic sources are four major emission sectors to ozone with different spatial distributions. High industrial $O_3\_NO_x$ of 8-15 ppb (20-25% of total ozone) is mainly located in north and northeast China, the YRD and part of SCB. Transportation $O_3\_NO_x$ accounts for 10-15% of total ozone in most urban areas. For power sector, high $O_3\_NO_x$ regions are located in Shanxi, Shaanxi, Ningxia and part of Shandong and Jiangsu provinces, also with 10-15% relative contributions to total ozone. Ozone attributed to biogenic NOx in west, central and south China with low NOx emissions from anthropogenic sources reaches as high as 10-15% of total ozone and

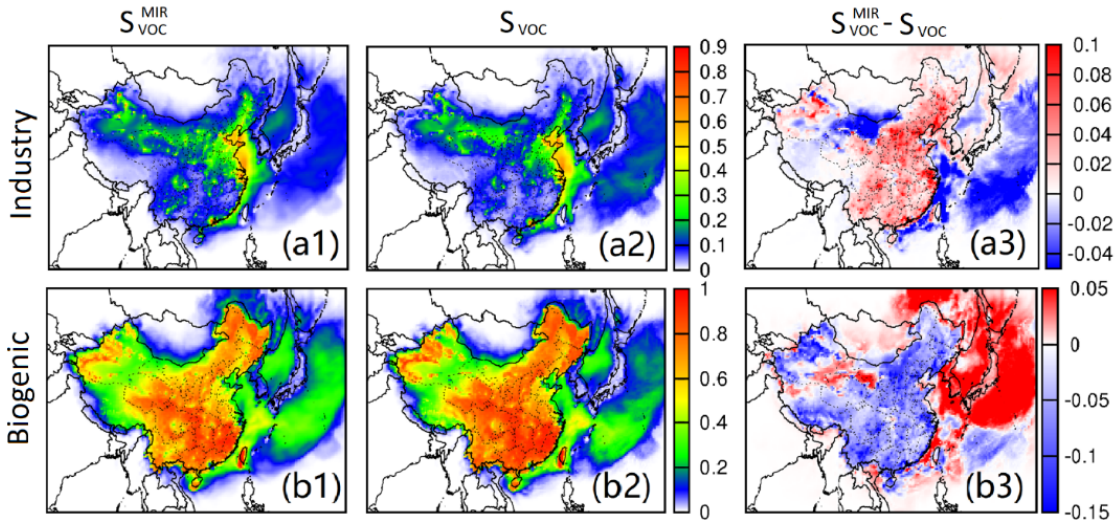


Figure 4.8: VOC source attribution fraction for industries (row a) and biogenic (row b) sectors based on the MIR weighted concentrations ($S_{VOC}^{MIR}$, E4-7' ) and the NO to $NO_2$ conversion rate due to VOC generated RO2/HO2 radicals ($S_{VOC}$, E4-7). The last column shows the difference in the source attribution fraction. This is calculated based on monthly averaged concentrations and conversion rates. The difference between the two methods for other sectors are small (Figure C - 6)

a maximum concentration of 12 ppb. Most of the VOC-limited grid cells are located at urban cores in big cities as well as some large city clusters in the YRD and PRD regions, making the regional distribution of $O_3\_VOC$ less prominent. Biogenic and industrial sectors are the most important emission sectors that contribute to $O_3\_VOC$, accounting for more than 85% of the $O_3\_VOC$ in China. The high concentration areas of biogenic sector are located in Shandong, Jiangsu, Henan and Anhui provinces, accounting for 20% of total ozone. The industrial contributions to $O_3\_VOC$ are high in areas along the east coast from Tianjin to Shanghai and in urban areas in the PRD and SCB regions, with a relative contribution to total ozone up to 20%. In nine provinces in north and east China, more than 50% of the ozone is non-background, with the provinces in north China having higher overall ozone. The BTH region has an area-averaged 8-hr ozone of 66 ppb in August 2013 and about half of it is non-background (32 ppb). Contributions of industries, transportation, power and biogenic sources to non-background ozone are 33%, 20%, 19% and 24%, respectively. The relative contribution of biogenic emissions to non-background ozone is lower on high 8-hr ozone days. The two-regime and three-regime approaches show significant differences in assessing the relative importance of $O_3\_NO_x$ and $O_3\_VOC$, with the 2-regime approach predicting lower $O_3\_NO_x$ but higher $O_3\_VOC$ in the transition regime in high ozone areas. The new source allocation method for $O_3\_VOC$ leads to up to 10% difference for industrial and biogenic sectors.

# 5. IMPROVED MEGAN PREDICTIONS OF BIOGENIC ISOPRENE IN THE CONTIGUOUS UNITED STATES *

## 5.1 Introduction

Isoprene, dominantly emitted from biogenic sources, is one of the most important precursors in atmospheric chemistry that contributes to the formation of ozone due to its large emission quantities and fast reactions with oxidants such as hydroxyl radicals (OH) [100]. Although mainly emitted from forested areas, it is found to be responsible for high ozone episodes in downwind areas, the formation of formaldehyde, and other reactive intermediates /citeying2010source,zhang2013source,dreyfus2002observational. It is also found that photochemical oxidation products of isoprene, such as glyoxal and isoprene epoxydiols, can lead to the formation of a significant amount of secondary organic aerosol (SOA) [40] and thus affecting regional and global climate [101].

Accurately estimating the influence of isoprene on regional and global air quality and climate requires accurate estimation of the emissions of isoprene from vegetated surfaces. For either regional or global scale air quality modeling studies, isoprene emissions are estimated via various biogenic emission modeling systems, such as the Global Biosphere Emissions and Interactions System (GloBEIS) [102], Biogenic Emissions Inventory System version 3 (BEIS3) [103] or Model of Emissions of Gases and Aerosols from Nature (MEGAN) model /citeguenther2006estimates,guenther2012model. All the isoprene emission models are based on emission factors (EFs) of isoprene under standard temperature and photosynthetically active radiation (PAR) conditions. However, the EF data adopted by different models can be different, and slightly differing algorithms are used to account

*Reprinted with permission from "Improved MEGAN predictions of biogenic isoprene in the contiguous United States" by Wang, P., Schade, G., Estes, M., & Ying, Q., 2017. Atmospheric Environment, 148, 337-351 [99]. Copyright 2017 by Elsevier

for leaf temperatures, incident radiation levels, and available soil moisture, among other factors, on the isoprene emission rates; together with influences of the selected biomass distribution, this can lead to very different estimates of isoprene emissions. For example, Warneke et al. [104] found the MEGAN model predicted isoprene emissions were always higher than emissions deduced from ambient measurements onboard of an airplane, while the emissions estimated using the BEIS3 model were generally lower than the deduced emission rates. The MEGAN and BEIS3 isoprene emission estimations can be different by as much as a factor of three. Carlton and Baker [105] compared ground level measurements of isoprene and its oxidation products at a forested site with predictions from a regional chemical transport model, using either MEGAN or BEIS3 derived emissions, and also found that ambient concentrations of isoprene were overestimated using MEGAN emissions but underestimated using BEIS emissions.

Due to isoprene's short atmospheric lifetime, strong horizontal concentration gradients may develop between emitting and non-emitting regions. However, isoprene's oxidation products, such as formaldehyde, are typically less heterogeneously distributed and may thus reflect isoprene emissions from a larger region much better. Satellite observations of formaldehyde (HCHO) were used to evaluate the MEGAN emission model. Millet et al. [106] compared emissions of isoprene derived using satellite observed HCHO columns and a global chemical transport model with those predicted by MEGAN using two different land cover data bases for North America. They found that MEGAN-estimated emissions were on average a factor of 2 higher, and in some locations a factor of 5 higher, than satellite derived emissions. It has been suspected that differences in isoprene reaction schemes and oxidation capacity predicted by different photochemical mechanisms could cause these differences. However, Stavrakou et al. [107] applied a number of different isoprene oxidation schemes in the same regional chemical transport model and showed that all schemes significantly over-predicted isoprene concentrations in the eastern US using

MEGAN generated isoprene emissions.

Attempts to improve MEGAN isoprene emission estimations, such as using satellite derived PAR [45] or incorporating CO2 influences on isoprene emissions [108], did also not lead to changes large enough to bring the MEGAN predictions in line with observations. While these studies lead to similar conclusions in that the MEGAN model likely overestimates the biogenic isoprene emissions in the continental US, no studies have yet been reported to evaluate the MEGAN model emissions along with CTMs using the extensive surface isoprene measurements available from the EPA's air quality monitoring network to fully evaluate the capability of emission models in estimating isoprene with large temporal and spatial coverages.

The objectives of this study are (1) to investigate the influence of different EF fields on predicted isoprene concentrations from the MEGAN model (v2.10) in a summer month using an otherwise identical regional CTM, and using all available surface isoprene measurements to determine if any EF fields could give more satisfactory estimates of isoprene emissions; and (2) to apply the EF field that gives the best model performance with MEGAN to estimate isoprene emissions and simulate ambient concentrations for 7 months (April to October), and then evaluate if the spatial and temporal variation of the isoprene can be successfully reproduced throughout the high isoprene emission season.

## 5.2 Methods

### 5.2.1 Gridded Emission Factor (EF) Fields For MEGAN

In the MEGAN model the emission rate (F) of isoprene in each model grid cell ($\mu$g $h^{-1}$) is calculated by E5-1 :

$$F = \gamma \times LAI_v \times EF \times A \tag{5.1}$$

where $\gamma$ is a lumped correction factor (unit-less) that accounts for the effects of PAR,

leaf temperature, soil moisture, leaf age, and CO2 level on isoprene emission; LAIv is the leaf area index for the vegetated surface ($m^2$ of leaf area per $m^2$ of vegetated surface area); EF is the emission factor of isoprene under standard conditions ($\mu$g $m^{-2}$ $h^{-1}$; see definition of EF below); and A is the area of the grid cell ($m^2$). In the default configuration, MEGAN v2.10 uses a gridded EF map for isoprene emissions. The EF map was prepared based on fractional areal coverage of vegetation species in a grid cell as shown in E5-2:

$$EF = \sum_{i=1}^{N} \chi_i \epsilon_i \tag{5.2}$$

where i is the vegetation type index, Îţ is the species specific emission factor ($\mu$g $m^{-2}$ $h^{-1}$ or more specifically $\mu$g per hour per $m^2$ of leaf surface area) at standard condition, ÏĞ is the fraction of the cell covered by a given vegetation emission type ($m^2$ $m^{-2}$, or more specifically, $m^2$ vegetated surface per $m^2$ of ground surface), and N and is the total number of vegetation types in a grid cell. Note that the units of EF are neither $\mu$g per $m^2$ ground area nor $\mu$g per $m^2$ of vegetation surface area.

### 5.2.2 Alternative EF Fields

Two alternative emission factor fields were generated using the input data for BEIS v3.14 (with Biogenic Emissions Landcover Database, version 3, or BELD3) and BEIS v3.61 (with BELD version 4, or BELD4) [109]. Unlike MEGAN that uses pre-gridded EF fields, both versions of the BEIS program calculate the gridded isoprene emissions using detailed land use specific emission factors along with detailed land use data bases. The BELD3 includes a 230-type land use database, which is generated from the USGS 1-km data (1992), and county-level tree and crop species information from forest and agricultural datasets. The BELD4 includes a preprocessing program (computeGridLandUse_beld4.exe in the Spatial Allocator tool distributed by the US EPA) that can utilize user specified National Land Cover Database (NLCD) data as well as a tree and crop frac-

tion table at county level to generate a BEISv3.61 compatible BELD4 data base for a given air quality model domain. Unlike the MEGAN model that uses year specific LAI values, the BEIS models use prescribed LAI for each land use category. Two sets of land use specific LAIs are used, one for plant growth season (summer) and one for non-growth season (winter).

In this study, the BEIS v3.14 program distributed with the Sparse Matrix Operator Kernel Emissions (SMOKE) version 2.5, and the BEIS v3.61 program distributed with SMOKE version 3.7, were modified to generate the gridded isoprene EF fields for use in MEGAN v2.10. A copy of the modified BEIS 3.61 program can be obtained from the corresponding author.

## 5.3 Model Application

### 5.3.1 Model Domain, Meteorology and Anthropogenic Emission Inputs

In this study, the Community Multiscale Air Quality model, version 5.0.1 (CMAQ v5.0.1) with CB05 photochemical mechanism and the 6th generation aerosol module (AERO6) was used to simulate regional isoprene concentrations from April to October 2011 within a 36-km horizontal resolution domain (148x112 grid cells, Lambert Conformal projection) that covers the entire contiguous US and parts of Canada and Mexico. Photolysis rates were calculated inline to account for the reduction of actinic flux due to aerosol loading. The meteorological inputs were generated by the Weather Research and Forecasting (WRF) model v3.6.1. The simulations were initialized using the North American Regional Reanalysis (NARR) data (from National Oceanic and Atmospheric Administration (NOAA), http://www.esrl.noaa.gov/psd/data/gridded/data.narr.html) with 32-km horizontal resolution and 3-h time resolution, for all variables except soil moisture, which was initialized using data from the North American Land Data Assimilation System (NLDAS). The LAI was based on the 8-day MODIS LAI product (MOD15A2) for 2011,

and land use/land cover classification was also updated using the 2011 MODIS product (MOD12Q1). Land surface processes were simulated using the Noah land surface model. Anthropogenic emissions were estimated using the National Emission Inventory (NEI) 2011 v6 platform. Details of the NEI 2011 as used in the EPA's 2011v6 platform can be found in ftp://ftp.epa.gov/EmisInventory/2011v6/v1platform/README_2011v6_package.txt. These raw emissions were processed using SMOKE v3.5.1 using the run scripts provided with the 2011v6 platform.

### 5.3.2 Biogenic Emission Inputs

Biogenic emissions, including isoprene, were generated using a modified MEGAN v2.10. LAI in non-urban grid cells was based on the 8-day MODIS LAI for 2011. LAI in the urban grid cells was determined based on an approach described by Kota et al. [110], which uses a seasonal variation profile based on the 8-day MODIS data to scale the maximum LAI (LAImax) values assigned for each of the four urban classifications (developed open, LAImax=3.3; developed low density, LAImax=2.3; developed medium density, LAImax=1.3; and developed high density, LAImax=0.3) from NLCD. The LAI values were then normalized by the fractional vegetation cover in a grid cell to calculate the LAI for the vegetated area (LAIv), which was used as input to the MEGAN model. MEGAN v2.10 follows the 16 plant functional type (PFT) classification scheme used in the community land model (CLM, version 4) [111]. The default 1-km resolution North American PFT grid provided along with the MEGAN v2.10 model was used directly without modifications. Reduction of isoprene emissions due to potential soil moisture limitation [45, 112],was not yet considered in this study. The effect of drought on isoprene emissions will be discussed in a separate study.

Four sets of isoprene emissions were generated using the MEGAN model with different EF fields: 1) the original global EF field provided by the MEGAN v2.10 distribution

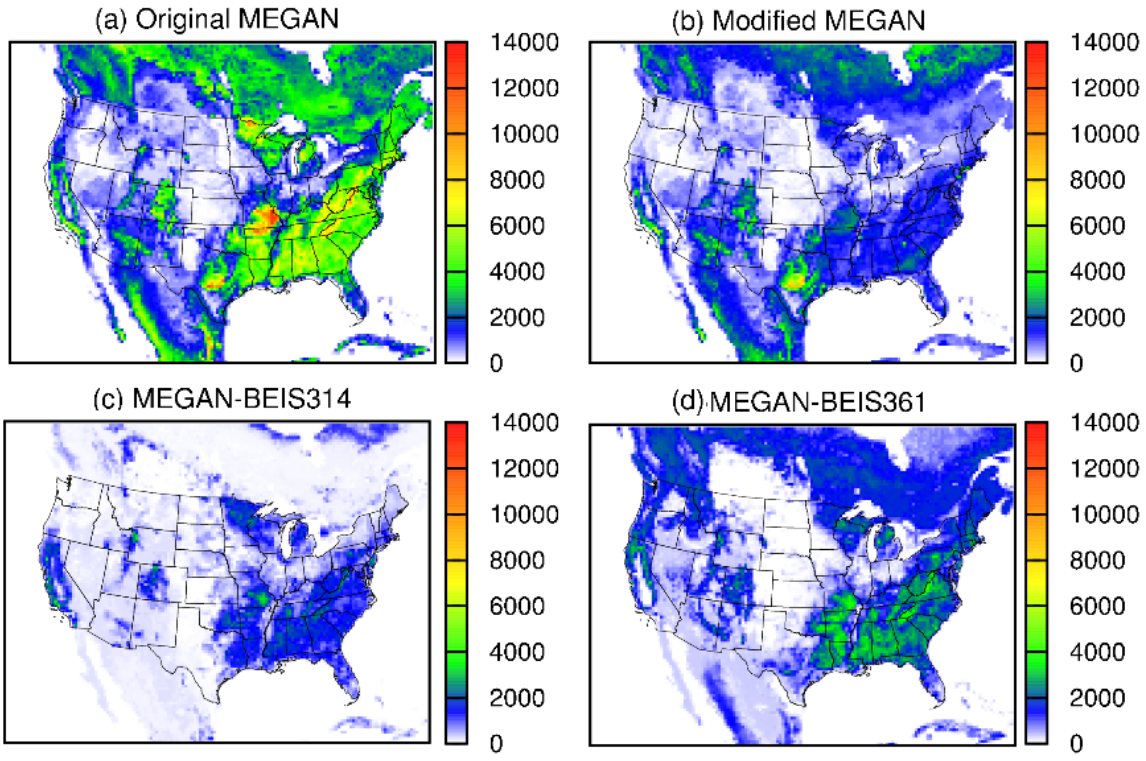


Figure 5.1: Emission factor (EF) of isoprene at standard condition: (a) original MEGAN database, (b) modified MEGAN, (c) BELD3 as used in BEIS3.14 and (d) BELD4 as used in BEIS3.61 for year 2011 (summer). Units are $\mu$g $hr^{-1}$ $km^{-2}$.

(original MEGAN); 2) the EF field based on data for BEIS3.14 (MEGAN-BEIS314); 3) the EF field based on data for BEIS3.61 (MEGAN-BEIS361); and 4) a modified EF field based on the original MEGAN EF field (modified MEGAN). Details of the MEGAN-BEIS314 and MEGAN-BEIS361 are described in Section 5.2. As the original MEGAN EF is much higher than EF from BEIS data, it was surmised that the original MEGAN EF fields might have a unit conversion problem (i.e. in unit of $\mu$g $hr^{-1}$ $m^{-2}$ ground area). For the modified MEGAN EF, the original MEGAN EF at each grid was thus divided by the overall LAIv to get the âĂIJcorrectâĂİ units. The four sets of gridded EF values are shown in Figure 5- 1. The original MEGAN database gives much higher EF than both versions of the BEIS, and BEIS3.14 gives the lowest EF.

Table 5.1: List of isoprene emissions used in the preliminary CMAQ modeling study.

| Simulation # | Isoprene Emission | Notes |
|---|---|---|
| a | MEGAN | Original isoprene EF field; MEGAN v2.10 |
| b | Modified MEGAN | Original EF field was divided by LAIv in each grid; MEGAN v2.10 |
| c | BEIS314 | Emission were generated using the BEIS3.14 and BELD3 land use database |
| d | MEGAN-BEIS314 | Gridded isoprene and other important VOCs EF based on BELD3 and leaf level emission factors used in BEIS3.14; MEGAN v2.10 |
| e | BEIS361 | Emission were generated using the BEIS3.61 and BELD4 land use database |
| f | MEGAN-BEIS361 | Gridded isoprene and other important VOCs EF based on BELD3 and leaf level emission factors used in BEIS3.61; MEGAN v2.10 |

In addition, two sets of isoprene emissions (BEIS314 and BEIS361) were generated using the two BEIS models (based on v3.14 and v3.61, respectively) for comparison with the four sets of emissions generated using the MEGAN model. As summarized in Table 5-1, a total of six sets of isoprene emissions were generated for a preliminary CMAQ modeling study for July 2011, mainly to determine which EF fields when used in the MEGAN model can best reproduce the observed ambient isoprene concentrations. Results using the two BEIS generated emissions were also analyzed and compared with the MEGAN based results. The emissions of other biogenic species such as $\alpha$-pinene and $\beta$-pinene are based on the original MEGAN EF fields and remain the same for all the simulations.

Figure 5- 2 shows the predicted monthly average isoprene emissions for July 2011. Although spatial distributions of isoprene are generally similar, with highest isoprene emissions occurring in the southeast states of Alabama and Georgia, the emission rates differ significantly. As expected, the original MEGAN predicted the highest emission rates of isoprene due to large EF values. The MEGAN-BEIS314 predicted the lowest emission

rates, and the MEGAN-BEIS predicted emissions were generally higher than their BEIS counterparts. While the BEIS3.14/BELD3 predicted lower isoprene emission rates, the emissions from BEIS361/BELD4 were significantly higher, and in some areas even higher than the original MEGAN predictions. The total July 2011 isoprene emissions were 9.7 Tg (teragram = 1012 g), 5.3 Tg, 3.7 Tg, 2.5 Tg, 8.4 Tg and 4.2 Tg, for simulations (a)-(f), respectively.

### 5.3.3 Available Isoprene Observation Data

Isoprene observation data were acquired from two sources. For Texas, the hourly ambient isoprene concentrations measured by a number of Automatic Gas Chromatography (Auto-GC) monitors were obtained from the Texas Commission of Environmental Quality (TCEQ). The reported limit of detection (LOD) of all hydrocarbons measured by the Auto-GC is approximately 0.4 ppbC, or 0.08 ppb for isoprene. The locations of the 23 Auto-GC sites where 2011 data were available are shown in Figure D- 1, and Table D- 1 lists the geographical coordinates of all the Auto-GC sites in Texas. Most of the Auto-GC sites in Texas are located in urban areas. Observations of isoprene outside Texas were downloaded from the AIRS database prepared by the US EPA. Only the hourly Auto-GC data were used in the analysis. Daily concentrations used in the analysis were calculated from the hourly data. Figure 5- 3 shows the locations of hydrocarbon monitors in other states. Most are located along the east coast of the US. Additionally, there is one site in California (in Livermore, an urban site near San Francisco) and three sites in Georgia near Atlanta. The geographical coordinates of these monitors are shown in Table D- 2.

## 5.4 Results

### 5.4.1 Determination Of The Control Run EF Distribution

Figure 5- 4 shows predicted spatial distribution of average July 2011 isoprene concentrations. While the spatial distributions are similar, the absolute concentrations from the

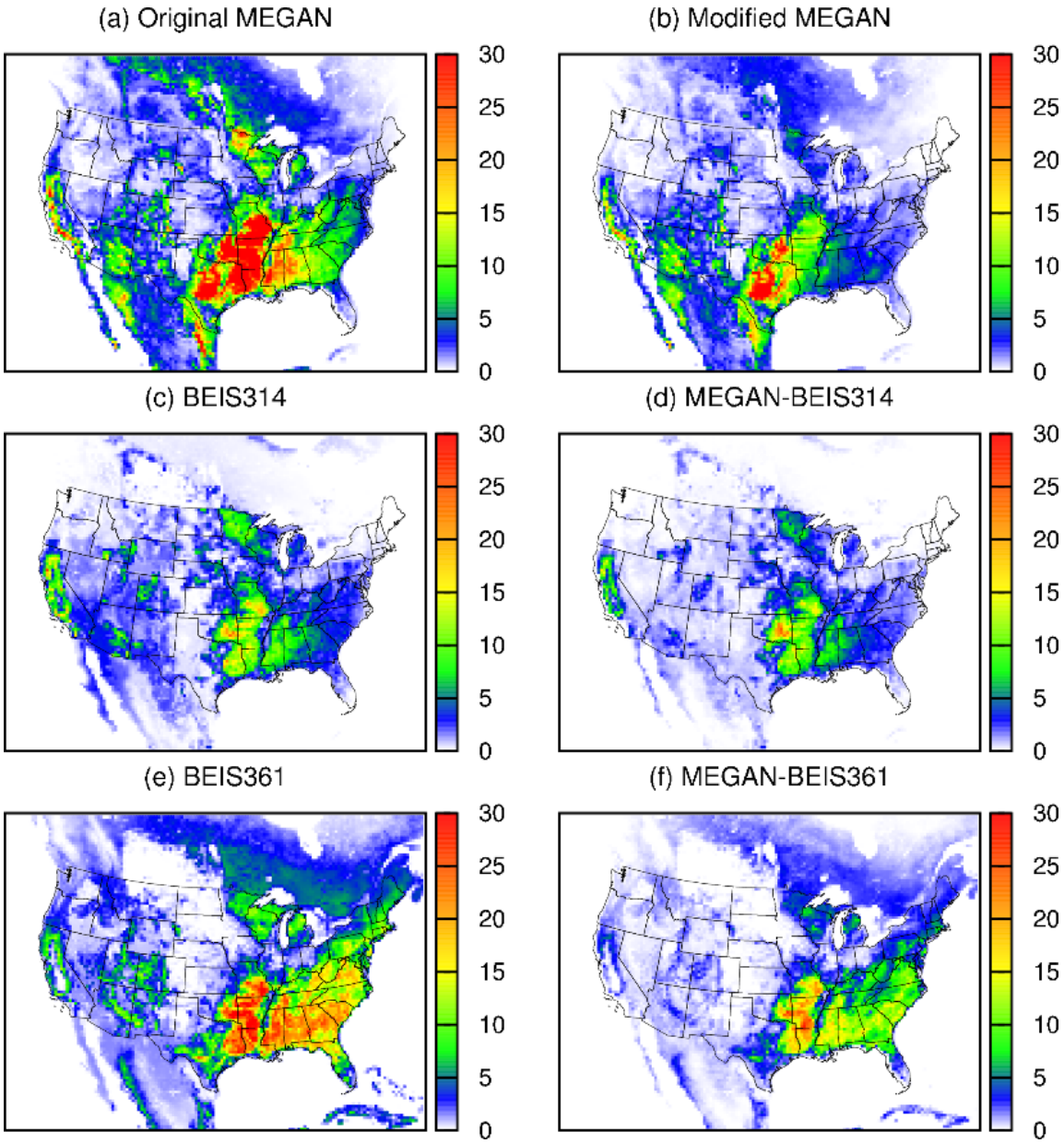


Figure 5.2: Predicted monthly average emissions of isoprene for July 2011. Units are moles s-1.

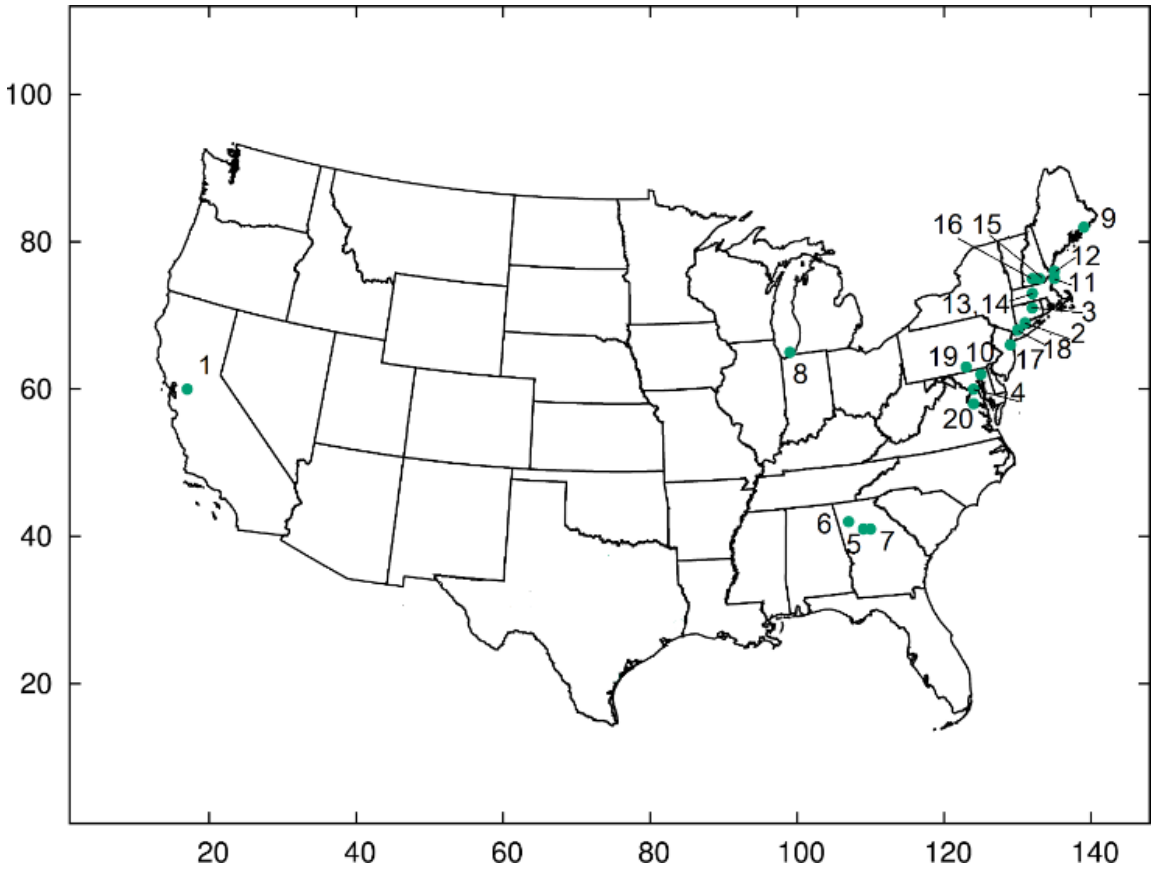


Figure 5.3: Model domain and location of non-Texas isoprene monitors. Locations of the Texas isoprene monitors are shown in Figure D- 1.

six cases differ significantly. The original MEGAN emissions lead to high concentrations of isoprene exceeding 10 ppb over vast areas in the south and southeast US. In order to determine which predictions agree better with observations, the model performance for the six cases was analyzed statistically. Figure 5- 5 shows the comparison of predicted and observed daily average isoprene concentrations at all monitoring sites in Texas and other states. Since the concentrations at the Texas sites were typically lower than the concentrations measured at other non-Texas sites, Texas and non-Texas data were analyzed separately. Model performance for the predicted isoprene concentrations was measured by the mean fractional bias (MFB) and mean fractional error (MFE), as defined by equations E5-3 and E5-4:

$$MFB \frac{2}{N} \sum_{i=1}^{N} \frac{C_{m,i} - C_{o,i}}{C_{m,i} + C_{o,i}} \tag{5.3}$$

$$MFE \frac{2}{N} \sum_{i=1}^{N} \frac{|C_{m,i} - C_{o,i}|}{C_{m,i} + C_{o,i}} \tag{5.4}$$

In the above equations, N is the number of prediction-observation pairs at each station within a month, and $C_m$ and $C_0$ are model predicted and observed concentrations, respectively. Since both fractional bias (FB) and fractional error (FE) are bounded, and a large number of data points are available, the MFB and MFE values used in this study to evaluate model performance are less likely affected by a few points with extremely poor model performance. The results are shown in Table 5- 2.

The original MEGAN model greatly over-predicted the daily-average isoprene concentrations at most locations (MFB = 0.98, MFE = 1.06). The MFB and MFE values indicate an average over-prediction by a factor of 3. Based on the model performance statistics, BEIS314 (overall MFB = -0.22 and MFE = 0.67) and MEGAN-BEIS361 (overall MFB = -0.34 and MFE = 0.72) were the best among the six sets of simulations. The MEGAN-

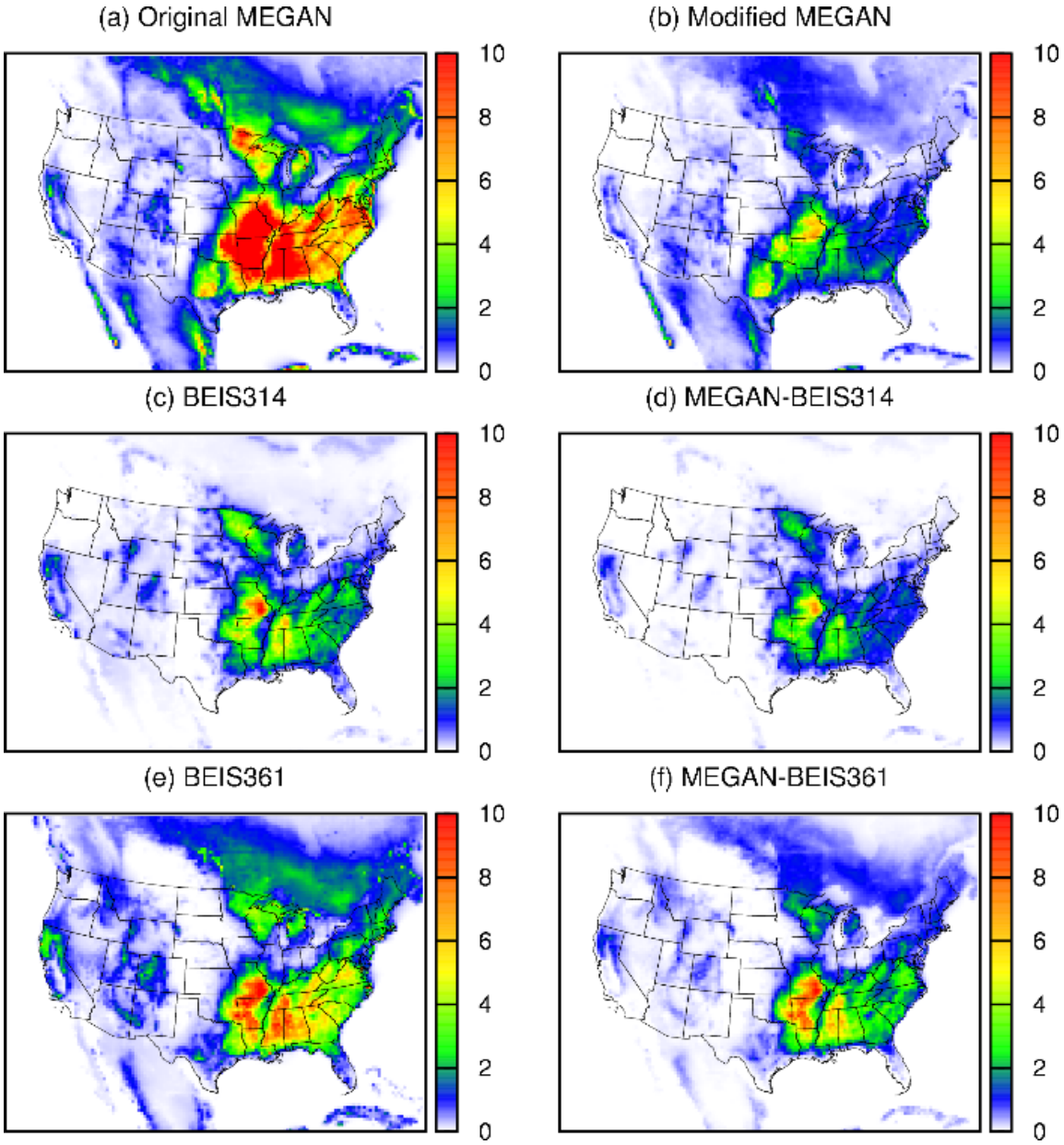


Figure 5.4: Predicted monthly average concentrations of isoprene for July 2011. Units are ppb.

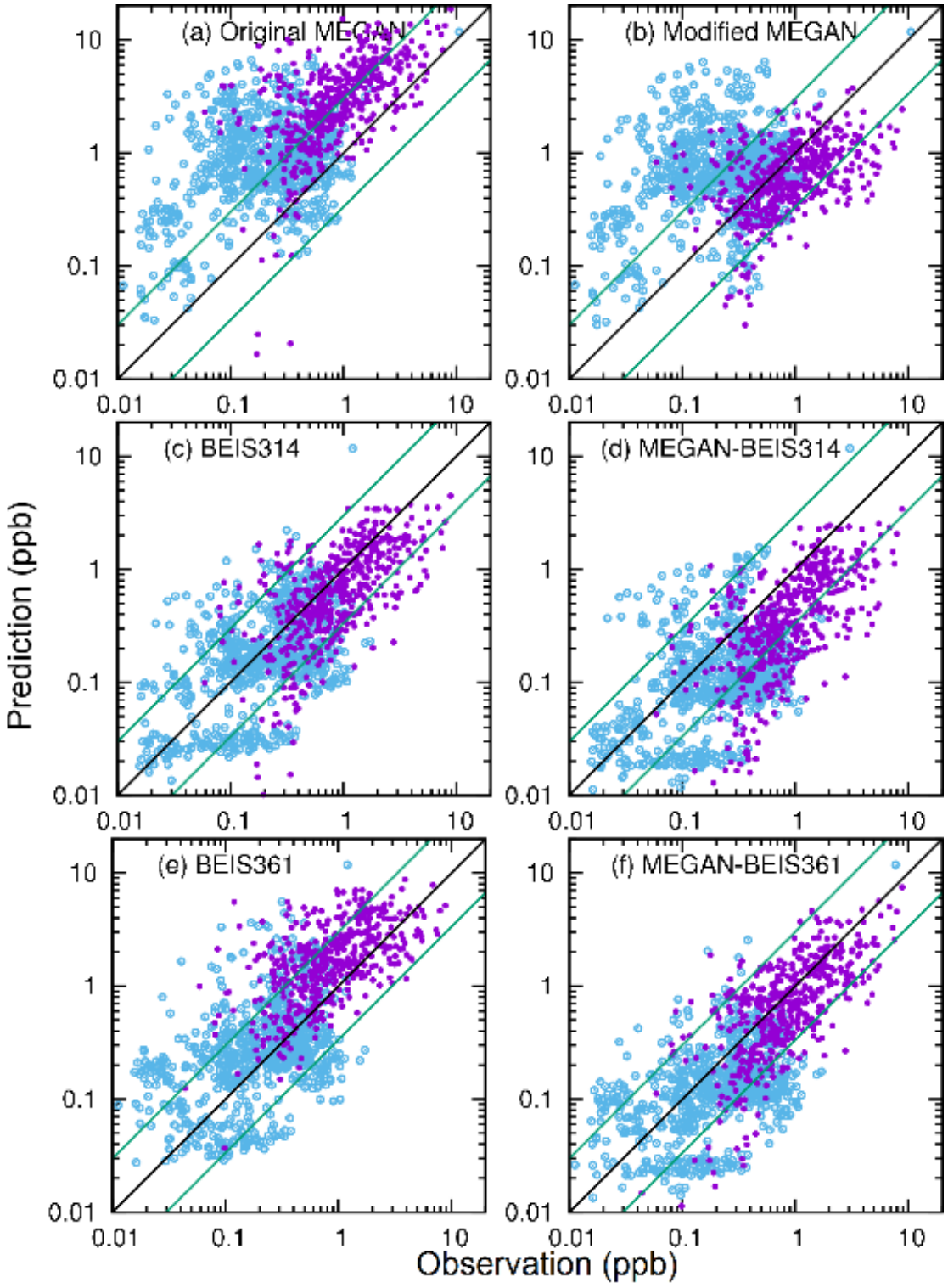


Figure 5.5: Predicted vs. observed daily average isoprene at all stations with valid measurements in July 2011. (Units are ppb). The green lines are 1:3 and 3:1 ratios. The light blue dots are observations made in Texas and the magenta dots are observations made in other states.

Table 5.2: Mean fractional bias (MFB) and mean fractional error (MFE) of isoprene for July 2011. The units for predicted and observed concentrations are ppb.

| Simulations | | Other States (OS) | OS_Rural | Texas (TX) | TX_Rural | Overall |
|---|---|---|---|---|---|---|
| MEGAN | MFB | 0.91 | 0.66 | 1.02 | 1.11 | 0.98 |
| | MFE | 0.99 | 0.81 | 1.11 | 1.16 | 1.06 |
| | Pred. | 3.63 | 4.04 | 1.18 | 1.46 | 2.14 |
| Modified -MEGAN | MFB | -0.34 | -0.63 | 0.88 | 1.02 | 0.4 |
| | MFE | 0.68 | 0.81 | 1.03 | 1.08 | 0.89 |
| | Pred. | 0.73 | 0.84 | 0.96 | 1.21 | 0.87 |
| BEIS314 | MFB | -0.29 | -0.48 | -0.17 | -0.25 | -0.22 |
| | MFE | 0.62 | 0.75 | 0.7 | 0.57 | 0.67 |
| | Pred. | 0.88 | 1.1 | 0.25 | 0.22 | 0.5 |
| MEGAN-BEIS314 | MFB | -0.79 | -0.94 | -0.51 | -0.45 | -0.62 |
| | MFE | 0.91 | 1.01 | 0.87 | 0.74 | 0.88 |
| | Pred. | 0.52 | 0.65 | 0.18 | 0.17 | 0.31 |
| BEIS361 | MFB | 0.56 | 0.51 | 0.21 | 0.16 | 0.35 |
| | MFE | 0.71 | 0.72 | 0.74 | 0.74 | 0.73 |
| | Pred. | 2.11 | 2.72 | 0.44 | 0.4 | 1.1 |
| MEGAN-BEIS361 | MFB | -0.11 | -0.31 | -0.42 | -0.49 | -0.34 |
| | MFE | 0.67 | 0.62 | 0.79 | 0.78 | 0.72 |
| | Pred. | 0.94 | 1.3 | 0.17 | 0.16 | 0.49 |
| | Obs. | 1.17 | 1.8 | 0.3 | 0.36 | 0.6 |
| | # Points | 503 | 196 | 737 | 154 | 1240 |

BEIS361 performed better than BEIS314 in predicting isoprene concentrations in forest and agriculture areas (MFB and MFE are -0.31 and 0.62 for MEGAN-BEIS361, and are -0.48 and 0.75 for BEIS314), where isoprene concentrations were highest ( 1.8 ppb). Isoprene concentrations were much lower in Texas, and the performance statistics were not as good as those at non-Texas sites. This worse model performance is expected because a large fraction of isoprene concentrations was below the detection limit, leading to large uncertainties. However, also in Texas MEGAN-BEIS361 yielded the best model performance (MFB = -0.42, MFE = 0.79) among the four sets of simulations using MEGAN generated emissions. Based on this model performance analysis, the MEGAN-BEIS361 model was used to generate baseline emissions for the 7-month long-term isoprene simu-

lation, as described in the following section.

### 5.4.2 Isoprene Concentrations April - October, 2011

#### *5.4.2.1 Model Performance Of Hourly And Daily-averaged Isoprene Concentrations*

Predicted hourly isoprene concentrations were compared with observations at all monitors. To the best of the authors' knowledge, this is the first time hourly isoprene concentrations are extensively evaluated with hourly observations in Texas and in the Northeastern US over extended periods. Figure 5- 6 shows a detailed comparison of predicted and observed hourly isoprene for each monitoring site outside Texas. Isoprene concentrations spanned three orders of magnitude in many of the 20 sites during this period, and the predictions were generally in good agreement with the observations. Isoprene concentrations were highest (up to 20 ppb in July) at the National Geodetic Survey site in VA (AIRS code 510330001), which is a rural forest site, and the predicted hourly isoprene concentrations generally agreed with the observations without an obvious bias. Reasonable agreement between the predictions and observations was also found at most of the other monitors. The worst model performance arose at the NYBG Pfizer Plant Research Lab in New York (360050133), which is located in downtown New York City. The other urban site (Livermore, 060010007) showed the lowest isoprene concentrations but observations and predictions agreed well for September and October, which have the most number of available observations at that site.

Table 5- 3 shows the monthly model performance statistics for the hourly isoprene concentrations in terms of MFB and MFE for monitors outside Texas based on the 36-km model results. While the scatter plots in Figure 5- 6 show there are similar levels of over- and under-predictions, the MFB values suggest that averaged over all the monitoring sites, there was a small negative bias in the predicted hourly concentrations in all months. The model performance was best in July (MFB = -0.22 and MFE = 0.89) when the isoprene

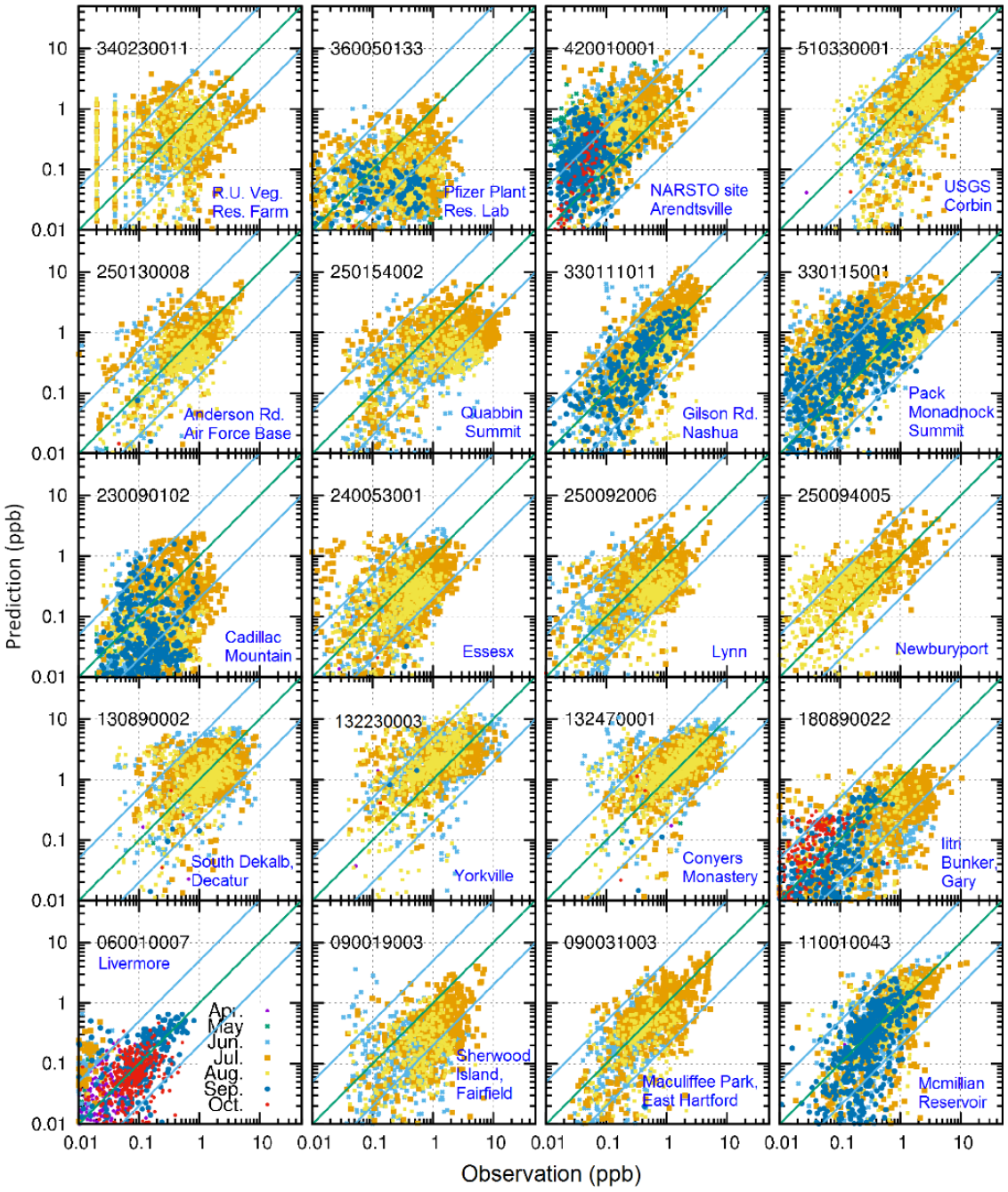


Figure 5.6: Predicted vs. observed hourly average isoprene at all non-Texas stations with valid measurements from April to October 2011. (Units are ppb). The green lines are 1:1, 1:5 and 5:1 ratios. The isoprene emissions are based on MEGAN-BEIS361.

concentrations were the highest, with average observed and predicted concentrations of 1.28 and 1.03 ppb, respectively. Model performance in June and August was also relatively good, with MFB -0.3 and MFE 0.9. Model performance decreased for spring and fall months, as the observed concentrations dropped significantly below 0.2 ppb.

Table 5.3: Model performance of predicted hourly isoprene concentrations at non-Texas monitors from April to October 2011 based on MEGAN-BEIS361 isoprene emissions

| Month | MFB | MFE | Obs. | Pred. | # points |
|---|---|---|---|---|---|
| April | -0.34 | 1.02 | 0.04 | 0.04 | 344 |
| May | -0.34 | 1.49 | 0.14 | 0.27 | 611 |
| June | -0.23 | 0.91 | 0.86 | 0.8 | 9960 |
| July | -0.22 | 0.89 | 1.28 | 1.03 | 11161 |
| August | -0.28 | 0.91 | 0.77 | 0.72 | 9928 |
| September | -0.43 | 1.07 | 0.2 | 0.22 | 3477 |
| October | -0.73 | 1.14 | 0.06 | 0.05 | 1249 |

Figure 5- 7 shows that the model performed better at the non-Texas stations when predicting daily-average rather than hourly isoprene concentrations. Predictions at a number of stations showed excellent agreement with observations within a factor of 2. Error! Reference source not found. demonstrates that both MFB and MFE values were much lower for daily average isoprene concentrations. The MFB values from June to October varied from -0.1 to 0.03, suggesting that the model can predict daily averages of isoprene in these months without significant overall bias. For the three summer months, MFE values varied from 0.67 to 0.75, which were also much lower than for the hourly values, as would be expected from averaging data that cluster around the true value.

Figure D- 2 and Figure D- 3 show the comparison of hourly and daily average isoprene concentrations at all auto-GC sites in Texas. The respective detailed model performance statistics are shown in Table 5- 5 and Table 5- 6. Concentrations at the auto-GC sites

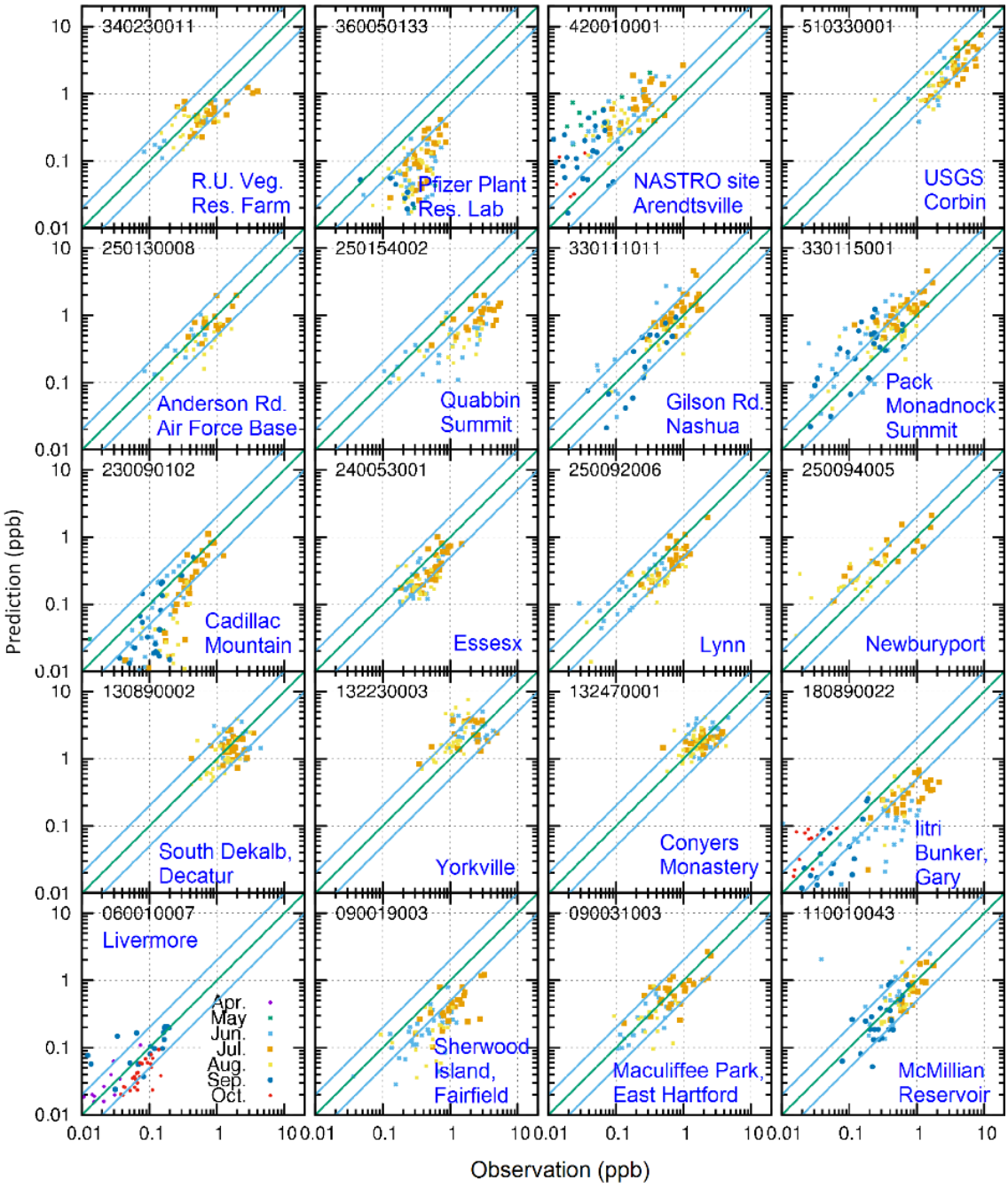


Figure 5.7: Predicted vs. observed daily average isoprene at all non-Texas stations with valid measurements from April to October 2011. (Units are ppb). The green lines are 1:1, 1:2 and 2:1 ratios

Table 5.4: Model performance of predicted daily isoprene concentrations at non-Texas monitors from April to October 2011 based on MEGAN-BEIS361 isoprene emissions.

| Month | MFB | MFE | Obs. | Pred. | # points |
|---|---|---|---|---|---|
| April | 0.89 | 1 | 0.01 | 0.03 | 28 |
| May | 0.64 | 1.6 | 0.03 | 0.11 | 70 |
| June | -0.06 | 0.75 | 0.74 | 0.7 | 450 |
| July | -0.11 | 0.67 | 1.17 | 0.94 | 503 |
| August | -0.09 | 0.72 | 0.69 | 0.65 | 468 |
| September | 0.03 | 0.88 | 0.15 | 0.18 | 182 |
| October | -0.05 | 0.88 | 0.04 | 0.04 | 69 |

Table 5.5: Model performance of predicted hourly ambient isoprene concentrations at Texas monitors from April to October 2011 based on MEGAN-BEIS361 isoprene emissions

| Month | MFB | MFE | Obs. | Pred. | # points |
|---|---|---|---|---|---|
| April | -0.41 | 1.02 | 0.12 | 0.09 | 9760 |
| May | -0.38 | 0.99 | 0.19 | 0.13 | 11605 |
| June | -0.51 | 1.07 | 0.33 | 0.19 | 12942 |
| July | -0.49 | 1.07 | 0.30 | 0.18 | 14253 |
| August | -0.47 | 1.12 | 0.29 | 0.22 | 14324 |
| September | -0.38 | 1.1 | 0.17 | 0.22 | 12398 |
| October | -0.71 | 1.09 | 0.09 | 0.06 | 9177 |

Table 5.6: Model performance of predicted daily ambient isoprene concentrations at Texas monitors from April to October 2011 based on MEGAN-BEIS361 isoprene emissions

| Month | MFB | MFE | Obs. | Pred. | # points |
|---|---|---|---|---|---|
| April | -0.19 | 0.65 | 0.11 | 0.08 | 637 |
| May | -0.24 | 0.7 | 0.18 | 0.12 | 721 |
| June | -0.37 | 0.79 | 0.32 | 0.18 | 696 |
| July | -0.42 | 0.79 | 0.30 | 0.17 | 737 |
| August | -0.28 | 0.76 | 0.28 | 0.21 | 758 |
| September | -0.18 | 0.75 | 0.16 | 0.20 | 716 |
| October | -0.54 | 0.78 | 0.09 | 0.06 | 587 |

in Texas were comparatively low, with hourly concentrations typically less than 1 ppb. Average monthly 1-hour concentration ranged from 0.09 ppb (in October) to 0.33 ppb (in June). The model performance statistics were similar to those at non-Texas stations under similar average isoprene concentrations, as shown in Figure S4. For example, MFB = -0.49 and MFE = 1.07 for July 2011 based on hourly concentrations and an average concentration of 0.3 ppb. Similarly, average hourly concentrations at non-Texas stations in September 2011 were 0.2 ppb, and the MFB and MFE values were 0.43 and 1.07, respectively. However, as the LOD of isoprene is only 0.08 ppb, many of the observed concentrations were not much higher than the LOD. Thus, the weaker model performance at the auto-GC sites in Texas is likely due to uncertainty in both measurements of low isoprene concentrations and emissions estimations in urban areas.

#### *5.4.2.2 Monthly-averaged Diurnal Variations*

In the previous sections, it was demonstrated that observed and predicted hourly concentrations varied significantly from day to day and that the simulations did not well capture such high resolution variations, as indicated by the large MFE values in Table 5- 3. While it was shown that daily average concentrations were better reproduced, it is not clear whether the general diurnal variation behavior can be correctly captured. In this section, an even longer period average of monthly diurnal variations is shown in Figure 5- 8 for the stations outside Texas and in Figure 5- 9 for stations in Texas, respectively. At the non-Texas sites, the predicted average diurnal variation agreed well with observations at most of the sites. Predicted concentrations were significantly lower than observations at AIRS sites 360050133 (urban residential site in NY), 250154002 (a forest site in MA), 180890002 (industrial urban site) and 090019003 (residential suburban site). Three of these four sites are located in residential or industrial regions, thus the error is likely due to the treatment of vegetation type and/or LAI in the urban/suburban areas. The agree-

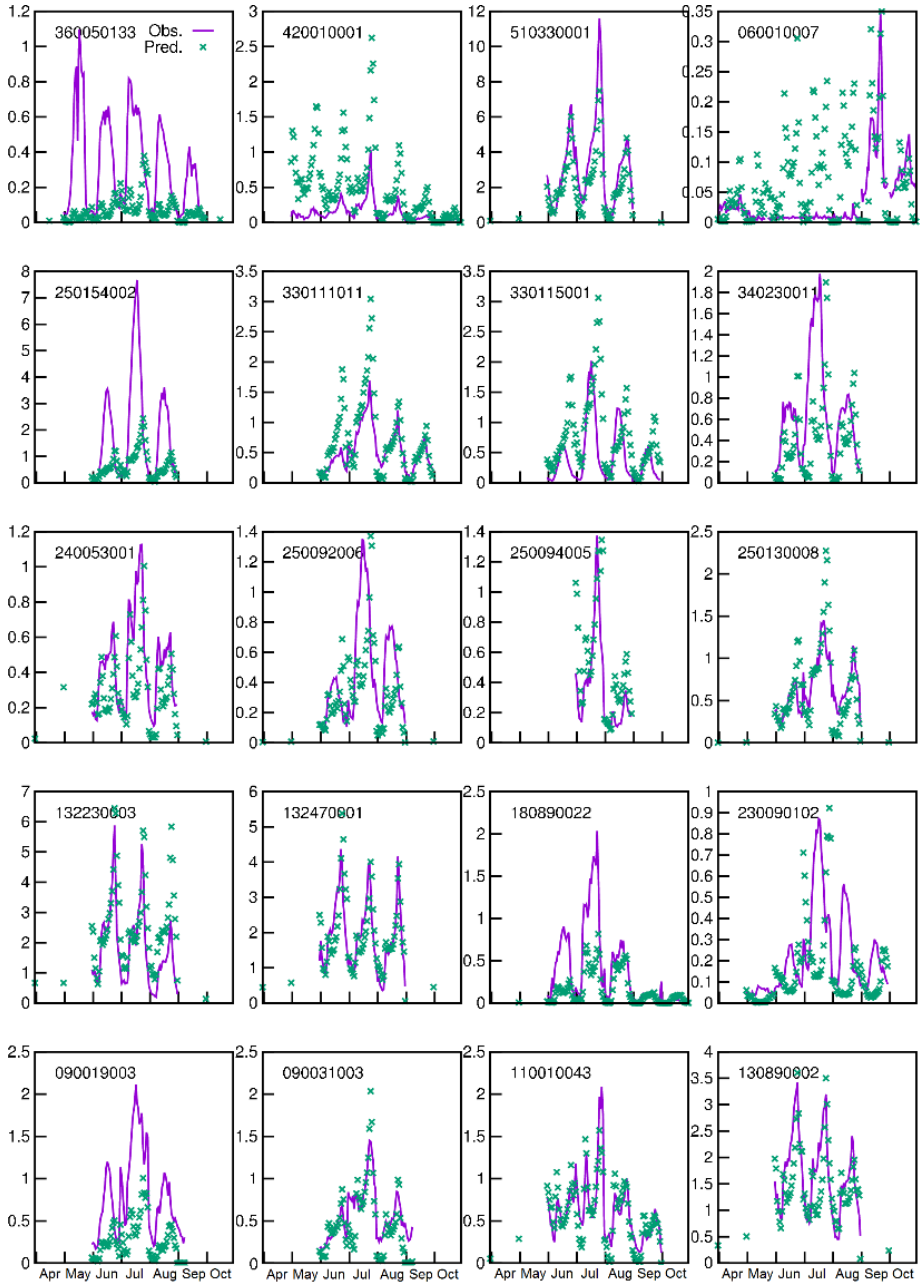


Figure 5.8: Monthly averaged diurnal variation of isoprene concentrations (ppb) at non-Texas sites from April (4) to October 2011. Observations are in purple lines, predicted values appear as green crosses.

ment of the average diurnal variation at the Texas monitor sites was similarly poor at the urban sites. The five sites with the most significant under-predictions, 482016000 (Cesar Chavez), 482010803 (HRM#3), 480391016 (Lake Jackson), 482010026 (Channel View) and 481211007 (Flower Mound Shiloh), are all urban or suburban locations. At these locations, predicted concentrations showed a morning and an evening peak, which are likely due to vehicle emissions of isoprene at lower mixing heights. However, observations showed clear mid-day peaks, which strongly suggest a biogenic source of the isoprene. Under-predictions of isoprene at these urban or suburban locations are likely due to insufficient grid resolution to resolve the sub-grid variations in 1) land use/land cover, particularly the variation in the coverage of isoprene emitters, which could lead to an underestimation of EF near the location where the monitor is located. This is further discussed in Section 5.4.2.4; 2) meteorological and hydrological drivers such as temperature, PAR and soil moisture that could greatly affect isoprene emissions. In particular, PAR and soil moisture data are not available at most of the monitors during the study period. IN summary, higher resolution simulations with more field data are needed to further investigate the isoprene concentration biases in urban areas.

#### *5.4.2.3 Formaldehyde Column Concentrations*

Although the comparison of predicted and observed isoprene concentrations at the monitoring sites provides a more direct evaluation of the accuracy of the emission estimations and the capability of the CMAQ model in predicting the observed isoprene concentrations, the spatial coverage of the stations is too limited. Most of the stations are located along the east coast, as shown in Figure 5- 3, but there are no hourly observation data in many states with higher predicted isoprene concentrations, particularly in Oklahoma, Louisiana, Tennessee, Alabama, Arkansas and Mississippi. It is also necessary to evaluate if the current predictions can provide reasonable estimations of the broad spatial distribu-

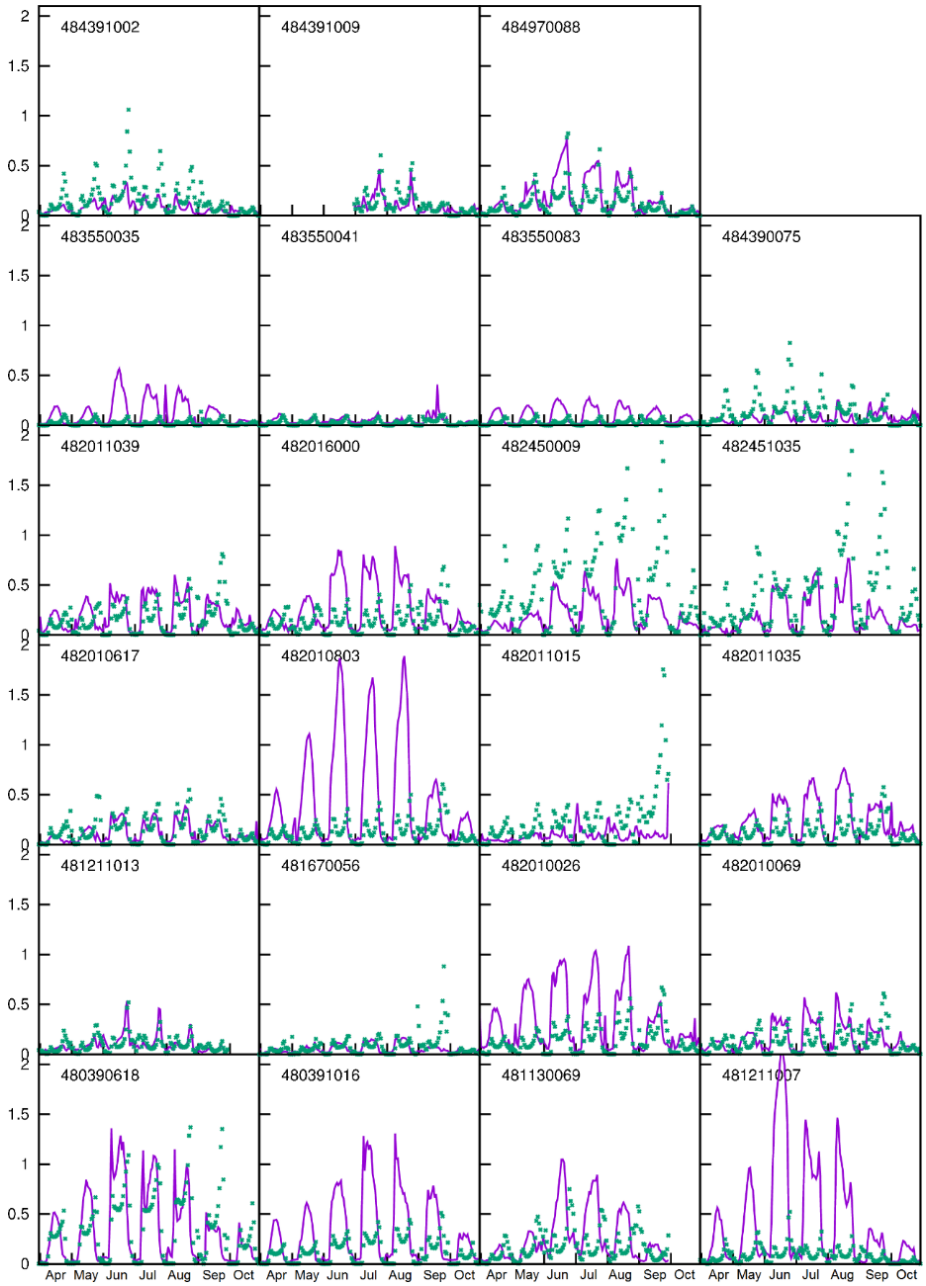


Figure 5.9: Monthly averaged diurnal variation of isoprene concentrations (ppb) at Texas sites from April (4) to October (10), 2011. . Observations are in purple lines, predicted values appear as green crosses.

tion of isoprene emissions and ambient concentrations in the US. Formaldehyde (HCHO) is a key product from isoprene photo-oxidation [113]. While it can also be directly emitted from anthropogenic sources or formed from oxidation of other anthropogenic VOC precursors, isoprene is the dominant source of HCHO in North America during summer [114]. Agreement in predicted HCHO and observed isoprene concentrations can serve as an additional evaluation of the accuracy of isoprene emission and concentrations [115]. Satellite data collected by the Ozone Monitoring Instrument (OMI) have been used to derive the column density of HCHO. In this study, the $0.25^\circ \times 0.25^\circ$ gridded daily HCHO vertical column density (VCD) data were taken from a level-3 global dataset (version 14) provided by the Belgian Institute for Space Aeronomy (BIRA-IASB) based on the level-1 OMI data provided by NASA [116]. The gridded daily level-3 data, which already removed columns with cloud fraction >40%, were re-projected to the CMAQ model domain. To compare with the satellite data, CMAQ predicted VCD was selected at the grid cells with valid satellite VCD. The satellite passing time information estimated using NASA's LaRC Satellite Overpass Predictor (http://cloudsgate2.larc.nasa.gov/cgi-bin/predict/predict.cgi) was used to determine the appropriate hourly CMAQ data to pick for the comparison. Daily data from both the OMI satellite and the CMAQ model were subsequently averaged to calculate nominal monthly average VCD, as shown in Figure 5- 10.

The predicted spatial distributions of HCHO VCD generally agree with the observations. Highest VCD occurred in the southeast US during the summer months (June âĂŞ August), with predicted density of more than 2.5$\times$1016 molecules $cm^{-2}$ over large areas, particularly in July and August. Monthly variation of the HCHO VCD is also properly captured. In April, lower VCD of 5-7$\times$1015 molecules $cm^{-2}$ were predicted and observed. For May, the increase of VCD to approximately 1.0-1.2$\times$1016 molecules $cm^{-2}$ in the State of Georgia was well predicted. The VCD then rapidly increased to more than 1.5$\times$1016 molecules $cm^{-2}$ in June. While the model correctly captured this change, the

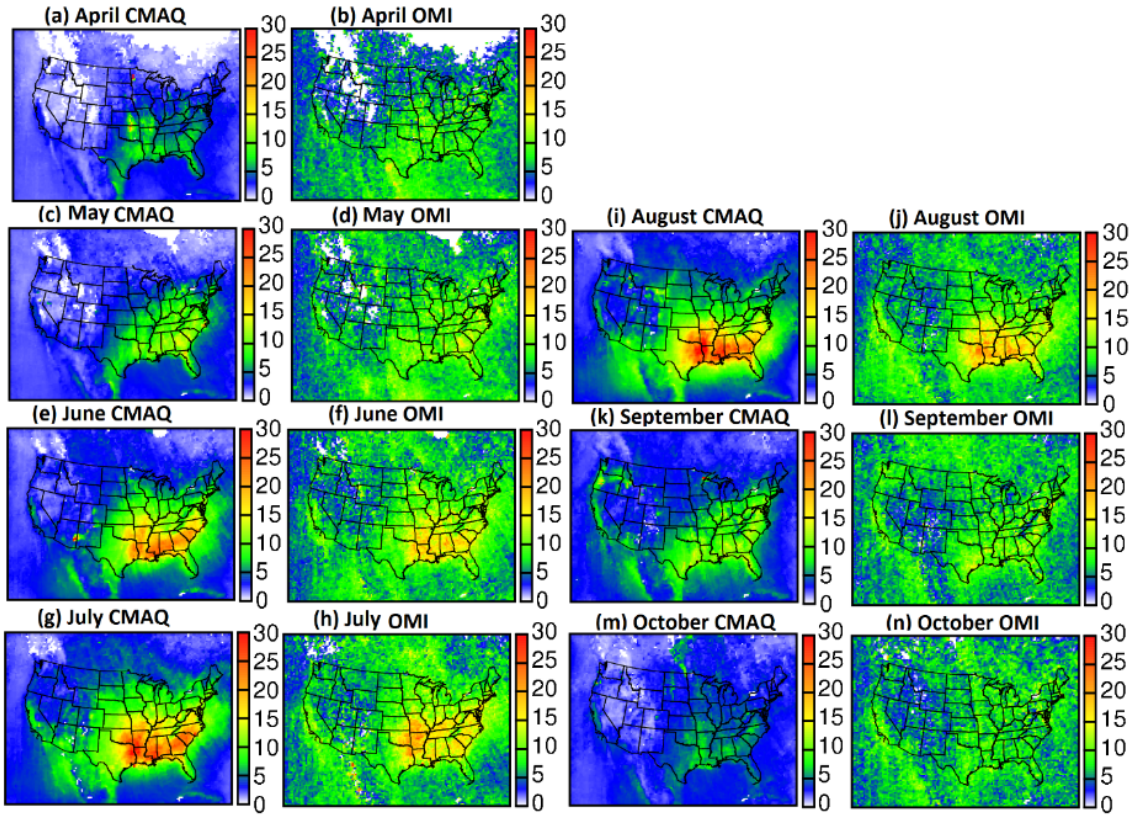


Figure 5.10: Predicted (a,c,e,g,i,k,m) and OMI monthly averaged (b,d,f,h,j,l,n) column density of HCHO ($\times$1015 molecules $cm^{-2}$) for April to October, 2011.

predicted column densities in the southeast states as a whole were slightly higher than observations. The observed and predicted VCD decreased quickly in September, although predictions were again slightly higher than observations. In October, both predictions and observations were back to the lower VCD of 5-7$\times$1015 molecules $cm^{-2}$ in the southeast US. Figure D- 7 includes scatter plots that compare predicted and observed monthly HCHO VCD for the columns that have VCD greater than 5$\times$1015 molecules $cm^{-2}$. The cut-off VCD was selected following Boeke et al. 135. The predicted and observed column concentrations were generally within a factor of 2, with under-predictions for lower concentrations and over-predictions for higher concentrations. Overall model performance in June (MFB=-0.509, MFE=0.551), July (-0.356; 0.456) and August (-0.353; 0.435) was better than that for other months. The model performance of HCHO VCD at each grid cell is demonstrated in Figure D- 8 by calculating the linear correlation between predicted and observed HCHO VCD at each grid cell based on monthly data from the seven months. In general, the correlation coefficients (R2) are greater than 0.7 in the southeast US with higher HCHO VCD concentrations. The slopes show that HCHO VCD is over-predicted in higher concentration regions and under-predicted in lower concentration regions, which corroborates the results shown in Figure D- 7.

#### *5.4.2.4 Effect Of Grid Resolution On Isoprene Predictions*

In order to evaluate if a higher grid resolution improves isoprene predictions at monitor sites, a nested simulation focused on Texas was conducted using a three-level domain. The 12-km and 4-km nested horizontal resolution domains cover Texas and surrounding states and eastern Texas, respectively. Emissions were generated for the 12-km and 4-km domains using the same approaches as those for the 36-km parent domain. A one-way nested CMAQ simulation was conducted and the predicted concentrations at the Texas monitoring sites from the 4-km resolution domain were compared with predictions. While

the daily averaged concentrations still showed reasonable correlations between observation and predictions, at a number of locations the predicted concentrations from the 4-km domain were lower than those from the 36-km domain (see Figure D- 5 and Figure D- 6), thus leading to more negative MFB values and larger MFE values (Table D- 3 and Table D- 4). To explain this apparent deterioration in model performance in isoprene predictions with higher spatial resolution, it is necessary to examine how isoprene emissions from the urban areas are determined in the current study.

Two major factors affecting isoprene emission estimates are LAIv and EF. The EF factor field used in MEGAN v2.10 is generated using the land use data base BELD4 and BEIS v3.61. In BEIS v3.61, emissions of isoprene from urban areas (NLCD categories 21, 22, 23 and 24, and MODIS sector 13) have been assigned a uniform basal emission factor of 10 gC $km^{-2}\ hr^{-1}$. A field survey in 2009 of a 1-km radius area near downtown Houston showed that temperate broadleaf deciduous trees accounted for approximately 25% of the ground coverage [117], one third of which were isoprene emitting oaks. In a number of locations in urban Houston, broadleaf deciduous trees account for 10-20% of the ground coverage 130. Based on the emission factor for the deciduous trees used in BEIS v3.61 (6707 gC $km^{-2}\ hr^{-1}$; MODIS type 4 and NLCD type 41), it is obvious that a uniform emission factor of 10 gC $km^{-2}\ hr^{-1}$ is likely too low for urban areas in Texas where oak trees are prevalent. For comparison, when the 36-km resolution domain is used, some of the monitors become located in a grid cell with lower urban fraction and higher tree fraction, and thus higher isoprene emissions. However, the grid cells where urban monitors are located in the 4-km domain have higher urban fractions and lower vegetation fractions, thus have lower isoprene emissions. To rectify this mismatch, the isoprene emission factor for urban land use type(s), specifically in Texas, should be increased in future simulations when using BEIS to generate MEGAN compatible EF fields. Ideally, city specific tree coverage should be applied to better reflect the difference in the tree coverage

and types among different urban areas. In addition, LAIv might be another source of error for the higher resolution simulations as these values are generically specified as described in Section 3.2. Kota et al. [110] showed that the prescribed LAIv of representative urban grid cells in Houston were only 60% of the field estimated LAIv, so it could contribute to the under-estimation of isoprene emissions in urban locations. It has also been suspected that inconsistent land use data used in MEGAN and in the land surface parameterization schemes of the WRF model could lead to uncertainties in the predicted isoprene concentrations. However, a recent study in California by Zhao et al. [110] clearly demonstrated that uncertainties in biogenic emissions caused by inconsistent land use data are much smaller than the uncertainties caused by vegetation distributions.

#### *5.4.2.5 Uncertainty In Photosynthetically Active Radiation And Temperature On Isoprene Emissions*

In addition to the LAIv and EF inputs, the predicted isoprene emissions are also affected by model inputs of PAR and temperature 45. Detailed studies on the effect of PAR and temperature on MEGAN predicted isoprene have been reported previously [118]. To investigate the uncertainty in predicted isoprene emissions due to these two factors in this study, two additional MEGAN sensitivity simulations based on simulation (a) for July 2011 were conducted. In the first sensitivity simulation, ambient temperatures in the 36-km resolution model domain were uniformly decreased by 1.0 K, resulting in monthly emissions of isoprene approximately 10-12% lower as compared to the base case. A 1.0 K lower temperature was chosen because the WRF model over-predicted the monthly temperature with mean biases ranging from 0.69-1.18 K (see Table S5 for model performance of temperature and other meteorological variables). In the second sensitivity simulation, hourly PAR at each grid cell was adjusted using hour-specific scaling factors based on the average ratio of observed PAR and the PAR used in the base case MEGAN simulations

(hereafter MEGAN PAR) at seven surface radiation (SURFRAD) network sites operated by the National Oceanic and Atmospheric Administration (NOAA). Table S6 shows the hourly MEGAN PAR values, which were calculated as 50% of the surface reaching solar radiation (RGRND) predicted by the WRF model. On average, the MEGAN PARs were approximately 40% higher (observation-to-prediction ratio  0.7), and as a result a reduction of monthly isoprene emission by approximately 30% was achieved when reducing MEGAN PAR by 40%. A 40% PAR over-prediction is consistent with those reported by previous study based on a comparison between WRF-based MEGAN PAR and satellite derived PAR for September 2013. The two simulations suggest that while the over-estimation of temperature and PAR can lead to over-estimation of isoprene, the uncertainties of these two variables in this study are too small to account for the large over-prediction discussed in Section 5.4.1.

## 5.5 Conclusions

In summary, the predicted isoprene concentrations from model combination MEGAN-BEIS361 generally agreed with the observations. Although hourly concentrations were slightly under-predicted (MFB $\approx$ -0.20-0.30, MFE $\approx$ 0.89-1.07), daily-average concentrations were better predicted and without significant biases, especially for the summer months (MFB $\approx$ -0.11-0.03, MFE $\approx$ 0.67-0.88). These results represent a significant improvement in predicted isoprene concentrations from previous studies as well as from the current study when using the original MEGAN-predicted emissions, which generally show a large positive bias. Better isoprene predictions can be obtained using MEGAN with the EF fields based on the BELD4 data base from the US-EPA for its BEIS v3.61 model. A seven-month simulation (April to October 2011) of isoprene emissions using the MEGAN-BEIS361 EF fields, and the resulting CMAQ-model ambient concentrations showed that observed spatial and temporal variations (both diurnal and seasonal) of iso-

prene concentrations, which span three orders of magnitude, can be reasonably well predicted (within a factor of two) at most non-urban monitors. At urban monitors, which dominate historically, low observed isoprene and high vegetation species and spatial heterogeneity strongly affect the observations, and as a result, neither low (36 km) nor high (4 km) resolution modeling could achieve reasonable, low-bias model results at all sites. However, the predicted large scale, monthly average column density of HCHO, a reactive volatile organic compound with dominant contributions from isoprene oxidation, agree fairly well with the isoprene column density derived using satellite data collected by the Ozone Monitoring Instrument (OMI). The agreement between observation and prediction may be further improved if more accurate PAR values, such as those derived from satellite-based observations, were used in modeling the biogenic emissions. In addition, less temporally dense (3-h or 24-h average) rural hydrocarbon measurements from EPA's National Ambient Air Toxics Trends Sites (NATTS), or Photochemical Assessment Monitoring Stations (PAMS), or other, state-operated sites could be used in future works to spatially expand the comparison.

# 6. CONCLUSIONS AND FUTURE RESEARCH

In China, predicted SOA concentrations are generally higher in summer (10-15 $\mu g \cdot m^{-3}$) due to large contributions of isoprene (country average, 61%) and lower in wintertime due to emissions of alkane and aromatic compounds (51%). Overall, 75% of total SOA in summer, 50-60% in autumn and spring, and approximately 24% in winter are due to biogenic SOA. The highest SOA in mainland China occurs in the Sichuan Basin in all seasons, with hourly concentrations as high as 50 $\mu g \cdot m^{-3}$. Manmade emissions facilitate biogenic SOA formation and controlling anthropogenic emissions would result in reduction of both anthropogenic and biogenic SOA.

Also the predicted SOA concentrations in summer are mainly due to large contributions of biogenic emissions within China (country average 60%) and in winter due to industrial and residential sectors (country average 78% total) based on the MEIC emission inventory. However, the transportation sector is predicted to be much more important while the residential sector is predicted to be less important based on REAS2 emissions. The SOA source apportionment differences among these three sets of simulations based on two emission inventories are consistent with the emission differences. The differences between these two emission inventories need to be investigated in future studies in order to set up efficient SOA and particulate pollution control policies.

In the ozone three-regime study, the Rts and Rte values for regime indicators $(p\mathrm{H_2O_2} + p\mathrm{ROOH})/p\mathrm{HNO_3}$ and $p\mathrm{H_2O_2}/p\mathrm{HNO_3}$ are (0.047$\pm$0.006, 5.142$\pm$0.411) and (0.033$\pm$0.006, 3.248$\pm$0.197), respectively. Most of the areas in China considered by the two-regime approach as NOx or VOC-limited are classified as transitional under the new three-regime scheme. For all these indicators, the VOC-limited regimes are located at urban areas, particularly in the YRD and PRD regions. The two ozone classification schemes lead

to relatively large differences in the assessment of the importance of NOx and VOCs to ozone formation in large areas in the NCP, the YRD and the PRD. The three-regime approach predicts higher NOx contributions to 8-hr ozone in these areas by up to 8 ppb with a relative difference as high as 80%.

Industries, transportation, power and biogenic sources are four major emission sectors to ozone with different spatial distributions. Transportation $O_3\_NO_x$ accounts for 10-15% of total ozone in most urban areas. For power sector, high $O_3\_NO_x$ regions are located in Shanxi, Shaanxi, Ningxia and part of Shandong and Jiangsu provinces, also with 10-15% relative contributions to total ozone. Ozone attributed to biogenic NOx in west, central and south China with low NOx emissions from anthropogenic sources reaches as high as 10-15% of total ozone and a maximum concentration of 12 ppb. Considering $O_3\_VOC$, biogenic and industrial sectors are the most important emission sectors that contribute to $O_3\_VOC$, accounting for more than 85% of the $O_3\_VOC$ in China. The high concentration areas of biogenic sector are located in Shandong, Jiangsu, Henan and Anhui provinces, accounting for 20% of total ozone. The industrial contributions to $O_3\_VOC$ are high in areas along the east coast from Tianjin to Shanghai and in urban areas in the PRD and SCB regions, with a relative contribution to total ozone up to 20%.

In the MEGAN EF study, the predicted isoprene concentrations from MEGAN-BEIS361 generally agreed with observations. Although hourly concentrations were slight under-predicted (MFB $\approx$ -0.20-0.30, MFE $\approx$ 0.89-1.07), daily-average concentrations were better predicted without significant biases, especially for summer months (MFB $\approx$ -0.11-0.03, MFE $\approx$ 0.67-0.88). These results represent a significant improvement in predicted isoprene concentrations from previous studies as well as from the current study when using the original MEGAN-predicted emissions, which generally show a large positive bias. Better isoprene predictions can be obtained using MEGAN with the EF fields based on the BELD4 data base from the US-EPA for its BEIS v3.61 model.

For the future studies:

1) Improve MEGAN performance at urban locations

From the results of Chapter 5, the modified MEGAN-BEIS361 has under-estimated the isoprene concentrations in the high-developed urban locations due to the inaccurate land cover information from the low resolution data. To fix this problem, a high horizontal resolution (e.g. 1km $\times$ 1km) of MEGAN-BEIS361 will be conducted in order to adjust the predicted isoprene concentrations from low resolution simulations.

2) Improve MEGAN model in China by modified EFs

The results from Chapter 5 shows the modified EF mothed has solved the problem of over-estimation isoprene in the original MEGAN to some extent. This method now is only applied in the US, however in China, the original MEGAN also has over-estimate the isoprene concentration (from objective1 results). This project is aiming in gathering the necessary land cover data and promoting the similar method in the objective 5 to improve the MEGAN performance in China.

3) Develop high-resolution vehicle emission in megacities in China

Based on the results of objective 2 (from the REAS2 emission inventories) and objective 4, the transportation sector is a significant contributor to both SOA and ozone formation in China and a certain portion of the emission is from the vehicles. In megacities, the vehicle population keep increasing every year, which may bring heavy burden to the environment. This project plan to use the vehicle emission model (e.g. Computer programme to calculate emissions from road transport, COPERT) combines with the real-time data to develop high-resolution vehicle emission inventories megacities in China.

# REFERENCES


[1] N. Englert, "Fine particles and human healthâĂŤa review of epidemiological studies," *Toxicology letters*, vol. 149, no. 1-3, pp. 235–242, 2004.

[2] F. Lu, D. Xu, Y. Cheng, S. Dong, C. Guo, X. Jiang, and X. Zheng, "Systematic review and meta-analysis of the adverse health effects of ambient pm2. 5 and pm10 pollution in the chinese population," *Environmental research*, vol. 136, pp. 196–204, 2015.

[3] C. A. Pope III and D. W. Dockery, "Health effects of fine particulate air pollution: lines that connect," *Journal of the air & waste management association*, vol. 56, no. 6, pp. 709–742, 2006.

[4] Y. J. Kaufman, D. TanrÃl', and O. Boucher, "A satellite view of aerosols in the climate system," *Nature*, vol. 419, no. 6903, pp. 215–223, 2002.

[5] D. Y. Pui, S.-C. Chen, and Z. Zuo, "Pm 2.5 in china: Measurements, sources, visibility and health effects, and mitigation," *Particuology*, vol. 13, pp. 1–26, 2014.

[6] R.-J. Huang, Y. Zhang, C. Bozzetti, K.-F. Ho, J.-J. Cao, Y. Han, K. R. Daellenbach, J. G. Slowik, S. M. Platt, and F. Canonaco, "High secondary aerosol contribution to particulate pollution during haze events in china," *Nature*, vol. 514, no. 7521, pp. 218–222, 2014.

[7] L. Wang, Z. Wei, J. Yang, Y. Zhang, F. Zhang, J. Su, C. Meng, and Q. Zhang, "The 2013 severe haze over southern hebei, china: model evaluation, source apportionment, and policy implications," *Atmos. Chem. Phys*, vol. 14, no. 6, pp. 3151–3173, 2014.

[8] P. Xu, Y. Chen, and X. Ye, "Haze, air pollution, and health in china," *The Lancet*, vol. 382, no. 9910, p. 2067, 2013.

[9] Y. Sun, Q. Jiang, Z. Wang, P. Fu, J. Li, T. Yang, and Y. Yin, "Investigation of the sources and evolution processes of severe haze pollution in beijing in january 2013," *Journal of Geophysical Research: Atmospheres*, vol. 119, no. 7, pp. 4380–4398, 2014.

[10] H. Li, Q. Zhang, Q. Zhang, C. Chen, L. Wang, Z. Wei, S. Zhou, C. Parworth, B. Zheng, F. Canonaco, *et al.*, "Wintertime aerosol chemistry and haze evolution in an extremely polluted city of the north china plain: significant contribution from coal and biomass combustion," *Atmospheric Chemistry and Physics*, vol. 17, no. 7, pp. 4751–4768, 2017.

[11] X. Zhang, Y. Zhang, J. Sun, Y. Yu, F. Canonaco, A. S. Prévôt, and G. Li, "Chemical characterization of submicron aerosol particles during wintertime in a northwest city of china using an aerodyne aerosol mass spectrometry," *Environmental pollution*, vol. 222, pp. 567–582, 2017.

[12] W. Hu, M. Hu, H. Wei-Wei, H. Niu, J. Zheng, Y. Wu, W. Chen, C. Chen, L. Li, M. Shao, *et al.*, "Characterization of submicron aerosols influenced by biomass burning at a site in the sichuan basin, southwestern china," *Atmospheric Chemistry and Physics*, vol. 16, no. 20, p. 13213, 2016.

[13] J. Zheng, M. Hu, J. Peng, Z. Wu, P. Kumar, M. Li, Y. Wang, and S. Guo, "Spatial distributions and chemical properties of pm2. 5 based on 21 field campaigns at 17 sites in china," *Chemosphere*, vol. 159, pp. 480–487, 2016.

[14] X. Shen, J. Sun, X. Zhang, Y. Zhang, L. Zhang, H. Che, Q. Ma, X. Yu, Y. Yue, and Y. Zhang, "Characterization of submicron aerosols and effect on visibility during

a severe haze-fog episode in yangtze river delta, china," *Atmospheric Environment*, vol. 120, pp. 307–316, 2015.

[15] Y. Sun, Z. Wang, W. Du, Q. Zhang, Q. Wang, P. Fu, X. Pan, J. Li, J. Jayne, and D. Worsnop, "Long-term real-time measurements of aerosol particle composition in beijing, china: seasonal variations, meteorological effects, and source analysis," *Atmospheric Chemistry and Physics*, vol. 15, no. 17, pp. 10149–10165, 2015.

[16] L.-Y. He, X.-F. Huang, L. Xue, M. Hu, Y. Lin, J. Zheng, R. Zhang, and Y.-H. Zhang, "Submicron aerosol analysis and organic source apportionment in an urban atmosphere in pearl river delta of china using high-resolution aerosol mass spectrometry," *Journal of Geophysical Research: Atmospheres*, vol. 116, no. D12, 2011.

[17] M. Hallquist, J. Wenger, U. Baltensperger, Y. Rudich, D. Simpson, M. Claeys, J. Dommen, N. Donahue, C. George, A. Goldstein, *et al.*, "The formation, properties and impact of secondary organic aerosol: current and emerging issues," *Atmospheric chemistry and physics*, vol. 9, no. 14, pp. 5155–5236, 2009.

[18] M. Crippa, F. Canonaco, V. Lanz, M. Äijälä, J. Allan, S. Carbone, G. Capes, D. Ceburnis, M. Dall'Osto, D. Day, *et al.*, "Organic aerosol components derived from 25 ams data sets across europe using a consistent me-2 based source apportionment approach," *Atmospheric chemistry and physics*, vol. 14, no. 12, pp. 6159–6176, 2014.

[19] Q. Zhang, J. L. Jimenez, M. Canagaratna, J. Allan, H. Coe, I. Ulbrich, M. Alfarra, A. Takami, A. Middlebrook, Y. Sun, *et al.*, "Ubiquity and dominance of oxygenated species in organic aerosols in anthropogenically-influenced northern hemisphere midlatitudes," *Geophysical Research Letters*, vol. 34, no. 13, 2007.

[20] C. Wu and J. Z. Yu, "Determination of primary combustion source organic carbon-to-elemental carbon (oc/ec) ratio using ambient oc and ec measurements: secondary

oc-ec correlation minimization method," *Atmospheric Chemistry and Physics*, vol. 16, no. 8, pp. 5453–5465, 2016.

[21] J. Hu, L. Wu, B. Zheng, Q. Zhang, K. He, Q. Chang, X. Li, F. Yang, Q. Ying, and H. Zhang, "Source contributions and regional transport of primary particulate matter in china," *Environmental pollution*, vol. 207, pp. 31–42, 2015.

[22] H. Wang, M. Tian, X. Li, Q. Chang, J. Cao, F. Yang, Y. Ma, and K. He, "Chemical composition and light extinction contribution of pm2. 5 in urban beijing for a 1-year period," *Aerosol Air Qual. Res*, vol. 15, no. 6, pp. 2200–2211, 2015.

[23] B. Yuan, W. Hu, M. Shao, M. Wang, W. Chen, S. Lu, L. Zeng, and M. Hu, "Voc emissions, evolutions and contributions to soa formation at a receptor site in eastern china," *Atmospheric Chemistry and Physics*, vol. 13, no. 17, pp. 8815–8832, 2013.

[24] X. Ding, X.-M. Wang, B. Gao, X.-X. Fu, Q.-F. He, X.-Y. Zhao, J.-Z. Yu, and M. Zheng, "Tracer-based estimation of secondary organic carbon in the pearl river delta, south china," *Journal of Geophysical Research: Atmospheres*, vol. 117, no. D5, 2012.

[25] J. Feng, M. Li, P. Zhang, S. Gong, M. Zhong, M. Wu, M. Zheng, C. Chen, H. Wang, and S. Lou, "Investigation of the sources and seasonal variations of secondary organic aerosols in pm2. 5 in shanghai with organic tracers," *Atmospheric environment*, vol. 79, pp. 614–622, 2013.

[26] J. Liu, J. Li, Y. Zhang, D. Liu, P. Ding, C. Shen, K. Shen, Q. He, X. Ding, X. Wang, *et al.*, "Source apportionment using radiocarbon and organic tracers for pm2. 5 carbonaceous aerosols in guangzhou, south china: Contrasting local-and regional-scale haze events," *Environmental science & technology*, vol. 48, no. 20, pp. 12002–12011, 2014.

[27] X. Huang, H. Ip, and J. Z. Yu, "Secondary organic aerosol formation from ethylene in the urban atmosphere of hong kong: A multiphase chemical modeling study," *Journal of Geophysical Research: Atmospheres*, vol. 116, no. D3, 2011.

[28] S. Wang, D. Wu, X.-M. Wang, J. C.-H. Fung, and J. Z. Yu, "Relative contributions of secondary organic aerosol formation from toluene, xylenes, isoprene, and monoterpenes in hong kong and guangzhou in the pearl river delta, china: an emission-based box modeling study," *Journal of Geophysical Research: Atmospheres*, vol. 118, no. 2, pp. 507–519, 2013.

[29] B. Zhao, S. Wang, N. M. Donahue, S. H. Jathar, X. Huang, W. Wu, J. Hao, and A. L. Robinson, "Quantifying the effect of organic aerosol aging and intermediate-volatility emissions on regional-scale aerosol pollution in china," *Scientific reports*, vol. 6, p. 28815, 2016.

[30] L. Li, J. An, M. Zhou, R. Yan, C. Huang, Q. Lu, L. Lin, Y. Wang, S. Tao, L. Qiao, *et al.*, "Source apportionment of fine particles and its chemical components over the yangtze river delta, china during a heavy haze pollution episode," *Atmospheric Environment*, vol. 123, pp. 415–429, 2015.

[31] J. Hu, P. Wang, Q. Ying, H. Zhang, J. Chen, X. Ge, X. Li, J. Jiang, S. Wang, J. Zhang, *et al.*, "Modeling biogenic and anthropogenic secondary organic aerosol in china," *Atmospheric Chemistry and Physics*, vol. 17, no. 1, pp. 77–92, 2017.

[32] J. Lin, J. An, Y. Qu, Y. Chen, Y. Li, Y. Tang, F. Wang, and W. Xiang, "Local and distant source contributions to secondary organic aerosol in the beijing urban area in summer," *Atmospheric Environment*, vol. 124, pp. 176–185, 2016.

[33] B. N. Murphy and S. N. Pandis, "Simulating the formation of semivolatile primary and secondary organic aerosol in a regional chemical transport model," *Environmental science & technology*, vol. 43, no. 13, pp. 4722–4728, 2009.

[34] E. Saikawa, H. Kim, M. Zhong, A. Avramov, Y. Zhao, G. Janssens-Maenhout, J.-i. Kurokawa, Z. Klimont, F. Wagner, V. Naik, *et al.*, "Comparison of emissions inventories of anthropogenic air pollutants and greenhouse gases in china," *Atmospheric Chemistry and Physics*, vol. 17, no. 10, p. 6393, 2017.

[35] J. Hu, X. Li, L. Huang, Q. Ying, Q. Zhang, B. Zhao, S. Wang, and H. Zhang, "Ensemble predictions of air pollutants in china in 2013 for health effects studies using 1 wrf/cmaq modeling system with four emission inventories 2," *Science*, vol. 3136, p. 13, 2017.

[36] D. Byun and K. L. Schere, "Review of the governing equations, computational algorithms, and other components of the models-3 community multiscale air quality (cmaq) modeling system," *Applied mechanics reviews*, vol. 59, no. 2, pp. 51–77, 2006.

[37] K. Foley, S. Roselle, K. Appel, P. Bhave, J. Pleim, T. Otte, R. Mathur, G. Sarwar, J. Young, R. Gilliam, *et al.*, "Incremental testing of the community multiscale air quality (cmaq) modeling system version 4.7," *Geoscientific Model Development*, vol. 3, no. 1, p. 205, 2010.

[38] K. Appel, G. Pouliot, H. Simon, G. Sarwar, H. Pye, S. Napelenok, F. Akhtar, and S. Roselle, "Evaluation of dust and trace metal estimates from the community multiscale air quality (cmaq) model version 5.0," *Geoscientific Model Development*, vol. 6, no. 4, p. 883, 2013.

[39] T. Wang, A. Ding, J. Gao, and W. S. Wu, "Strong ozone production in urban plumes from beijing, china," *Geophysical Research Letters*, vol. 33, no. 21, 2006.

[40] Q. Ying, J. Li, and S. H. Kota, "Significant contributions of isoprene to summertime secondary organic aerosol in eastern united states," *Environmental science & technology*, vol. 49, no. 13, pp. 7834–7842, 2015.

[41] H. Zhang, J. Li, Q. Ying, J. Z. Yu, D. Wu, Y. Cheng, K. He, and J. Jiang, "Source apportionment of pm2. 5 nitrate and sulfate in china using a source-oriented chemical transport model," *Atmospheric environment*, vol. 62, pp. 228–242, 2012.

[42] J. Hu, J. Chen, Q. Ying, and H. Zhang, "One-year simulation of ozone and particulate matter in china using wrf/cmaq modeling system.," *Atmospheric Chemistry & Physics*, vol. 16, no. 16, 2016.

[43] J. Kurokawa, T. Ohara, T. Morikawa, S. Hanayama, G. Janssens-Maenhout, T. Fukui, K. Kawashima, and H. Akimoto, "Emissions of air pollutants and greenhouse gases over asian regions during 2000–2008: Regional emission inventory in asia (reas) version 2," *Atmospheric Chemistry and Physics*, vol. 13, no. 21, pp. 11019–11058, 2013.

[44] K. He, "Multi-resolution emission inventory for china (meic): model framework and 1990-2010 anthropogenic emissions," in *AGU Fall Meeting Abstracts*, 2012.

[45] A. Guenther, T. Karl, P. Harley, C. Wiedinmyer, P. Palmer, and C. Geron, "Estimates of global terrestrial isoprene emissions using megan (model of emissions of gases and aerosols from nature)," *Atmospheric Chemistry and Physics*, vol. 6, no. 11, pp. 3181–3210, 2006.

[46] P. Wang, Q. Ying, H. Zhang, J. Hu, Y. Lin, and H. Mao, "Source apportionment of secondary organic aerosol in china using a regional source-oriented chemical transport model and two emission inventories," *Environmental Pollution*, 2017.

[47] W. P. Carter and G. Heo, "Development of revised saprc aromatics mechanisms," *Atmospheric environment*, vol. 77, pp. 404–414, 2013.

[48] W. P. Carter, "Documentation of the saprc-99 chemical mechanism for voc reactivity assessment," *Contract*, vol. 92, no. 329, pp. 95–308, 2000.

[49] W. P. Carter, "Implementation of the saprc-99 chemical mechanism into the models-3 framework," *Report to the United States Environmental Protection Agency, January*, vol. 29, 2000.

[50] X. Qiao, Y. Tang, J. Hu, S. Zhang, J. Li, S. H. Kota, L. Wu, H. Gao, H. Zhang, and Q. Ying, "Modeling dry and wet deposition of sulfate, nitrate, and ammonium ions in jiuzhaigou national nature reserve, china using a source-oriented cmaq model: Part i. base case model results," *Science of the Total Environment*, vol. 532, pp. 831–839, 2015.

[51] C. Wiedinmyer, S. Akagi, R. J. Yokelson, L. Emmons, J. Al-Saadi, J. Orlando, and A. Soja, "The fire inventory from ncar (finn): a high resolution global model to estimate the emissions from open burning," *Geoscientific Model Development*, vol. 4, no. 3, p. 625, 2011.

[52] D. Streets, K. Yarber, J.-H. Woo, and G. Carmichael, "Biomass burning in asia: Annual and seasonal estimates and atmospheric emissions," *Global Biogeochemical Cycles*, vol. 17, no. 4, 2003.

[53] C. Huang, H. Wang, L. Li, Q. Wang, Q. Lu, J. De Gouw, M. Zhou, S. Jing, J. Lu, and C. Chen, "Voc species and emission inventory from vehicles and their soa formation potentials estimation in shanghai, china," *Atmospheric Chemistry and Physics*, vol. 15, no. 19, pp. 11081–11096, 2015.

[54] M. Jerrett, R. T. Burnett, C. A. Pope III, K. Ito, G. Thurston, D. Krewski, Y. Shi, E. Calle, and M. Thun, "Long-term ozone exposure and mortality," *New England Journal of Medicine*, vol. 360, no. 11, pp. 1085–1095, 2009.

[55] J. Lelieveld, J. S. Evans, M. Fnais, D. Giannadaki, and A. Pozzer, "The contribution of outdoor air pollution sources to premature mortality on a global scale," *Nature*, vol. 525, no. 7569, p. 367, 2015.

[56] M. L. Bell, A. McDermott, S. L. Zeger, J. M. Samet, and F. Dominici, "Ozone and short-term mortality in 95 us urban communities, 1987-2000," *Jama*, vol. 292, no. 19, pp. 2372–2378, 2004.

[57] L. Skärby, H. Ro-Poulsen, F. A. Wellburn, and L. J. Sheppard, "Impacts of ozone on forests: a european perspective," *The New Phytologist*, vol. 139, no. 1, pp. 109–122, 1998.

[58] V. E. Wittig, E. A. Ainsworth, S. L. Naidu, D. F. Karnosky, and S. P. Long, "Quantifying the impact of current and future tropospheric ozone on tree biomass, growth, physiology and biochemistry: a quantitative meta-analysis," *Global Change Biology*, vol. 15, no. 2, pp. 396–424, 2009.

[59] D. Shindell, J. C. Kuylenstierna, E. Vignati, R. van Dingenen, M. Amann, Z. Klimont, S. C. Anenberg, N. Muller, G. Janssens-Maenhout, F. Raes, *et al.*, "Simultaneously mitigating near-term climate change and improving human health and food security," *Science*, vol. 335, no. 6065, pp. 183–189, 2012.

[60] R. Van Dingenen, F. J. Dentener, F. Raes, M. C. Krol, L. Emberson, and J. Cofala, "The global impact of ozone on agricultural crop yields under current and future air quality legislation," *Atmospheric Environment*, vol. 43, no. 3, pp. 604–618, 2009.

[61] A. J. Haagen-Smit, "Chemistry and physiology of los angeles smog," *Industrial & Engineering Chemistry*, vol. 44, no. 6, pp. 1342–1346, 1952.

[62] M. J. Molina and L. T. Molina, "Megacities and atmospheric pollution," *Journal of the Air & Waste Management Association*, vol. 54, no. 6, pp. 644–680, 2004.

[63] P. Solomon, E. Cowling, G. Hidy, and C. Furiness, "Comparison of scientific findings from major ozone field studies in north america and europe," *Atmospheric Environment*, vol. 34, no. 12-14, pp. 1885–1920, 2000.

[64] J. H. Seinfeld and S. N. Pandis, *Atmospheric chemistry and physics: from air pollution to climate change*. John Wiley & Sons, 2016.

[65] U. G. ENVIRON, "Comprehensive air quality model with extensions (camx). version 6.20," *ENVIRON International Corporation, Novato*, 2015.

[66] R. Kwok, K. Baker, S. Napelenok, and G. Tonnesen, "Photochemical grid model implementation and application of voc, no x, and o 3 source apportionment," *Geoscientific Model Development*, vol. 8, no. 1, p. 99, 2015.

[67] S. Sillman, "The use of no y, h2o2, and hno3 as indicators for ozone-no x-hydrocarbon sensitivity in urban locations," *Journal of Geophysical Research: Atmospheres*, vol. 100, no. D7, pp. 14175–14188, 1995.

[68] J. Li, H. Zhang, and Q. Ying, "Comparison of the saprc07 and saprc99 photochemical mechanisms during a high ozone episode in texas: Differences in concentrations, oh budget and relative response factors," *Atmospheric environment*, vol. 54, pp. 25–35, 2012.

[69] S. Sillman and D. He, "Some theoretical results concerning o3-nox-voc chemistry and nox-voc indicators," *Journal of Geophysical Research: Atmospheres*, vol. 107, no. D22, 2002.

[70] J. B. Milford, A. G. Russell, and G. J. McRae, "A new approach to photochemical pollution control: Implications of spatial patterns in pollutant responses to reductions in nitrogen oxides and reactive organic gas emissions," *Environmental Science & Technology*, vol. 23, no. 10, pp. 1290–1301, 1989.

[71] C.-H. Lu and J. S. Chang, "On the indicator-based approach to assess ozone sensitivities and emissions features," *Journal of Geophysical Research: Atmospheres*, vol. 103, no. D3, pp. 3453–3462, 1998.

[72] S. Sillman, "The relation between ozone, nox and hydrocarbons in urban and polluted rural environments," *Atmospheric Environment*, vol. 33, no. 12, pp. 1821–1845, 1999.

[73] Z. Shi, J. Li, L. Huang, P. Wang, L. Wu, Q. Ying, H. Zhang, L. Lu, X. Liu, H. Liao, *et al.*, "Source apportionment of fine particulate matter in china in 2013 using a source-oriented chemical transport model," *Science of the Total Environment*, vol. 601, pp. 1476–1487, 2017.

[74] X. Qiao, Q. Ying, X. Li, H. Zhang, J. Hu, Y. Tang, and X. Chen, "Source apportionment of pm2. 5 for 25 chinese provincial capitals and municipalities using a source-oriented community multiscale air quality model," *Science of the Total Environment*, vol. 612, pp. 462–471, 2018.

[75] J. Xing, S. Wang, C. Jang, Y. Zhu, and J. Hao, "Nonlinear response of ozone to precursor emission changes in china: a modeling study using response surface methodology," *Atmospheric Chemistry and Physics*, vol. 11, no. 10, pp. 5027–5044, 2011.

[76] X.-H. Liu, Y. Zhang, J. Xing, Q. Zhang, K. Wang, D. G. Streets, C. Jang, W.-X. Wang, and J.-M. Hao, "Understanding of regional air pollution over china using cmaq, part ii. process analysis and sensitivity of ozone and particulate matter to precursor emissions," *Atmospheric Environment*, vol. 44, no. 30, pp. 3719–3727, 2010.

[77] M. Brauer, G. Freedman, J. Frostad, A. Van Donkelaar, R. V. Martin, F. Dentener, R. v. Dingenen, K. Estep, H. Amini, J. S. Apte, *et al.*, "Ambient air pollution exposure estimation for the global burden of disease 2013," *Environmental science & technology*, vol. 50, no. 1, pp. 79–88, 2015.

[78] M. Lippmann, "Health effects of tropospheric ozone: review of recent research findings and their implications to ambient air quality standards.," *Journal of exposure*

*analysis and environmental epidemiology*, vol. 3, no. 1, pp. 103–129, 1993.

[79] T. Liu, T. T. Li, Y. H. Zhang, Y. J. Xu, X. Q. Lao, S. Rutherford, C. Chu, Y. Luo, Q. Zhu, X. J. Xu, *et al.*, "The short-term effect of ambient ozone on mortality is modified by temperature in guangzhou, china," *Atmospheric environment*, vol. 76, pp. 59–67, 2013.

[80] T. Li, M. Yan, W. Ma, J. Ban, T. Liu, H. Lin, and Z. Liu, "Short-term effects of multiple ozone metrics on daily mortality in a megacity of china," *Environmental Science and Pollution Research*, vol. 22, no. 11, pp. 8738–8746, 2015.

[81] Z. Feng, E. Hu, X. Wang, L. Jiang, and X. Liu, "Ground-level o3 pollution and its impacts on food crops in china: a review," *Environmental Pollution*, vol. 199, pp. 42–48, 2015.

[82] S. Madronich, M. Shao, S. Wilson, K. Solomon, J. Longstreth, and X. Tang, "Changes in air quality and tropospheric composition due to depletion of stratospheric ozone and interactions with changing climate: implications for human and environmental health," *Photochemical & Photobiological Sciences*, vol. 14, no. 1, pp. 149–169, 2015.

[83] T. Wang, L. Xue, P. Brimblecombe, Y. F. Lam, L. Li, and L. Zhang, "Ozone pollution in china: A review of concentrations, meteorological influences, chemical precursors, and effects," *Science of the Total Environment*, vol. 575, pp. 1582–1596, 2017.

[84] M. Shao, X. Tang, Y. Zhang, and W. Li, "City clusters in china: air and surface water pollution," *Frontiers in Ecology and the Environment*, vol. 4, no. 7, pp. 353–361, 2006.

[85] J. Ou, Z. Yuan, J. Zheng, Z. Huang, M. Shao, Z. Li, X. Huang, H. Guo, and P. K. Louie, "Ambient ozone control in a photochemically active region: short-term despiking or long-term attainment?," *Environmental science & technology*, vol. 50, no. 11, pp. 5720–5728, 2016.

[86] Z. Ma, J. Xu, W. Quan, Z. Zhang, W. Lin, and X. Xu, "Significant increase of surface ozone at a rural site, north of eastern china," *Atmospheric Chemistry and Physics*, vol. 16, no. 6, pp. 3969–3977, 2016.

[87] Y. Wang, L. Shen, S. Wu, L. Mickley, J. He, and J. Hao, "Sensitivity of surface ozone over china to 2000–2050 global changes of climate and emissions," *Atmospheric environment*, vol. 75, pp. 374–382, 2013.

[88] G. Li, N. Bei, J. Cao, J. Wu, X. Long, F. Tian, W. Dai, S. Liu, Q. Zhang, and X. Tie, "Widespread and persistent ozone pollution in eastern china during the non-winter season of 2015: observations and source attributions," *Atmospheric Chemistry and Physics*, vol. 17, no. 4, p. 2759, 2017.

[89] L. T. Molina, "Summertime ozone formation in xi'an and surrounding areas, china," *Atmospheric Chemistry and Physics*, vol. 16, no. 7, p. 4323, 2016.

[90] Y. Qu, J. An, J. Li, Y. Chen, Y. Li, X. Liu, and M. Hu, "Effects of nox and vocs from five emission sources on summer surface o3 over the beijing-tianjin-hebei region," *Advances in Atmospheric Sciences*, vol. 31, no. 4, pp. 787–800, 2014.

[91] X. Wang, J. Li, Y. Zhang, S. Xie, and X. Tang, "Ozone source attribution during a severe photochemical smog episode in beijing, china," *Science in China Series B: Chemistry*, vol. 52, no. 8, pp. 1270–1280, 2009.

[92] Y. Li, A.-H. Lau, J.-H. Fung, J. Zheng, L. Zhong, and P. K. K. Louie, "Ozone source apportionment (osat) to differentiate local regional and super-regional source con-

tributions in the pearl river delta region, china," *Journal of Geophysical Research: Atmospheres*, vol. 117, no. D15, 2012.

[93] J. Gao, B. Zhu, H. Xiao, H. Kang, X. Hou, and P. Shao, "A case study of surface ozone source apportionment during a high concentration episode, under frequent shifting wind conditions over the yangtze river delta, china," *Science of the Total Environment*, vol. 544, pp. 853–863, 2016.

[94] H. Zhang and Q. Ying, "Contributions of local and regional sources of nox to ozone concentrations in southeast texas," *Atmospheric environment*, vol. 45, no. 17, pp. 2877–2887, 2011.

[95] Q. Ying and A. Krishnan, "Source contributions of volatile organic compounds to ozone formation in southeast texas," *Journal of Geophysical Research: Atmospheres*, vol. 115, no. D17, 2010.

[96] Q. Ying, M. Feng, D. Song, L. Wu, J. Hu, H. Zhang, M. J. Kleeman, and X. Li, "Improve regional distribution and source apportionment of pm 2.5 trace elements in china using inventory-observation constrained emission factors," *Science of The Total Environment*, vol. 624, pp. 355–365, 2018.

[97] G. S. Tonnesen and R. L. Dennis, "Analysis of radical propagation efficiency to assess ozone sensitivity to hydrocarbons and no x: 1. local indicators of instantaneous odd oxygen production sensitivity," *Journal of Geophysical Research: Atmospheres*, vol. 105, no. D7, pp. 9213–9225, 2000.

[98] M. of Environmental Protection of China, "Chinese ambient air quality standards (gb3095-2012)," *In Ministry of Environmental Protection of China: Beijing*, 2012.

[99] P. Wang, G. Schade, M. Estes, and Q. Ying, "Improved megan predictions of biogenic isoprene in the contiguous united states," *Atmospheric Environment*, vol. 148,

pp. 337–351, 2017.

[100] J. D. Fuentes, L. Gu, M. Lerdau, R. Atkinson, D. Baldocchi, J. Bottenheim, P. Ciccioli, B. Lamb, C. Geron, A. Guenther, *et al.*, "Biogenic hydrocarbons in the atmospheric boundary layer: a review," *Bulletin of the American Meteorological Society*, vol. 81, no. 7, pp. 1537–1575, 2000.

[101] A. H. Goldstein, C. D. Koven, C. L. Heald, and I. Y. Fung, "Biogenic carbon and anthropogenic pollutants combine to form a cooling haze over the southeastern united states," *Proceedings of the National Academy of Sciences*, vol. 106, no. 22, pp. 8835–8840, 2009.

[102] G. Yarwood, G. Wilson, C. Emery, and A. Guenther, "Development of globeis-a state of the science biogenic emissions modeling system," *Final Report to the Texas Natural Resource Conservation Commission, Austin, TX. Available from http://www. globeis. com*, 1999.

[103] J. Vukovich and T. Pierce, "The implementation of beis3 within the smoke," in *11th International Emission Inventory Conference: Emission InventoriesâĂŤPartnering for the Future*, 2002.

[104] C. Warneke, J. De Gouw, L. Del Negro, J. Brioude, S. McKeen, H. Stark, W. Kuster, P. Goldan, M. Trainer, F. Fehsenfeld, *et al.*, "Biogenic emission measurement and inventories determination of biogenic emissions in the eastern united states and texas and comparison with biogenic emission inventories," *Journal of Geophysical Research: Atmospheres*, vol. 115, no. D7, 2010.

[105] A. G. Carlton and K. R. Baker, "Photochemical modeling of the ozark isoprene volcano: Megan, beis, and their impacts on air quality predictions," *Environmental science & technology*, vol. 45, no. 10, pp. 4438–4445, 2011.

[106] D. B. Millet, D. J. Jacob, K. F. Boersma, T.-M. Fu, T. P. Kurosu, K. Chance, C. L. Heald, and A. Guenther, "Spatial distribution of isoprene emissions from north america derived from formaldehyde column measurements by the omi satellite sensor," *Journal of Geophysical Research: Atmospheres*, vol. 113, no. D2, 2008.

[107] T. Stavrakou, J. Peeters, and J.-F. Müller, "Improved global modelling of ho x recycling in isoprene oxidation: evaluation against the gabriel and intex-a aircraft campaign measurements," *Atmospheric Chemistry and Physics*, vol. 10, no. 20, pp. 9863–9878, 2010.

[108] C. L. Heald, M. J. Wilkinson, R. K. Monson, C. A. Alo, G. Wang, and A. Guenther, "Response of isoprene emission to ambient co2 changes and implications for global budgets," *Global Change Biology*, vol. 15, no. 5, pp. 1127–1140, 2009.

[109] J. O. Bash, K. R. Baker, and M. R. Beaver, "Evaluation of improved land use and canopy representation in beis v3. 61 with biogenic voc measurements in california," *Geoscientific Model Development*, vol. 9, no. 6, p. 2191, 2016.

[110] S. H. Kota, G. Schade, M. Estes, D. Boyer, and Q. Ying, "Evaluation of megan predicted biogenic isoprene emissions at urban locations in southeast texas," *Atmospheric Environment*, vol. 110, pp. 54–64, 2015.

[111] D. M. Lawrence, K. W. Oleson, M. G. Flanner, P. E. Thornton, S. C. Swenson, P. J. Lawrence, X. Zeng, Z.-L. Yang, S. Levis, K. Sakaguchi, *et al.*, "Parameterization improvements and functional and structural advances in version 4 of the community land model," *Journal of Advances in Modeling Earth Systems*, vol. 3, no. 1, 2011.

[112] A. Guenther, X. Jiang, C. Heald, T. Sakulyanontvittaya, T. Duhl, L. Emmons, and X. Wang, "The model of emissions of gases and aerosols from nature version 2.1 (megan2. 1): an extended and updated framework for modeling biogenic emissions," 2012.

[113] H. Zhang, J. Li, Q. Ying, B. B. Guven, and E. P. Olaguer, "Source apportionment of formaldehyde during texaqs 2006 using a source-oriented chemical transport model," *Journal of Geophysical Research: Atmospheres*, vol. 118, no. 3, pp. 1525–1535, 2013.

[114] P. I. Palmer, D. S. Abbot, T.-M. Fu, D. J. Jacob, K. Chance, T. P. Kurosu, A. Guenther, C. Wiedinmyer, J. C. Stanton, M. J. Pilling, *et al.*, "Quantifying the seasonal and interannual variability of north american isoprene emissions using satellite observations of the formaldehyde column," *Journal of Geophysical Research: Atmospheres*, vol. 111, no. D12, 2006.

[115] P. I. Palmer, D. J. Jacob, A. M. Fiore, R. V. Martin, K. Chance, and T. P. Kurosu, "Mapping isoprene emissions over north america using formaldehyde column observations from space," *Journal of Geophysical Research: Atmospheres*, vol. 108, no. D6, 2003.

[116] I. De Smedt, T. Stavrakou, F. Hendrick, T. Danckaert, T. Vlemmix, G. Pinardi, N. Theys, C. Lerot, C. Gielen, C. Vigouroux, *et al.*, "Diurnal, seasonal and long-term variations of global formaldehyde columns inferred from combined omi and gome-2 observations.," *Atmospheric Chemistry & Physics Discussions*, vol. 15, no. 8, 2015.

[117] C. Park, G. W. Schade, and I. Boedeker, "Characteristics of the flux of isoprene and its oxidation products in an urban area," *Journal of Geophysical Research: Atmospheres*, vol. 116, no. D21, 2011.

[118] A. B. Tawfik, R. Stöckli, A. Goldstein, S. Pressley, and A. L. Steiner, "Quantifying the contribution of environmental factors to isoprene flux interannual variability," *Atmospheric environment*, vol. 54, pp. 216–224, 2012.

# APPENDIX A

## SUPPLEMENTARY MATERIAS OF SOURCE APPORTIONMENT OF SECONDARY ORGANIC AEROSOL IN CHINA USING A REGIONAL CHEMICAL TRANSPORT MODEL AND TWO EMISSION

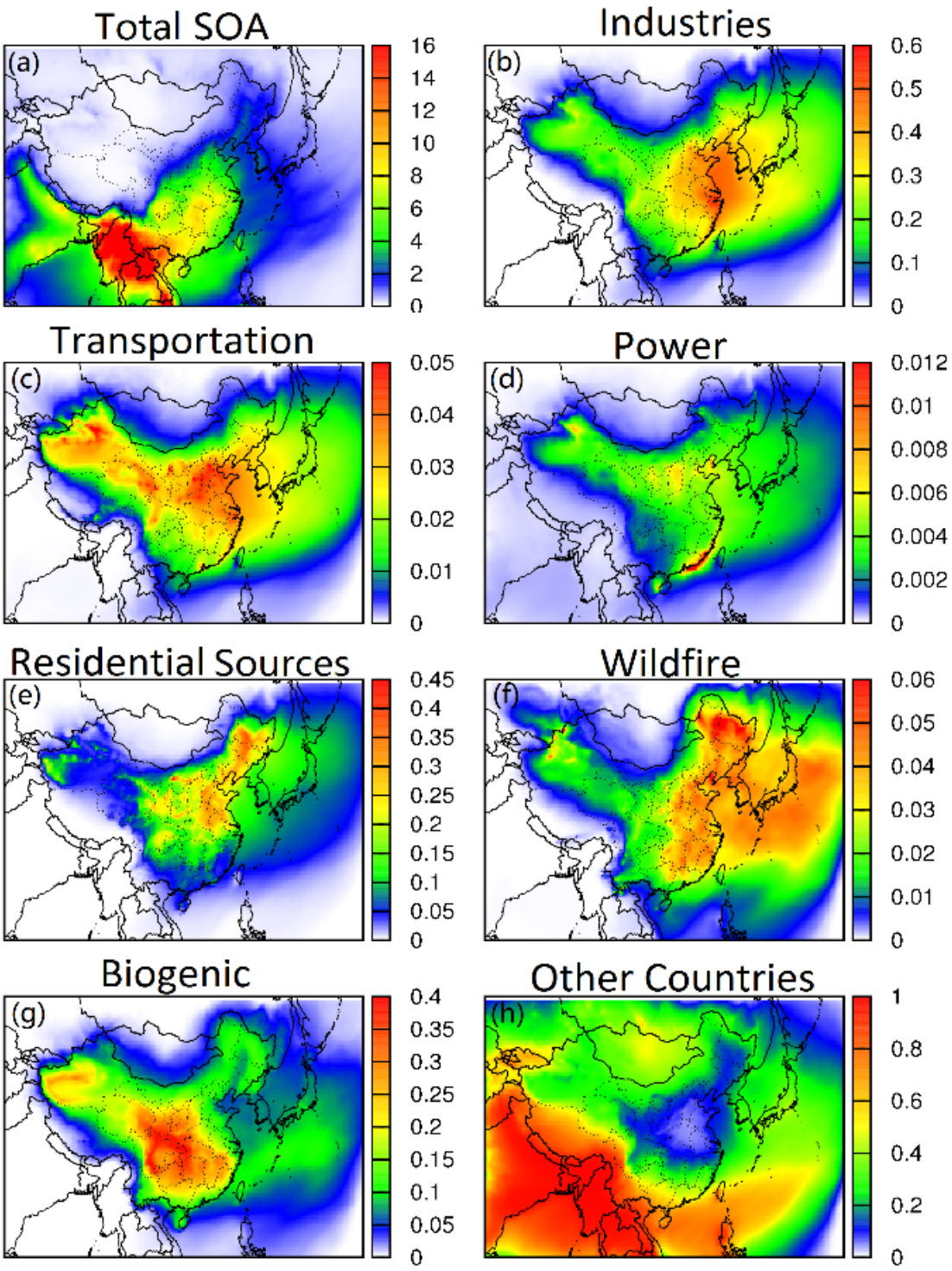


Figure A.1: Predicted spring (March, April and May) average SOA concentration (in $\mu g \cdot m^{-3}$, panel (a)) and fractional contributions due to (b) industries, (c) transportation, (d) power, (e) residential sources, (f) wildfire, (g) biogenic and (h) other countries.

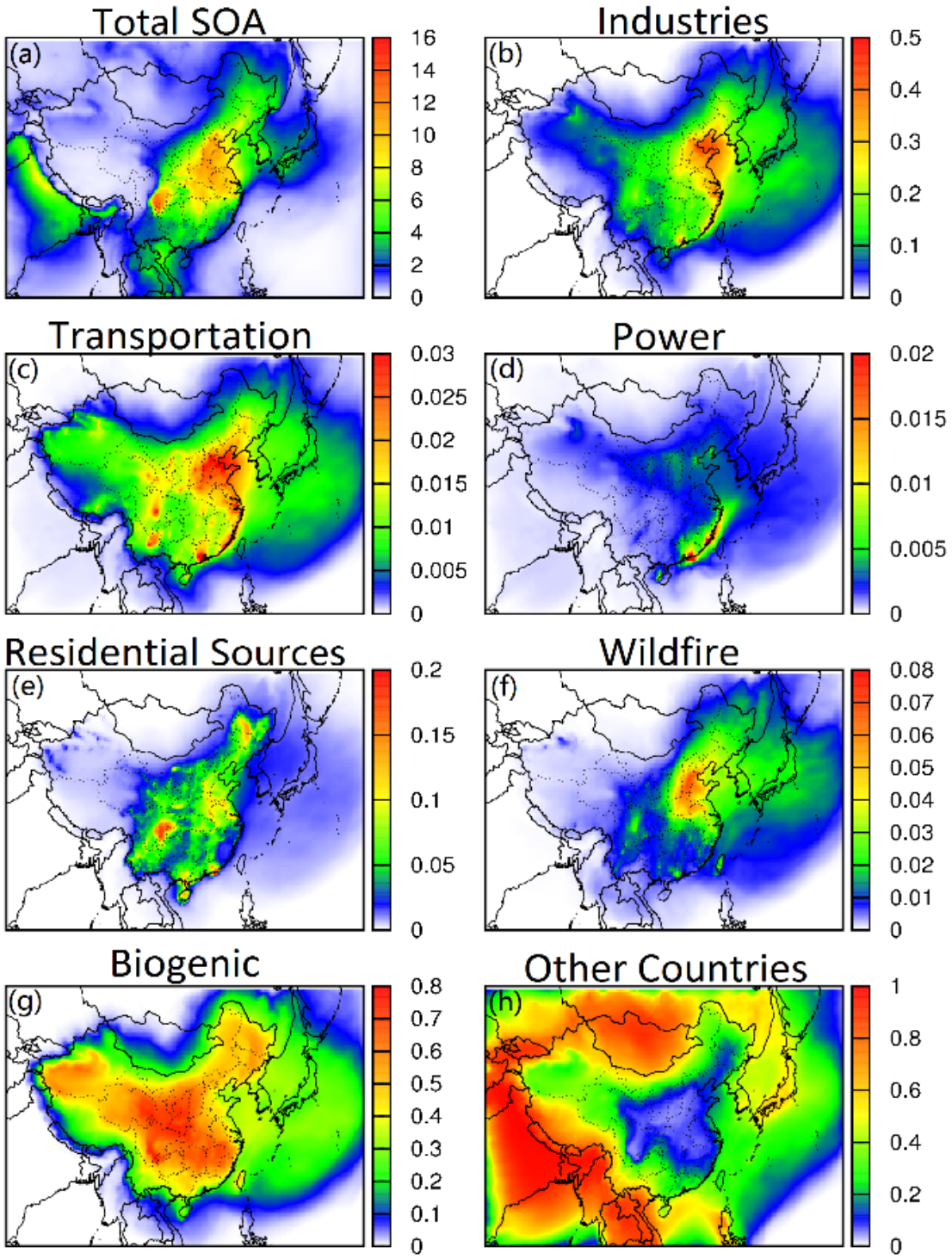


Figure A.2: Predicted summer (June, July and August) average SOA concentration (in $\mu g \cdot m^{-3}$, panel (a)) and fractional source contributions due to (b) industries, (c) transportation, (d) power, (e) residential sources, (f) wildfire, (g) biogenic and (h) other countries.

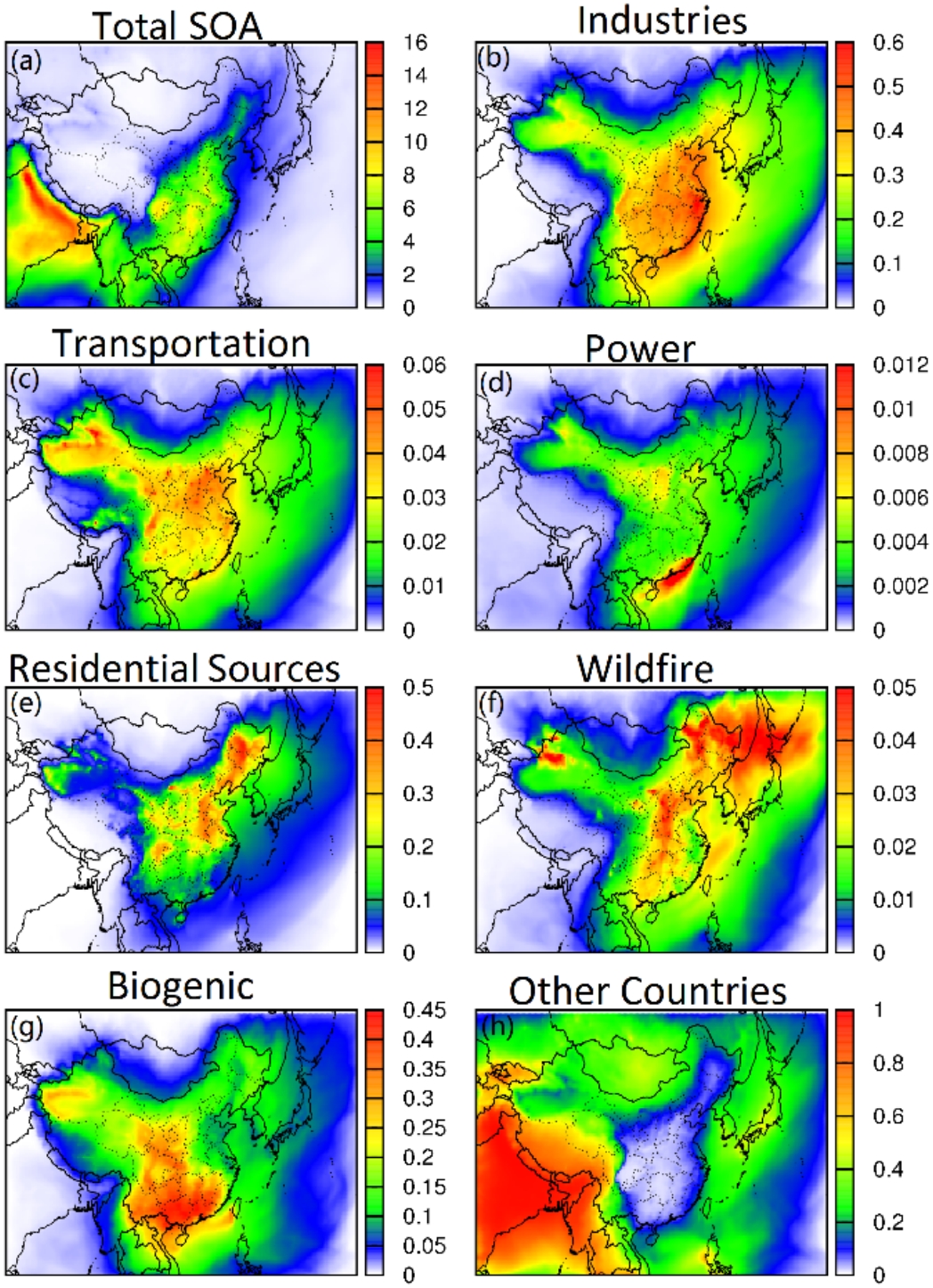


Figure A.3: Predicted autumn (September, October and November) average SOA concentration (in $\mu g \cdot m^{-3}$, panel (a)) and fractional source contributions due to (b) industries, (c) transportation, (d) power, (e) residential sources, (f) wildfire, (g) biogenic and (h) other countries.

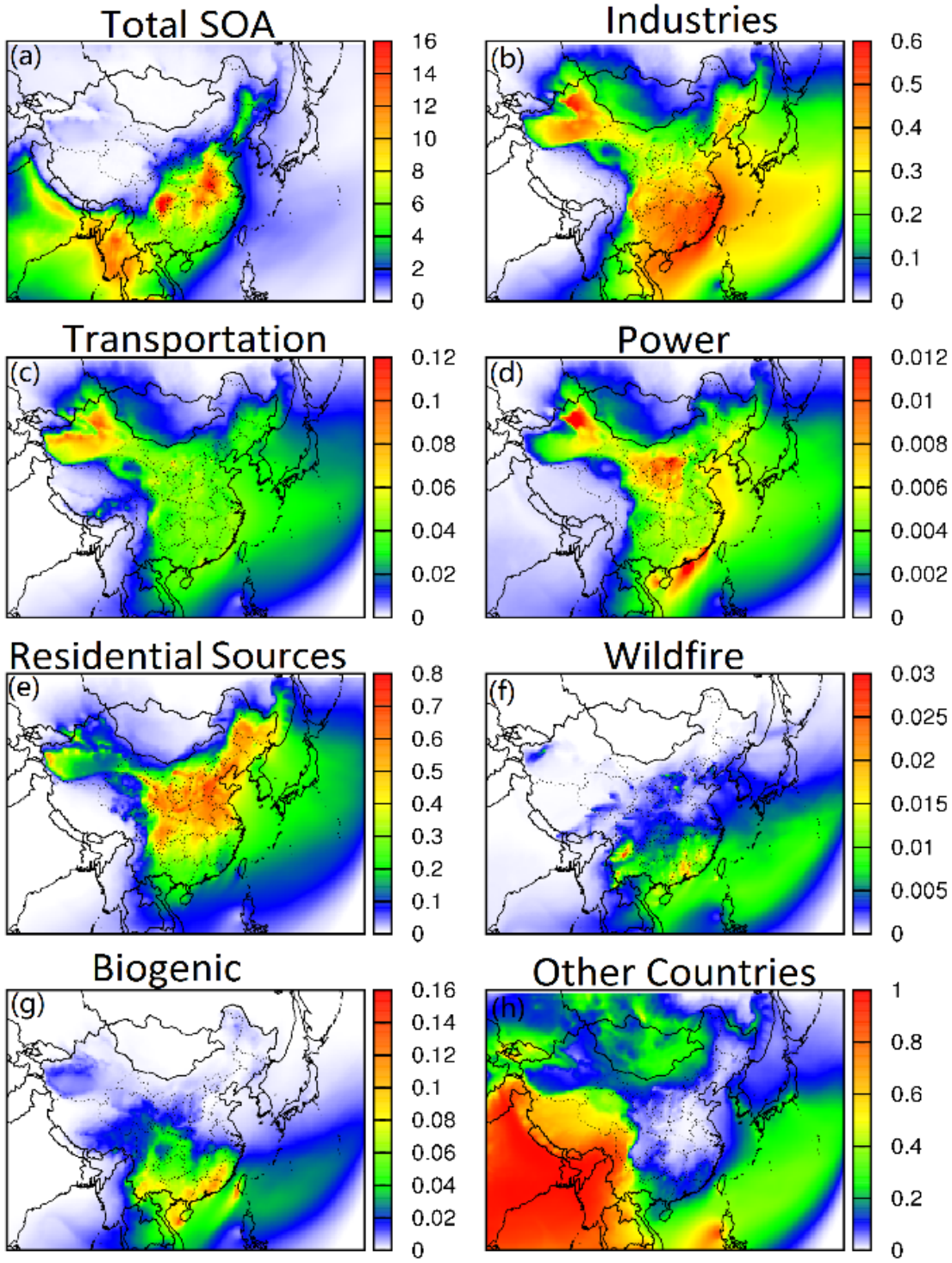


Figure A.4: Predicted winter (December, January and Febrary) average SOA concentration (in $\mu g \cdot m^{-3}$, panel (a)) and fractional contributions due to (b) industries, (c) transportation, (d) power, (e) residential sources, (f) wildfire, (g) biogenic and (h) other countries.

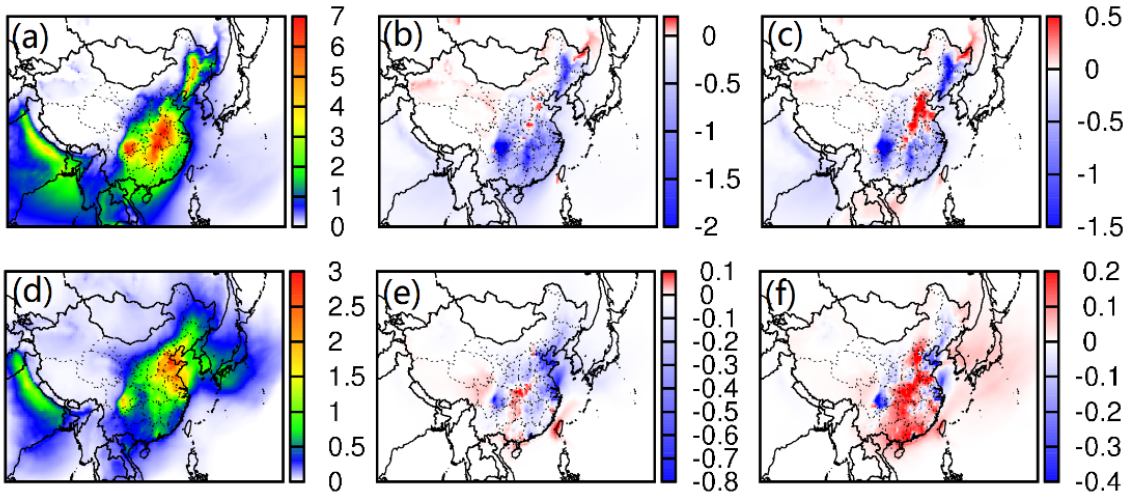


Figure A.5: Predicted (a, d) spatial distribution of SOA from aromatic compounds (excluding those from secondary glyoxal and methylglyoxal) for January and August 2013 using MEIC emission inventory, and change of concentrations due to (b, e) REAS2-a and (c, f) REAS2-b emission inventories. Units are $\mu g \cdot m^{-3}$.

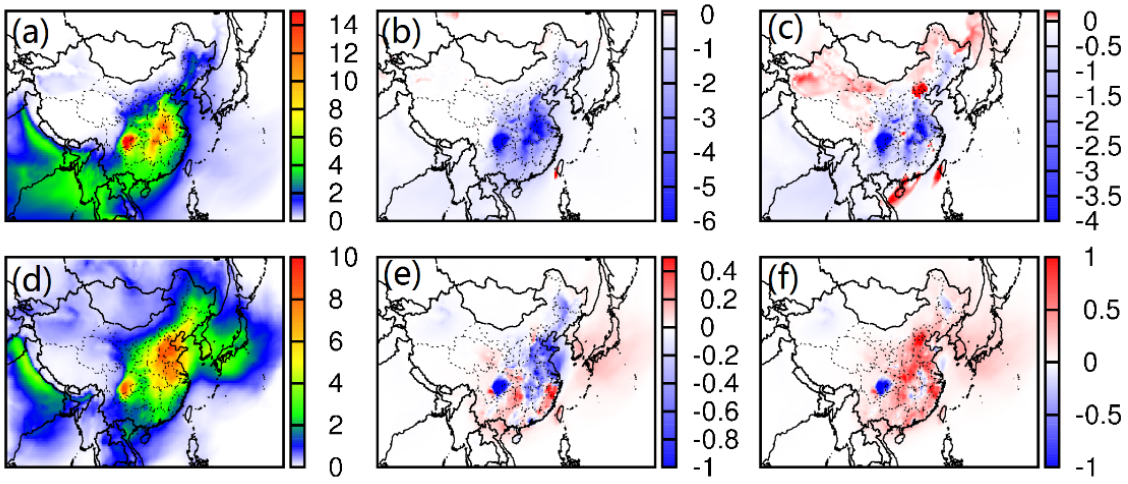


Figure A.6: Predicted (a, d) spatial distribution of SOA from dicarbonyls (primary + secondary, AGLY+AMGLY) for January and August 2013 using MEIC emission inventory, and change of dicarbonyls SOA concentrations due to (b, e) REAS2-a and (c, f) REAS2-b emission inventories. Units are $\mu g \cdot m^{-3}$.

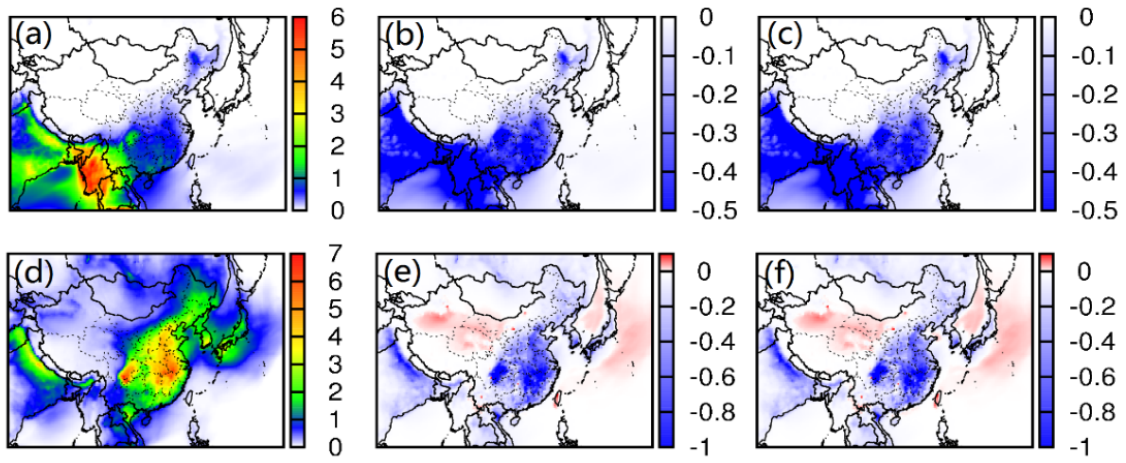


Figure A.7: Predicted (a, d) spatial distribution of biogenic SOA (excluding secondary dicarbonyls, AISO+ASQT+ATRP+AIEMAX+AIEPOX) for January and August 2013 using MEIC emission inventory, and change of biogenic SOA concentrations due to (b, e) REAS2-a and (c, f) REAS2-a emission inventories. Units are $\mu g \cdot m^{-3}$.

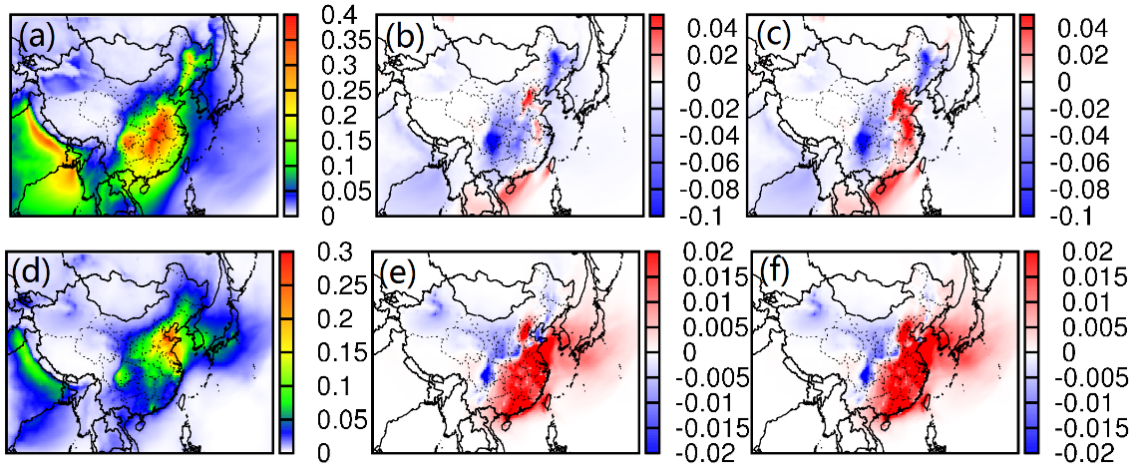


Figure A.8: Predicted (a, d) spatial distribution of long chain alkanes SOA for January and August 2013 using MEIC emission inventory, and change of long chain alkanes SOA concentrations due to (b, e) REAS2-a and (c, f) REAS2-b emission inventories. Units are $\mu g \cdot m^{-3}$.

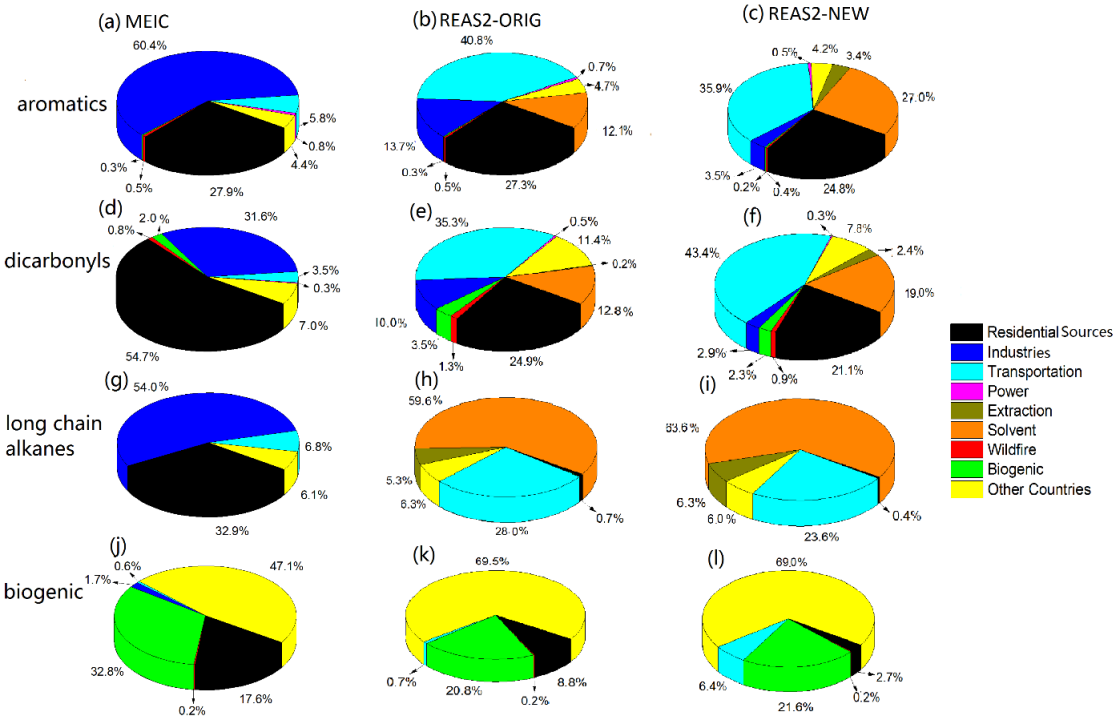


Figure A.9: Predicted fractional source contributions fo different (a-c) aromatics, (d-f) dicarbonyls, (g-i) long chain alkanes and (j-l) biogenic SOA in January 2013 based on MEIC, REAS2-a and REAS2-b emission inventoris (columns).

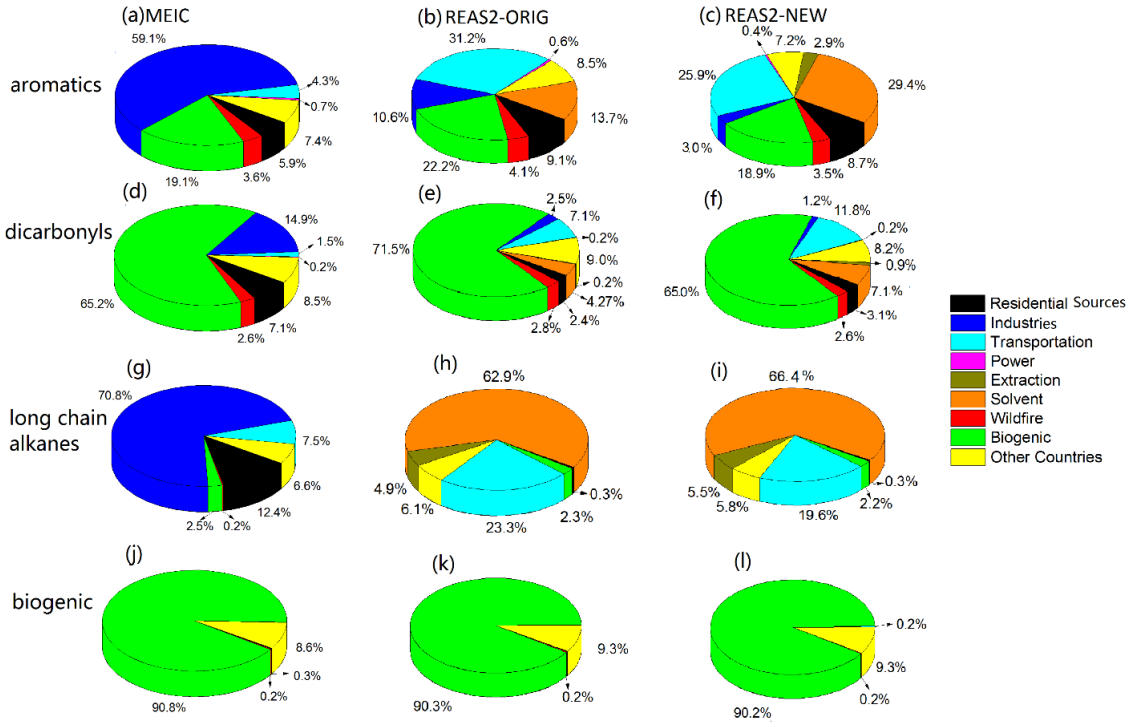


Figure A.10: Predicted fractional source contributions fo different (a-c) aromatics, (d-f) dicarbonyls, (g-i) long chain alkanes and (j-l) biogenic SOA in August 2013 based on MEIC, REAS2-a and REAS2-b emission inventoris (columns).

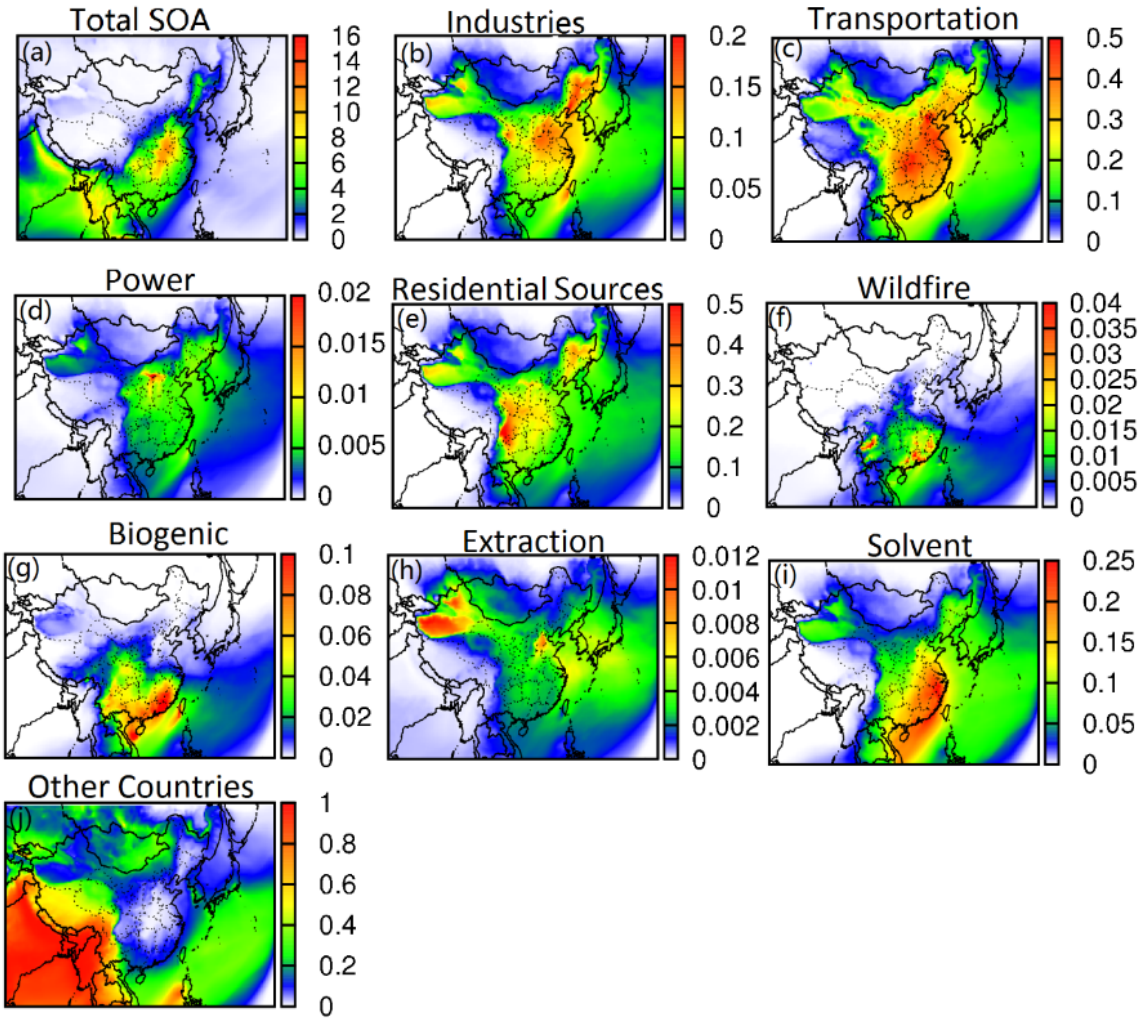


Figure A.11: Predicted average January SOA concentration based on REAS2-a inventory (in $\mu g \cdot m^{-3}$, panel (a)) and fractional source contributions due to (b) industries, (c) transportation, (d) power, (e) residential sources, (f) wildfire, (g) biogenic, (h) extraction, (i) solvent utilization and
(j) other countries.

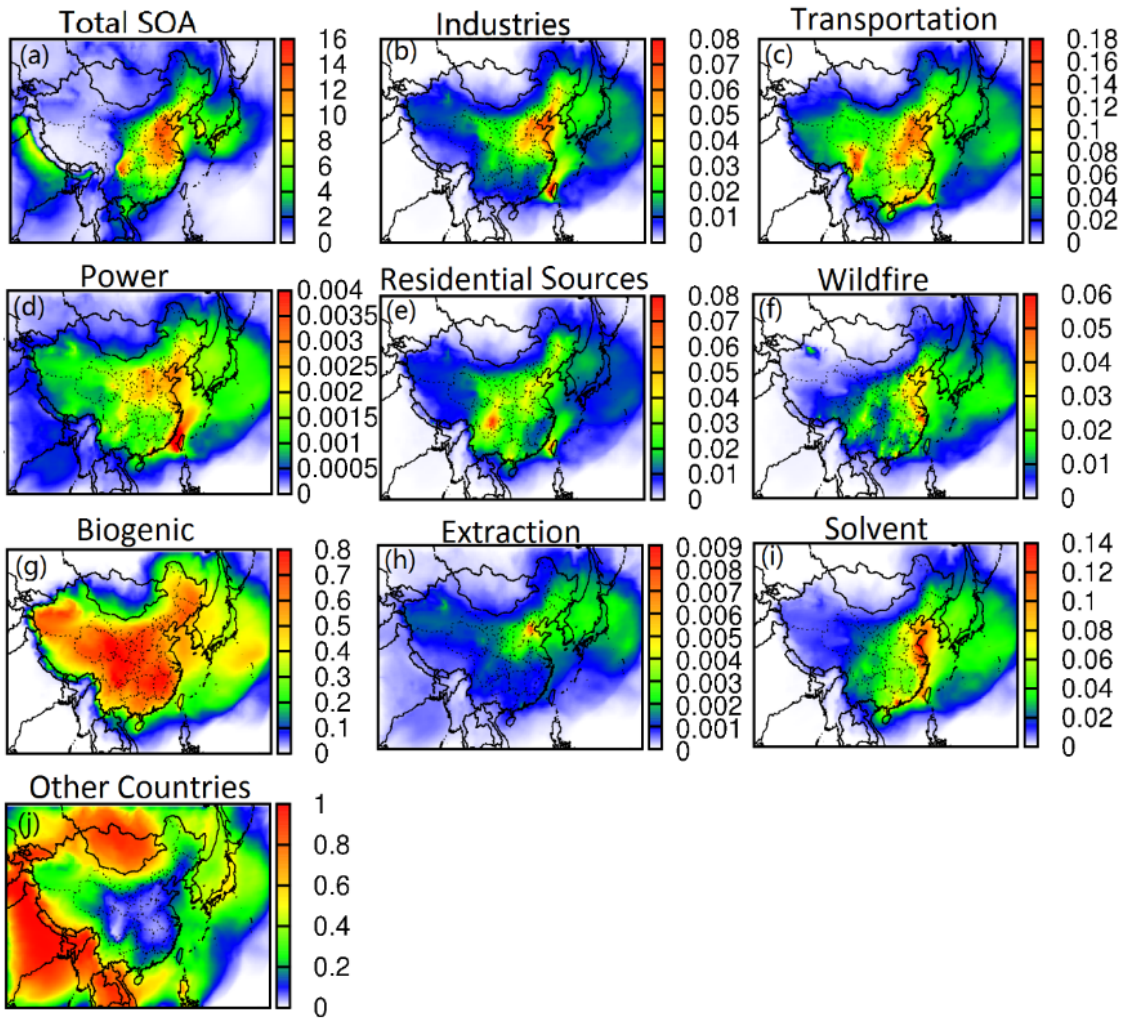


Figure A.12: Predicted August average SOA concentration based on REAS2-a inventory (in $\mu g \cdot m^{-3}$, panel (a)) and fractional source contributions due to (b) industries, (c) transportation, (d) power, (e) residential sources, (f) wildfire, (g) biogenic, (h) extraction, (i) solvent utilization and
(j) other countries.

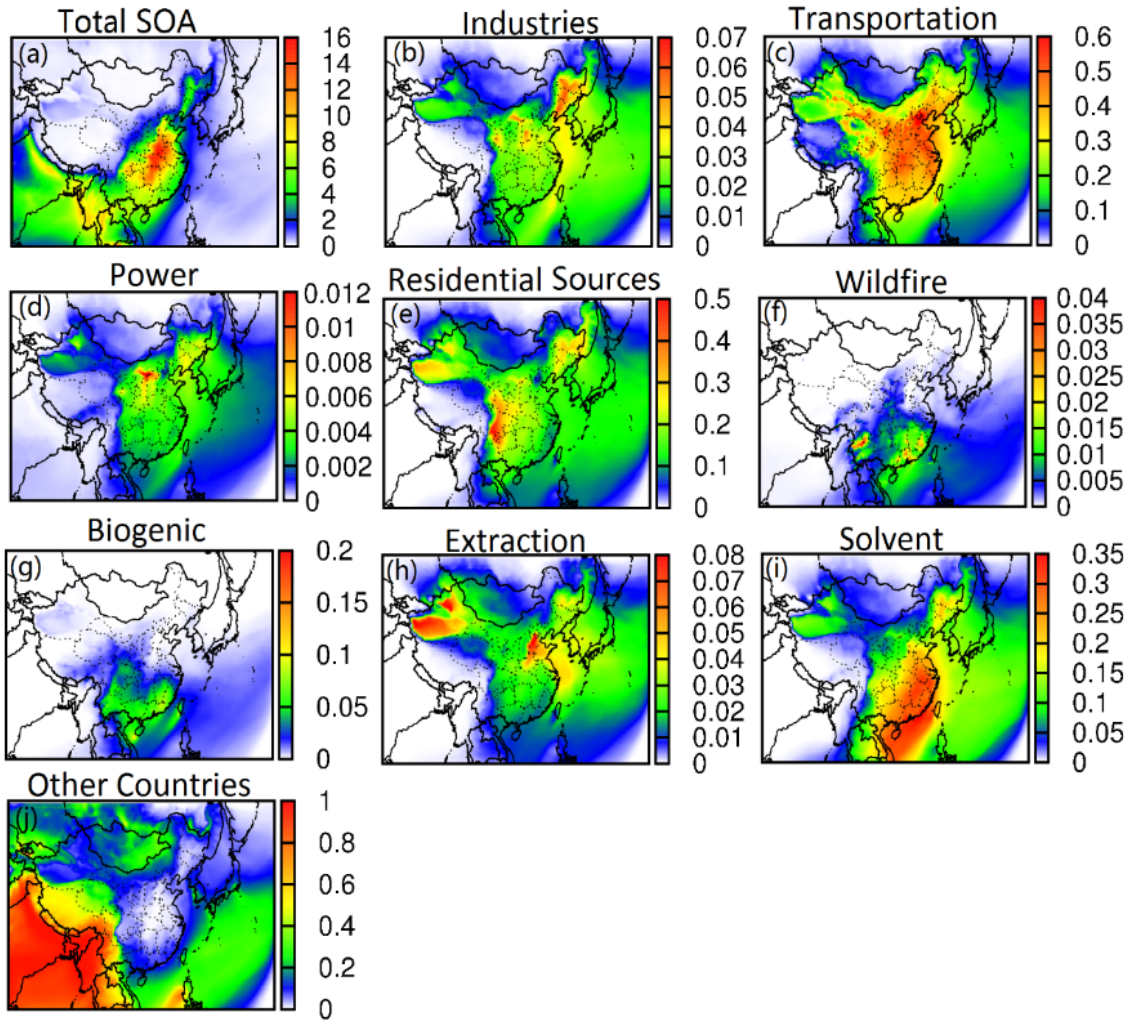


Figure A.13: Predicted January average SOA concentration based on REAS2-b inventory (in $\mu g \cdot m^{-3}$, panel (a)) and fractional source contributions due to (b) industries, (c) transportation, (d) power, (e) residential sources, (f) wildfire, (g) biogenic, (h) extraction, (i) solvent utilization and
(j) other countries.

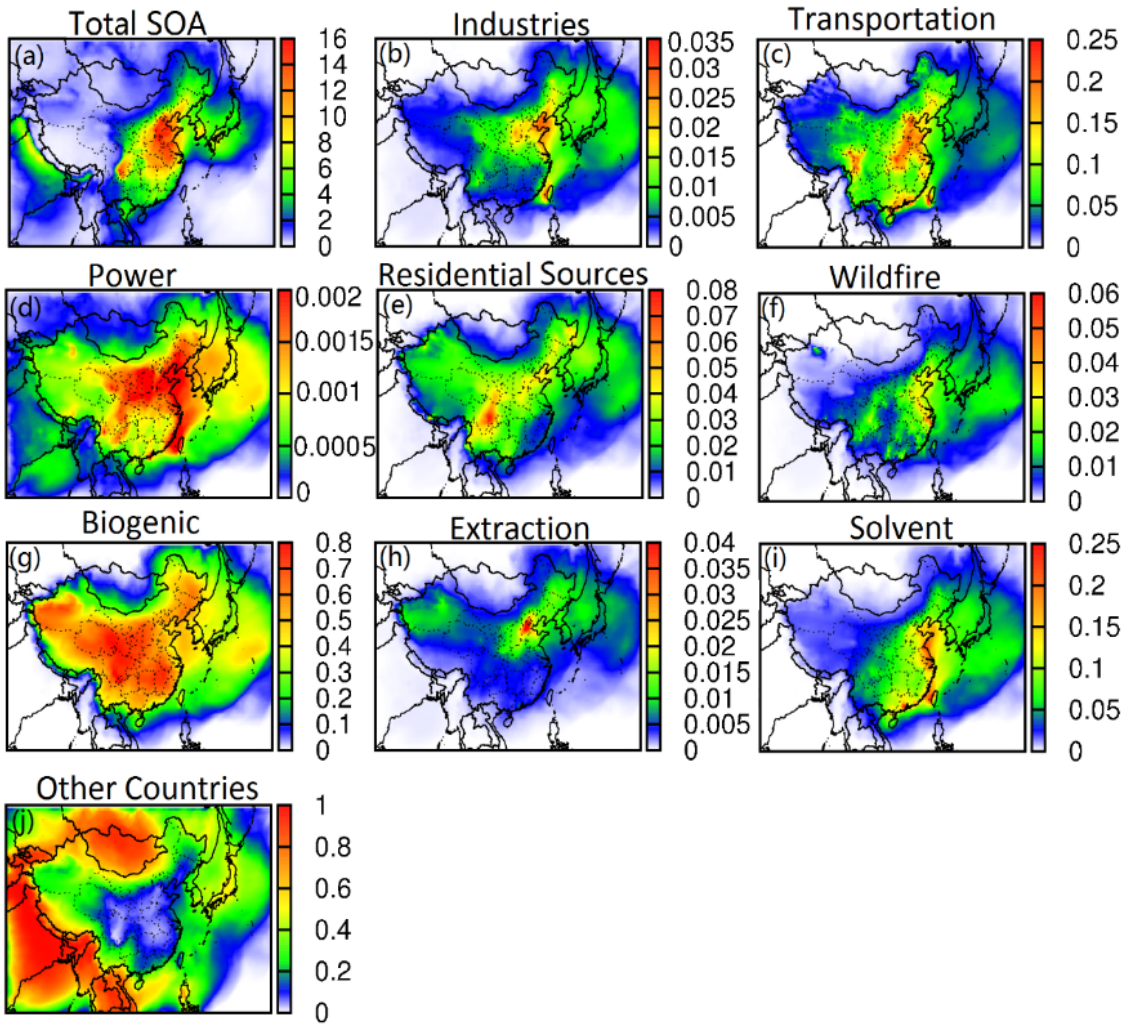


Figure A.14: Predicted August average SOA concentration based on REAS2-b inventory (in $\mu g \cdot m^{-3}$, panel (a)) and fractional source contributions due to (b) industries, (c) transportation, (d) power, (e) residential sources, (f) wildfire, (g) biogenic, (h) extraction, (i) solvent utilization and
(j) other countries.

APPENDIX B

# SUPPLEMENTARY MATERIAS OF ATTRIBUTION OF TROPOSPHERIC OZONE TO NOX AND VOC EMISSIONS: CONSIDERING OZONE FORMATION IN THE TRANSITION REGIME

Table B.1: Indicator threshold values for the start (Rts) and end (Rte) of the transition regime, based on 10%, 20% and 40% increase of NOx and VOCs.

| | | | $R_ts$ | | |
|---|---|---|---|---|---|
| | 10% | 20% | 40% | Avg. | Std. |
| R1 | 0.042 | 0.045 | 0.054 | 0.047 | 0.006 |
| R2 | 0.027 | 0.033 | 0.038 | 0.033 | 0.006 |
| R3 | 4.896 | 4.967 | 5.313 | 5.059 | 0.223 |
| R4 | 0.293 | 0.300 | 0.315 | 0.303 | 0.011 |
| R5 | 0.129 | 0.138 | 0.150 | 0.139 | 0.011 |
| | | | $R_te$ | | |
| | 10% | 20% | 40% | Avg. | Std. |
| R1 | 5.611 | 4.846 | 4.970 | 5.142 | 0.411 |
| R2 | 3.476 | 3.125 | 3.144 | 3.248 | 0.197 |
| R3 | 32.892 | 28.897 | 30.401 | 30.730 | 2.018 |
| R4 | 1.306 | 1.225 | 1.250 | 1.260 | 0.041 |
| R5 | 1.357 | 1.226 | 1.273 | 1.285 | 0.066 |

Table B.2: List of VOC species used in the S11L mechanism in this study*.

| S11L Name | Species |
|---|---|
| ACET | Acetone |
| ALK1 | Alkanes and other non-aromatic compounds that react only with OH, and have kOH between 2 and $5 \times 10^2$ ppm$^{-1}$ min$^{-1}$ |
| ALK2 | Alkanes and other non-aromatic compounds that react only with OH, and have kOH between $5 \times 10^2$ and $2.5 \times 10^3$ ppm$^{-1}$ min$^{-1}$ |
| ALK3 | Alkanes and other non-aromatic compounds that react only with OH, and have kOH between $2.5 \times 10^3$ and $5 \times 10^3$ ppm$^{-1}$ min$^{-1}$ |
| ALK4 | Alkanes and other non-aromatic compounds that react only with OH, and have kOH between $5 \times 10^3$ and 1 x 104 ppm$^{-1}$ min$^{-1}$ |
| ALK5 | Alkanes and other non-aromatic compounds that react only with OH, and have kOH greater than 1 x 104 ppm$^{-1}$ min$^{-1}$ |
| ARO1 | Aromatics with kOH < $2 \times 10^4$ ppm$^{-1}$ min$^{-1}$ |
| ARO2 | Aromatics with kOH > $2 \times 10^4$ min$^{-1}$ |
| BACL | Biacetyl |
| BALD | Aromatic aldehydes |
| CCHO | Acetaldehyde |
| CCOOH | Acetic Acid. |
| CRES | Cresols |
| HCHO | Formaldehyde |
| ETHE | Ethene |
| GLY | Glyoxal |
| HCOOH | Formic Acid |
| ISOP | Isoprene |
| IPRD | Lumped isoprene product species |
| MACR | Methacrolein |
| MEK | Ketones and other non-aldehyde oxygenated products which react with OH radicals faster than $5 \times 10^{-13}$ but slower than $5 \times 10^{-12}$ cm$^3$ molec$^{-2}$ sec$^{-1}$ |
| MEOH | Methanol |
| MGLY | Methyl Glyoxal |
| MVK | Methyl Vinyl Ketone |
| OLE1 | Alkenes (other than ethene) with kOH < $7 \times 10^4$ ppm$^{-1}$ min$^{-1}$ |
| OLE2 | Alkenes with kOH > $7 \times 10^4$ ppm$^{-1}$ min$^{-1}$ |
| PHEN | Phenol |
| PROD2 | Ketones and other non-aldehyde oxygenated products which react with OH radicals faster than $5 \times 10^{-12}$ cm$^3$ molec$^{-2}$ sec$^{-1}$ |
| RCHO | Lumped C3+ Aldehydes |
| RCOOH | Higher organic acids and peroxy acids |
| TERP | Terpenes |
| RNO3 | Lumped Organic Nitrates |
| SESQ | Sesquiterpenes |

*: From http:www.engr.ucr.edu∼carterSAPRCsaprc11.pdf

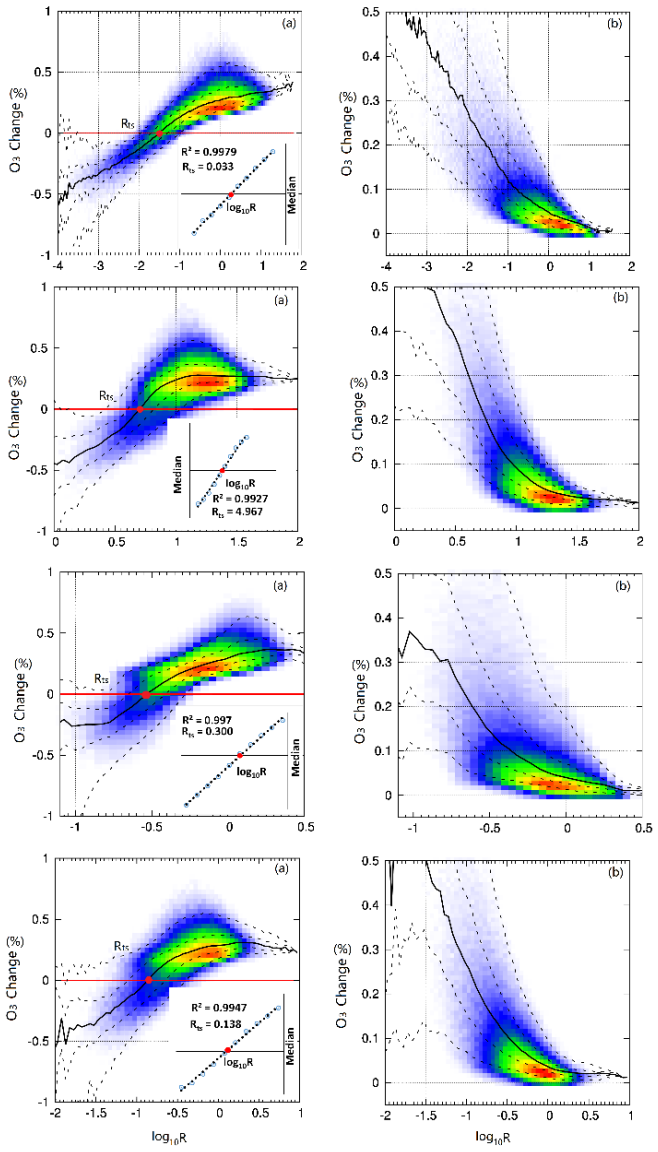


Figure B.1: Relative change of O3 with respect to indicator R2-R5 (log scale) due to 20% increase of (a) NOx and (b) primary VOCs based on hourly predicted concentrations at 10 am, noon and 2 pm in August 2013. All grid cells at the surface level with net O3 formation (defined as >1% ozone increase in a 10-minute simulation using the concentrations from the base case) are included. The solid black line is the median value of $O_3$ change, and the dashed lines show the 95, 75, 25, and 5 percentile values from top to bottom. The color shows the relative frequency of occurrence of the data.

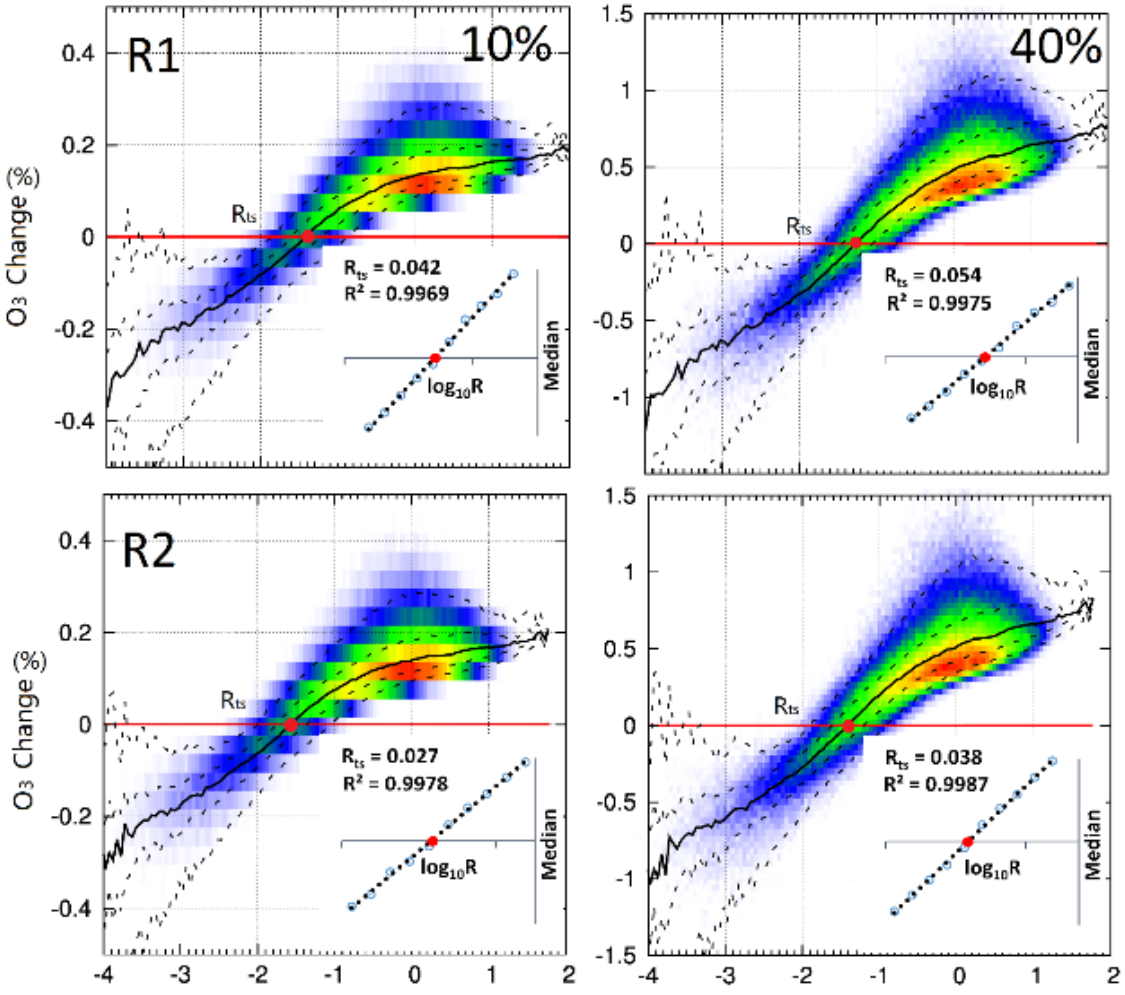


Figure B.2: Relative changes of ozone with respect to indicators R1 and R2 (in log scale) from sensitivity simulations with 10% and 40% NOx increase. The start of the transition regime is illustrated on each panel.

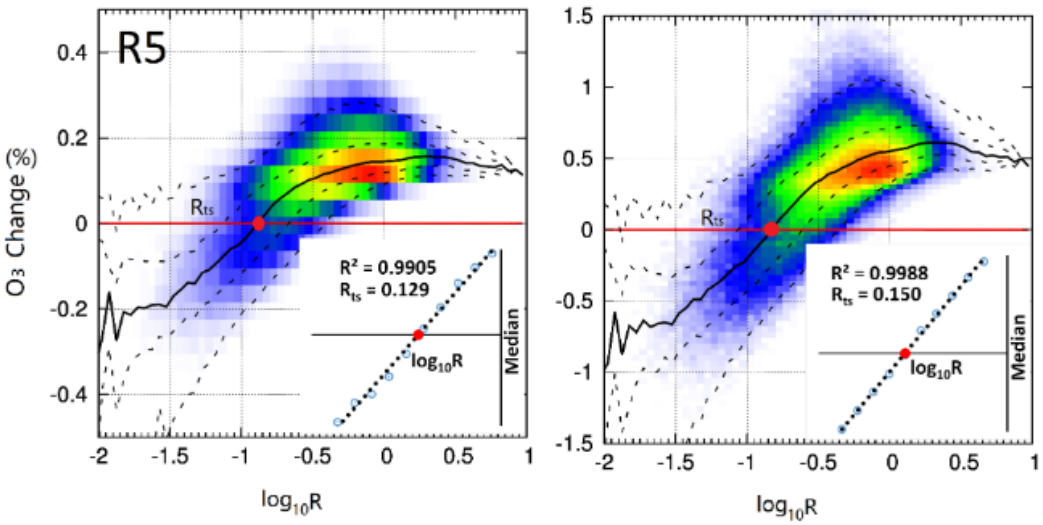


Figure B.3: Same as Figure 2-a, for indicators R3 -R5.

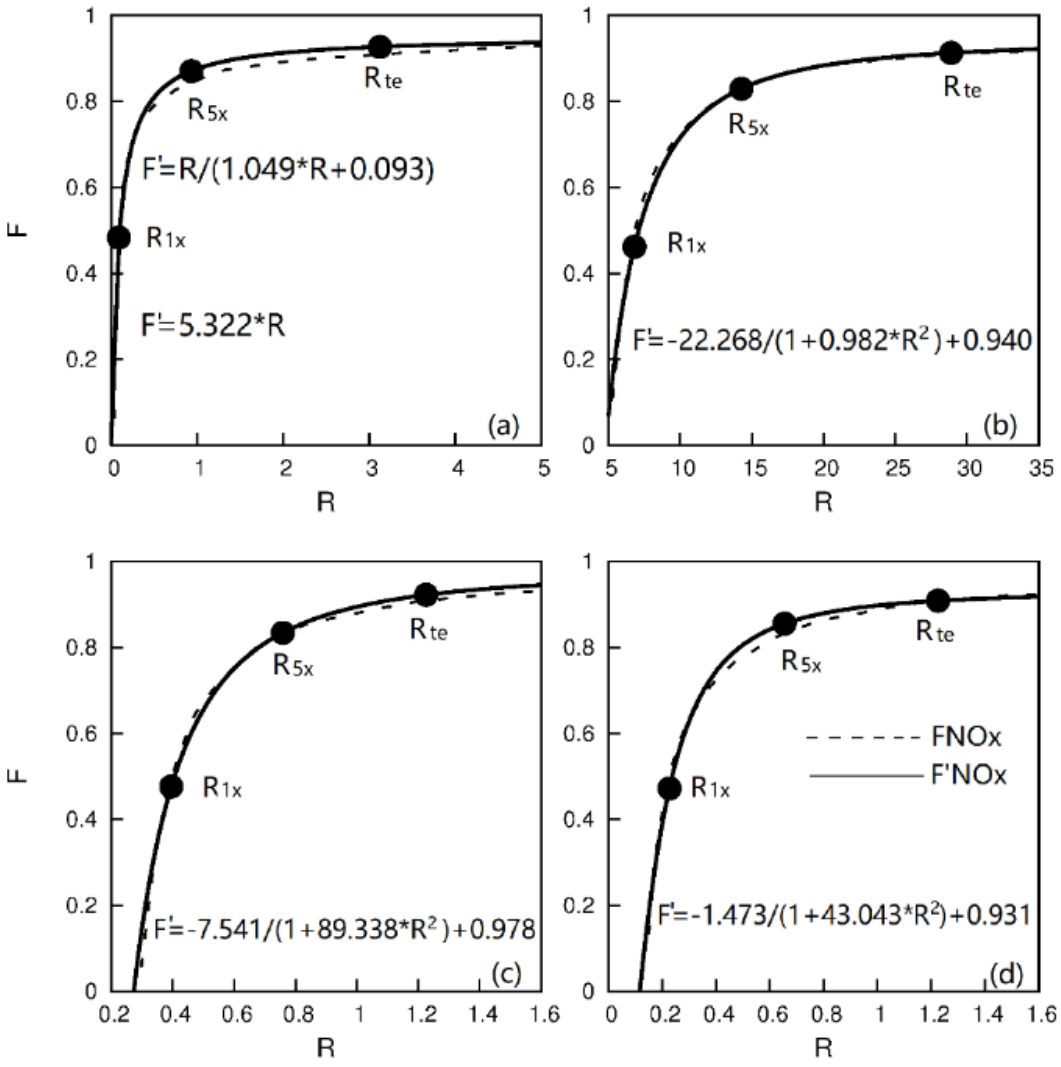


Figure B.4: Fraction of $O_3$ formation in the transition regime due to $NO_x$ ($F_{NO_x}$) based on the sensitivity calculations (dashed line) and fitted equations (solid line) of (a) R2, (b) R3, (c) R4, and (d) R5.

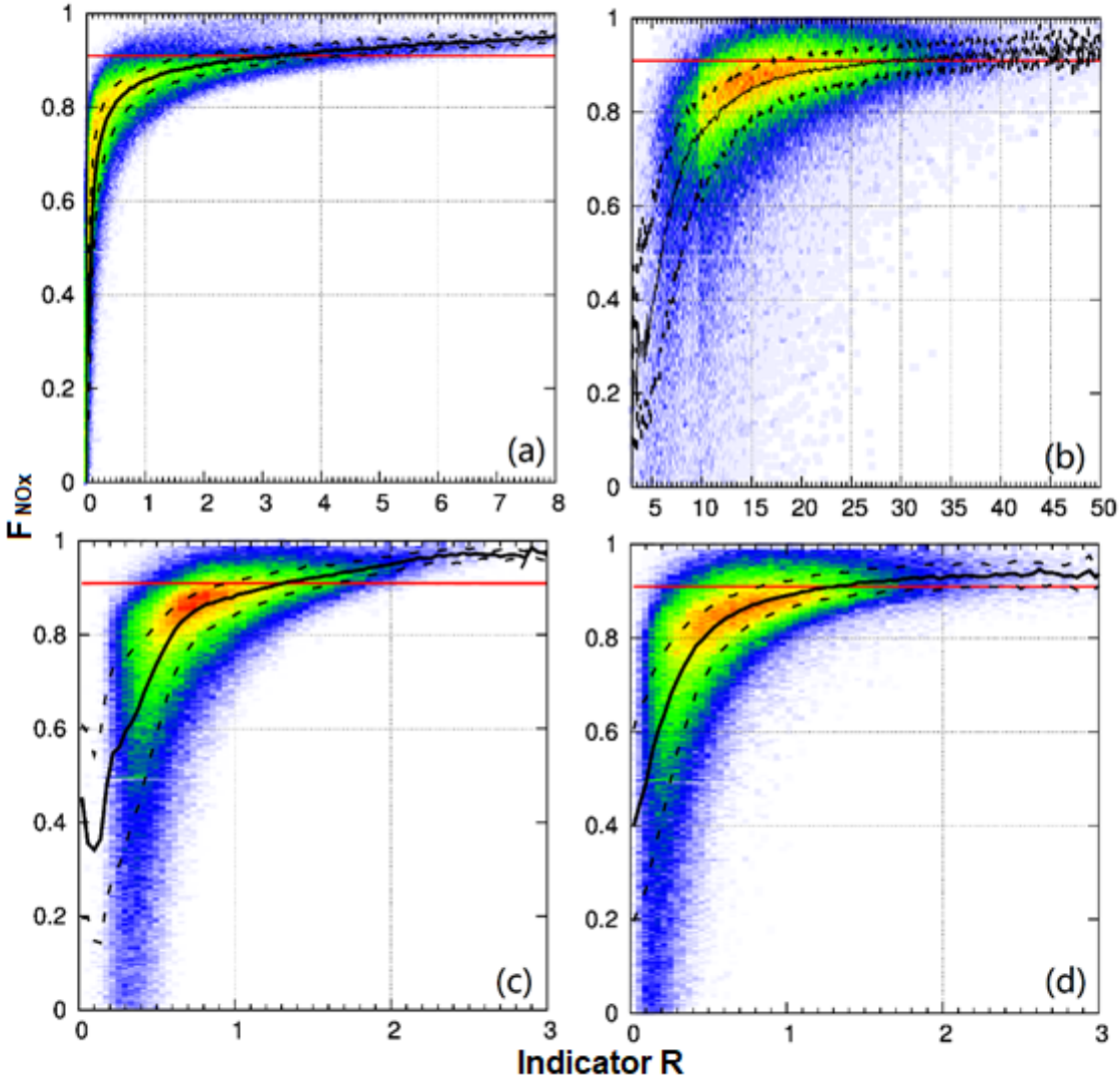


Figure B.5: Rte spread for (a) R2, (b) R3, (c) R4, and (d) R5.

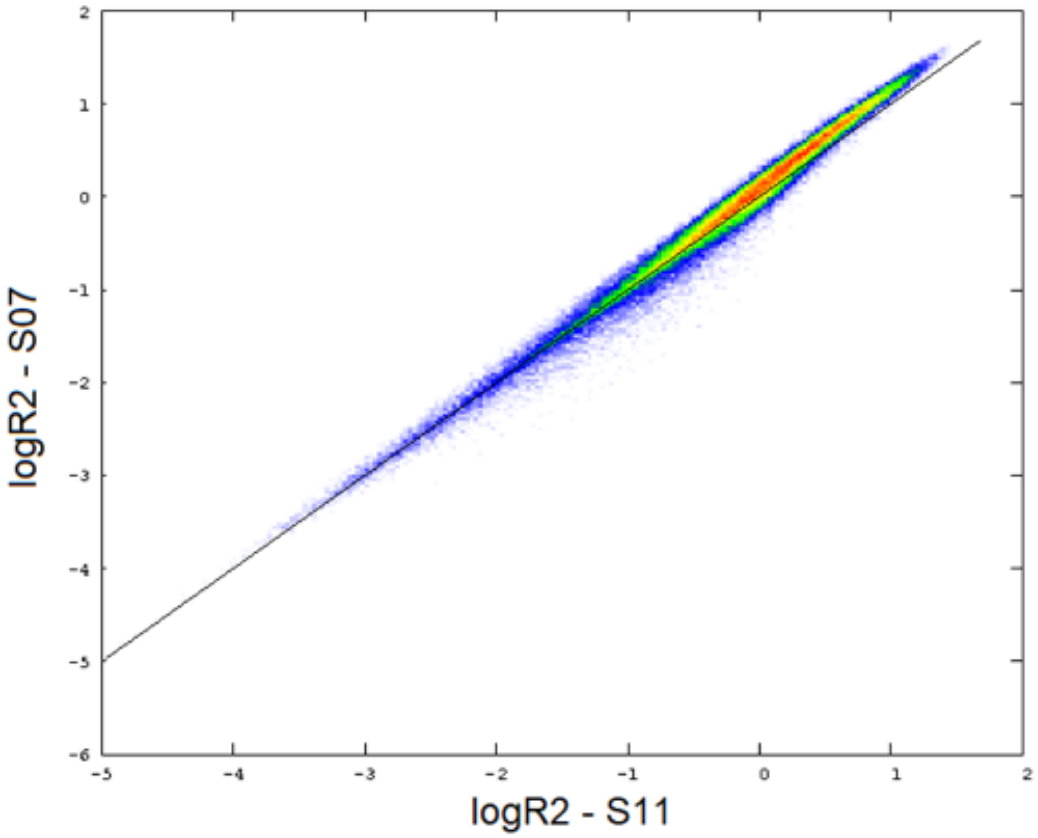


Figure B.6: Two-dimensional histogram comparison of indicator R2 (pH2O2/pHNO3) based on SAPRC-11 (S11) and SARPC-07 (S07) for the same grid cells with >1% ozone formation in the baseline simulation. Color represents frequency of occurrence with red color represent higher frequencies. Solid line represents 1:1 ratio.

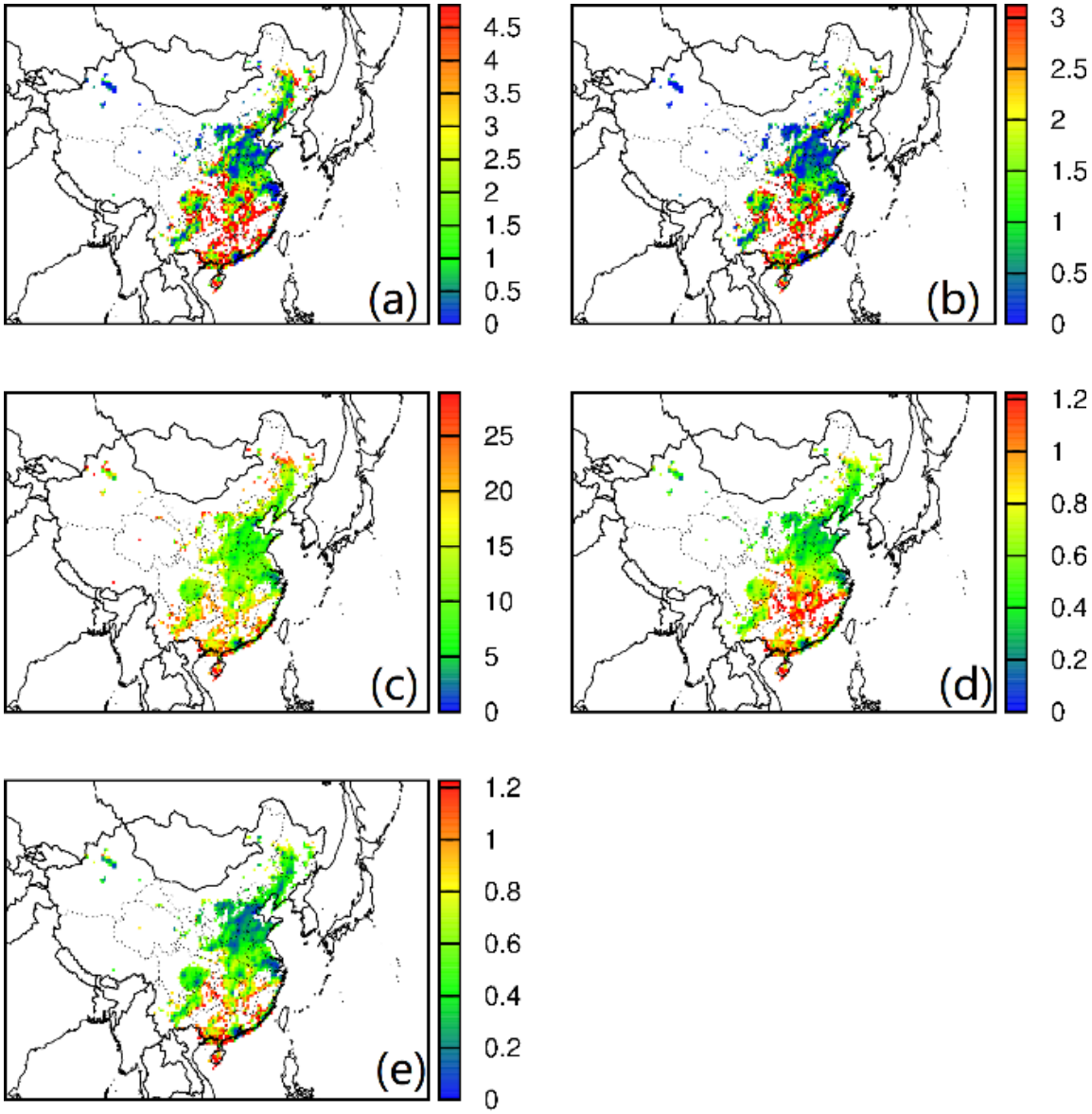


Figure B.7: Predicted monthly average R values for (a) R1, (b) R2, (c) R3, (d) R4, and (e) R5 in August 2013 based on hours 0800-1600.

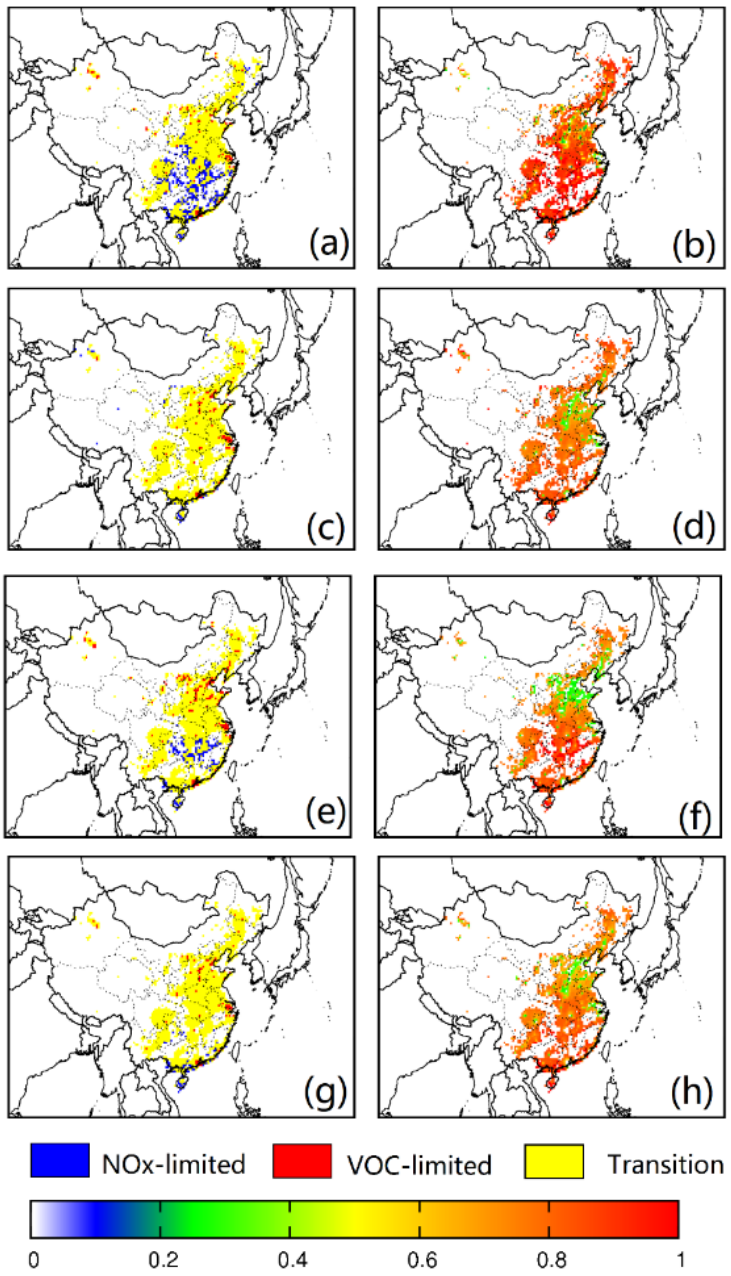


Figure B.8: Predicted monthly average O3 sensitivity regimes results (a), (b), (d), (f), and (h) for R0, R2, R3, R4, and R5 and FâĂŹNOx results (c), (e), (g), and (i) for R0, R2, R3, R4, and R5 in August, 2013 noon time. The blank areas mean there is no net $O_3$ formation (($O_{3,basecase}O_{3,initialcondition}$ /$O_{3,initialcondition}$ < %).

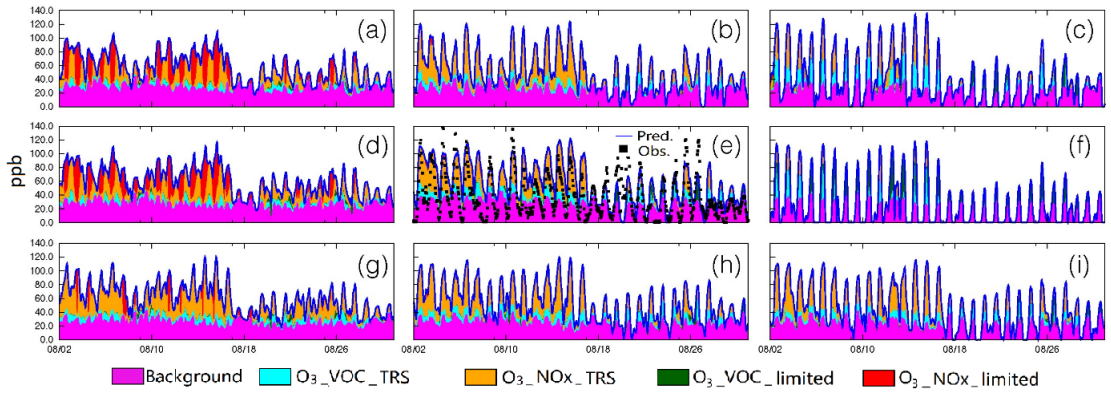


Figure B.9: Time series of $O_3$ attributed to VOC and $NO_x$ based on the three-regime approach and indicator R1 for the urban Beijing grid cell (panel (e)) and eight other surrounding grid cells in August 2013. Units are ppb. Background ozone is estimated by subtracting the concentrations of the four different ozone attribution tracers from the total ozone.

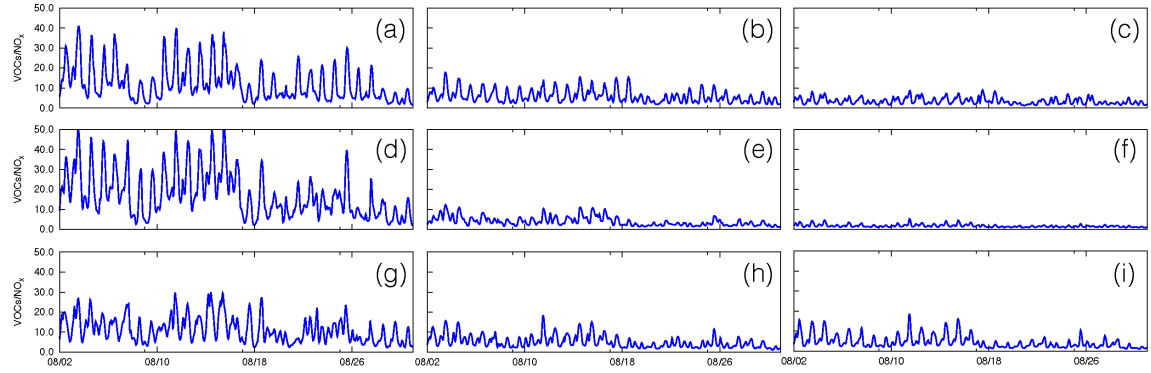


Figure B.10: Time series of molar ratio of VOCs to NOx in the grid cells surrounding the urban Beijing site (panel (e)) in August 2013. The VOCs included in the calculations are: ACET, ALK1, ALK2, ALK3, ALK4, ALK5, ACET, ARO1, ARO2, ETHE, ISOP, GLY, TERP, HCOOH, MGLY, SESQ, OLE1, OLE2, RNO3, and MEOH.

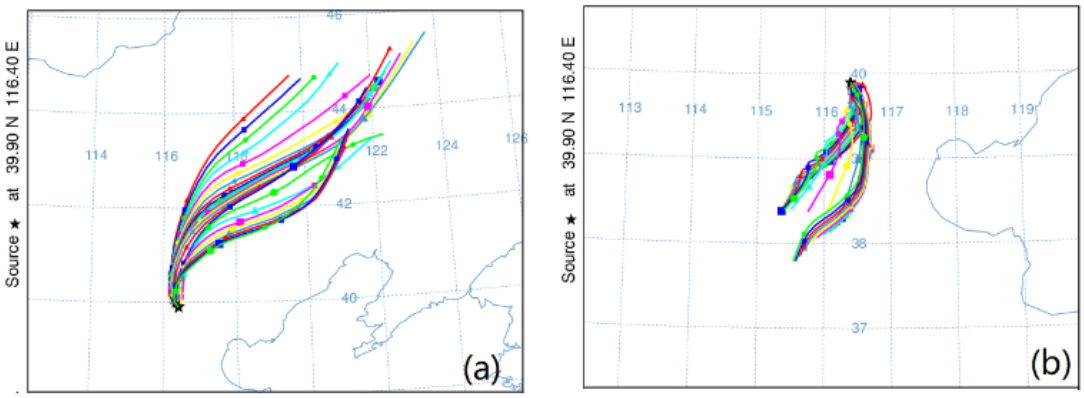


Figure B.11: 24-hour back-trajectory of air parcels ending at the urban Beijing grid cell 100 m above surface at each hour on (a) August 11, and (b) August 21, 2013, estimated by the Hybrid Single Particle Lagrangian Integrated Trajectory Model (HYSPLIT, https://ready.arl.noaa.gov/HYSPLIT.php).

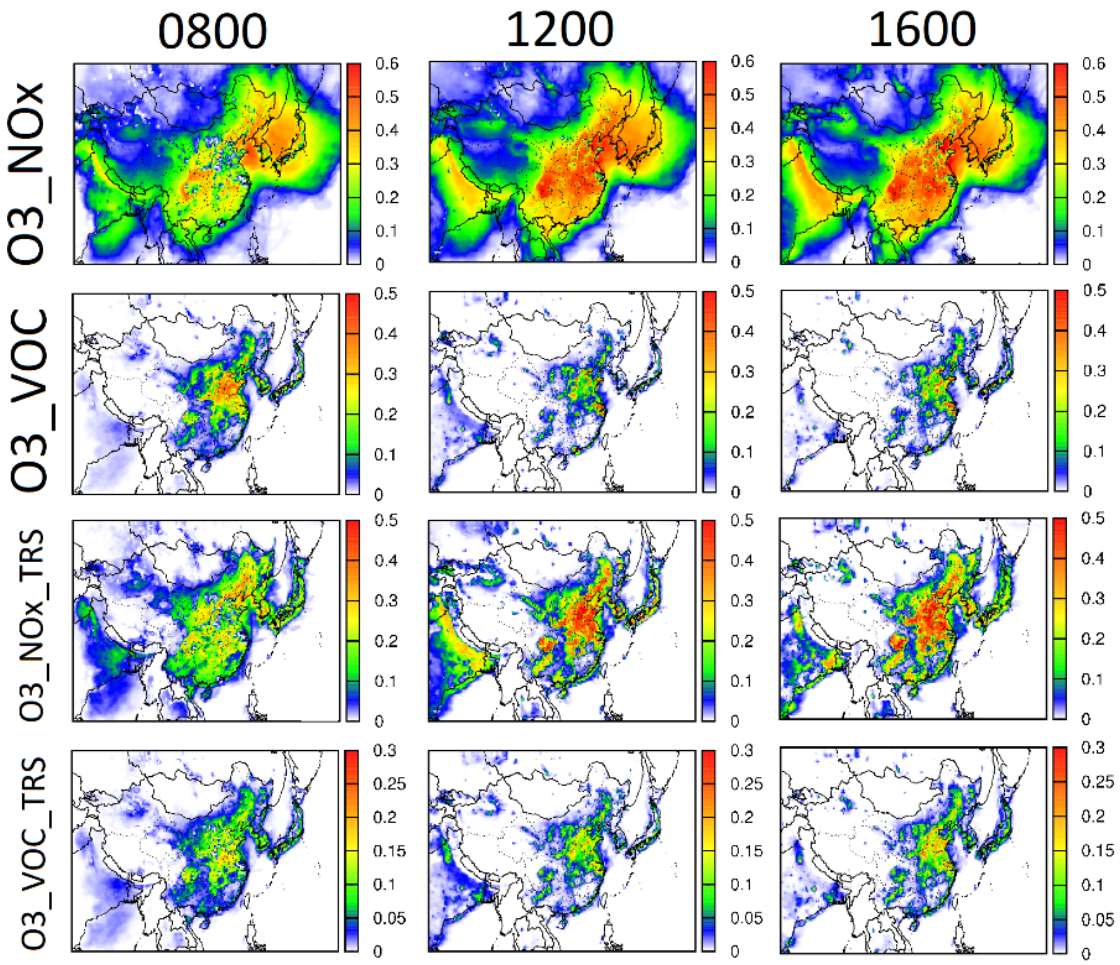


Figure B.12: Predicted monthly average fraction of hourly (a) $O_3$_NOx, (b) $O_3$N_TRS, (c) $O_3$_VOC, and (d) $O_3$V_TRS in total $O_3$ concentration at 8 am, 10 am and 10 pm in August 2013.

# APPENDIX C

## SUPPLEMENTARY MATERIAS OF SOURCE APPORTIONMENT OF SUMMERTIME OZONE IN CHINA USING A SOURCE-ORIENTED CHEMICAL TRANSPORT MODEL

Table C.1: Maximum ozone incremental reactivity (MIR) (mol/mol) for VOC species used in this study

| Species | CMAQ | MIR[1] |
|---|---|---|
| Alkanes and other non-aromatic compounds that react only with OH, and have kOH between 2 and $5 \times 10^2$ ppm$^{-1}$ min$^{-1}$ | ALK1* | 0.39 |
| kOH $5 \times 10^2$ - $2.5 \times 10^3$ ppm$^{-1}$ min$^{-1}$ | ALK2* | 0.80 |
| kOH $2.5 \times 10^3$ - $5 \times 10^3$ ppm$^{-1}$ min$^{-1}$ | ALK3* | 2.19 |
| kOH $5 \times 10^3$ - $1 \times 10^4$ ppm$^{-1}$ min$^{-1}$ | ALK4* | 3.11 |
| kOH > $1 \times 10^4$ ppm$^{-1}$ min$^{-1}$ | ALK5* | 4.95 |
| Ethene | ETHE* | 5.44 |
| Alkenes (other than ethene) with kOH < $7 \times 10^4$ ppm$^{-1}$ min$^{-1}$ | OLE1* | 9.73 |
| kOH > $7 \times 10^4$ ppm$^{-1}$ min$^{-1}$ | OLE2* | 10.98 |
| Isoprene | ISOP | 12.62 |
| Terpenes | TERP* | 8.54 |
| Gyloxal | GLY* | 14.22 |
| Methylglyoxal | MGLY* | 16.21 |
| Aromatics with kOH < $2 \times 10^4$ ppm$^{-1}$ min$^{-1}$ | ARO1* | 6.72 |
| kOH > $2 \times 10^4$ ppm$^{-1}$ min$^{-1}$ | ARO2* | 15.36 |
| Formaldehyde | HCHO* | 6.49 |
| Acetaldehyde | CCHO* | 5.79 |
| Lumped C3+ Aldehydes | RCHO* | 9.45 |
| Methanol | MEOH* | 1.34 |

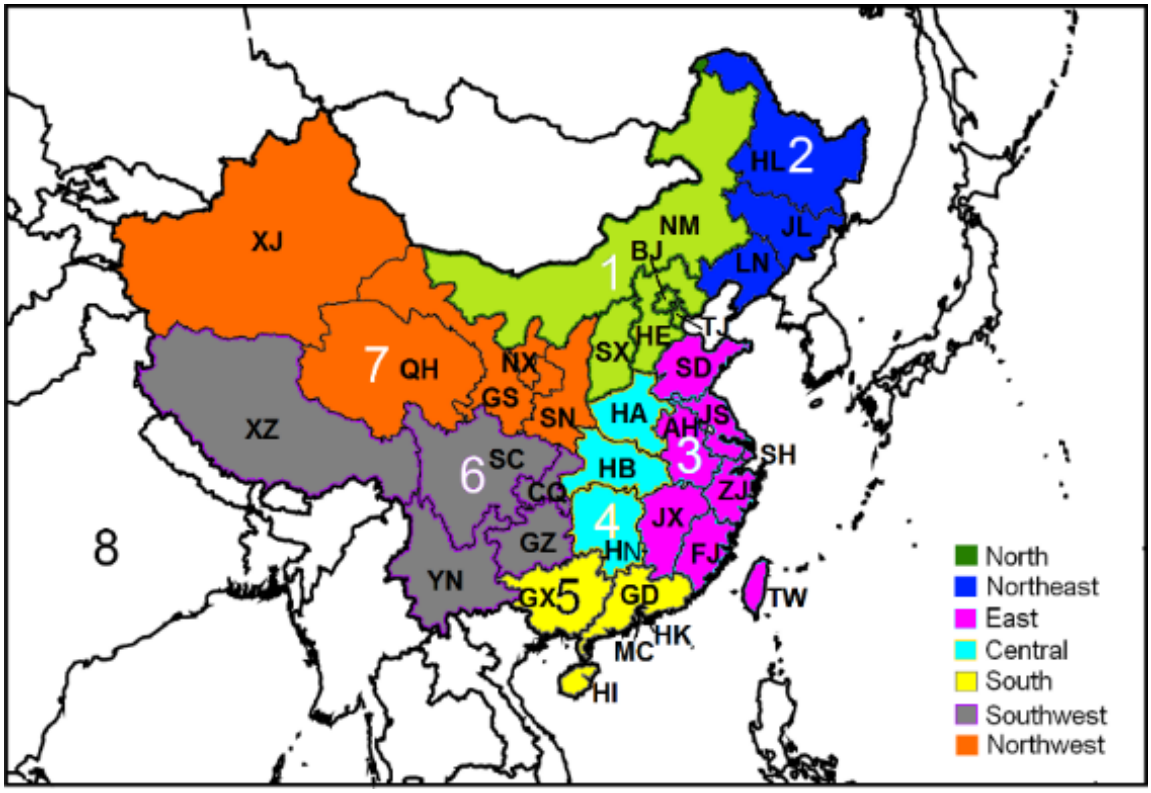


Figure C.1: China provinces map.

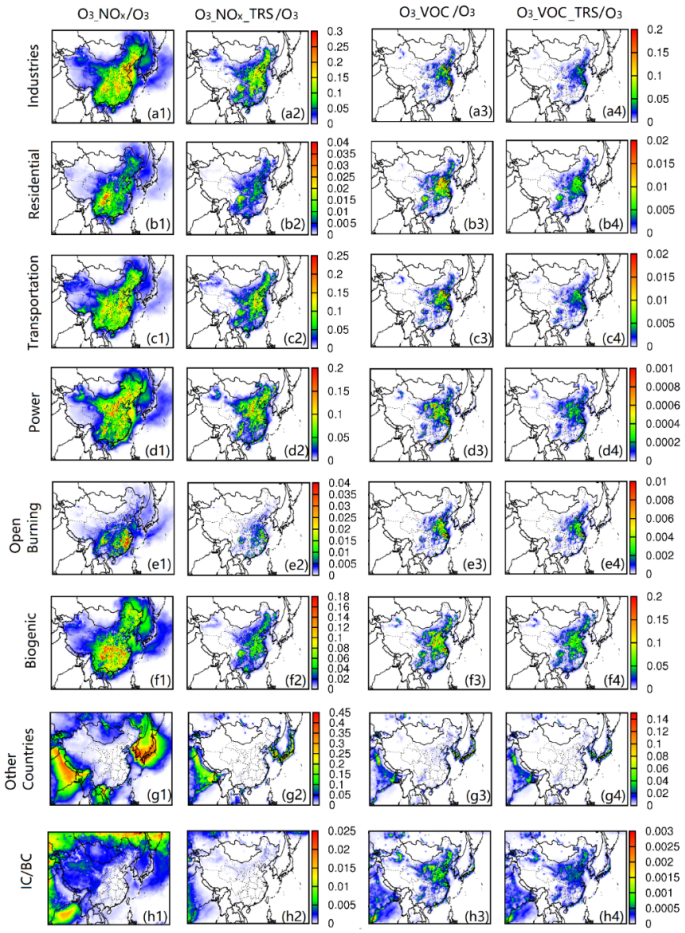


Figure C.2: Average source contributions to 8-hr ozone attributed to $NO_x$ ($O_3$_$NO_x$, column 1), VOCs ($O_3$_VOC, column 3), and to 8-hr ozone formed in the transition regime attributed to $NO_x$ ($O_3$_$NO_x$_TRS, column 2) and VOCs ($O_3$_VOC_TRS, column 4). Emissions from different sectors in other counties are combined and considered as a single class. The IC/BC contributions are ozone formed attributed to $NO_x$ and VOCs entered the domain through initial and boundary conditions. Ozone directly enters the domain though initial and boundary conditions are referred to as "background" ozone and is not included in the IC/BC class.

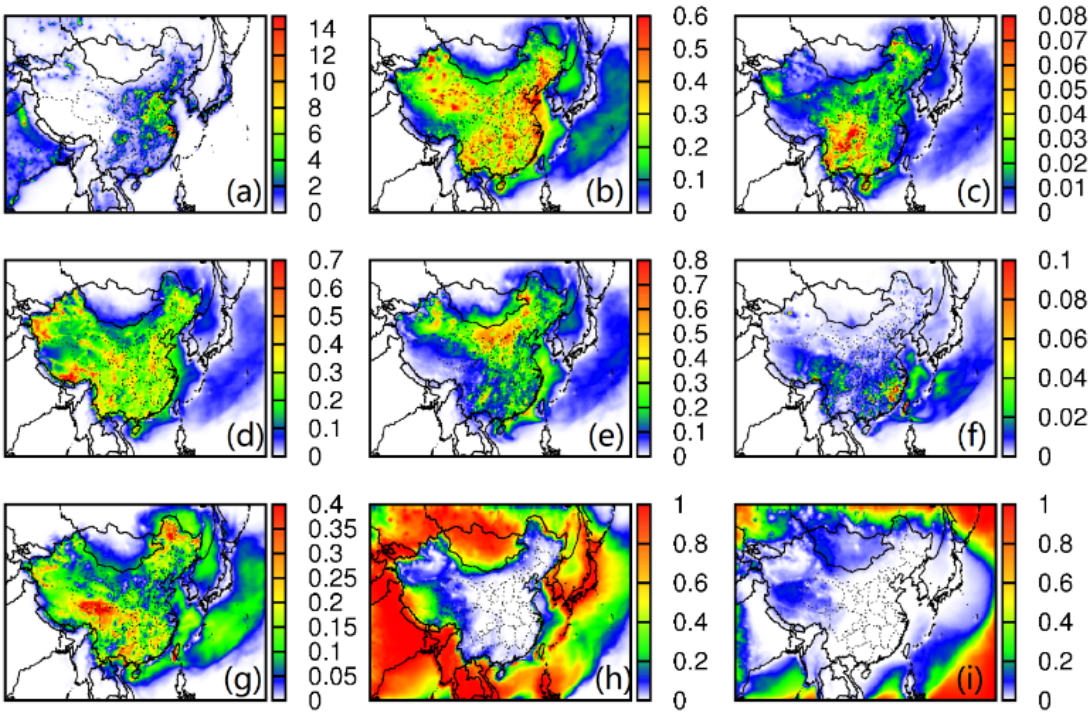


Figure C.3: Predicted 8-hour average NO2 concentration (in ppb, panel (a)) and fractional source contributions due to (b) industries, (c) residential, (d) transportation, (e) power, (f) wildfire, (g) biogenic, (h) other countries and (i) IC/BC.

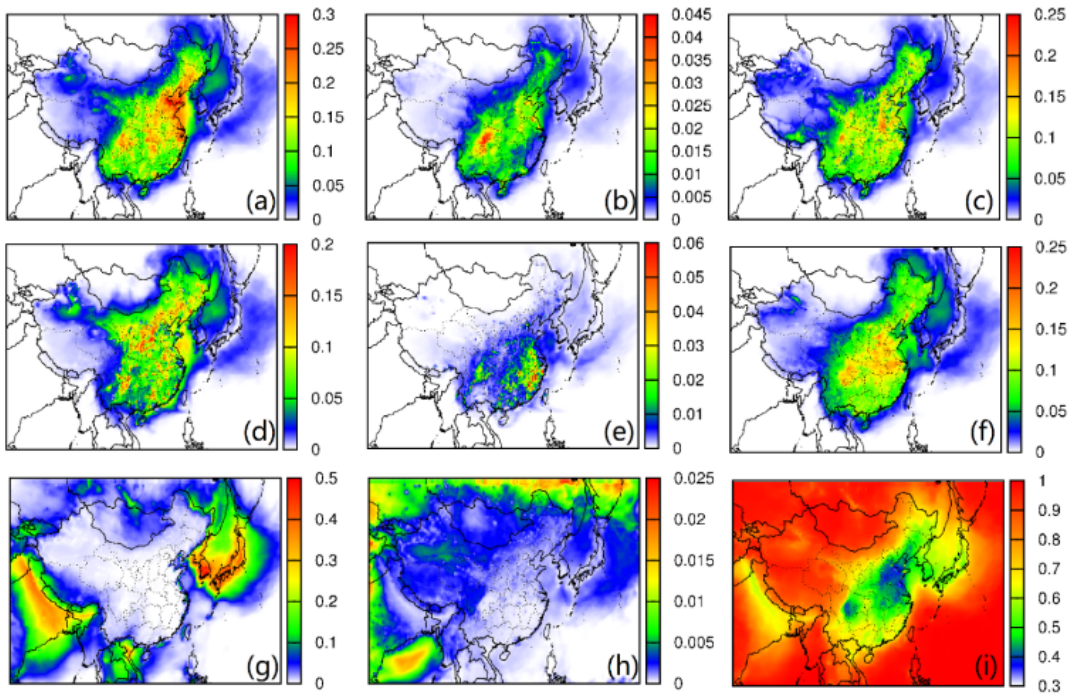


Figure C.4: Monthly average fractional contributions to 8-hr ozone attributed to $NO_x$ and VOCs ($O_3$_$NO_x$ + $O_3$_VOC) emitted from (a) industry, (b) residential, (c) transportation, (d) power, (e) open burning, (f) biogenic, (g) other countries and (h) initial and boundary conditions. Estimated concentrations of background ozone are shown in panel (i).

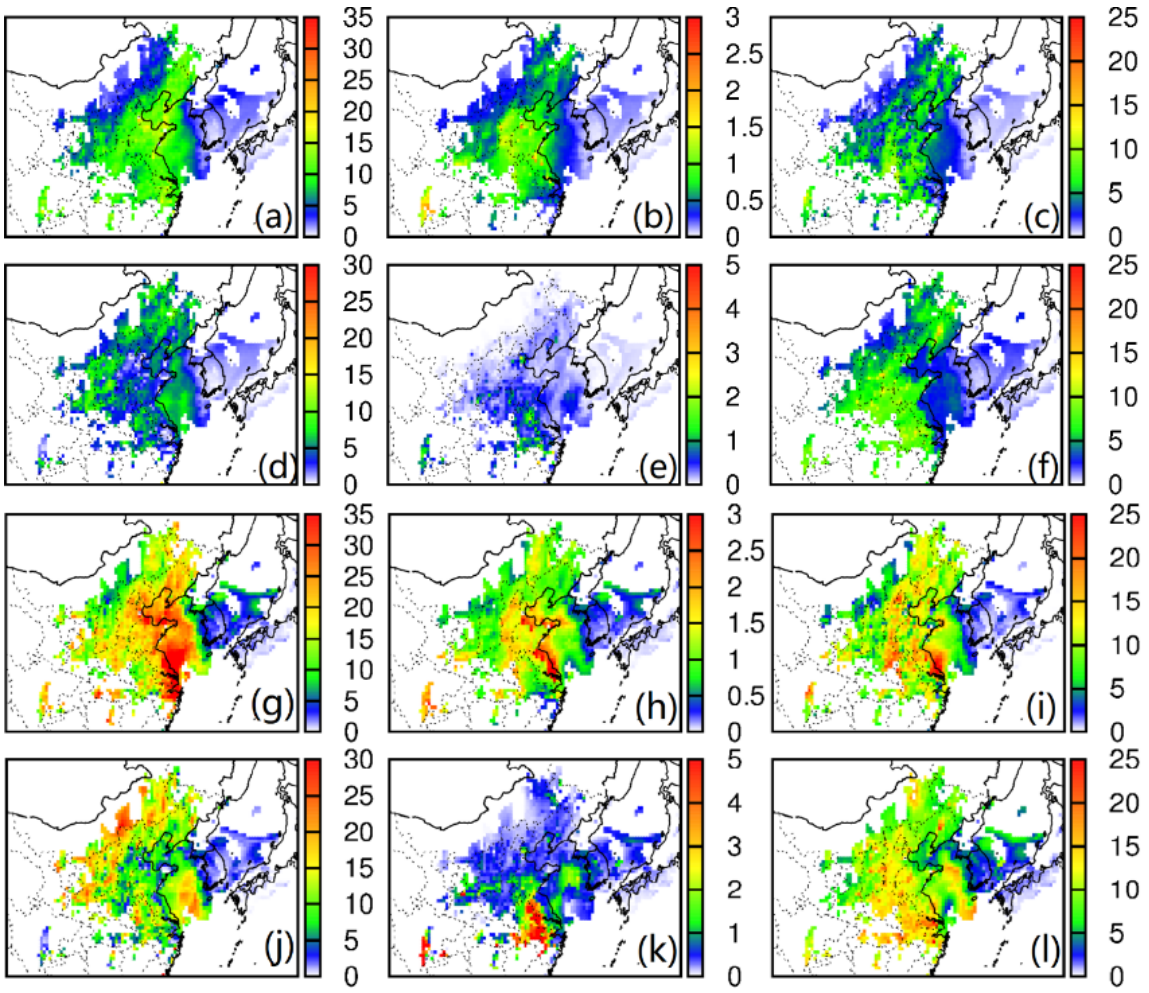


Figure C.5: Average source contributions of (a) industries, (b) residential, (c) transportation, (d) power, (e) open burning and (f) biogenic emissions to 8-hr ozone on low ozone days (8-hr ozone within 40 and 80 ppb), and (g) industries, (h) residential, (i) transportation, (j) power, (k) open burning and (l) biogenic emissions to 8-hr ozone on high ozone days (8-hr ozone > 80 ppb) in August 2013. Units are ppb. Only the regions with high ozone days are shown in the panels.

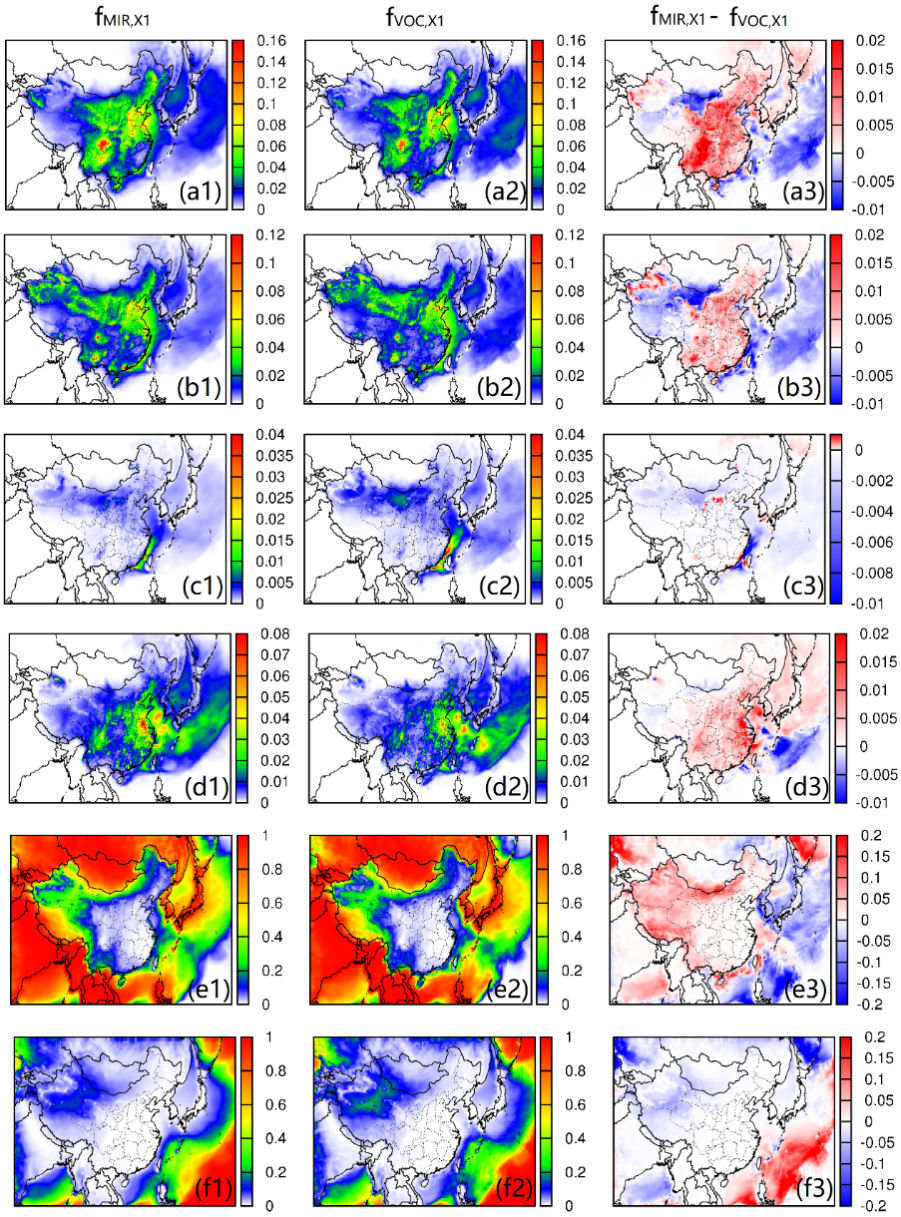


Figure C.6: $O_3$_VOC source attribution fraction for residential (row a), transportation (row b), power plants (row c), open burning (row d), other countries (row e) and initial and boundary conditions (row f) based on the MIR weighted concentrations ($S_{VOC}^{MIR}$, equation 7', first column) and the NO to NO2 conversion rate due to VOC generated RO2/HO2 radicals ($S_{VOC}$ , equation 7, second column). The last column shows the difference in the source attribution fraction. This is calculated based on monthly (August 2013) averaged concentrations and conversion rates between 8 am and 4 pm.

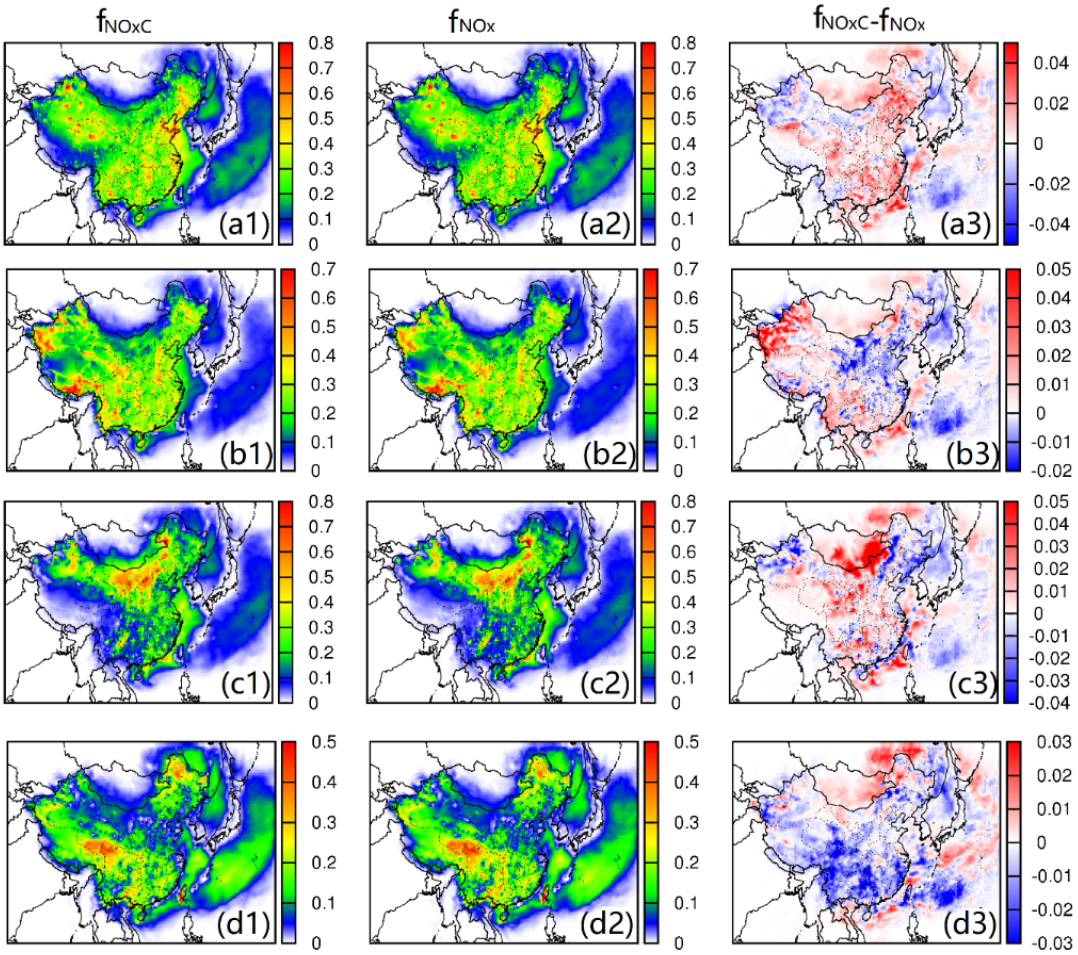


Figure C.7: $O_3$_$NO_x$ source attribution fraction for industry (row a), transportation (row b), power plants (row c) and biogenic (row d) sectors based on fractional $NO_x$ concentrations (equation 6', first column) and the $O^3P$ radical formation rate due to NO2 photolysis (equation 6, second column). The last column shows the difference in the source attribution fraction. This is calculated based on monthly (August 2013) averaged concentrations and conversion rates between 8 am and 4 pm.

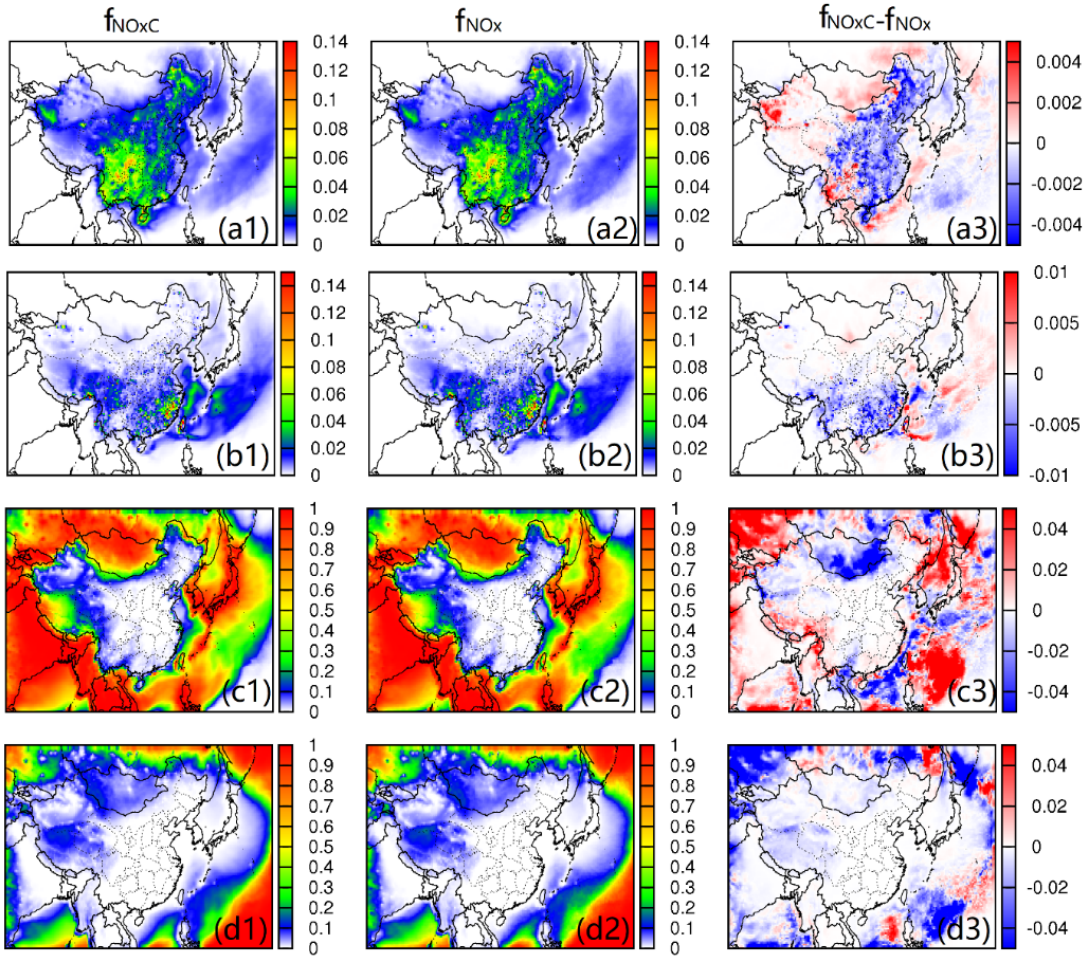


Figure C.8: $O_3$_$NO_x$ source attribution fraction for residential (row a), open burning (row b), other countries (row c) and initial and boundary conditions (row d) based on fractional $NO_x$ concentrations (equation 6', first column) and the $O^{3P}$ radical formation rate due to $NO_2$ photolysis (equation 6, second column). The last column shows the difference in the source attribution fraction. This is calculated based on monthly (August 2013) averaged concentrations and conversion rates between 8 am and 4 pm.

Table C.2: Monthly average 8-hr $O_3$_$NO_x$ and source contributions to non-background 8-h ozone for each province in China, August 2013.

| Province | Avg. ppb | Relative contributions to $O_3$_$NO_x$ (%) | | | | | | | |
|---|---|---|---|---|---|---|---|---|---|
| | | Ind. | Res. | Transp. | Power | OB | Biog. | Other | IC/BC |
| BJ | 26.4 | 34.0 | 2.3 | 32.3 | 18.2 | 0.4 | 12.4 | 0.3 | 0.1 |
| TJ | 22.5 | 42.1 | 1.8 | 27.7 | 17.7 | 0.8 | 9.4 | 0.5 | 0.0 |
| HE | 23.2 | 33.3 | 1.8 | 24.6 | 26.2 | 0.6 | 13.1 | 0.3 | 0.1 |
| SX | 22.6 | 29.7 | 1.6 | 20.2 | 34.0 | 1.0 | 13.3 | 0.2 | 0.1 |
| NM | 9.0 | 23.0 | 1.9 | 16.4 | 36.0 | 0.3 | 17.0 | 4.3 | 1.0 |
| LN | 24.3 | 38.3 | 1.5 | 22.9 | 22.2 | 0.6 | 10.9 | 3.5 | 0.1 |
| JL | 20.5 | 35.0 | 1.6 | 19.6 | 23.3 | 0.5 | 13.8 | 5.9 | 0.2 |
| HL | 13.0 | 25.9 | 2.0 | 22.9 | 21.1 | 0.4 | 20.4 | 6.5 | 0.7 |
| SH | 11.2 | 41.0 | 0.4 | 19.6 | 22.2 | 4.9 | 6.8 | 5.1 | 0.0 |
| JS | 22.2 | 33.4 | 1.6 | 25.7 | 21.2 | 4.0 | 13.5 | 0.7 | 0.0 |
| ZJ | 17.3 | 33.6 | 0.8 | 26.2 | 14.0 | 6.8 | 17.3 | 1.3 | 0.0 |
| AH | 24.9 | 27.2 | 2.1 | 26.6 | 20.1 | 3.4 | 20.5 | 0.2 | 0.0 |
| FJ | 12.9 | 30.1 | 1.1 | 22.9 | 19.5 | 6.2 | 19.4 | 0.9 | 0.1 |
| JX | 18.9 | 27.0 | 1.8 | 25.9 | 18.5 | 3.8 | 22.4 | 0.5 | 0.0 |
| SD | 24.6 | 36.9 | 1.8 | 27.2 | 20.3 | 1.3 | 12.1 | 0.4 | 0.0 |
| HA | 23.6 | 33.8 | 1.8 | 25.9 | 19.1 | 1.1 | 18.1 | 0.2 | 0.0 |
| HB | 20.8 | 35.0 | 2.7 | 22.3 | 15.8 | 2.0 | 21.7 | 0.5 | 0.1 |
| HN | 16.6 | 32.6 | 2.5 | 24.2 | 16.5 | 2.8 | 20.5 | 0.8 | 0.1 |
| GD | 12.1 | 26.5 | 3.2 | 23.5 | 22.3 | 2.0 | 19.2 | 3.2 | 0.1 |
| GX | 12.7 | 30.3 | 2.8 | 23.6 | 11.9 | 2.0 | 24.3 | 5.0 | 0.1 |
| HI | 6.5 | 24.0 | 3.8 | 22.0 | 12.4 | 0.9 | 16.4 | 20.4 | 0.2 |
| CQ | 19.5 | 32.1 | 3.6 | 25.7 | 15.4 | 1.6 | 20.3 | 1.1 | 0.1 |
| SC | 16.7 | 30.8 | 4.7 | 24.2 | 11.8 | 2.4 | 23.7 | 2.1 | 0.5 |
| GZ | 14.2 | 30.1 | 3.9 | 20.9 | 20.6 | 1.1 | 20.2 | 3.2 | 0.1 |
| YN | 10.3 | 31.4 | 3.7 | 27.4 | 11.9 | 1.6 | 17.5 | 6.1 | 0.3 |
| XZ | 5.0 | 9.5 | 0.8 | 18.6 | 3.5 | 0.8 | 10.5 | 54.6 | 1.9 |
| SN | 22.3 | 28.1 | 3.2 | 24.2 | 22.0 | 1.0 | 20.7 | 0.7 | 0.2 |
| GS | 11.8 | 29.0 | 2.6 | 26.2 | 21.9 | 0.7 | 17.0 | 1.6 | 0.9 |
| QH | 5.0 | 29.0 | 2.1 | 24.3 | 12.8 | 0.9 | 21.5 | 7.3 | 2.2 |
| NX | 16.8 | 26.1 | 2.5 | 28.6 | 26.0 | 0.7 | 15.1 | 0.5 | 0.4 |
| XJ | 3.5 | 26.6 | 0.8 | 21.9 | 20.3 | 0.3 | 13.4 | 13.2 | 3.4 |
| TW | 2.7 | 14.7 | 0.7 | 10.3 | 12.9 | 3.8 | 24.5 | 32.8 | 0.4 |

Table C.3: Monthly average 8-hr $O_3$_VOC and source contributions to non-background 8-h ozone for each province in China, August 2013.

| Province | Avg. ppb | Relative contributions to $O_3$_VOC (%) | | | | | | | |
|---|---|---|---|---|---|---|---|---|---|
| | | Ind. | Res. | Transp. | Power | OB | Biog. | Other | IC/BC |
| BJ | 9.1 | 35.5 | 4.7 | 5.4 | 0.1 | 1.0 | 52.0 | 0.9 | 0.3 |
| TJ | 13.6 | 42.0 | 5.3 | 5.2 | 0.2 | 1.8 | 43.7 | 1.4 | 0.4 |
| HE | 7.7 | 27.5 | 5.6 | 4.2 | 0.3 | 1.6 | 58.9 | 1.4 | 0.5 |
| SX | 11.1 | 21.0 | 3.8 | 3.3 | 0.3 | 1.3 | 67.8 | 1.8 | 0.7 |
| NM | 1.0 | 19.4 | 3.8 | 3.0 | 0.5 | 0.7 | 66.6 | 4.5 | 1.4 |
| LN | 5.6 | 32.0 | 3.7 | 3.0 | 0.2 | 1.3 | 56.3 | 2.9 | 0.6 |
| JL | 2.3 | 24.8 | 3.9 | 2.7 | 0.2 | 0.9 | 61.7 | 5.0 | 0.9 |
| HL | 0.9 | 20.7 | 4.1 | 2.2 | 0.2 | 0.4 | 63.7 | 7.6 | 1.1 |
| SH | 11.9 | 51.7 | 2.2 | 3.9 | 0.3 | 3.1 | 34.4 | 4.0 | 0.3 |
| JS | 9.8 | 34.2 | 4.3 | 3.8 | 0.2 | 2.7 | 53.2 | 1.3 | 0.3 |
| ZJ | 2.7 | 36.2 | 1.9 | 3.4 | 0.2 | 2.4 | 52.8 | 2.8 | 0.4 |
| AH | 4.2 | 21.9 | 5.7 | 3.0 | 0.2 | 2.2 | 65.5 | 1.1 | 0.4 |
| FJ | 1.1 | 26.5 | 1.8 | 3.9 | 1.0 | 1.5 | 62.9 | 1.7 | 0.6 |
| JX | 0.9 | 14.8 | 2.5 | 2.3 | 0.1 | 1.3 | 77.4 | 1.1 | 0.4 |
| SD | 13.0 | 34.7 | 6.0 | 4.6 | 0.2 | 2.3 | 50.0 | 1.7 | 0.5 |
| HA | 6.2 | 25.8 | 5.4 | 3.9 | 0.2 | 1.5 | 61.4 | 1.3 | 0.5 |
| HB | 2.7 | 22.0 | 5.3 | 2.8 | 0.1 | 1.4 | 66.9 | 1.0 | 0.4 |
| HN | 1.3 | 16.2 | 3.6 | 2.1 | 0.1 | 0.8 | 75.1 | 1.6 | 0.4 |
| GD | 1.9 | 38.7 | 2.3 | 6.6 | 0.2 | 1.1 | 46.0 | 4.5 | 0.6 |
| GX | 0.68 | 12.6 | 3.3 | 2.6 | 0.1 | 1.1 | 73.3 | 6.5 | 0.6 |
| HI | 0.3 | 8.9 | 4.1 | 2.7 | 0.1 | 0.8 | 66.8 | 15.7 | 0.9 |
| CQ | 2.6 | 19.1 | 6.0 | 2.2 | 0.1 | 1.0 | 68.5 | 2.7 | 0.3 |
| SC | 1.0 | 19.8 | 9.3 | 4.5 | 0.1 | 1.6 | 62.1 | 2.2 | 0.3 |
| GZ | 1.3 | 15.7 | 7.3 | 3.3 | 0.2 | 0.8 | 64.3 | 7.8 | 0.7 |
| YN | 0.5 | 17.8 | 5.3 | 5.7 | 0.1 | 0.6 | 61.0 | 8.8 | 0.7 |
| XZ | 0.01 | 2.3 | 0.6 | 3.6 | 0.0 | 0.4 | 30.1 | 60.9 | 2.0 |
| SN | 2.0 | 20.7 | 5.6 | 3.8 | 0.2 | 1.2 | 65.9 | 2.0 | 0.6 |
| GS | 0.7 | 21.0 | 5.0 | 4.0 | 0.3 | 0.7 | 65.3 | 2.4 | 1.3 |
| QH | 0.1 | 22.6 | 4.8 | 5.8 | 0.2 | 0.9 | 62.0 | 2.3 | 1.5 |
| NX | 2.3 | 20.8 | 3.8 | 3.3 | 0.4 | 0.9 | 67.6 | 2.2 | 1.1 |
| XJ | 0.2 | 22.2 | 1.0 | 3.4 | 0.2 | 0.2 | 60.5 | 9.5 | 3.1 |
| TW | 0.03 | 25.4 | 2.5 | 4.0 | 0.9 | 2.3 | 49.3 | 13.5 | 2.1 |

# APPENDIX D

# SUPPLEMENTARY MATERIAS OF IMPROVED MEGAN PREDICTIONS OF BIOGENIC ISOPRENE IN THE CONTIGUOUS UNITED STATES

Table D.1: Auto-GC sites in Texas

| | AIRScode | Latitude | Longitude | Region | Name | Location Type |
|---|---|---|---|---|---|---|
| 1 | 484970088 | 33.2217 | -97.584 | Dallas/Fort Worth | Decatur Thompson | Urban |
| 2 | 481211013 | 33.1309 | -97.298 | Dallas/Fort Worth | Dish Airfield | Rural |
| 3 | 481211007 | 33.0459 | -97.13 | Dallas/Fort Worth | Flower Mound Shiloh | Suburban |
| 4 | 481130069 | 32.8201 | -96.86 | Dallas/Fort Worth | Dallas Hinton | Urban |
| 5 | 484391002 | 32.8058 | -97.357 | Dallas/Fort Worth | Fort Worth Northwest | Urban |
| 6 | 484391009 | 32.6211 | -97.29 | Dallas/Fort Worth | Everman Johnson Park | Suburban |
| 7 | 484390075 | 32.9879 | -97.477 | Dallas/Fort Worth | Eagle Mountain Lake | Rural |
| 8 | 483550041 | 27.8292 | -97.544 | Corpus Christi | Solar Estates | Suburban |
| 9 | 483550035 | 27.7989 | -97.434 | Corpus Christi | Oak Park | Urban |
| 10 | 483550083 | 27.8029 | -97.42 | Corpus Christi | Corpus Christi Palm | Suburban |
| 11 | 482450009 | 30.0364 | -94.071 | Beaumont | Beaumont Downtown | Suburban |
| 12 | 482451035 | 29.9789 | -94.011 | Beaumont | Nederland High School | Suburban |
| 13 | 480390618 | 29.1489 | -95.765 | Houston | Danciger | Suburban |
| 14 | 480391016 | 29.0438 | -95.473 | Houston | Lake Jackson | Urban |
| 15 | 481670056 | 29.4057 | -94.947 | Houston | Texas City 34th Street | Urban |
| 16 | 482011035 | 29.7337 | -95.258 | Houston | Clinton | Suburban |
| 17 | 482010069 | 29.7062 | -95.261 | Houston | Milby Park | Suburban |
| 18 | 482016000 | 29.6844 | -95.254 | Houston | Cesar Chavez | Suburban |
| 19 | 482010617 | 29.8214 | -94.99 | Houston | Wallisville Road | Suburban |
| 20 | 482010026 | 29.8027 | -95.126 | Houston | Channelview | Urban |
| 21 | 482011039 | 29.67 | -95.129 | Houston | Houston Deer Park | Suburban |
| 22 | 482010803 | 29.7648 | -95.179 | Houston | HRM #3 Haden Rd | Suburban |
| 23 | 482011015 | 29.7617 | -95.081 | Houston | Lynchburg Ferry | Suburban |

Table D.2: Location of the isoprene monitors in other states

| | AIRS Code | Name | State | Longitude | Latitude | Land Use | Location Type |
|---|---|---|---|---|---|---|---|
| 1 | 060010007 | Livermore | CA | -121.7842 | 37.6875 | Commercial | Urban |
| 2 | 090019003 | Sherwood Island | CT | -73.3367 | 41.1183 | Forest | Rural |
| 3 | 090031003 | McAuliffe Park, East Hartford | CT | -72.6317 | 41.7847 | Residential | Suburban |
| 4 | 110010043 | McMillian Reservoir (S.E. end) | DC | -77.0132 | 38.9218 | Commercial | Urban |
| 5 | 130890002 | South DeKalb, Decatur | GA | -84.2905 | 33.6880 | Residential | Suburban |
| 6 | 132230003 | Yorkville | GA | -85.0453 | 33.9285 | Agricultural | Rural |
| 7 | 132470001 | Conyers Monastery | GA | -84.0653 | 33.5911 | Agricultural | Rural |
| 8 | 180890022 | IITRI Bunker, Gary | IN | -87.3047 | 41.6067 | Industrial | Urban |
| 9 | 230090102 | Top of Cadillac Mountain | ME | -68.2270 | 44.3517 | Mobile | Rural |
| 10 | 240053001 | Essex | MD | -76.4744 | 39.3108 | Residential | Suburban |
| 11 | 250092006 | Lynn | MA | -70.9708 | 42.4746 | Commercial | Urban |
| 12 | 250094005 | Newburyport | MA | -70.8178 | 42.8144 | Industrial | Urban |
| 13 | 250130008 | Anderson Road Air Force Base | MA | -72.5551 | 42.1944 | Commercial | Suburban |
| 14 | 250154002 | Quabbin Summit, Ware | MA | -72.3341 | 42.2985 | Forest | Rural |
| 15 | 330111011 | Gilson Road, Nashua | NH | -71.5224 | 42.7189 | Residential | Suburban |
| 16 | 330115001 | Pack Monadnock Summit | NH | -71.8784 | 42.8618 | Forest | Rural |
| 17 | 340230011 | R.U. Veg Research Farm | NJ | -74.4294 | 40.4622 | Agricultural | Rural |
| 18 | 360050133 | Pfizer Plant Research Laboratory | NY | -73.8781 | 40.8679 | Residential | Urban |
| 19 | 420010001 | NARSTO Site - Arendtsville | PA | -77.3097 | 39.9200 | Residential | Rural |
| 20 | 510330001 | National Geodetic Survey, Corbin | VA | -77.3774 | 38.2009 | Forest | Rural |

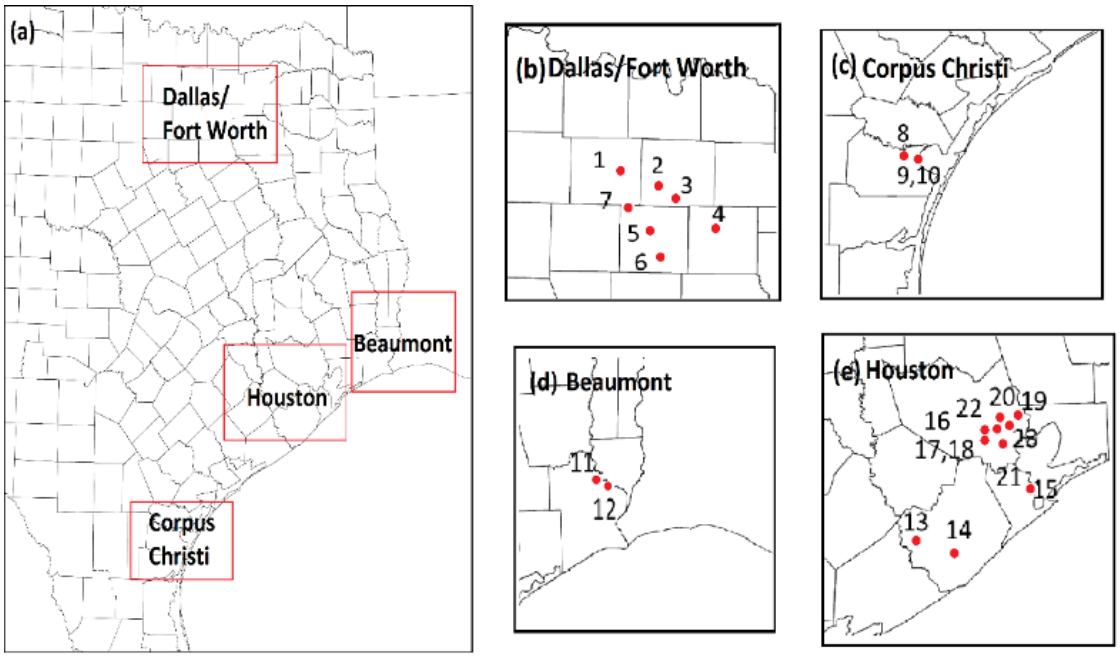


Figure D.1: Location of the Auto-GC sites in the East Texas. Panel (a) Auto-GC sites allocations in the Texas domain, (b) Auto-GC sites at Dallas/Fort Worth area, (c) Auto-GC sites at Corpus Christi area, (d) Auto-GC sites at Beaumont area and (e) Auto-GC sites at Houston area.

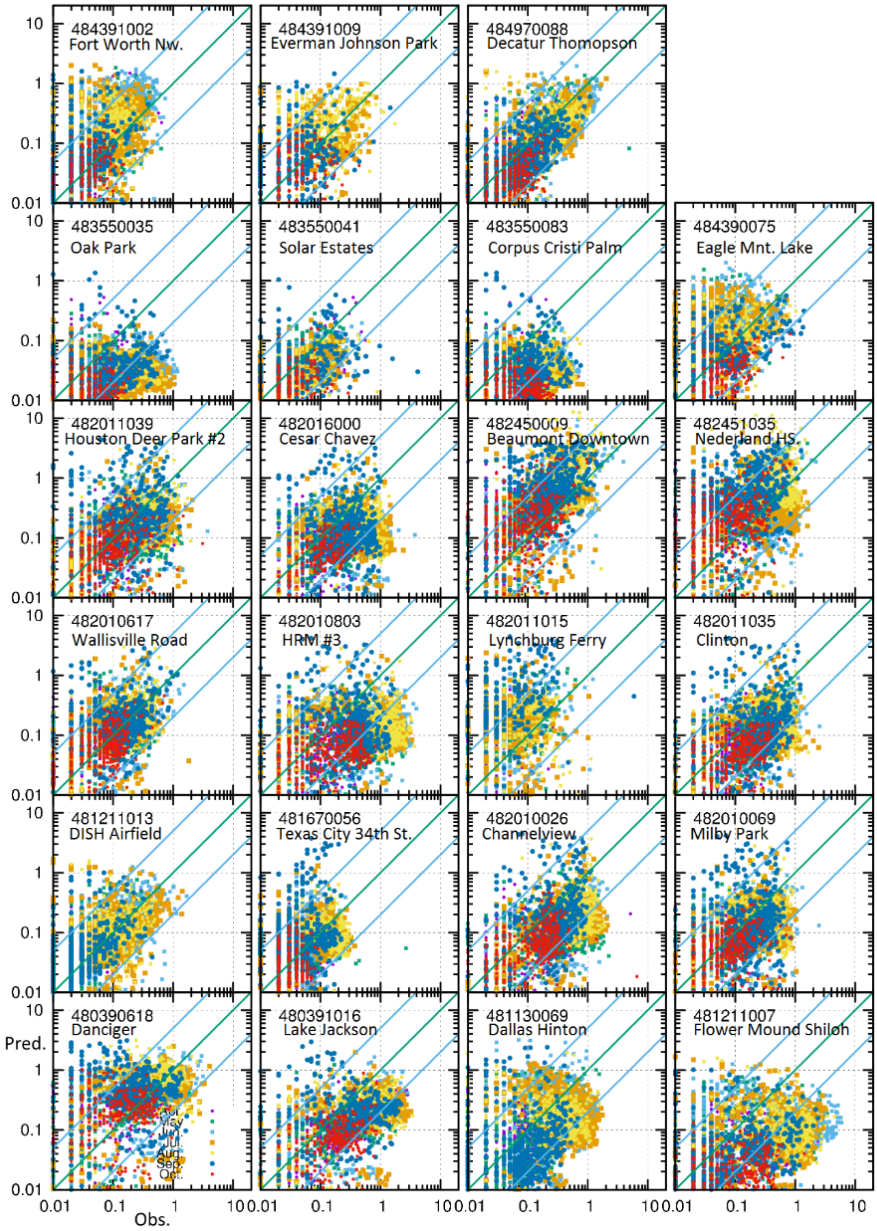


Figure D.2: Predicted (36-km) vs. observed hourly average isoprene at all Texas Auto-GC sites with valid measurements in April to October 2011. (Units are ppb). The green lines are 1:1, 1:5 and 5:1 ratios. Horizontal axes are predictions; vertical axes are observations.

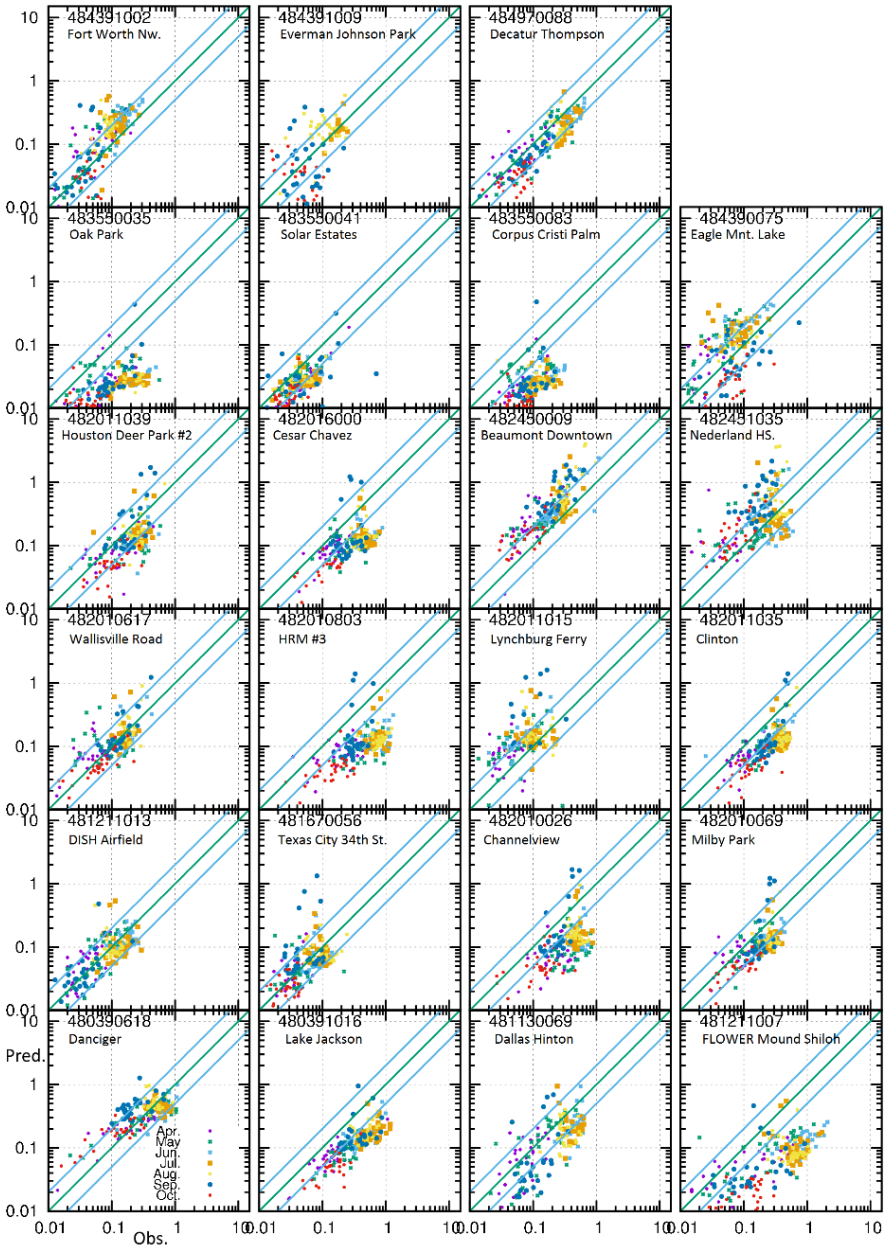


Figure D.3: Predicted vs. observed daily average isoprene at all Texas sites with valid measurements in April to October 2011. (Units are ppb). The green lines are 1:1, 1:5 and 5:1 ratios. Horizontal axes are predictions; vertical axes are observations.

Table D.3: Model performance of isoprene for April to October, 2011 based on hourly 4-km results at Auto-GC monitors in Texas.

| Month | MFB | MFE | Obs. | Pred. | # points |
|---|---|---|---|---|---|
| April | -0.63 | 1.19 | 0.12 | 0.10 | 9513 |
| May | -0.64 | 1.15 | 0.20 | 0.13 | 11015 |
| June | -0.81 | 1.20 | 0.36 | 0.17 | 12022 |
| July | -0.81 | 1.24 | 0.32 | 0.18 | 13199 |
| August | -0.77 | 1.27 | 0.31 | 0.22 | 13232 |
| September | -0.60 | 1.26 | 0.18 | 0.24 | 11356 |
| October | -0.98 | 1.28 | 0.10 | 0.06 | 8313 |

Table D.4: Model performance of isoprene for April to October, 2011 based on daily average 4-km results at Auto-GC monitors in Texas.

| Month | MFB | MFE | Obs. | Pred. | # points |
|---|---|---|---|---|---|
| April | -0.39 | 0.89 | 0.11 | 0.09 | 618 |
| May | -0.50 | 0.86 | 0.19 | 0.13 | 663 |
| June | -0.75 | 0.93 | 0.34 | 0.17 | 636 |
| July | -0.75 | 1.00 | 0.32 | 0.18 | 678 |
| August | -0.62 | 0.94 | 0.30 | 0.21 | 696 |
| September | -0.40 | 0.93 | 0.17 | 0.22 | 656 |
| October | -0.79 | 1.02 | 0.09 | 0.06 | 534 |

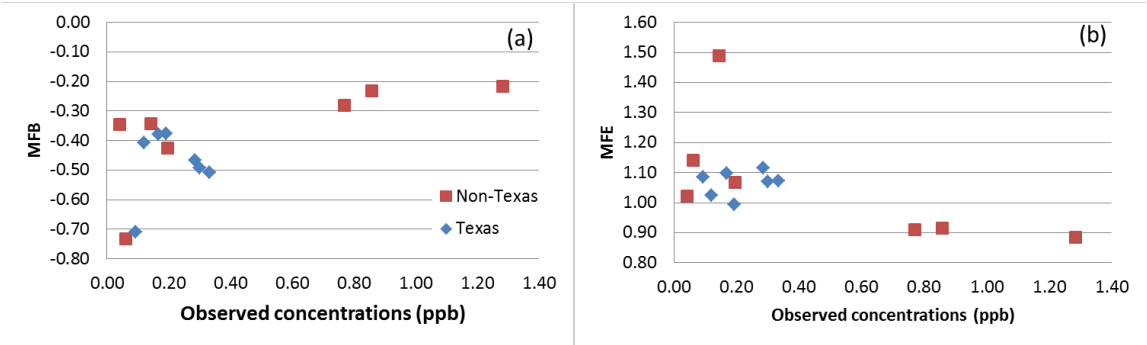


Figure D.4: Comparison of MFB and MFE based hourly concentrations at monitors in Texas and other states.

Table D.5: Meteorology performance for April to October 2011 (OBS is mean observation; PRE is mean prediction; MB is mean bias; GE is gross error; RMSE is root mean square error). The benchmarks are suggested standard for the MM5 model in the eastern USA with 4 * 12 km grid resolution. The values that do not meet the criteria are denoted in bold.

| | | Apr | May | Jun | Jul | Aug | Sep | Oct | Bench -mark |
|---|---|---|---|---|---|---|---|---|---|
| T2 (K) | OBS | 283.57 | 287.98 | 292.79 | 296.37 | 295.39 | 291.36 | 286.28 | |
| | PRE | 284.30 | 288.50 | 293.43 | 296.97 | 296.41 | 292.46 | 287.10 | |
| | MB | 0.94 | 0.76 | 0.69 | 0.75 | 1.10 | 1.18 | 1.03 | $\leq \pm 0.5$ |
| | GE | 2.32 | 2.35 | 2.33 | 2.31 | 2.32 | 2.32 | 2.19 | $\leq 2.0$ |
| | RMSE | 3.17 | 3.21 | 3.23 | 3.13 | 3.13 | 3.11 | 2.91 | |
| WS (m/s) | OBS | 4.50 | 4.35 | 4.11 | 3.73 | 3.71 | 3.80 | 4.06 | |
| | PRE | 5.34 | 5.04 | 4.71 | 4.24 | 4.12 | 4.23 | 4.66 | |
| | MB | 0.84 | 0.68 | 0.6 | 0.51 | 0.41 | 0.42 | 0.6 | $\leq \pm 0.5$ |
| | GE | 1.77 | 1.67 | 1.61 | 1.54 | 1.5 | 1.5 | 1.57 | $\leq 2.0$ |
| | RMSE | 2.26 | 2.14 | 2.08 | 1.99 | 1.94 | 1.96 | 2.03 | $\leq 2.0$ |
| WD (°) | OBS | 188.88 | 173.52 | 186.07 | 196.07 | 202.33 | 184.97 | 190.15 | |
| | PRE | 199.22 | 180.17 | 195.33 | 204.08 | 209.95 | 187.43 | 199.32 | |
| | MB | 10.56 | 7.98 | 9.03 | 8.4 | 7.87 | 4.38 | 10.19 | $\leq \pm 10$ |
| | GE | 32.87 | 34.76 | 36.4 | 40.53 | 40.06 | 38.69 | 34.29 | $\leq \pm 30$ |
| | RMSE | 48.1 | 50.75 | 52.44 | 57.03 | 56.44 | 55.39 | 50.15 | |
| RH (%) | OBS | 74.25 | 72.17 | 68.61 | 67.29 | 67.07 | 69.03 | 70.35 | |
| | PRE | 68.64 | 70.33 | 69.03 | 66.61 | 64.11 | 65.33 | 65.89 | |
| | MB | -5.61 | -1.82 | 0.41 | -0.69 | -2.97 | -3.69 | -4.45 | |
| | GE | 13.06 | 11.79 | 11.2 | 11.34 | 11.55 | 11.33 | 12.03 | |
| | RMSE | 17.39 | 15.55 | 14.73 | 15 | 15.26 | 15.05 | 15.93 | |

Table D.6: Predicted hourly (local standard time) photosynthetically active radiation (PAR, W/m2) for July 2011 based on half of the solar radiation reaching surface (RGRND) and the ratio of observed to predicted PAR values at seven SURFRAD network stations: BND (Bondville, IL), DRA (Desert Rock, NV), FPK (Fort Peck, MT), GCM (Goodwin Creek, MS), PSU (Penn State, PA), SXF (Sioux Falls, SD), and TBL (Boulder, CO). The details of the SURFRAD stations can be found in http://www.esrl.noaa.gov /gmd/grad/surfrad/sitepage.html.

| | BND | | DRA | | FPK | | GCM | | PSU | | SXF | | TBL | |
|---|---|---|---|---|---|---|---|---|---|---|---|---|---|---|
| Hour | PRE | O/P | PRE | O/P | PRE | O/P | PRE | O/P | PRE | O/P | PRE | O/P | PRE | O/P |
| 5 | 39 | 0.76 | 45 | 0.97 | 54 | 0.89 | 25 | 0.69 | 25 | 0.78 | 19 | 0.76 | 35 | 0.80 |
| 6 | 123 | 0.67 | 140 | 0.84 | 132 | 0.82 | 100 | 0.67 | 92 | 0.78 | 78 | 0.74 | 120 | 0.82 |
| 7 | 219 | 0.69 | 241 | 0.81 | 219 | 0.80 | 196 | 0.69 | 179 | 0.76 | 158 | 0.77 | 219 | 0.84 |
| 8 | 309 | 0.68 | 333 | 0.82 | 302 | 0.83 | 288 | 0.73 | 266 | 0.71 | 245 | 0.80 | 314 | 0.86 |
| 9 | 385 | 0.70 | 416 | 0.78 | 369 | 0.82 | 372 | 0.72 | 344 | 0.72 | 326 | 0.79 | 395 | 0.85 |
| 10 | 440 | 0.71 | 475 | 0.75 | 416 | 0.83 | 440 | 0.69 | 393 | 0.74 | 392 | 0.74 | 455 | 0.79 |
| 11 | 473 | 0.70 | 507 | 0.74 | 448 | 0.81 | 476 | 0.74 | 433 | 0.74 | 437 | 0.72 | 474 | 0.75 |
| 12 | 480 | 0.68 | 511 | 0.75 | 461 | 0.78 | 483 | 0.75 | 464 | 0.73 | 460 | 0.70 | 460 | 0.76 |
| 13 | 456 | 0.68 | 482 | 0.76 | 443 | 0.80 | 466 | 0.73 | 447 | 0.72 | 459 | 0.69 | 440 | 0.70 |
| 14 | 401 | 0.68 | 426 | 0.76 | 397 | 0.77 | 414 | 0.72 | 400 | 0.68 | 428 | 0.70 | 396 | 0.61 |
| 15 | 329 | 0.66 | 348 | 0.76 | 338 | 0.79 | 339 | 0.68 | 337 | 0.63 | 367 | 0.73 | 328 | 0.58 |
| 16 | 250 | 0.60 | 251 | 0.74 | 272 | 0.76 | 248 | 0.69 | 266 | 0.65 | 292 | 0.72 | 250 | 0.51 |
| 17 | 163 | 0.50 | 148 | 0.68 | 193 | 0.69 | 151 | 0.61 | 180 | 0.62 | 211 | 0.65 | 179 | 0.42 |
| 18 | 73 | 0.41 | 53 | 0.48 | 108 | 0.60 | 66 | 0.43 | 91 | 0.54 | 132 | 0.56 | 86 | 0.46 |

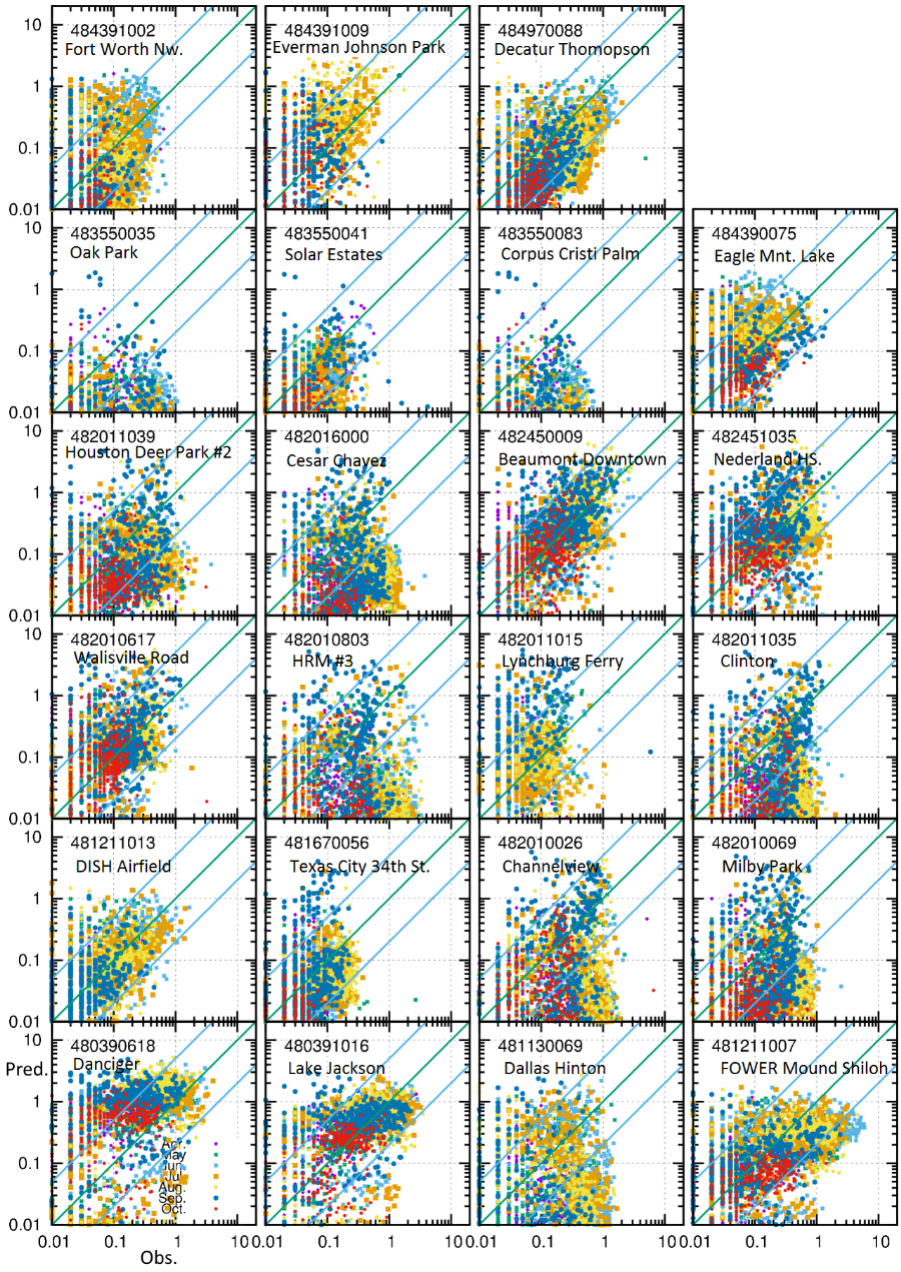


Figure D.5: Predicted (4-km) vs. observed hourly average isoprene at all Texas sites with valid measurements in April to October 2011. (Units are ppb). The green lines are 1:1, 1:5 and 5:1 ratios. Horizontal axes are predictions; vertical axes are observations.

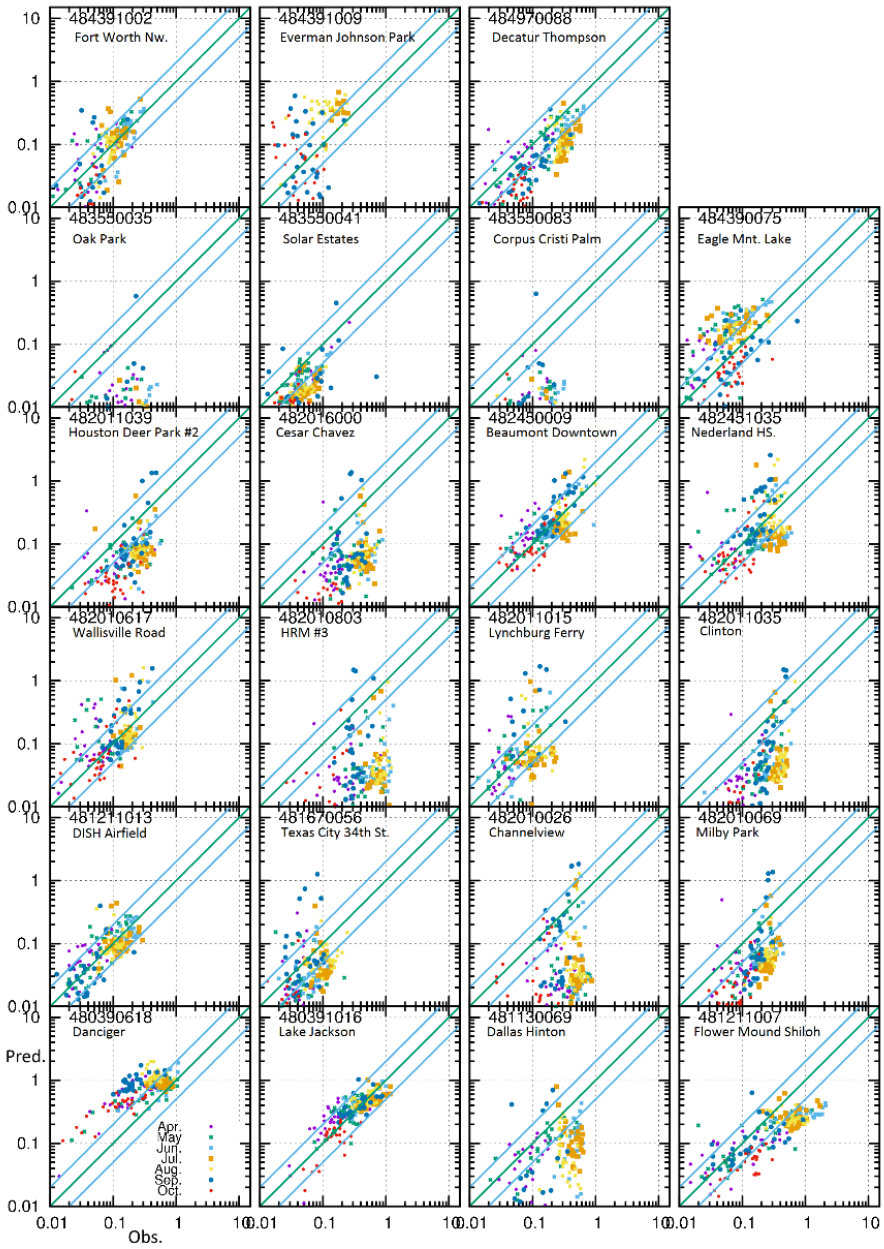


Figure D.6: Predicted (4-km) vs. observed daily average isoprene at all Texas sites with valid measurements in April to October 2011. (Units are ppb). The green lines are 1:1, 1:5 and 5:1 ratios. Horizontal axes are predictions; vertical axes are observations.

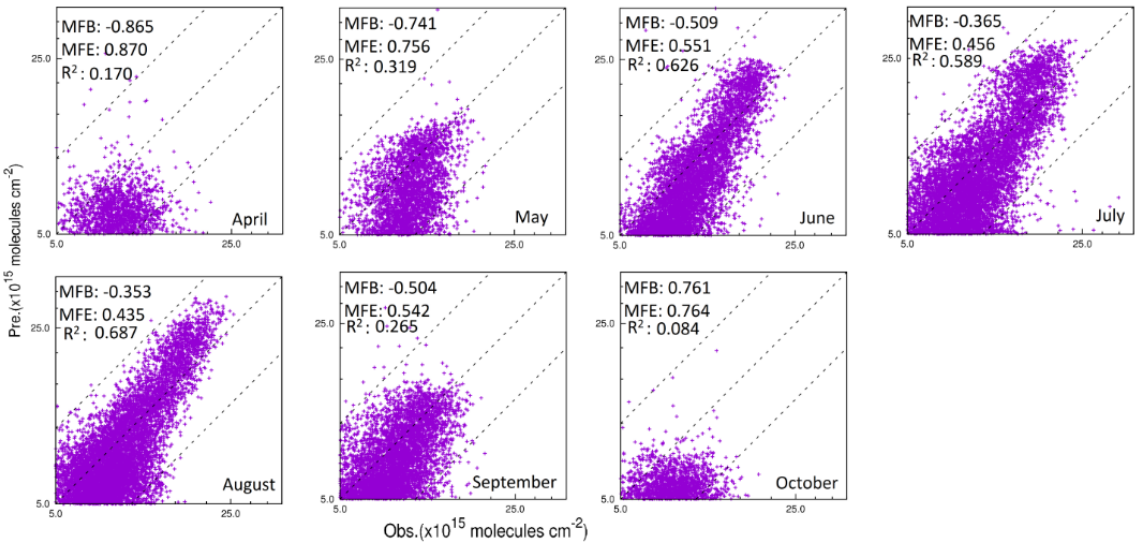


Figure D.7: CMAQ predicted vs OMI monthly HCHO columns for April to October 2011. The dash lines are 1:1, 1:2 and 2:1 ratios.

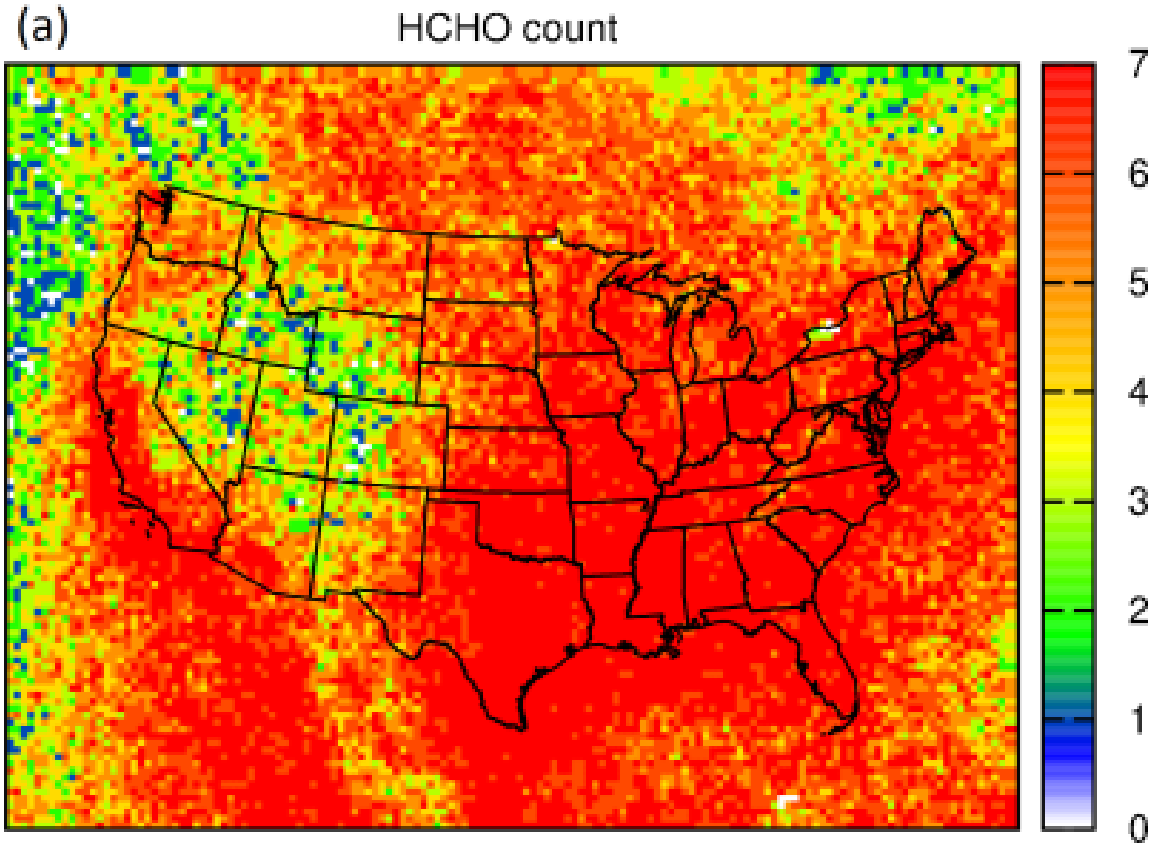


Figure D.8: Available number of data points (max=7) in the linear regression between observed (O) and predicted (P) monthly HCHO vertical column density; (b) the correlation coefficient (R2) for the linear regression; (c) the slope (k) of the linear regression. The linear relationship determined from the regression analysis is: $P = k \times O + b$, where b is the intercept.